The Pennsylvania State University

The Graduate School

College of Engineering

TURBULENCE MEASUREMENTS IN HIGH-SPEED WIND TUNNELS USING FOCUSING LASER DIFFERENTIAL INTERFEROMETRY

A Dissertation in

Mechanical Engineering

by

Matthew R. Fulghum

Submitted in Partial Fulfillment
of the Requirements
for the Degree of

Doctor of Philosophy

December 2014

The dissertation of Matthew R. Fulghum was reviewed and approved* by the following:

Gary S. Settles
Professor of Mechanical Engineering
Dissertation Adviser
Chair of Committee

Asok Ray
Distinguished Professor of Mechanical Engineering & Mathematics

John M. Cimbala
Professor of Mechanical Engineering

Philip J. Morris
Boeing/A. D. Welliver Professor of Aerospace Engineering

Daniel C. Haworth
Professor of Mechanical Engineering
Professor-In-Charge of MNE Graduate Programs

* Signatures are on file in the Graduate School.

Abstract

Characterization of freestream disturbances and their effect on laminar boundary layer transition is of great importance in high-speed wind tunnel testing, where significant differences between the behavior of scale-model and free-flight transition have long been noted. However, the methods traditionally used to perform this characterization in low-speed flows present significant difficulties when applied to supersonic and especially hypersonic wind tunnels. The design and theory of a focusing laser differential interferometer (FLDI) instrument, originally invented by Smeets at the Institut Saint-Louis in the 1970s and used recently by Parziale in the CalTech T5 shock tunnel, is presented. It is a relatively-simple, non-imaging common-path interferometer for measuring refractive signals from transition and turbulence, and it has a unique ability to look through facility windows, ignore sidewall boundary-layers and vibration, and concentrate only on the refractive signal near a pair of sharp beam foci in the core flow. The instrument's low cost and ease of implementation make it a promising alternative to traditional hot-wire anemometry and particle-based methods for turbulence characterization. Benchtop experiments using a turbulent supersonic air jet demonstrate its focusing ability, frequency response, unwanted signal rejection, and ease of use. The instrument is used to optically interrogate the flow in the Penn State University Supersonic Wind Tunnel and USAF AEDC Hypervelocity Tunnel 9 for measurement of the overall intensity and spectra of freestream disturbances. Precise characterization of the strength and spectral content of the disturbances provides insight into their nature and potential effect upon boundary layer transition. A special feature of the FLDI instrument used here is the replacement of traditional fixed Wollaston prisms with variable Sanderson prisms for laser-beam separation and recombination.

Table of Contents

List of Tables

List of Figures

List of Symbols

c – Contraction ratio of wind tunnel nozzle

u, v, w – Flow velocity vector components

ρ – Density of fluid

γ – Ratio of specific heats

M – Mach number

T_0 – Stagnation temperature

T – Static temperature

T_w – Hot-wire operating temperature

T_r – Recovery temperature

τ – Hot-wire overheat ratio $(T_w - T_r) / T_0$

r – Recovery factor

P_0 – Stagnation pressure

Pr – Prandtl number

U – Mean flow velocity

U_C – Convective velocity of turbulent disturbances

L – Distance from center of Sanderson prisms to outer load point

X – Maximum deflection of Sanderson prism

Y – Distance between Sanderson prism load points

h – Height of Sanderson prism

b – Thickness of Sanderson prism

φ – Phase difference induced by Berek compensator

θ – Tilt angle of the Berek compensator

t – Thickness of the Berek compensator window

λ – Wavelength of the laser light

n – Refractive index

n_o, n_e – Birefringent indices of refraction of the Berek compensator window

A_j, λ_j – Sellmeier coefficients of Berek compensator window material

R_L – Photodiode load resistance

dx, dt – Measured beam displacement and time delay from crossed-beam schlieren

δ – Displacement of crossed-beam schlieren beam on detector

K_{GD} – Gladstone-Dale coefficient

ε_x, ε_y – Deflection angles from deflectometry

s – Optical beam path

$\Delta\varphi$ – Beam phase delay from density inhomogeneities

I – Beam intensity

x – Beam displacement axis

z – Optical axis of FLDI system

y – Axis perpendicular to the beam displacement and propagation axes

E_x, E_y – Amplitude of light polarization components

ϕ_x, ϕ_y – Phase of light polarization components

I_p, I_s – Intensity measured by photodiodes

σ – Principal axes of stress in the Sanderson prism

q_{11}, q_{12} – Stress-optic coefficients of Sanderson prism material

P – Load on prism

M – Bending moment in prism

E – Modulus of elasticity of prism material

I_{zz} – Area moment of inertia of prism

t – Time

τ – Time difference between samples of signal for finite difference

η – Kolmogorov microscale

$\vec{r}$ – Position vector of turbulence signal for FLDI finite difference

F_+, F_- – Signal from the two FLDI beams for the finite difference

$H(k)$ – Transfer function of spatial filters

k – Wavenumber

w_0 – Gaussian beam waist

d – Focal distance of the FLDI system

$D_{4\sigma}$ – Beam diameter at the field lenses

L – Distance from test section windows to tunnel centerline

σ_{jet} – Standard deviation width of Gaussian turbulent jet

z_0 – Distance from beam focus to turbulent jet centerline

L_o – Outer scale of turbulence

L_i – Inner scale of turbulence2

Tu_{BL} – Boundary layer turbulence intensity

Tu_{∞} – Freestream turbulence intensity

f_L – Focal length of meniscus lens used for FLDI calibration

f_2 – Focal length of FLDI field lenses

F_{AB} – Photodiode difference signal

$\Delta\varphi_A$, $\Delta\varphi_B$ – FLDI beam phase difference

x – Streamwise distance from jet exit to beam focus

D – Turbulent jet nozzle diameter

κ – Kleinstein proportionality constant

Acknowledgements

I am grateful for the advice and assistance of my thesis advisor, Prof. Gary Settles, whose dedication to his students and to his craft is endlessly appreciated. I would also like to thank my committee members, Profs. John Cimbala, Philip Morris, and Asok Ray, whose advice and commitment to the success of this research has been immensely helpful.

I would also like to acknowledge the financial support of the USAF Arnold Engineering Development Center and the crew of AEDC Hypervelocity Wind Tunnel #9 for all of their help in testing and development of the instrument presented in this research.

Finally, I need to thank my friends, family, and the staff of the Penn State Gas Dynamics Lab, whose moral support helped to keep me going to the end. I could not have made it here without them.

Chapter 1: Introduction

Turbulence, and the transition from laminar to turbulent flow, are poorly-understood but crucially important features of fluid dynamics: they dramatically change the behavior of flows and their interactions with their surroundings. Accurate characterization of turbulence is important for modeling this behavior. Turbulent energy in the freestream of a flow is known to couple into laminar boundary layers on objects in the flow[1], and can influence if and where on the object those boundary layers may transition to turbulence. In high-speed wind tunnels, turbulence encountered by models in the wind tunnel flow is typically somewhat stronger than that experienced in free-flight. This poses a problem not only for engineering testing of scale models, but also in verification of computational models, where the behavior of the two cases will not match unless the inlet conditions of the simulation realistically model the turbulence in the wind tunnel. Measurement of flow turbulence, and its parameterization, is therefore necessary for accurate comparison of wind tunnel, computational, and free-flight conditions.

Traditionally, hot wire anemometry (HWA) is used for these turbulence measurements. However, there are cases where it is unsuited for use in a particular flow. Other options for quantitative measurements of turbulence, such as LDV/PIV or pressure fluctuation measurement, have their own associated difficulties and limitations.

The focusing laser differential interferometer (FLDI), developed in this thesis, is a non-intrusive optical technique that can make high-frequency-response measurements of turbulence in high-speed flows. It provides a "point-like" measurement, comparable to HWA, and can be applied in many cases so long as there is optical access: unlike LDV and PIV, FLDI does not require that the flow be seeded with particles, since it tracks fluctuations in the density of the flow, instead of particle motion.

The FLDI instrument is not a new concept, having been originally developed in the early 1970's, however no comprehensive theory of its behavior exists. This thesis presents techniques for the design, implementation, and characterization of FLDI, and it develops a new theoretical description of the frequency-response characteristics of the FLDI instrument. The FLDI technique is applied in this research to the measurement of turbulence intensity and spectra in high-speed wind tunnels and in a reference turbulent air jet, for comparison with the literature.

1.1 Motivations for Characterizing Turbulent Flowfields

In wind tunnel testing, it is well known that turbulence in the freestream affects the behavior of laminar-to-turbulent transition of boundary layers on objects in the flow, which can lead to discrepancies between the wind-tunnel model's aerodynamics and those of a full-scale prototype in free flight. The transition to turbulence has dramatic effects on heat transfer, skin friction, flow separation, and other aerodynamic properties. However, the process of transition and the mechanisms by which energy is fed into boundary layers to induce transition are not well understood.

Schneider[2] examines measurements of transition Reynolds numbers of sharp cones in free-flight and in various high-speed wind tunnel facilities, demonstrating dramatic differences in the locations of boundary-layer transition between free-flight and wind tunnel tests. He notes that ground-test data are ambiguous, since they are collected at much higher freestream disturbance levels than in flight, and the boundary-layer transition mechanisms in noisy flows are generally poorly understood and are often much different than those in low-noise flight. These high-noise mechanisms are presumed to be the cause of the much-earlier transition to turbulence noted in wind tunnel testing. Conventional supersonic and hypersonic wind tunnels are reported by Schneider[2] to have pressure fluctuation levels 10 to 100 times greater than free-flight conditions, although he notes that the techniques used to measure these disturbance levels vary in frequency response and that there is considerable difficulty in interpretation of the data. “The difficulty of making low-noise, high-frequency measurements is second only to the difficulty of fabricating a quiet tunnel.”[2]

Equally difficult to the interpretation of measured wind-tunnel noise data is determining the effect of the noise on boundary-layer stability, which has dominant frequencies where energy from the freestream appears to couple into the boundary layer. It may be that, even when a wind-tunnel has a high level of freestream noise, the disturbance level at the frequencies associated with boundary layer instability waves might be low enough to avoid transition in some cases. The high-frequency-response measurement of disturbance levels and spectra in wind-tunnel and free-flight testing is necessary for understanding these mechanisms. Any prediction of how a model might perform in free-flight will depend heavily on the accuracy of these measurements and their interpretation.

1.2 Laufer’s Work on the Origins of High-Speed Wind Tunnel Noise

Uberoi explores the effect of a wind-tunnel nozzle contraction on the turbulence intensity in a subsonic flow[3]. He notes that vorticity in the supply section of wind tunnels is the primary variable for turbulence in this case. In subsonic flow, as the nozzle contracts and the mean velocity of the flow increases, the vortex filaments of the flow in the direction of mean flow, corresponding to velocity fluctuations perpendicular to the mean flow, are stretched by the contraction ratio, c. Meanwhile, vortex filaments perpendicular to the mean flow direction, corresponding to velocity fluctuations in the direction of mean flow, contract by $\sqrt{c}$. Neglecting viscous effects, the strength of these incoming vortices remains constant. In this case, the strength of turbulent fluctuations in these directions changes inversely to the effect on vorticity: velocity fluctuations perpendicular to the mean flow increase from the inlet condition by a factor of $\sqrt{c}$, while fluctuations in the direction of mean flow decrease by a factor of c. The resulting effect of contraction in a subsonic nozzle on velocity fluctuations is shown in Eqs. 1.1a,b.

$$\begin{aligned} \frac{u_2}{u_1} &= \frac{1}{c} \\ \frac{v_2}{v_1} &= \frac{w_2}{w_1} = \sqrt{c} \end{aligned} \qquad (1.1a,b)$$

Here, u is the velocity fluctuation in the mean flow direction, while v and w are the fluctuations perpendicular to this direction, and subscripts 1 and 2 represent conditions before and after the contraction.

This model is extended to supersonic flow by taking density changes in the flow into account. In this case, velocity fluctuations along the nozzle axis scale as before, but fluctuations perpendicular to the mean flow direction scale by the factor $\sqrt{c\rho_2/\rho_1}$. The effect of a contraction on velocity fluctuations in supersonic nozzles is shown in Eqs. 1.2a,b.

$$\begin{aligned} \frac{u_2}{u_1} &= \frac{1}{c} \\ \frac{v_2}{v_1} &= \frac{w_2}{w_1} = \sqrt{\frac{c\rho_2}{\rho_1}} \end{aligned} \qquad (1.2a,b)$$

The density of an accelerating flow drops in supersonic flow, compared to the stagnation condition, calculated by the compressible isentropic flow relation:

$$\frac{\rho_2}{\rho_1} = \left(\frac{1 + \frac{\gamma - 1}{2} M_1^2}{1 + \frac{\gamma - 1}{2} M_2^2} \right)^{\frac{1}{\gamma - 1}} \qquad (1.3)$$

Here, ρ is the density of the flow at Mach number M, and γ is the ratio of specific heats of the fluid. At high Mach numbers the density ratio can be much smaller than $1/c$, such that both the u and v components of velocity fluctuations will be reduced in strength by the nozzle contraction. Additionally, with the high contraction ratios required for supersonic nozzles, the vorticity may be compressed to scales where Uberoi's inviscid assumption may not hold, and these vortices may dissipate into heat.

Laufer's work on the experimental characterization of freestream disturbances in supersonic wind tunnels serves to motivate much of the research into the characterization of freestream turbulence[4]. It was well known that, in subsonic wind tunnels, turbulence in the freestream strongly influences the laminar-to-turbulent transition Reynolds number of boundary layers on models in the flow. However supersonic wind tunnel research showed that freestream disturbances differed in cause and behavior from those in subsonic tunnels. Laufer found that, at higher Mach numbers, the correlation between velocity fluctuations in the supply section of supersonic tunnels and the transition Reynolds number on models in the test section was not significant. A tenfold increase in these supply-section velocity fluctuations had no significant effect on transition on models beyond Mach 2.5, despite having a large effect at lower Mach numbers. Hot-wire anemometry measurements that Laufer performed in the Jet Propulsion Laboratory's 18 x 20 in. supersonic wind tunnel showed that the observed test-section fluctuations could not be due to transverse velocity fluctuations of turbulence, nor could they be due to pure temperature fluctuations in the flow. This conclusion is supported by knowledge that the contraction ratio from the supply section to the nozzle (for the JPL tunnel, this was 40:1 at $M = 1.6$ and 1500:1 at $M = 5$) effectively squeezes vortices in the supply section until they are below the Kolmogorov length scale[3] so that they dissipate before reaching the test section. Instead, if the hot-wire fluctuation measurements were assumed to come from a pure sound field, this model is then consistent with the measurements. Laufer therefore finds that the source of the sound field must be turbulence in the boundary layers on the walls of the wind tunnel nozzle, the influence of which which is radiated into the freestream. He warns (in 1961) that the difficulty in characterizing this sound field and its effect on the stability and transition of boundary layers on models may render measurements of transition Reynolds number meaningless in supersonic wind-tunnel testing. Laufer's work[4] is an often-cited masterpiece of understanding turbulence in high-speed wind tunnels.

1.3 Aeroacoustics and Radiated Tunnel "Noise" from Boundary Layers

Lighthill's founding work in aeroacoustics forms the basis of the theory explaining how turbulence generates a sound field, and demonstrates that an eddy moving downstream radiates circular acoustic wavefronts at a semi-angle equal to the Mach angle, with a direction of propagation defined by the complement of this Mach angle[5,6]. Ffowcs-Williams[7] builds on Lighthill's work to develop an aeroacoustic theory to explain the formation of Mach-wave fields radiated by supersonic turbulent shear flows such as those observed by Laufer. In his theory, Ffowcs-Williams relates the strength of the radiated Mach-wave field to measurements of surface pressure, showing excellent agreement with Laufer's[4] experimental results. Ffowcs-Williams identifies two sources of the sound-wave radiation noted by Laufer: eddy Mach wave radiation, and shivering Mach waves. Eddy Mach wave radiation behaves as quadrupole and dipole acoustic sources, and originates at the boundary layers that develop along the walls of a supersonic de Laval nozzle. Shivering Mach waves occur due to flaws in the nozzle wall, producing standing waves that are modulated to "shiver" by passing eddies of the nozzle-wall turbulent boundary layer. These two sources form the basis of the modern understanding of freestream disturbances in high-speed flows.

1.4 Boundary Layer Transition due to Freestream Disturbances

Saric[8] provides background into boundary layer receptivity theory, which explains how energy from freestream turbulence couples into a boundary layer's spectrum, potentially tripping it into turbulence. Boundary layer stability is a critically-important field in fluid mechanics. Nonetheless, Saric[8] stresses that there is currently no mathematical model that will accurately predict the transition Reynolds number of flat-plate laminar boundary-layers or other geometries, despite decades of research. Many disparate features of flows come together to make the problem so difficult: freestream turbulence, the roughness of surfaces over which they flow, boundary-layer interaction with acoustic waves, etc.

Despite the difficulty in fully modeling boundary layer stability, emphasis has been placed on understanding the initial, individual sources of boundary layer disturbances and their impact on boundary layers. Fundamentally, all disturbances from the freestream that interact with boundary layers will influence the transition of those boundary layers to a greater or lesser degree: this process is called *receptivity*. The amplitude, frequency, and phase of those disturbances all must be considered in determining how strong their effect on a boundary layer may be. Morkovin et al.[9] illustrate different paths for how energy disturbances of different amplitudes may couple into laminar boundary layers, and their transition to turbulence, seen in Fig. 1:

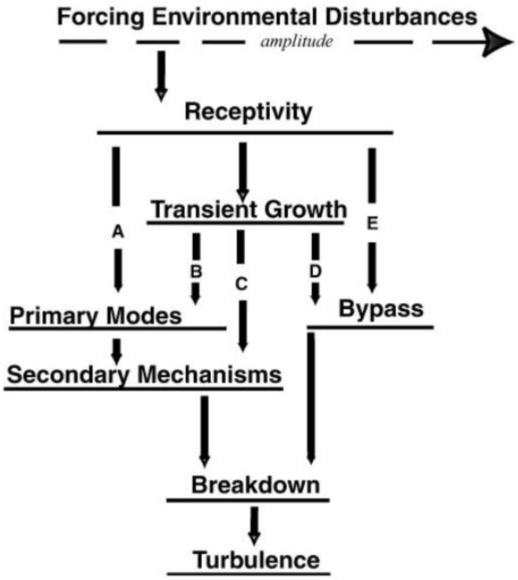

Figure 1.1: Receptivity paths that disturbance energy may follow to initiate transition in boundary layers[9]

Very weak disturbances follow path A, driving primary-mode disturbances in boundary layers. These disturbances are treated by linear stability theory[10], where they are modeled by coupling them into the linearized unsteady Navier-Stokes equations. For these disturbances, the growth of the primary-mode fluctuations in the boundary layer is slow, and they are heavily affected by pressure and temperature gradients, as well as by changes in mass flux near the surface. Saric notes that many studies consider only these primary modes, arguing that the freestream disturbances in free-flight are typically very weak.

This approximation fails in some wind-tunnel testing, however, because of the substantially-higher freestream disturbance levels encountered in wind tunnels compared to external flows, even in so-called “quiet” wind tunnels. While linear stability theory can be used to predict the growth of second-mode fluctuations in some flows, stronger disturbances than those that directly drive primary modes (disturbances following paths B, C, and D) may require much more complicated analysis to understand their effect on transition to turbulence. The spectral properties of these disturbances have a very large effect on the degree to which they influence boundary layer transition. Schlichting[11] developed an early theory for the behavior of these second-mode instabilities, called Tollmien-Schlichting (T-S) waves, and noted that the relative length scales of a disturbance and the boundary layer it influences have a major effect on their impact on transition: disturbances with much shorter or longer wavelengths than the boundary-layer scales do not have much effect. This observation drives the need for frequency-resolved measurements of disturbance strength.

To characterize the acoustic disturbances known to be present in high-speed flows, Kendall[12], building on the work of Laufer[4], performed wind tunnel experiments demonstrating boundary layer transition in supersonic and hypersonic flow. He used hot-wire anemometry to measure the spectra of freestream disturbances and boundary layers on flat plates in flows with Mach numbers ranging from 1.6 to 8.5. The freestream spectra measured in the wind tunnel are deconvolved from their associated boundary layer spectra, resulting in a plot of the amplification ratio of the spectra seen in the boundary layers compared to the freestream as a function of frequency. The turbulence spectra in Kendall's results showed energy content to well over 100 kHz, and the second-mode amplification peaks occurred at similarly high frequencies. Higher Mach number flows are thus shown to require higher frequency response to adequately resolve these amplification peaks. For the hot-wire anemometry system Kendall used, the frequency compensation circuit limited the frequency response of his measurements to around 50 kHz for freestream measurements and 100-200 kHz for measurements in the boundary layer, in order to maintain amplifier stability.

1.5 Difficulties in High-Speed Testing

As mentioned earlier, hot-wire anemometry (HWA) is the most commonly used method of measuring turbulence in wind tunnel testing. However, high-speed flow poses a particular difficulty, discussed by Kovasznay[13]. Hot-wire anemometry is sensitive to variations in both mass flux, ρu, and stagnation temperature, T_0, in high-speed flow. The hot-wire overheat ratio, as described in Eq. 1.4, has a large effect on the extent to which any variations in flow stagnation temperature affect the output of the anemometer.

$$\tau = \frac{T_w - T_r}{T_0} \tag{1.4}$$

Here, T_w is the temperature of the heated wire in operation and T_0 is the stagnation temperature of the flow. T_r is the recovery temperature of the unheated wire: the mean temperature the wire attains when exposed to the flow. This temperature is usually slightly less than the stagnation temperature, but is much higher than the static temperature of the flow, and is calculated using the following relationship[14]:

$$\frac{T_r}{T} = 1 + r\frac{\gamma - 1}{2}M^2 \tag{1.5}$$

This can also be expressed in terms of the stagnation temperature:

$$\frac{T_r}{T_0} = \frac{1 + r\frac{\gamma - 1}{2}M^2}{1 + \frac{\gamma - 1}{2}M^2} \tag{1.6}$$

In this calculation, γ is the ratio of specific heats in the fluid, M is the freestream Mach number, T is the static temperature of the flow, and r is the so-called "recovery factor." For gases, r is approximately equal to $Pr^{1/2}$ in laminar flow, and $Pr^{1/3}$ in turbulent flow, where Pr is the molecular Prandtl number of the fluid[15]. For air, where $Pr \sim 0.7$ over a wide range of temperatures, this gives $r = 0.84$ for laminar flow and $r = 0.89$ for turbulent flow. With high overheat ratios, where

$\tau >> 1$, stagnation temperature fluctuations change the hot-wire output very little, and the anemometer measures essentially only the mass flux component. Low overheat ratios where where $\tau < 1$, on the other hand, can be greatly affected by temperature fluctuations when present, and therefore have severely reduced frequency response[16].

In oxidizing gas mixtures, the oxidation temperature of the hot-wire probe material is a major limiting factor to overheat ratio, because the operating temperature of the probe must be below this temperature. For tungsten wires, which are commonly used due to their durability, the oxidizing temperature limit is typically considered to be around 300°C, and wires are typically held at 250°C in routine testing to avoid oxidation[17]. In unheated wind tunnels, where the stagnation temperature of the flow is around ambient temperature, this limits the overheat ratio of the wire to around 0.8, at which Smits et al.[16] predict that the sensitivity of the HWA system to temperature fluctuations will be roughly equal to the sensitivity to mass flux fluctuations.

Problems from oxidation due to high overheats can be postponed by the use of platinum and platinum-alloy wires. According to Lomas[17], the oxidation temperature of pure platinum wire is around 1100°C, although it is significantly weaker than tungsten wire, limiting its use to low-speed flows. Platinum alloys, particularly the alloys with iridium or rhodium, have high oxidation temperatures (~800°C[17]) but do not sacrifice as much strength as pure platinum. The ultimate tensile strength (UTS) of tungsten at room temperature is around 1000 MPa[18], while pure platinum has an ultimate tensile strength of only ~125 MPa[19]. Typical alloys of platinum are those with 20% iridium or 10% rhodium. The alloy with 10% rhodium (90% Pt, 10% Rh) has a UTS of ~300 MPa, while the alloy with 20% iridium (80% Pt, 20% Ir) has a UTS of ~700 MPa, significantly reducing concerns about the strength of the hot-wire compared to that of tungsten wire.

In non-oxidizing gas mixtures, the temperature limit from oxidation can of course be ignored. Instead, the limiting temperature of the wire is the maximum temperature that the anemometer system can achieve based on the bridge electronics, or, in extreme cases where the wire is very thin or the bridge is very powerful, the melting point of the wire material. In this case, tungsten is definitely the better material, boasting the highest melting point of all elements, around 3400°C[18]. Platinum and the alloys mentioned previously, on the other hand, have melting points of only ~1800°C.

Because of the extreme difference between static temperature and stagnation temperature in hypersonic flow, almost all hypersonic wind tunnel facilities must heat the supply gas to avoid gas liquefaction. For nitrogen, with a specific heat ratio of 1.4, the stagnation temperature of a flow at Mach 10 is 21 times that of the static temperature. The liquefaction point of nitrogen at atmospheric pressure is 77.4 K. For a wind tunnel to achieve Mach 10 flow, while running nitrogen as a working fluid, with one atmosphere of static pressure and no liquefaction, the stagnation temperature must be at least 21 times that: around 1630 K. In this case, the best overheat that a hot-wire probe can achieve for a turbulent flow is about 1.4 for a tungsten wire and 0.4 for a platinum wire. Atmospheric static pressure is unrealistically high, but even at a static pressure of 5 mbar (500 Pa), the liquefaction point of nitrogen drops only to around 50 K, giving a required stagnation temperature of 1050 K at Mach 10. With this stagnation temperature, tungsten wires should be able to achieve adequate overheat if the bridge electronics are of very high power, with a possible overheat ratio of 2.6, while platinum wires may achieve an overheat ratio of around 1.1. While these overheat ratios may be adequate for rejecting the temperature fluctuations compared to that of the mass flux fluctuations, high wire temperatures nonetheless significantly reduce the yield strength of the wires, which may preclude their use in a wind tunnel even if adequate overheat ratios can be achieved.

A single hot-wire probe operated at constant overheat cannot differentiate between the effects of the mass flux and stagnation temperature fluctuations in the anemometer output. Walker[20] describes two methods to overcome this difficulty: a single wire with varying overheat ratios over the course of a wind-tunnel run (or several runs), or a dual-wire setup where each wire is at a different overheat ratio. With either of these methods, it is possible to generate a calibration that will isolate the effects of the stagnation temperature variation in the flow from the mass flux fluctuation, by constructing so-called mode diagrams. Masutti et al.[21] use this technique, alongside high-speed Pitot pressure measurements, to attempt to characterize the freestream disturbance level of the VKI H3 Mach 6 Wind Tunnel at the von Kármán Institute for Fluid Dynamics in Belgium. This facility uses dried air as its working fluid, and the high disturbance level of the tunnel necessitated the extra strength of 9 μm diameter platinum-plated tungsten hot-wire probes. The combination of these two features limited the maximum overheat ratio of the wires to 1.4. To achieve an appreciable difference in the response of the two wires, while maximizing their frequency response, the second wire was set at an overheat ratio of 1.1. The frequency response of this setup was found by square-wave testing to be around 25 kHz for the wire with overheat ratio 1.4, and 10 kHz for the wire with overheat ratio 1.1.

1.6 AEDC Hypervelocity Tunnel 9

The sponsor of this research, the USAF Arnold Engineering Development Center, is interested in developing methods of characterizing free-stream disturbances in Hypervelocity Wind Tunnel No. 9: the primary high-Reynolds-number hypersonic ground testing facility for the Air Force and the Department of Defense[22]. The 1.5 m diameter tunnel is capable of speeds up to

Mach 14, stagnation temperatures and pressures of 1700°C and 190 MPa, and test times up to 15 seconds. In addition to the high stagnation temperature and pressure in the tunnel, instruments must contend with boundary layers or free shear layers on the order of 0.25 to 0.6 m thick at the tunnel walls. Instrusive instruments must also be able to withstand the tunnel's starting shock wave and fine particulate matter in the freestream generated by disintegration of the graphite heaters used to heat the flow. Non-intrusive optical instruments must cope with low freestream densities, two to three orders of magnitude below atmospheric conditions. Tunnel 9 is a good example of a hostile environment for flow instrumentation.

Lafferty and Norris[23] note the impracticality of the hot-wire anemometry technique in Tunnel 9 due to the high stagnation temperatures involved and large swings in dynamic pressure. Noting that fluctuating quantities in the freestream, such as density, pressure, or velocity, are generally believed to be proportionally related to one another, they use a surface-mounted pressure transducer (Kulite XT-140a) on the tip of a Pitot probe to quantify tunnel noise by pressure fluctuation levels. A protective screen mounted in front of the pressure transducer limited the frequency response of the transducer to only 20 kHz. Even with this low frequency response, measurements of root mean square (RMS) pressure fluctuations were successfully made at Mach numbers of 8, 10, and 14, and at a range of unit Reynolds numbers. The results fell within a reasonable range compared to those of similar facilities.

Bounitch et al.[24] extend this testing with the addition of PCB 132A31 pressure transducers, which are capable of much higher frequency response than the Kulite transducer, giving a range of 11-1000 kHz for frequency response. Testing at $M = 10$, $Re/L = 2\times10^6$ / ft (6.6×10^6 / m) showed that RMS noise levels measured by the Kulite transducer from 0-25 kHz averaged 3.65% of static pressure, while noise levels from the PCB transducer from 25-1000 kHz averaged

3.32%. The total noise level, found by taking the RMS of these two values, was 4.94%. Extension of the frequency range of the disturbance level measurement from 0-25 kHz to 0-1 MHz resulted in only a 35% increase in the measured disturbance level; most of the disturbance energy in the flow is at relatively low frequencies. From laminar boundary layer stability theory, however, it is expected that stability is most affected by frequencies somewhat greater than 25 kHz at the flow conditions encountered in Tunnel 9. Computational models by Berridge[25,26] predict an amplification peak around 200 kHz for Tunnel 9 at Mach 10 for a unit Reynolds number of 6.5×10^6 / m. Over the full operating range of the tunnel, the amplification peak ranges between about 60 and 500 kHz. Measurements of not only disturbance strength but also the spectra of disturbances are necessary for meaningful characterization of tunnel noise, as mentioned before.

A numerical simulation of pitot-tube response to freestream noise was performed by Hornung and Parziale[27]. Results show a Mach-number-dependent amplification of freestream noise level, which is worst at lower Mach numbers. The effect of this amplification is not clear, but the authors conclude that “The results emphasize the superiority of optical methods over pitot pressure for measuring noise.”

Part of the difficulty presented by this problem is that invasive measurement techniques, like hot-wire anemometry or the pressure transducers mentioned previously, must take the effect of boundary layers and bow shocks in front of the transducers into account. While the effect of these phenomena on overall signal strength is fairly well characterized[28], their effect on the "flatness" of frequency response is not. They necessarily cannot measure a true freestream spectrum.

Non-invasive optics, like the shadowgraph, schlieren, and interferometry techniques, have long been a mainstay of wind tunnel testing for qualitative, and sometimes quantitative, measurements. These techniques are useful because interpretation of the images they produce is generally intuitive, allowing the visual examination of shocks and instabilities in flow fields. The path-integrating nature of these methods leads to the observation of whole-field phenomena, however, rather than the local variations of flow properties that are sometimes required. A major consequence of this feature of these techniques is that phenomena such as boundary layers on the periphery of the flow often overpower the refractive strength of the phenomena of interest, requiring the sensitivity of the optics to be reduced to keep the images within their limited dynamic range. To successfully measure disturbances in the freestream of a wind tunnel, an optical system must be arranged such that it can "see through" these boundary layers and measure primarily the disturbances in the core of the wind tunnel flow.

The “focusing”-schlieren technique can be used to significantly reduce the depth-of-field of the optics to limit the strength of unwanted boundary effects[29,30]. However, doing so comes with an associated reduction in sensitivity. This technique uses a large extended light source and cutoff grids to produce a schlieren image where the refractive index gradients at the focus of the instrument are well resolved, but those that are off-focus are blurred, significantly reducing their contrast. With a large-enough source so that the depth-of-field of the instrument adequately rejects boundary layer noise, global measurements of density fluctuations can be made with high-speed cameras. At the time of this writing, however, frame rates are somewhat limited: the fastest commercially available cameras are capable of approximately one million frames per second (1 MHz) and only at significantly reduced frame sizes and pixel bit depths (for example, 64x16 12-bit pixels at one million frames per second for the Photron FASTCAM SA5). While the framing speed and pixel count of high speed cameras will undoubtedly improve with time, they are currently inadequate for the measurement of very-high-speed, small-amplitude fluctuations.

One method to avoid the requirement of extremely-high-speed cameras is the schlieren deflectometry method developed by McIntyre et al.[31] and extended by Alvi et al.[32] McIntyre's device uses a standard schlieren optical system, but the image is projected onto two ground glass screens, where fiberoptic probes sample the image intensity at a known position and a relative displacement from one another. Alvi extends this device by replacing the standard schlieren optics with a focusing-schlieren setup to minimize the effect of boundary layer noise in a wind tunnel on the output. This focusing-schlieren deflectometry technique has been used by Garg and Settles[33] to measure convective velocity in boundary layers in the Penn State University Supersonic Wind Tunnel, and by VanDercreek[34] to examine second-mode instability waves in laminar boundary layers in AEDC Hypervelocity Tunnel 9. Garg notes that, while the focusing-schlieren technique performs well enough in focusing the image so as to ignore "noise" from outside the region of best focus for measurement of a boundary layer velocity profile, it may not be practical to shrink the depth-of-field as much as may be needed to adequately reject unwanted signals in some flows. On the other hand, it can be shown that schlieren sensitivity is inversely related to the depth-of-field, so that very weak disturbances require longer depth-of-focus to resolve, at odds with the requirement to minimize unwanted signals by sharpening the depth-of-focus. Despite this difficulty, VanDercreek was able to image (using focusing schlieren) and measure (using schlieren deflectometry) boundary layer instability waves on the Tunnel 9 transition cone, resolving clear instability peaks in the 200-300 kHz range for Mach 10 flow at a unit Reynolds number of 10×10^6 / ft (33×10^6 / m), which correlated well with pressure peaks from the high frequency pressure transducer[35].

1.7 Crossed-Beam Schlieren Deflectometry

While focusing schlieren deflectometry largely reduces interference from signals away from best focus, it is a very complicated design to implement. Another schlieren deflectometry technique that accomplishes similar results, but is significantly easier to build, is crossed-beam schlieren (CBS) deflectometry. The current research began with CBS deflectometry and then later moved on to the focusing laser differential interferometer (FLDI) instrument. Nonetheless, CBS deflectometry is an important preliminary step, and is therefore described next in more detail.

Recognizing the limitations of hot-wire anemometry, particularly in the analysis of high-speed flows, Fisher, Krause, and Wilson[36-38] developed the optical crossed-beam correlation technique for quantifying turbulent properties in cases where HWA may not be applied reliably. This includes cases when intrusive measurements are not acceptable in a flow, or when the temperatures involved are too high to allow adequate HWA wire overheat. With the crossed-beam technique, the intensities of two laser beams, intersecting in the flow at some angle relative to one another, are measured by photodetectors. These measurements represent an optical-path-integrated signal of the scalar quantity of interest over the length of the each of the beams. They encounter uncorrelated turbulent boundary layer disturbances near where each beam enters and exits the test section, but pass through a volume close to the intersection where the disturbances experienced by the two beams are highly correlated. By taking the cross-correlation of each signal, the majority of the integrated “noise” on the signal from outside this correlated volume is removed, leaving the correlated portion of the two signals intact, corresponding to the disturbances local to the region where the beams cross.

Fisher’s initial work in developing this technique uses water droplets suspended in a subsonic M = 0.2 jet, although later he uses UV light at 185 nm, which is absorbed readily by oxygen at moderate pressures, to probe the properties of a turbulent, supersonic jet. Wilson, meanwhile, utilized infrared light generated by glowbars at an effective temperature of 1100 K and filtered by a monochromator to resolve the 4.3 μm absorption band of CO_2 for measuring the sound source intensity of jet noise. In all three cases the authors noted unwanted contributions of scattered light to the measured absorption signals, as well as fluctuations due to variation in the absorptivity of gases based on temperature and pressure.

A natural extension of this crossed-beam technique that would limit the problems encountered above with direct intensity measurements is to measure the refractive displacement of each beam. Funk and Johnston[39] take the instrument used by Wilson for his UV absorption experiments and add knife-edges before the photodetectors, while replacing the UV sources with HeNe lasers, to perform crossed-beam schlieren measurements. They note that the schlieren system appears more promising than absorption or scattering because the sensitivity of the device is adjustable by manipulating the cutoff, and because the signals themselves are more easily related to the local density of the flow, simplifying interpretation.

Meanwhile, Wilson and Damkevala[40] revisit this problem and utilize the crossed-beam Schlieren technique to establish the mathematical relationships between the signals measured experimentally in subsonic jets (U = 100 to 210 m/s) to the statistics of turbulent properties. Martin[41] examines the application of the crossed-beam schlieren technique to the analysis of scalar turbulence generated by a heated grid, which should be approximately isotropic and homogeneous, and gives an extensive explanation of how the spectra generated from the photodiode signals are processed.

All of the CBS studies presented so far were pre-digital, and were greatly limited in frequency response by the analog cross-correlators and tape-recording equipment available to the authors at the time (approximately 80 kHz maximum for Fisher's recording equipment). This generally precluded their ability to examine higher-speed phenomena.

Grandke[42,43] leverages developments in high-speed digitization and desktop workstations to improve the crossed-beam schlieren correlation method. The digitizer used for Grandke's research was capable of around 25 MHz maximum frequency response, several orders of magnitude higher than previously available. The crossed-beam correlation technique was applied to examine heated grid turbulence and the turbulent wake of a cylinder in one study[42] and a subsonic round turbulent jet in another[43]. In both cases the result was compared to hot-wire surveys, showing excellent agreement. While Fisher and Wilson note that the convective velocities measured by the crossed-beam correlation method appear to be somewhat slower than the mean flow, Grandke's instrument measures convective velocities very close to the mean flow velocity, which he attributes to better measurement of small-scale structures in the turbulent flows because of his instrument's improved frequency response.

Rather than using knife-edges to perform traditional schlieren measurements, the CBS technique used in an early phase of the present research measures beam deflection directly using position-sensitive diodes. This is an improvement upon the knife-edge design, because it allows for compensation of fluctuations in laser power and absorption of beam power in the test section, but otherwise provides an output that is directly comparable to the knife-edge setup. This instrument is described further in the Apparatus section of this thesis.

1.8 Focusing Laser Differential Interferometry

For reasons described later in the Results section of this thesis, crossed-beam schlieren deflectometry was found unsuitable for freestream disturbance measurements in high-speed wind tunnels. Attempts to apply focusing methods to the CBS instrument, to reduce its sensitivity to tunnel-wise boundary layer disturbances, were not successful. Ultimately, crossed-beam schlieren was abandoned in favor of a different technique, focusing laser differential interferometry.

Focusing laser differential interferometry (FLDI) is a technique originally developed by Smeets and George of the French-German Research Institute Saint-Louis in the mid-1970s[44-48]. The FLDI instrument is a variation of the lateral-shearing interferometer, which gives a single-point measurement (rather than a global measurement, as with focusing schlieren imaging) of the local refractive index gradient, similar to deflectometry. However, as a focusing technique, its sensitivity to disturbances away from best focus is significantly reduced. Smeets and George describe a large variety of uses for FLDI, demonstrating its use for measurements of acoustic disturbances, turbulence, density profiles in boundary layers, electron densities in plasmas, etc. Despite this broad applicability of the FLDI technique, it appears rarely in the literature, even compared to the crossed-beam schlieren technique. Moreover, Smeets and George presented the instrument in broad terms of its function and applicability, but without any detailed optical analysis.

Recently, however, the FLDI technique was used by Parziale for characterization of boundary layer transition in the CalTech T5 reflected-shock tunnel[49-52]. Turbulence spectra of boundary layers on a 5-degree-half-angle cone in high-enthalpy Mach 5.5 flow are measured and compared to measurements of the turbulence spectra in the freestream flow, showing the amplification factor of boundary layer spectra due to second-mode instability waves. Parziale demonstrates the high frequency response of the FLDI instrument by resolving instability amplification peaks out to around 2 MHz, well beyond the best-case frequency response of about 1 MHz of the surface-mounted pressure transducers mentioned earlier. In addition to single-point measurements, Parziale describes two-point FLDI measurements, intended to track the motion and growth of turbulent spots propagating along the boundary layer of the cone. Cross-correlation of the two signals gives an estimate of the velocity of the spot in the boundary layer, by measuring the time delay of the point of maximum correlation. These turbulent spots were found to propagate at a velocity very close to the velocity at the edge of the boundary layer.

1.9 Goals of the Present Study

Unlike the case of more common quantitative techniques, there is very little published theory for the behavior of the focusing laser differential interferometer. No comprehensive study of the frequency response or away-from-focus signal rejection of the instrument exists, and no generally applicable methods to calibrate an FLDI instrument have been described. Without a solid theoretical foundation, quantitative measurements of turbulence using this technique, particularly the characterization of turbulence spectra, are somewhat suspect. This thesis aims to describe a general theory by which the sensitivity of an FLDI instrument can be estimated, and presents calibration techniques for accurate in-situ measurements of the optical properties of the instrument.

To this end, a theoretical model for the response of the FLDI instrument to turbulence and simple methods for measurement of the beam separation and beam diameter of an instrument are presented. This allows calibration of the instrument for direct quantitative measurements of turbulent properties.

The theory is verified using measured and simulated turbulence spectra from a round turbulent jet, which is a well-characterized turbulence source that is common in the literature. Measurements are made of freestream turbulence spectra in the Penn State supersonic wind tunnel (PSUSWT) at Mach 3 and in AEDC Hypervelocity Tunnel 9 at Mach 10, demonstrating the usefulness of the FLDI technique for characterization of these spectra. Finally, possible improvements to the instrument are identified for future work.

Chapter 2: Experimental Apparatus and Facilities

2.1 FLDI Optics - Basic Layout

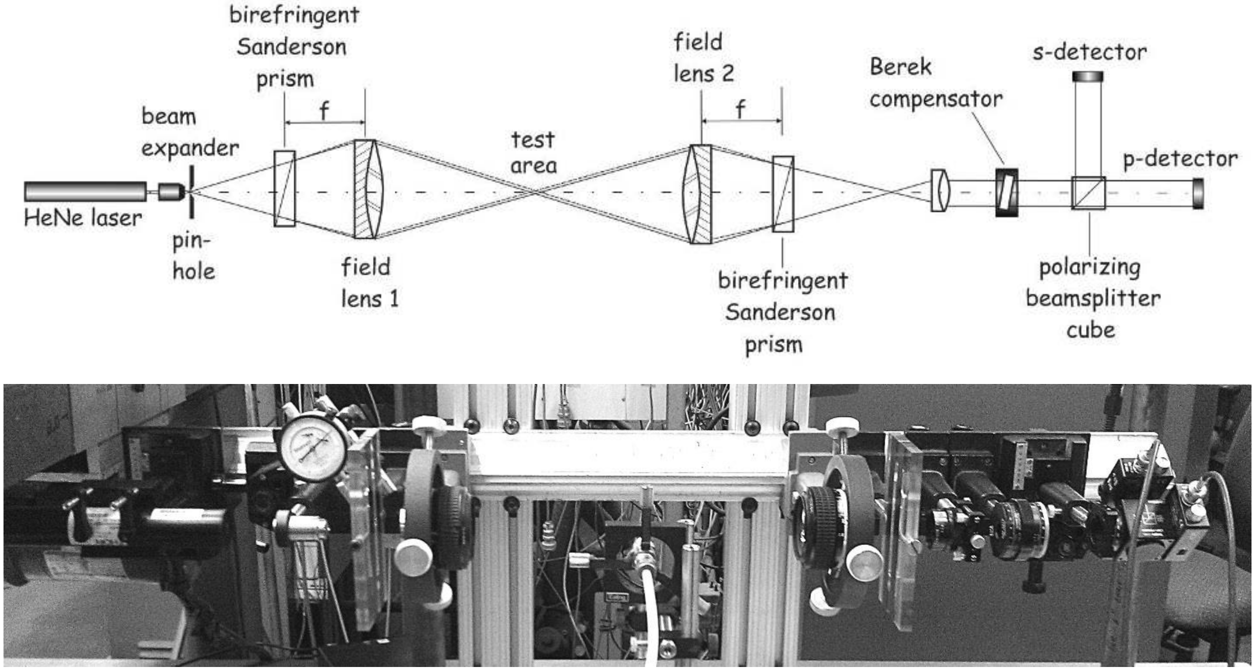

Figure 2.1a,b: Basic layout of FLDI instrument and a photograph of the instrument used for the present research. Here, the instrument is set up to measure the turbulence profile of a round turbulent jet.

A basic focusing laser differential interferometer consists of a laser, some method of expanding the laser beam, two field lenses to focus that beam within the desired test area, two birefringent prisms to split and then recombine two beams to perform the interferometry, and some detector to sense the polarization and phase of the output. The layout of the instrument developed during the present research is shown above in Fig. 2.1a, with a photograph of the instrument shown in Fig. 2.1b. A photograph of the transmitting side of the FLDI instrument is shown in Fig. 2.2, and a photograph of the receiving side of the FLDI instrument is shown in Fig. 2.3.

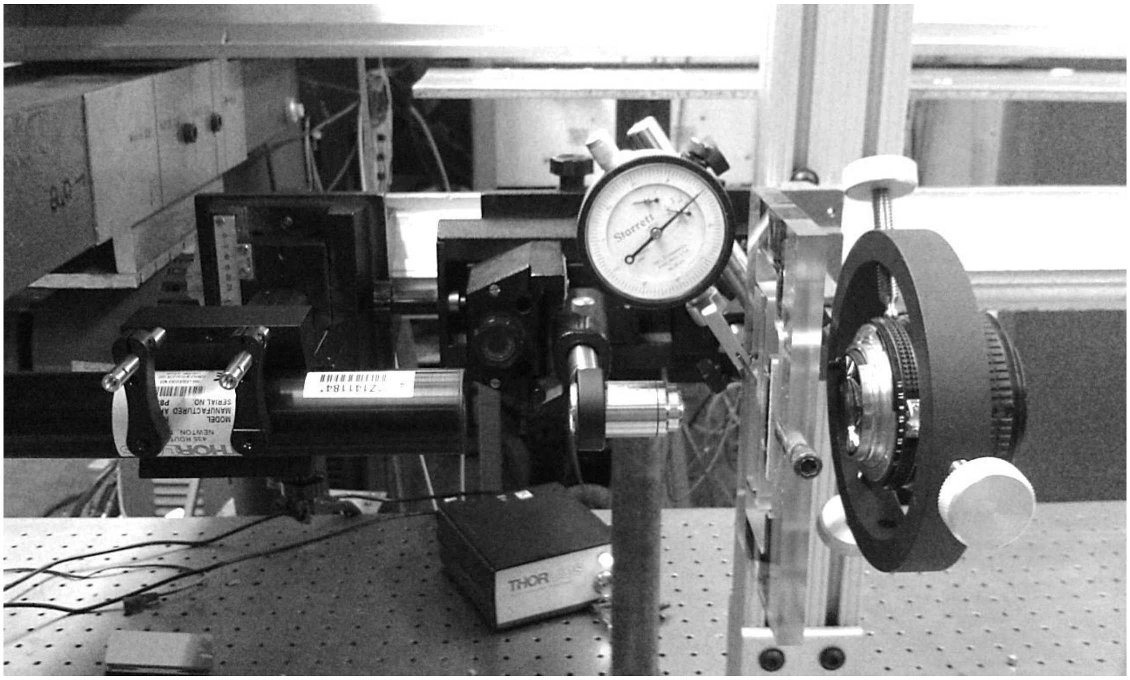

Figure 2.2: Photograph of the transmitting side of the FLDI instrument. Here, a helium-neon laser is projected through a 100x microscope object. The expanding beam passes through a polycarbonate "Sanderson" prism to create the two perpendicularly-polarized beams of the interferometer. A Nikon camera lens is used for the field lens.

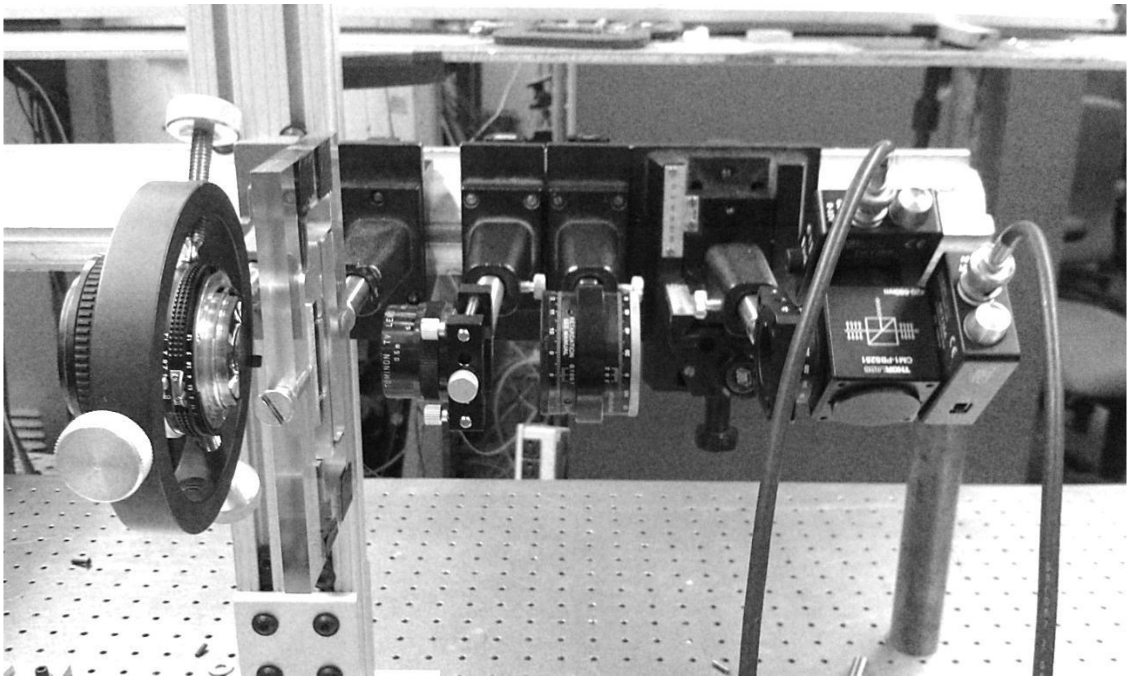

Figure 2.3: Photograph of the receiving side of the FLDI instrument. Here, the second field lens collects the FLDI beams on the far side of the test area. The two perpendicularly-polarized FLDI beams are recombined in the second Sanderson prism. The beam is collimated by a small security camera lens. A Berek compensator adjusts the phase of the recombined beam. Finally, the beam passes through a polarizing beam-splitter cube, where two photodiodes measure the intensity of the resulting interference patterns.

A Thorlabs 0.8 mW HeNe laser was used as the source for the instrument detailed in this research. This laser was chosen due to its thin 0.48 mm $1/e^2$ beam diameter rating, as beam diameter is critical to the frequency resolution of the device. The beam quality of such HeNe lasers is excellent, which reduces the importance of spatial filtering somewhat. This HeNe laser is strongly polarized, with a polarization ratio of 500:1. A 100x microscope objective is used to expand the laser beam to fill the aperture of the field lens as much as possible, combined with a 5 μm pinhole to spatially filter the beam.

For bench testing with a round turbulent jet, and for use in the Penn State supersonic wind tunnel, Nikon 50mm f/1.2 camera lenses are used for field lenses. These modern, high-quality lenses allow for large beam diameters outside of the test area, without introducing large aberrations to the beam, which would otherwise reduce the quality of the beam focal point. For testing in the much larger AEDC Hypervelocity Tunnel #9, two large 200-mm-focal-length triplet lenses were purchased, which were a good match to the long beam path from the field lenses to the focal point in the center of the tunnel.

The birefringent Sanderson prisms used to split and recombine the laser beam into the two perpendicularly-polarized FLDI beams, the Berek phase compensator used to adjust the phase of the interferometer output beam for maximum sensitivity, and the polarization measurement electronics are described below.

2.1.1 Adjustable Sanderson Prisms for Variable Beam Separation

Instead of the traditional Wollaston prisms typically used in previous FLDI instruments, stress-birefringent plastic Sanderson prisms[53] are used here, where the divergence angle of the prism depends on the stress induced in the prism by loading it in four-point bending. High-quality, low-divergence Wollaston prisms are expensive, typically more than $1000, and for this instrument a closely-matched pair must be used. If the divergences of the two prisms differ, the signal response of the interferometer will be reduced. Sanderson prisms, on the other hand, are optically equivalent to Wollaston prisms at small divergence angles[54], yet are adjustable so that they can be made to match one another exactly. They can be also made at a much lower cost than Wollaston prisms. The Sanderson prisms must be calibrated to determine their divergence angle for a given applied stress, and the method by which this calibration is performed is explained in the Procedures section. The theory of the operation of Sanderson prisms is given in the Theory section of this thesis (3.6.2).

A photograph of the interference pattern produced by observing a Sanderson prism under stress is shown in Fig. 2.4. This is one of the two identical geometry prisms used for this research. The backlighting is polarized light from an LCD computer monitor. A polarizer is mounted on the camera and aligned in the same direction as the monitor's polarization to take a bright field picture of the prism. The red component of the original RGB color photograph is isolated here for clarity in reproduction of the image in grayscale.

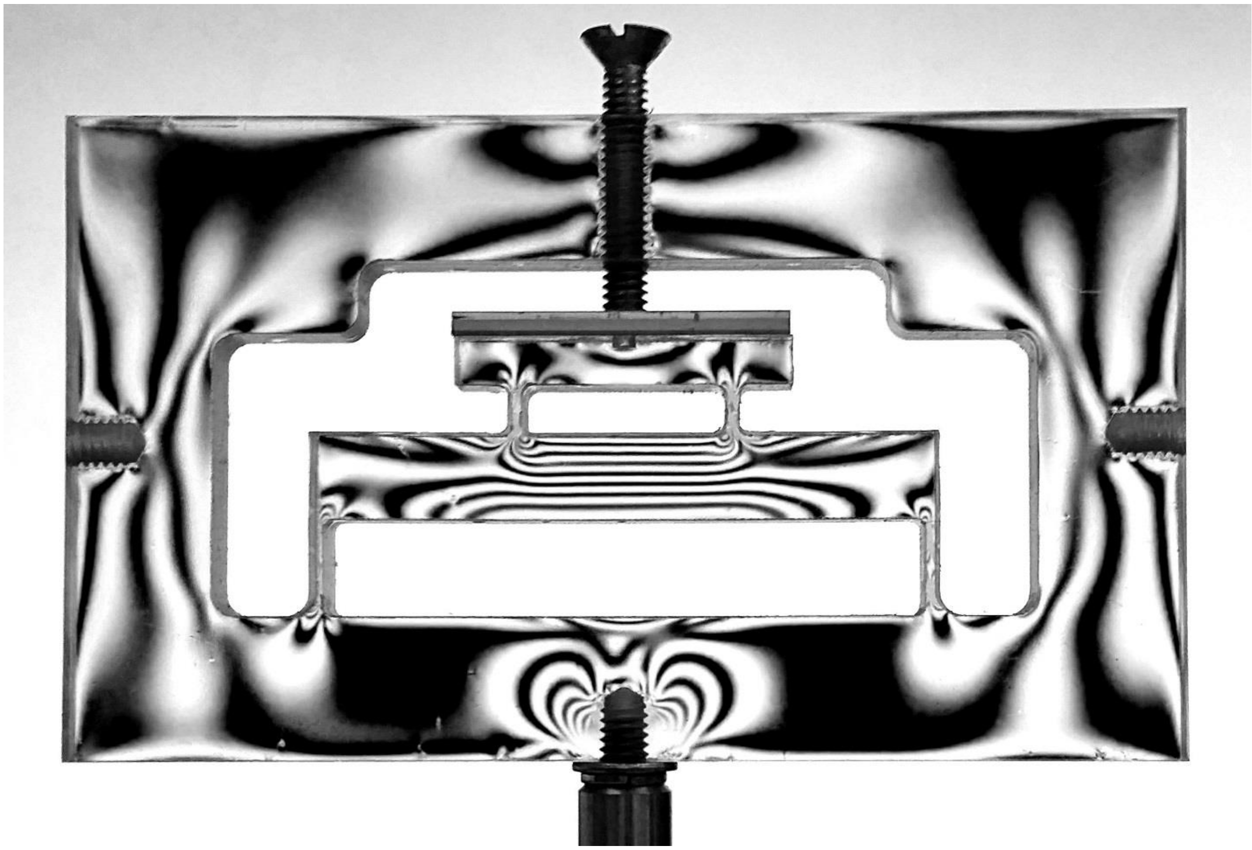

Figure 2.4: Interference pattern of a Sanderson prism under stress. The background lighting is provided by an LCD computer monitor, which is polarized. A polarizer in front of the camera lens causes the interference pattern seen here.

The horizontal bars of the interference pattern in the center of the Sanderson prism are caused by the uniaxial state of stress generated in the prism in four-point bending. The two perpendicularly-polarized beams that emerge from the prism diverge from one another in the axis normal to these horizontal bars.

A photograph of one of the two identical Sanderson prisms used for this research is shown in Fig. 2.5. It is annotated with the critical dimensions of the prism, described in detail in the Theory chapter of this thesis (3.6.2).

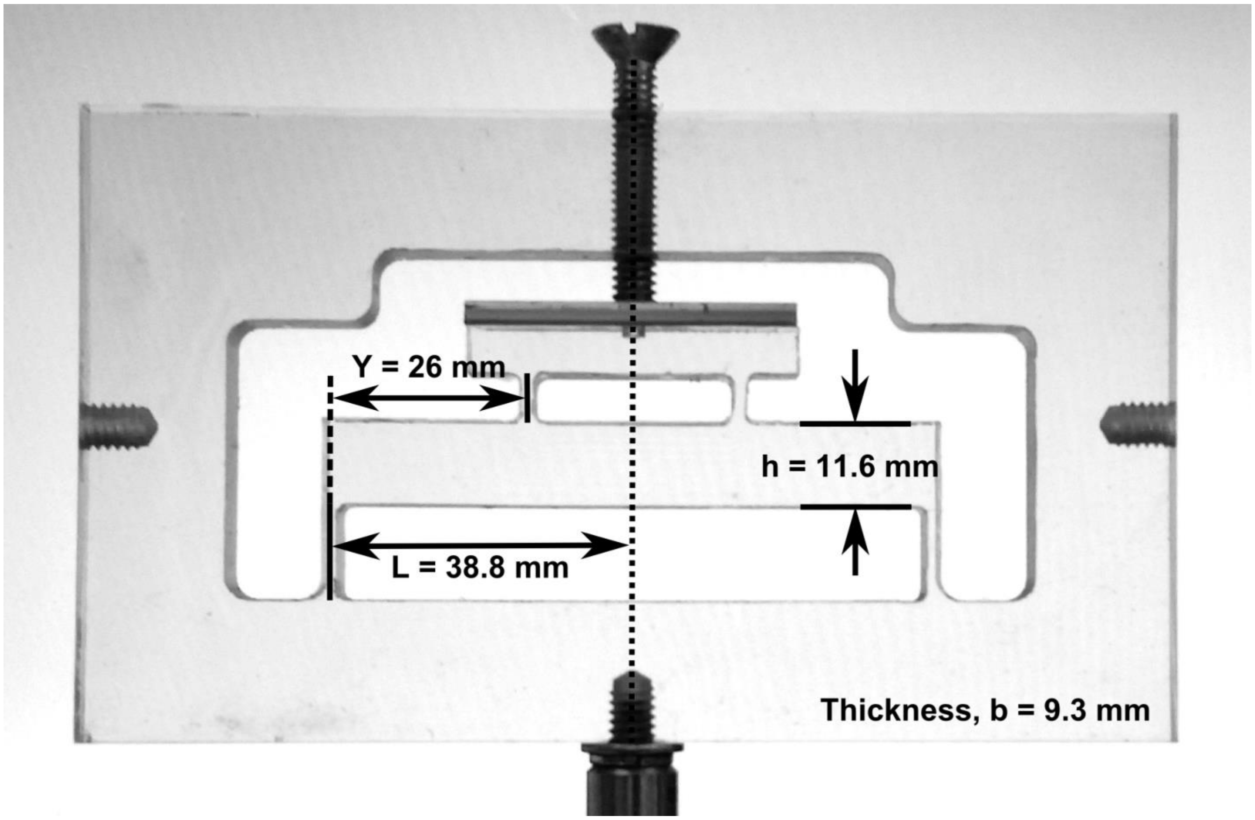

Figure 2.5: Sanderson prism from Fig. 2.4 viewed without polarizer, annotated with critical dimensions of the prism. The use of these dimensions is detailed in Theory section 3.6.2.

Here, L is the distance from the outer load point to the centerline of the prism, while Y is the distance between the inner and outer load points. The height of the prism is h, and the thickness of the prism is b.

2.1.2 Berek Compensator

The FLDI instrument is a polarization interferometer which measures subtle shifts in the phase of the polarization of two laser beams passing through the test volume. This phase shift is related to the difference in optical path length encountered by each beam. To avoid ambiguity in calculating the optical path difference in the interferometer, the mean phase shift of the interferometer must be shifted to the zero degree point on the sinusoidal response curve of the instrument. This ensures that the instrument will respond identically to phase shifts in either direction and maximizes its sensitivity.

Many different designs for phase compensators exist, with the Soleil-Babinet compensator being probably the most well-known. The Soleil-Babinet compensator is a very precise instrument and is easy to calibrate, but it is very expensive and its high precision is not strictly required for the FLDI instrument. A different design, the Berek compensator, fills the requirements at much lower cost. A Newport 5540 “Berek's variable wave plate” was obtained for present purposes.

A Berek compensator consists of an optical window made of a birefringent material, cut so that the beam is parallel to the c-axis of the crystal (the crystal’s optic axis) at normal incidence. At this angle there is no effect from the birefringence of the material. However, tilting the window splits the incoming beam according to its polarization, and displaces each resulting beam by a slightly different amount due to the differing refractive indices for the two polarizations. Berek compensators are typically made either of MgF_2 (as is the case with the Newport 5540) or of sapphire (Al_2O_3), so the refractive-index difference between the two polarizations is so small that there is negligible separation between the resulting beams. The slightly-different path length between the two polarized beams behaves as if it was a small phase difference (0-5 waves over the full tilt range of the window, typically) in the original beam. A diagram showing the behavior of a Berek compensator, with greatly exaggerated beam separation, is shown in Fig. 2.6.

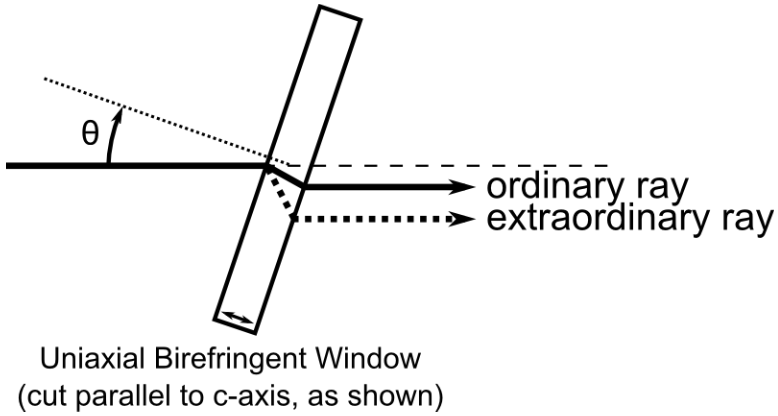

Figure 2.6: Berek compensator diagram showing light entering the compensator window from the left. The component of the light with polarization perpendicular to the crystal axis follows the "ordinary" path, while the component with polarization parallel to the crystal axis follows the "extraordinary" path.

As seen here, the Berek compensator behaves like the displacement from a tilted window, with different refractive indices for the two polarizations. The induced phase difference from the tilt is described by Eq. 2.1.

$$\varphi = \frac{2\pi t n_{\mathrm{o}}}{\lambda}\left(\sqrt{1-\frac{\sin^2\theta}{n_e^2}}-\sqrt{1-\frac{\sin^2\theta}{n_o^2}}\right) \tag{2.1}$$

Here, φ is the phase difference from the Berek compensator in radians, θ is the tilt angle of the window in radians, λ is the wavelength of the laser, t is the thickness of the window, and n_o and n_e are the refractive indices for the ordinary and extraordinary rays through the window, respectively.

It is important to note that this calculation depends on the beam being collimated for its passage through the compensator. If the beam is expanding or contracting as it passes through the compensator, it will retard different parts of the beam to a greater or lesser degree depending on the angle-of-incidence. This error would prevent the Berek compensator from fulfilling its necessary function.

The Newport 5540 Berek compensator is a 2-mm-thick MgF_2 window. From Dodge (1984)[55], the ordinary and extraordinary refractive indices for MgF_2 can be determined for a given wavelength using a three-term Sellmeier equation:

$$n_{o,e}^2 - 1 = \sum A_j \frac{\lambda^2}{\lambda^2 - \lambda_j^2} \tag{2.2}$$

The coefficients A_j and λ_j for MgF_2 are given by Dodge[55], and are repeated here in Table 2.1:

Table 2.1: Sellmeier coefficients for MgF2 from Dodge (1984)[55]

	o-ray	**e-ray**
A_1	0.48755108	0.41344023
A_2	0.39875031	0.50497499
A_3	2.3120353	2.4904862
λ_1	0.04338408	0.03684262
λ_2	0.09461442	0.09076162
λ_3	23.793604	23.771995

Using these coefficients, a plot of phase retardance versus compensator tilt angle for the Newport 5540 Berek compensator is shown in Fig. 2.7.

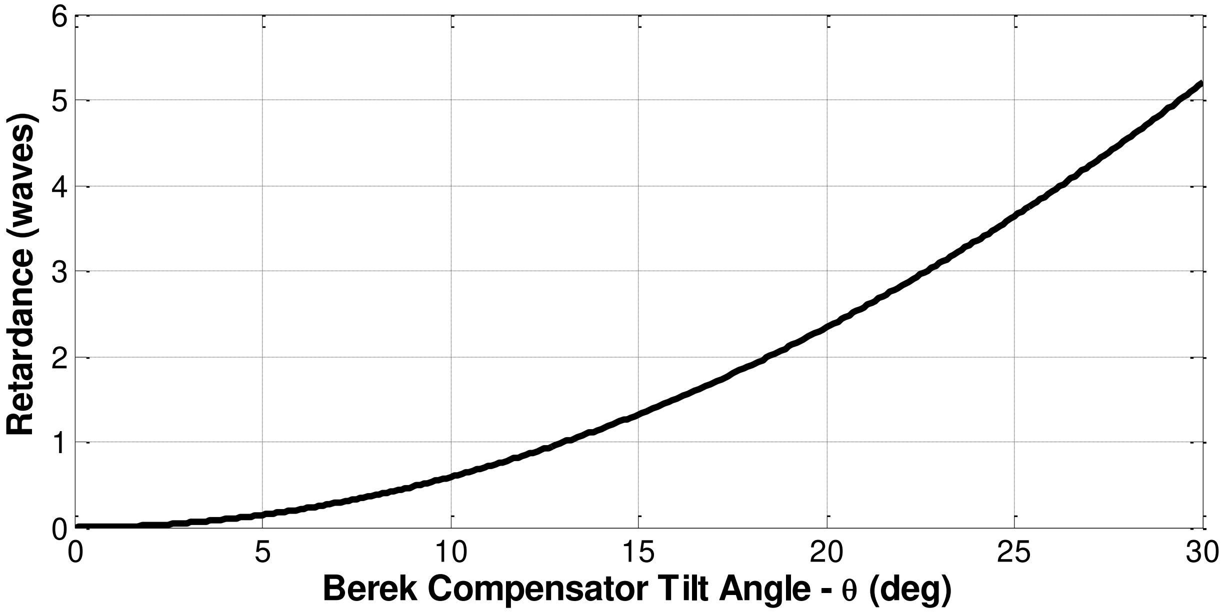

Figure 2.7: Phase retardance, in waves of 632.8 nm HeNe light, for the Newport 5540 compensator calculated using Eq. 2.1. The actual compensator is capable of slightly over 2 waves of retardance over its full adjustment range, as seen in Fig. 4.2.

This calibration of compensator tilt angle with retardance is important for use with the beam-separation measurement explained in the Procedures chapter of this thesis.

2.1.3 Simultaneous Measurement of P- and S-Polarizations

Two Thorlabs DET36 photodetectors are used to measure the polarization shift due to refractive index differences between the two laser-beam paths in the FLDI instrument. By using two photodetectors it is possible to largely reject electronic noise and stray light, and this allows the direct measurement of interferometer phase. The photodetectors are battery biased to further reduce susceptibility to electrical noise, especially that from the 60 Hz noise of power mains. The interferometer signals measured by the two photodiodes are identical, but 180 degrees out of phase from one another. Measurements of the coherence between the signals from each photodiode are used to determine what segments of measured spectra from the instrument are generally free of electronic noise.

Thorlabs VT1 variable terminators are used to convert the current from the photodetector to a usable voltage signal for the data acquisition system, which has high input impedance (1 MΩ, 13 pF typical). Ideally, the photodiodes would be terminated with R_L = 50 Ω loads to match the impedance of the cabling, maximizing photodiode frequency response, however this results in very small signal voltages for the low-power lasers used in this research. Instead, the terminator resistance, R_L, was typically set to 1 kΩ resistance, which was found to provide adequate signal voltages with minimal effect on frequency response. The procedure used to measure reduction in frequency response due to termination resistance is described later in the Procedures chapter of this thesis.

2.2 *Crossed-Beam Schlieren Optics*

The crossed-beam optical correlation instrument used in early stages of this research uses the cross-correlation of the signals measured from two crossed laser beams to measure the convective velocity of a turbulent flow. The refractive displacement of the beams due to this turbulence is measured using position-sensitive detectors (hence the device is not a true Schlieren technique), rather than using photodiodes with pinholes or knife edges as is sometimes reported in literature. One beam is actively panned along the flow direction, and the relationship between the measured beam displacements, dx, and the time delay estimate from cross-correlation, dt, is used to measure the convective velocity of freestream turbulence directly. A schematic of the CBS instrument is shown in Fig. 2.8.

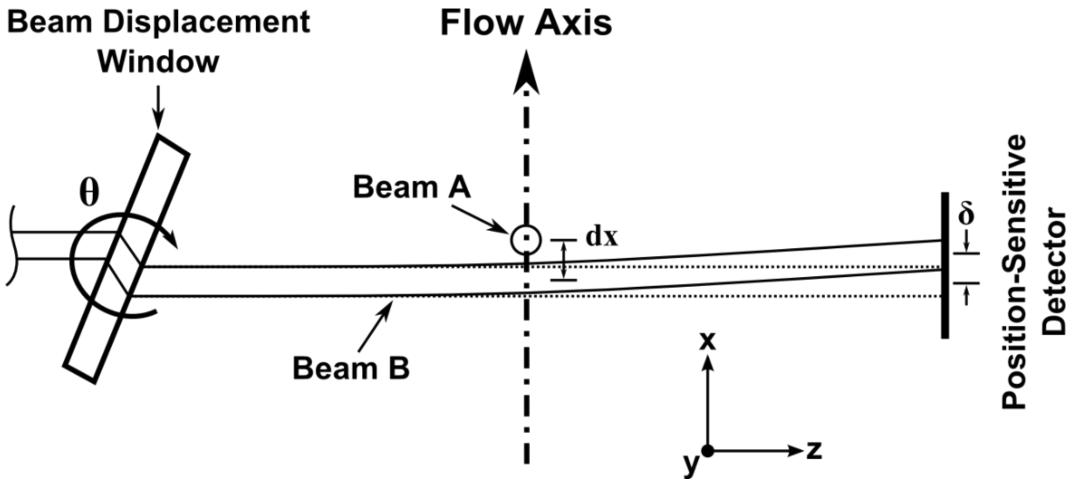

Figure 2.8: Schematic of the crossed-beam optical correlation instrument presented in this research. A glass window is mounted to a servo motor and is used to adjust the separation between the two crossed laser beams. The time delay between the two signals is estimated using cross-correlation at a range of beam separations to determine the convective velocity of the flow.

Here, θ is the tilt angle of a glass window used to displace beam B to a distance dx (along the flow axis) from the centerline of fixed beam A. The dotted line for beam B shows its beam path without a turbulent disturbance from the flow, and the solid line shows beam B displaced on the position sensitive detector due to turbulence. The distance that beam B is displaced on the detector is δ. The position-sensitive detector for beam A is not shown in this diagram for clarity. A photograph of the CBS instrument set up to measure centerline velocity decay in a turbulent round jet is shown in Fig. 2.9.

To get a precise estimate of convective velocity, time delay estimation from the cross-correlation of the two laser-beam signals with known beam separation is used to measure it for each test run. One of the laser beams passes through a small glass window (as seen in Fig. 2.8), mounted to a servo motor. During a test, the window is rotated over an arc to displace the beam along the flow axis without affecting its direction. The amount of displacement is measured as a function of time from the detector outputs and is used with the time delay estimation scheme to perform a least squares fit to obtain the convective velocity.

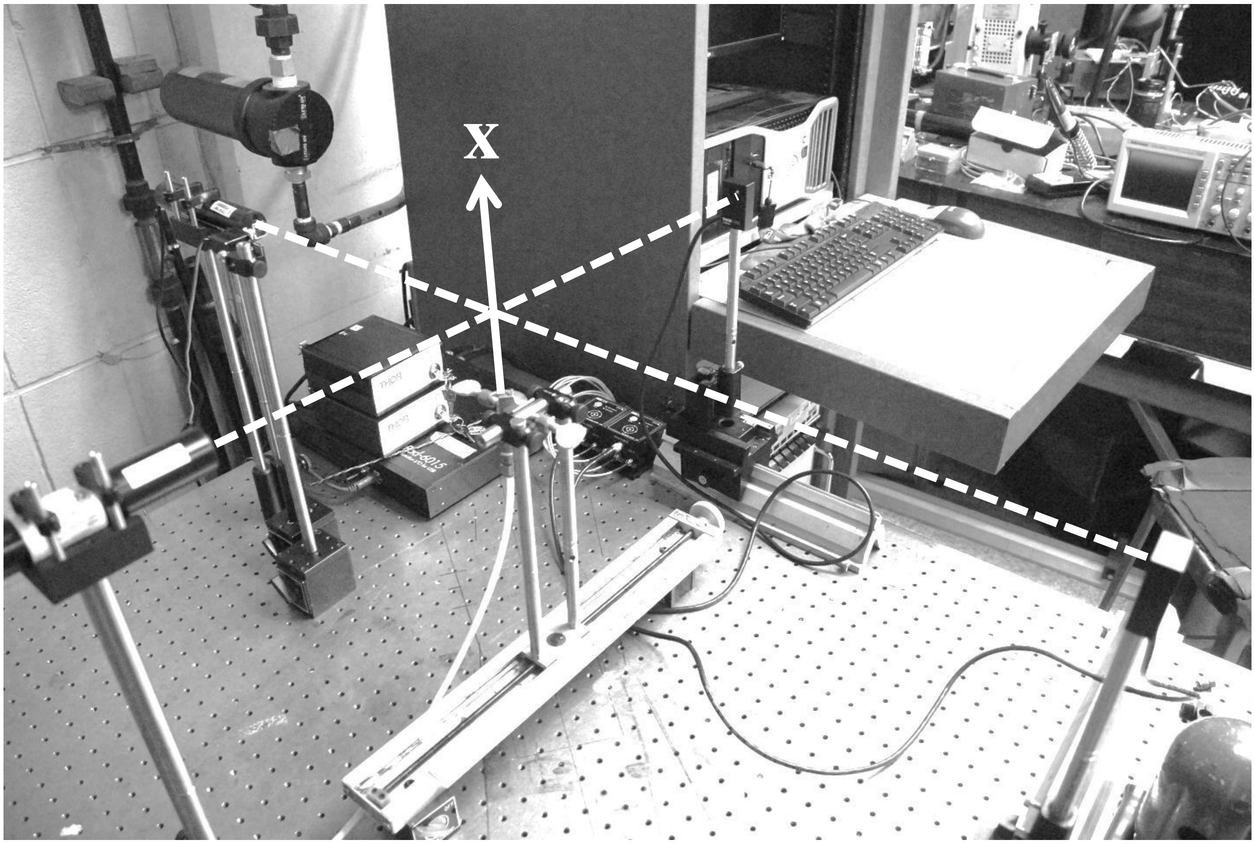

Figure 2.9: Benchtop crossed-beam schlieren instrument set up to measure centerline velocity decay in a turbulent round jet. The beam displacement window is visible in front of the laser in the background.

Two ThorLabs PDP90A two-dimensional lateral effect position sensors are used for measuring the displacement of the beams. These detectors consist of a large pin-cushion-shaped photodiode biased by a common cathode and with anodes in the four corners. Light incident on the photodiode's surface generates a photocurrent in the detector, distributed over the anodes, which corresponds to the centroid of the beam. This allows the detector to measure the position of a beam on its surface across its entire active area to high precision: despite having an active region of 9 mm x 9 mm, the detectors are capable of measuring displacements down to a noise floor of less than 1 µm. The laser beam is continuous, so the response time of the detectors to laser beam displacements is negligible. Testing with an optical chopper showed the detectors to be capable of a frequency response greater than 10 MHz, which is well above the expected frequency response required for this research.

2.3 HWA Setup

A TSI IFA 300 constant-temperature hot-wire anemometer system was used for comparison with the FLDI instrument's response. The IFA 300, with very small diameter wires for minimum thermal mass, is capable of a 300 kHz bandwidth according to its documentation. For the present research, 5 μm tungsten wires, copper-clad to improve the wires' survivability, are used to achieve reasonably-high frequency response. The hot-wire anemometer Wheatstone bridge voltage is measured directly by the data acquisition system, with samples taken simultaneously with the output of the FLDI instrument. This allows the direct comparison from individual tests of density fluctuation spectra from the FLDI instrument and mass flux fluctuation spectra from the hot-wire anemometer.

2.4 Data Acquisition System

The data acquisition system used in this research is a PicoScope 5443B, which is a compact oscilloscope/DAQ. It is a four-channel model, capable of taking data at bit depths of 16-bits for one channel, 15-bits for two channels, or 14-bits for all four channels simultaneously. It can take data at up to 125 MS/s-ch (million samples per second per channel), although its sample memory is limited to 64 MS, split between the active channels. The PicoScope 5443B additionally includes an arbitrary waveform generator, which was used to produce the square wave signals needed for calibration of the photodiode frequency response, as detailed in Procedures section 4.5.

2.5 Facilities

2.5.1 Cold Air Jet

A cold air jet was used to calibrate and characterize the FLDI instrument. Shop air, supplied at 480 kPa absolute pressure to a small nozzle, provided the refractive index disturbance needed for this experiment, cooled by expansion into the surrounding air. The nozzle used in this research is 1 mm in diameter and is a simple converging nozzle. A pressure regulator allows control of the pressure ratio of the jet, and the exit velocity and temperature, to determine the lowest feasible density gradient resolvable by the instrument. Translation stages with vernier scales are used to position the jet relative to the FLDI instrument's point of best focus. A photograph of the benchtop cold air jet test is shown in Fig. 2.10.

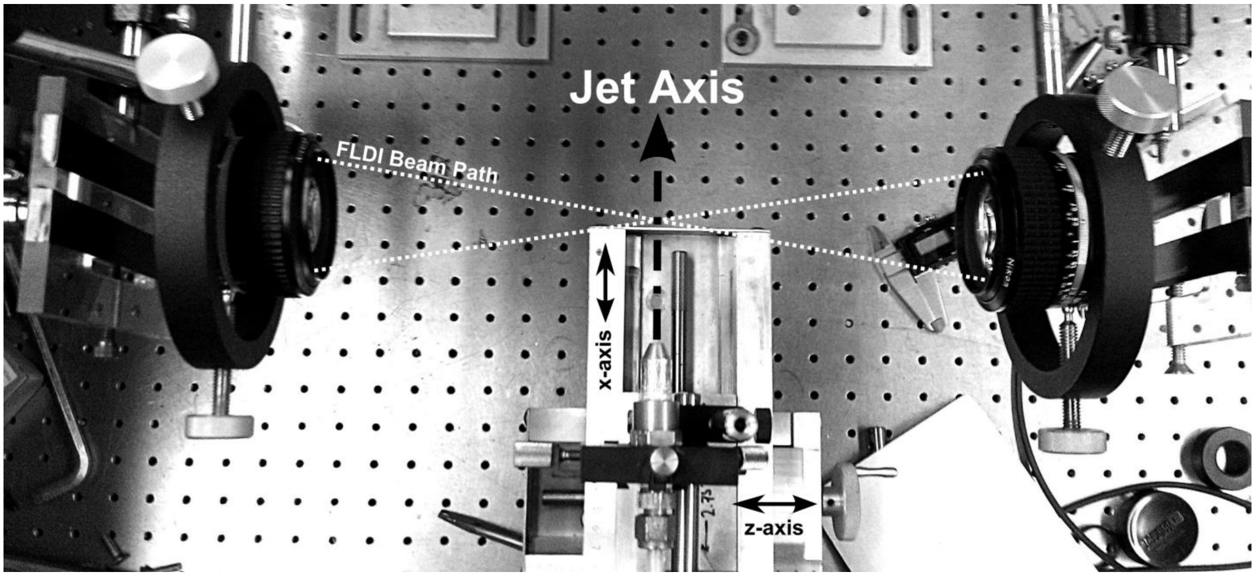

Figure 2.10: Benchtop cold air jet setup, showing the cold air jet, translation stages, and the path of the FLDI beams through the test area. The x-axis is both the axis of FLDI beam separation and the jet axis, and the z-axis is the axis of the FLDI beam propagation. The y-axis is oriented toward the reader.

2.5.2 PSU Supersonic Wind Tunnel

Local wind tunnel testing was performed in the Penn State Gas Dynamics Laboratory's supersonic wind tunnel, abbreviated here as the PSUSWT. A drawing of the tunnel is shown below in Fig. 2.11.

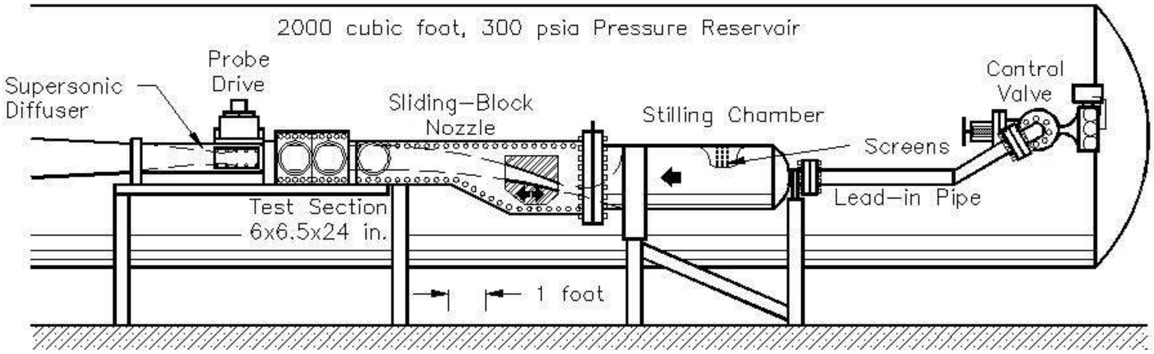

Figure 2.11: Penn State Supersonic Wind Tunnel (PSUSWT). The Mach number of the tunnel can be adjusted by sliding the floor of the rectangular nozzle back and forth, as shown in the diagram.

The PSUSWT is an intermittent blowdown tunnel with an adjustable sliding-block nozzle, which allows a Mach number range of 1.5 to 4.0. The test section measures 6 x 6.5 x 24 in. (15 x 16 x 61 cm) and is optically accessible from the sides through 8 inch (20 cm) diameter windows. The tunnel is supplied by a 200 m^3, 20 atm pressure reservoir which permits test runs of 30+ seconds. The operating envelope of the PSUSWT is shown in Fig. 2.12 for comparison with AEDC Hypervelocity Wind Tunnel 9's operating characteristics, to be discussed next.

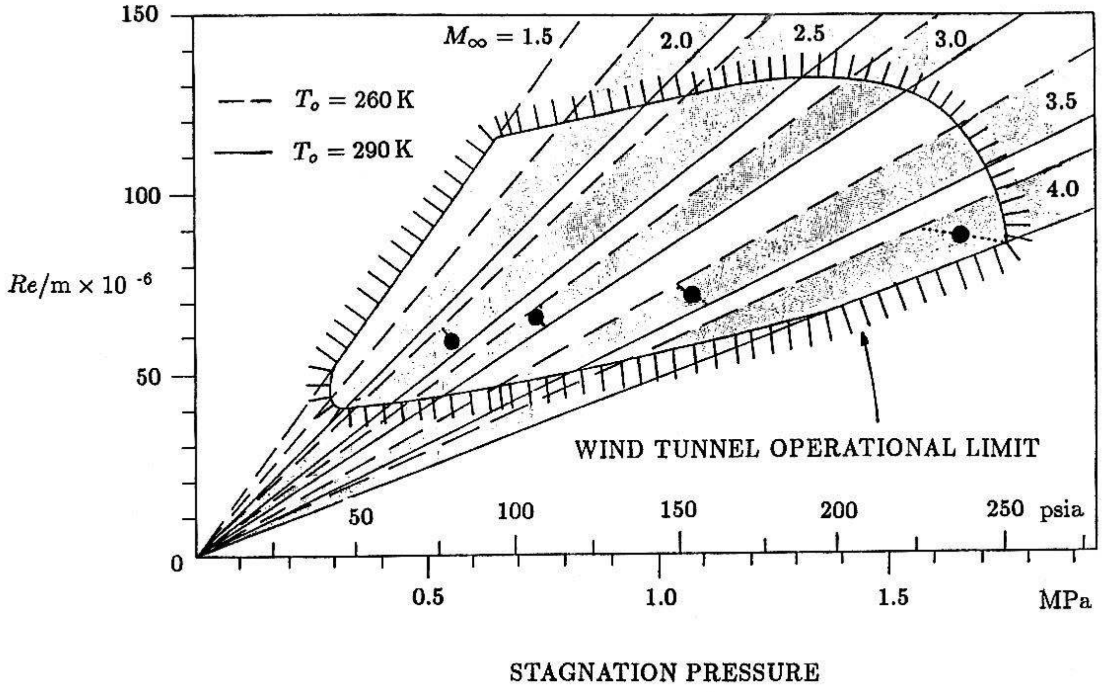

Figure 2.12: Operating envelope of PSUSWT[56]. Testing for this research was performed at *M* = 3.0 with a stagnation pressure of 100 psia (0.7 MPa), giving a unit Reynolds number of ~60 x 10^6 / m.

Testing was performed at $M = 3.0$, with a stagnation pressure of 100 psia (0.7 MPa). At these conditions, the unit Reynolds number of the tunnel is approximately 60 x 10^6 / m, with a freestream density of 0.64 kg/m^3, U_∞ of 598 m/s, and sidewall boundary thickness of approximately 1 inch (25 mm).

2.5.3 AEDC Hypervelocity Wind Tunnel #9

Testing was also performed at AEDC Hypervelocity Wind Tunnel No. 9, in White Oak, MD. A photograph of Hypervelocity Tunnel 9 is shown in Fig. 2.13.

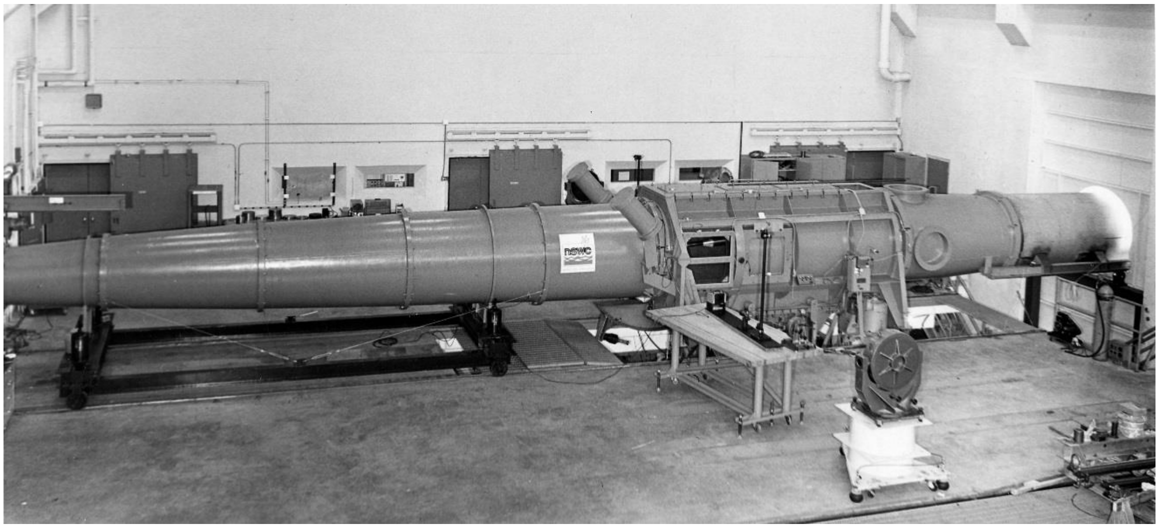

Figure 2.13: AEDC Tunnel #9. The tunnel is optically accessible using two sets of rectangular windows on the side of the test section. In this photograph, the downstream windows have been replaced with metal plates. In this research, the instrument presented here was installed on the upstream windows, while the downstream windows were used with the facility's schlieren system.

Tunnel 9 is, like the PSUSWT, an intermittent blowdown wind tunnel, and is capable of Mach numbers of 7 to 14 by interchangeable nozzles. It uses nitrogen gas to avoid real gas effects from condensation of the oxygen in air at the low static temperature run conditions encountered in Tunnel 9. Ablative graphite heaters are used to heat the gas to 1000+ K, to achieve very high freestream velocities and unit Reynolds numbers. This allows the simulation of high-speed flight at lower effective altitudes than is possible in most hypersonic facilities. The test section is circular and 60 inches (1.5 m) in diameter, however the useful core diameter, uncorrupted by tunnel wall boundary layers, is heavily dependent on which nozzle is in use and the operating unit Reynolds number. The freestream density of the flow at higher Mach numbers in T9 is substantially less than is possible in the PSUSWT. It is between approximately 0.5-7.5 x 10^{-3} kg/m^3 at Mach 10, which is the Mach number at which the current tests were performed. In the $M = 10$ nozzle, the core diameter, clear of boundary layer turbulence, is approximately 1.02 m. This means that roughly one third of the optical path that the FLDI instrument must look through is corrupted by boundary-layer turbulence. Photographs of the FLDI optics installed in Tunnel 9 are shown in Figs. 2.14 and 2.15.

To overcome some of the noise problems experienced with the long cable lengths and electrically noisy environment of T9, two Stanford Research SR560 battery-powered preamplifiers were used. The SR560 is capable of gain from 1 to 50,000, and has built in high- and low-pass filters that can be set from DC to 1 MHz cutoff frequencies.

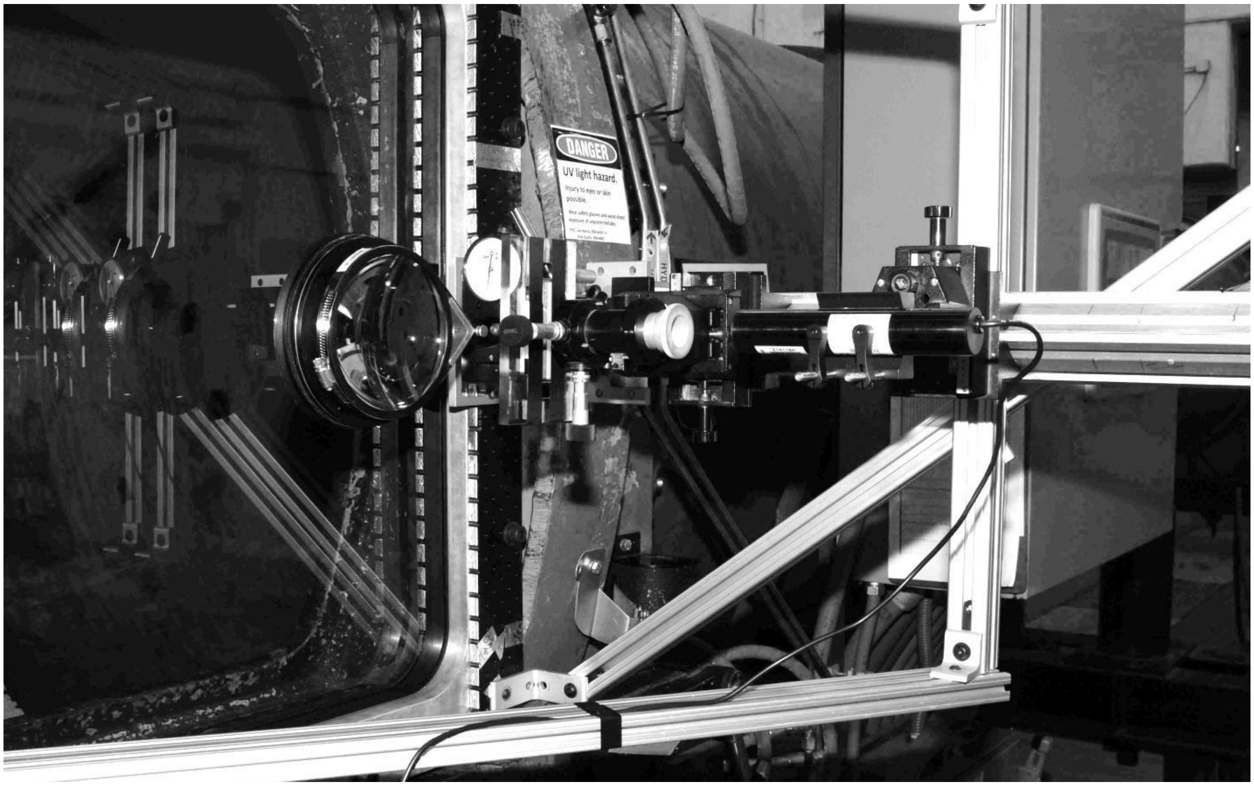

Figure 2.14: Transmitting optics for FLDI instrument installed in Tunnel 9.

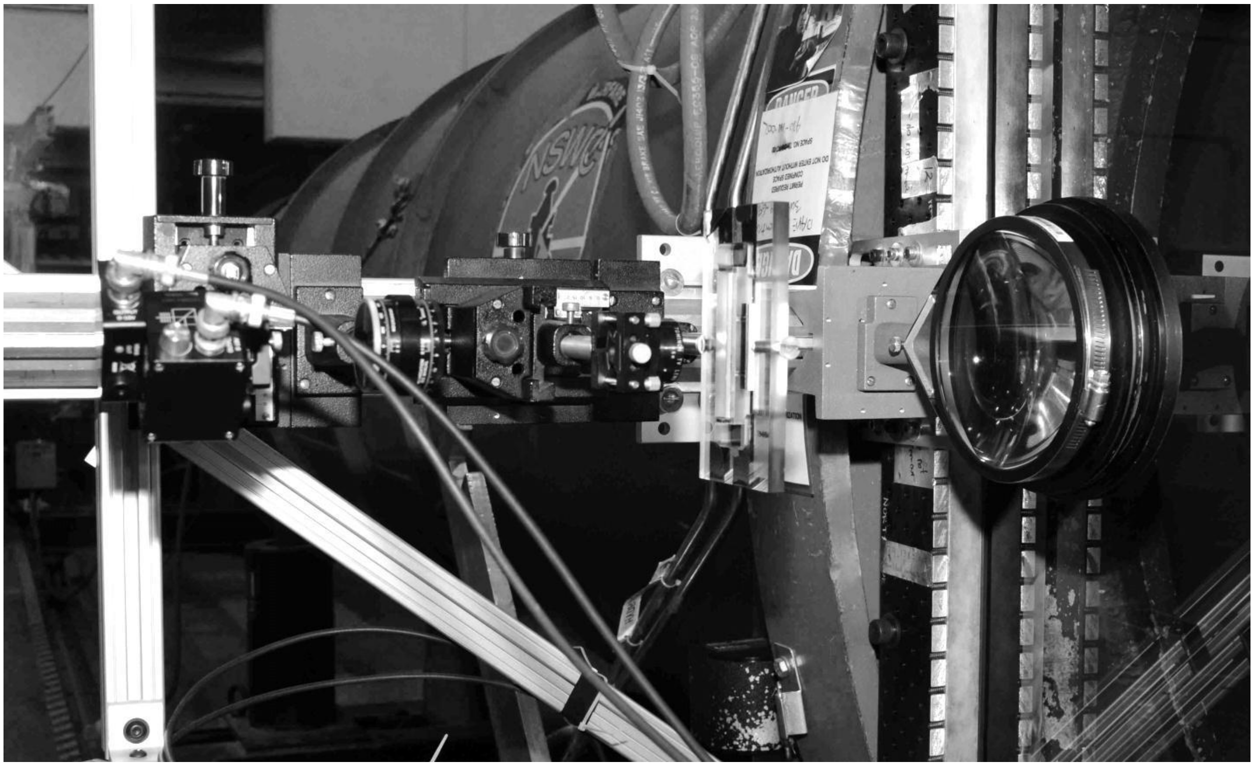

Figure 2.15: Receiving optics for FLDI instrument installed in Tunnel 9.

Chapter 3: Theory

3.1 *Aero-optics*

As a beam of light passes through density inhomogeneities in a fluid, these inhomogeneities impart aberrations in the beam. The shimmering effect seen when looking past hot objects, like cars and roads in the sun, is an example of strong aberrations stemming from the density gradient between the hot surface and cooler air. The study of these aberrations and how to relate them to the fluid dynamic effects that cause them is a field called aero-optics. All optical flow-visualization techniques leverage these aberrations to allow researchers to "see" the density field of a flow or one of its derivatives.

These optical techniques are often hampered by their path-integrated nature, wherein the light beam is affected by all the inhomogeneities along the entire optical path, and not just those in the desired testing volume. A typical example of this problem is the corruption of schlieren and shadowgraph images by turbulent boundary layers on the windows of wind tunnels. The instrument developed in this research, while still path-integrating, leverages spatial filtering effects to achieve a "point-like" measurement of turbulence properties, despite aero-optic effects elsewhere along the optical path.

3.2 *The Gladstone-Dale Relation*

Central to aero-optics is the Gladstone-Dale relation[57], which shows that the refractive index of a fluid is directly proportional to the density of the fluid. This relation is shown in Eq. 3.1a for a general case, and Eq. 3.1b shows the extension of the relation to the derivatives of a density field. Here, $K_{GD,i}$ is the Gladstone-Dale constant at a given wavelength of light for each species of fluid in the volume, and ρ_i is the density of that species. At 632.8 nm, the wavelength of the HeNe lasers used in this research, the Gladstone-Dale constant of air is approximately 2.257 x 10^{-4} m^3 / kg, while the Gladstone-Dale constant for pure nitrogen gas is approximately 2.38 x 10^{-4} m^3 / kg.

$$n-1=\sum_i K_{GD,i}\rho_i \qquad \frac{\partial n}{\partial x_j}=\sum_i K_{GD,i}\frac{\partial \rho_i}{\partial x_j} \tag{3.1a,b}$$

Because of the direct proportionality between refractive index and density, local fluctuations in the density field lead to a corresponding variation in the refractive index. The spectra of refractive index disturbances measured by the device presented here should thus behave in the same manner as the spectra of density disturbances in the flow.

3.3 Deflectometry

The most basic aero-optical technique, and the easiest to describe, is deflectometry. With deflectometry, a collimated beam is propagated through a fluid medium. As mentioned above, fluctuations in density throughout the medium lead to variations in the local refractive index. Gradients in fluid refractive index deflect light rays as they pass through them. Inhomogeneities on a scale larger than the beam diameter tilt the beam, causing it to be deflected as a whole (as shown in Fig. 3.1), while inhomogeneities smaller than the beam only deflect a portion of it, leading to effects such as defocusing.

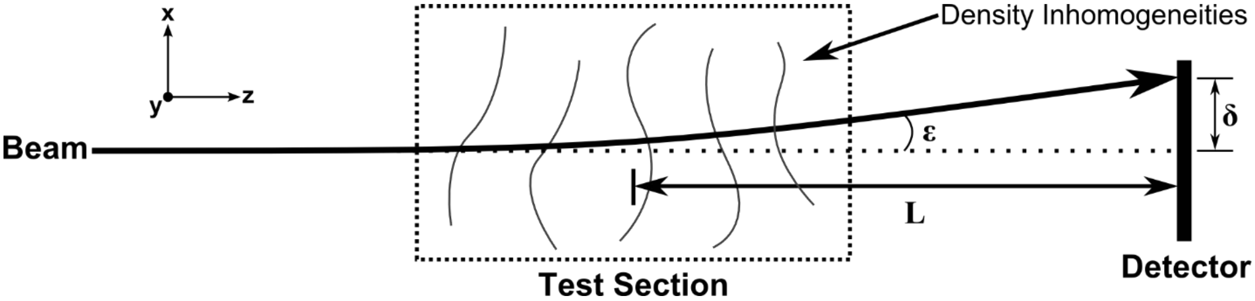

Figure 3.1: Deflection of a beam due to density inhomogeneities in the path of the beam. The deflection of the beam measured at the detector comes from disturbances integrated over the entire path of the beam from the laser to the detector.

These small disturbances tend to average out in the direction they deflect the beam, and cause the beam spot on a detector to blur. The mean deflection of the beam, measured as a shift, *δ*, on the detector, is the integrated effect of all of the refractive index gradients along the path that the beam follows through the medium, as shown in Eq. 3.2.

$$\begin{aligned} \varepsilon_x &= \tan^{-1}\left(\int_{s_1}^{s_2} \frac{1}{n}\frac{\partial n}{\partial x} ds \right) \\ \varepsilon_y &= \tan^{-1}\left(\int_{s_1}^{s_2} \frac{1}{n}\frac{\partial n}{\partial y} ds \right) \end{aligned} \qquad (3.2)$$

Here, ε_x and ε_y represent the mean deflection angles of the beam at the measurement plane, *n* is the local refractive index field, and the integral is over beam path *s*. When the deflection angles are very small, the small-angle approximation can be invoked, and the integral can be considered over the *z*-axis instead of requiring a path integral. This simplified calculation is shown in Eq. 3.3.

$$\begin{aligned} \varepsilon_x &\approx \int_{z_1}^{z_2} \frac{1}{n}\frac{\partial n}{\partial x} dz \\ \varepsilon_y &\approx \int_{z_1}^{z_2} \frac{1}{n}\frac{\partial n}{\partial y} dz \end{aligned} \qquad (3.3)$$

Using position-sensitive diodes as a detector (as in Fig. 3.1) allows direct measurement of beam displacement which, when divided by the distance between the origin of the beam deflection and the detector, gives the deflection angles shown above. The schlieren technique is an imaging form of deflectometry, in which a sharp edge is placed at a focus after the test section to spatially filter the beam. Beam tilt toward or away from the edge causes the transmitted intensity to increase or decrease which, when calibrated, can also be used to determine the deflection angle of the beam, perpendicular to the edge.

3.4 Interferometry

Deflectometry is limited by the difficulty of measuring very small deflections. Beam paths must be long enough to ensure that the beam displacement signal from the sensors is significantly greater than measurement noise. The dynamic range of a position sensitive detector is limited by the active area of the sensor. Large area sensors, however, have lower frequency response. Photodetector junction capacitance scales with the area of the detector, which increases the time constant of the detector. A technique related to deflectometry that overcomes some of these difficulties is interferometry, which uses constructive and destructive interference of waves of coherent light to measure wavefront tilt[58]. Typically, interferometers split an input beam into two beams, where one beam passes through the volume under test, while the other passes around this volume and serves as a reference beam. This arrangement is called a double-path interferometer. The wavefront of the reference beam ideally is undisturbed throughout its path, while the wavefront of the test beam is aberrated by flow disturbances. A typical double-path interferometer design is the Mach-Zender interferometer, as diagrammed in Fig. 3.2.

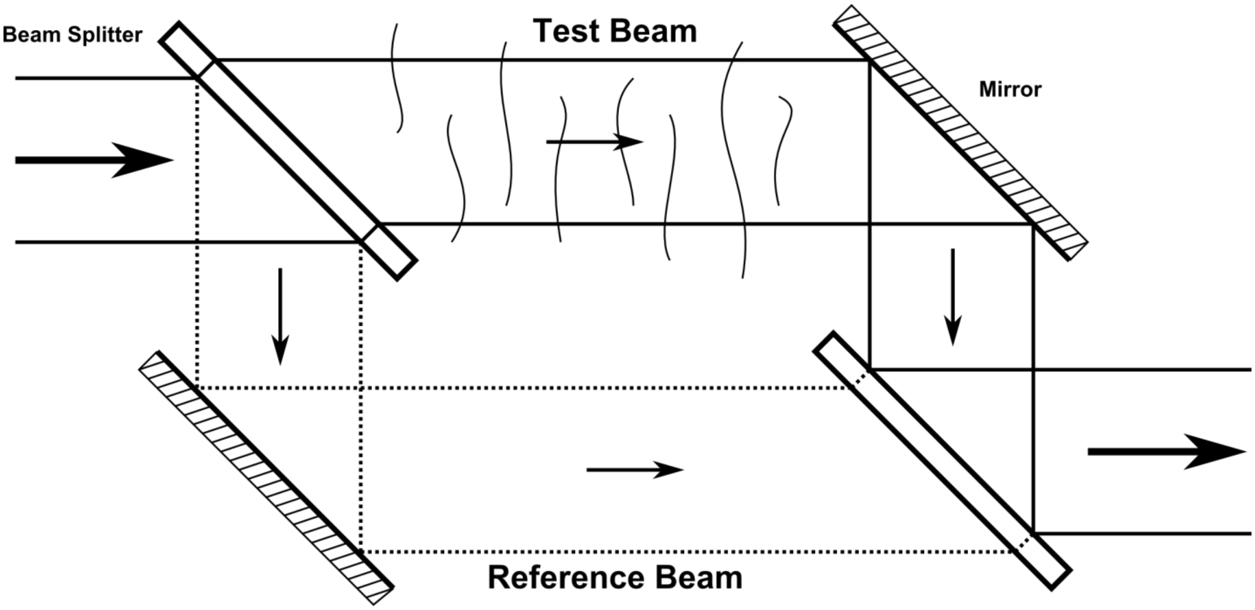

Figure 3.2: Mach-Zender interferometer layout. Arrows show the beam paths through the instrument. The difference in optical path length experienced by the two otherwise identical beams results in interference patterns at the output of the interferometer.

The phase velocity of a wavefront is the speed of light in vacuum divided by the local refractive index. Variations in the phase velocity of the test beam due to density inhomogeneities induce phase delays relative to the reference beam. This relative phase delay from the test volume is described in Eq. 3.4. $\Delta\varphi$ is the relative phase delay of each point on the recombined beam at the measurement plane, λ is the wavelength of the monochromatic light source used in the interferometer, and the beam is again integrated over path s, as with deflectometry.

$$\Delta\varphi = \frac{2\pi}{\lambda}\int_{s_1}^{s_2}[n(x,y,z) - n_\infty]ds \tag{3.4}$$

When the beams are recombined, they will interfere with one another: portions of the test beam that are in phase with the reference beam will appear bright, while out of phase portions of the beams will appear dark: fringes appear. The intensity of the interferogram is described by Eq. 3.5.

$$I = I_1 + I_2 + 2\sqrt{I_1 I_2}\cos(\Delta\varphi) \tag{3.5}$$

While deflectometry typically requires relatively large deflections to make accurate measurements, interferometry is limited in the opposite manner. As interference occurs over periods of light waves, large deflections may wrap over many wavelengths of light, causing many fringes to appear in the interferogram. In imaging applications, careful unwrapping of this phase signal can sometimes mitigate this issue, however in non-imaging systems like the instrument developed here, this is not possible. Because of this issue, the interference must be kept in the –π/2 to π/2 range on a sine curve to avoid phase ambiguity, and ideally it should be restricted to a much smaller range to keep the signal response as linear as possible. This is demonstrated in Fig. 3.3.

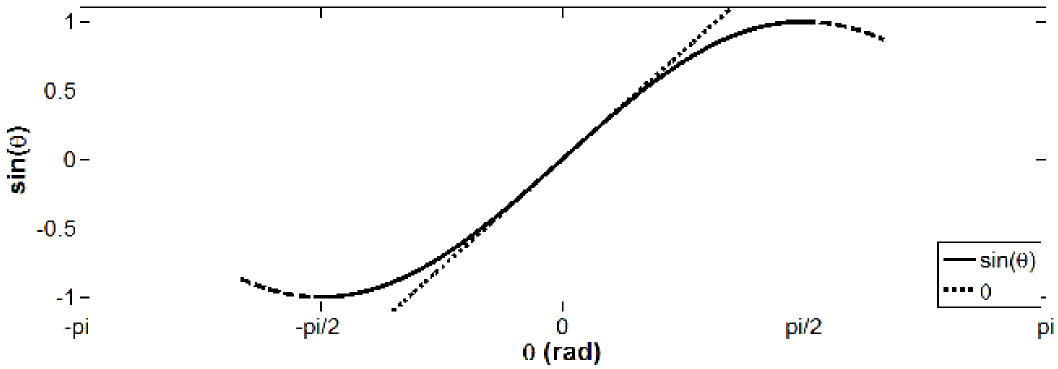

Figure 3.3: Sinusoidal response curve of interferometer, showing linear region around the 0 radian point on the sine.

Here, possible aliasing of the interferometer response outside the range of –π/2 to π/2 is plainly evident. Meanwhile, if the phase is kept within a range of –π/10 to π/10, the difference between sin(θ) and θ is less than 1%, and the small-angle approximation can be invoked. In practice, many refractive fields are strong enough to exceed this linear region, which limits the usefulness of double-path interferometry for the turbulence measurements being performed in this research.

3.5 Common-path Interferometry

The sensitivity of an interferometer and its susceptibility to vibration can be reduced by replacing the reference beam with another test beam, separated by a small distance from the path of the original test beam. This is called common-path interferometry, since the two beams share almost all of their optical paths with one another. With this arrangement (sometimes called a shearing interferometer), the interference behaves as a finite difference between the two wavefronts, measuring $\Delta\varphi/\Delta x$ instead of φ as the double-path interferometer does, where x is perpendicular to the optical axis, z. This is described by Eq. 3.6.

$$\frac{\Delta\varphi_A - \Delta\varphi_B}{\Delta x} = \frac{2\pi}{\lambda \Delta x}\left\{ \int_{s_{1A}}^{s_{2A}} \left[n\left(x + \frac{\Delta x}{2}, y, z \right) - n_\infty \right] ds_A - \int_{s_{1B}}^{s_{2B}} \left[n\left(x - \frac{\Delta x}{2}, y, z \right) - n_\infty \right] ds_B \right\} \tag{3.6}$$

Here, the relative phase delay is similar to double-path interferometry, however the reference beam is replaced by a second beam path, s_B, while the test beam follows path s_A, separated by a small distance, Δx.

This particular type of common-path interferometer is called a lateral-shearing interferometer, as diagrammed in Fig. 3.4. The coordinate system used here is displayed for reference.

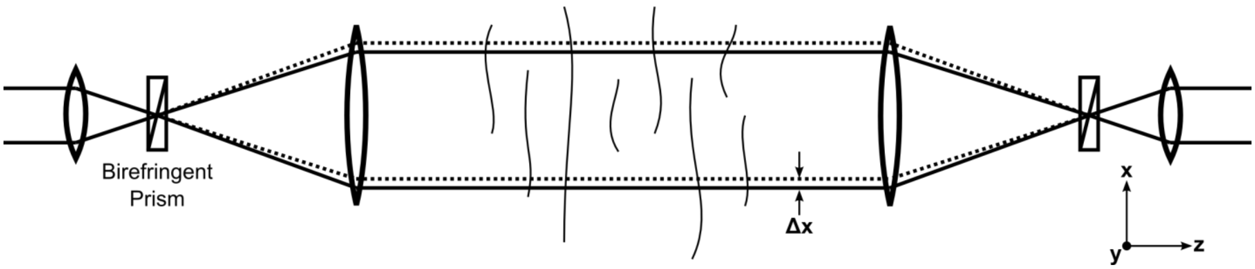

Figure 3.4: Lateral shearing interferometer. Unlike with a Mach-Zender interferometer, the two beams follow a mostly common path, separated by a small distance, Δx. Because of this, the lateral shearing interferometer gives an approximation of the gradient of the refractive index field along the axis of beam separation, rather than a direct measurement of refractive index.

The phase range of the interference can be reduced by reducing the separation Δx (the shear) of the two beams. However, the amplitude of the interference is also reduced in doing this. With too small a beam separation, the signal from the interferometer may drop below the noise floor of the detectors. As will be demonstrated later, smaller beam separations are also important for maximizing the frequency response of the instrument. All of these factors must be considered on a case-by-case basis in determining the ideal beam separation to use.

By definition, the finite difference becomes a derivative in the limit as the separation Δx approaches zero in Eq. 3.6. In this case, shown in Eq. 3.7, the two beams can be assumed to follow the same path with regards to the path integration.

$$\begin{aligned}\frac{\partial \varphi_{AB}}{\partial x} &= \lim_{\Delta x\to 0}\frac{\Delta\varphi_A-\Delta\varphi_B}{\Delta x}\\ &= \lim_{\Delta x\to 0}\frac{2\pi}{\lambda\Delta x}\int_{z_1}^{z_2}\left[n\left(x+\frac{\Delta x}{2},y,z\right)-n\left(x-\frac{\Delta x}{2},y,z\right)\right]dz \\ &=\frac{2\pi}{\lambda}\int_{z_1}^{z_2}\frac{\partial n}{\partial x}dz\end{aligned} \tag{3.7}$$

Because the response of the instrument is reduced to zero at zero beam separation, this case is not physically realizable. However, it serves to demonstrate the similarity of lateral-shearing interferometry to deflectometry. Also, as will be shown later, depending on the flow properties, this approximation may be appropriate even with finite beam separation. Using the Gladstone-Dale relation, the refractive index gradient field may be related to the density field, as in Eq. 3.8:

$$\frac{\partial \varphi_{AB}}{\partial x}=\frac{2\pi K_{GD}}{\lambda}\int_{z_1}^{z_2}\frac{\partial \rho}{\partial x}dz \tag{3.8}$$

3.6 Focusing-Laser Differential Interferometry

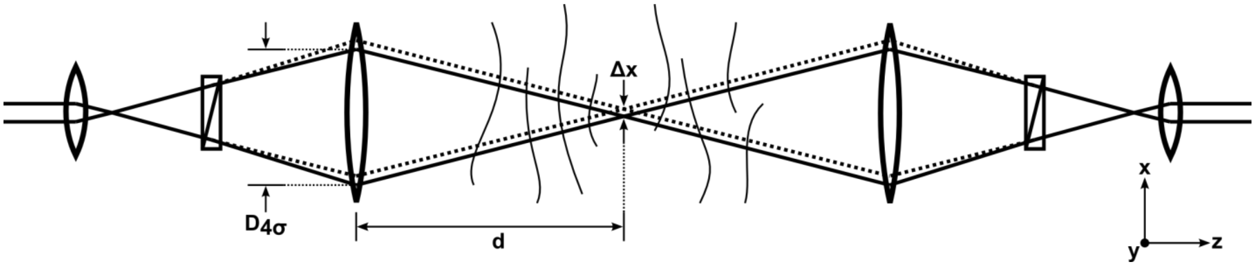

Figure 3.5: Focusing-laser differential interferometer. The FLDI instrument is an extension of the lateral shearing interferometer concept which uses focused beams to improve sensitivity to disturbances at the focus of the instrument and reject signal from disturbances outside of this focal region.

The technique investigated in this research, focusing-laser differential interferometry (FLDI), is a non-imaging common-path interferometer. With this technique, the laser beam is laterally sheared by a small amount and the resulting beams are expanded to a large diameter at the edges of the measurement volume. The beams are brought to sharp focus in the region of interest. The basic layout of the FLDI system is shown in Fig. 3.5. Focusing of the two FLDI beams spatially filters inhomogeneities along the beam paths, significantly reducing the contribution to the output signal of disturbances that are distant from the focal point. This gives a "point-like" measurement of density fluctuations in the flow.

3.6.1 Polarized Light Analysis

The FLDI technique is more specifically a polarization interferometer, where the input laser beam is split into two beams of mutually-perpendicular polarization, with a small divergence angle between them, by the use of a birefringent prism. The input beam is linearly polarized. However, each of the sheared beams' wavefronts encounter slightly different refractive index fields, as explained above, and when recombined, these relative phase differences result in an elliptically-polarized output beam. A brief introduction to the polarized light analysis used for this research is given here, but more in-depth explanations of these concepts can be found in textbooks such as Born & Wolf's "Principles of Optics."[59]

For the coherent, fully-polarized beams used by the FLDI instrument, wavefronts can be represented simply by arrays of polarization vectors, called Jones vectors. At each point on the wavefront, the local polarization (the electric field, or "E-field", of the light) can be decomposed into a two-dimensional complex vector (Eq. 3.9) that fully describes the possible states of polarization of light throughout the FLDI instrument, from the laser source to the photodetectors.

$$E = \begin{bmatrix} E_x e^{i\phi_x} \\ E_y e^{i\phi_y} \end{bmatrix} \tag{3.9}$$

Here, E_x is the amplitude of the electric field of the wavefront in the x-direction, and ϕ_x is the phase of the field in the x-direction. Likewise, E_y and ϕ_y are the amplitude and phase of the field in the y-direction.

The "shape" of the light's state of polarization is defined by Lissajous curves, which are x-y plots of the instantaneous amplitude of both components of the electric field through one full sinusoidal oscillation of the wave. In the case that ϕ_x and ϕ_y are equal, or if one of the E_x or E_y amplitude components is zero, the light is said to be linearly polarized, as both components are oscillating in phase with one another, so the Lissajous curve appears linear. If E_x and E_y are equal, and ϕ_x and ϕ_y are 90 degrees out of phase from one another, the light is circularly polarized and the Lissajous curve traces a circle. All other states of polarization are elliptical. An example of the effect of delaying one component's phase in initially-linearly-polarized light at 45 degrees is shown in Fig. 3.6.

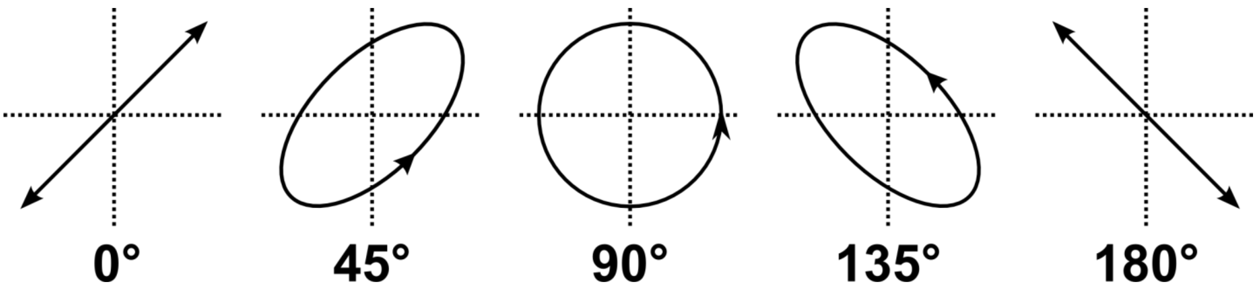

Figure 3.6: Lissajous curves for initially-linearly-polarized light at 45 degrees (equal intensity in E_x and E_y), where one component's phase is retarded by the angle indicated below each curve. A relative phase difference between the *x*- and *y*-components of polarization results in elliptical polarization, except when their polarization is 90 degrees out of phase, which results in circular polarization.

By forming a two-dimensional array of these vectors, an "image" of a wavefront can be constructed, where each pixel contains the local complex polarization vector. A diagram of this method is shown in Fig. 3.7.

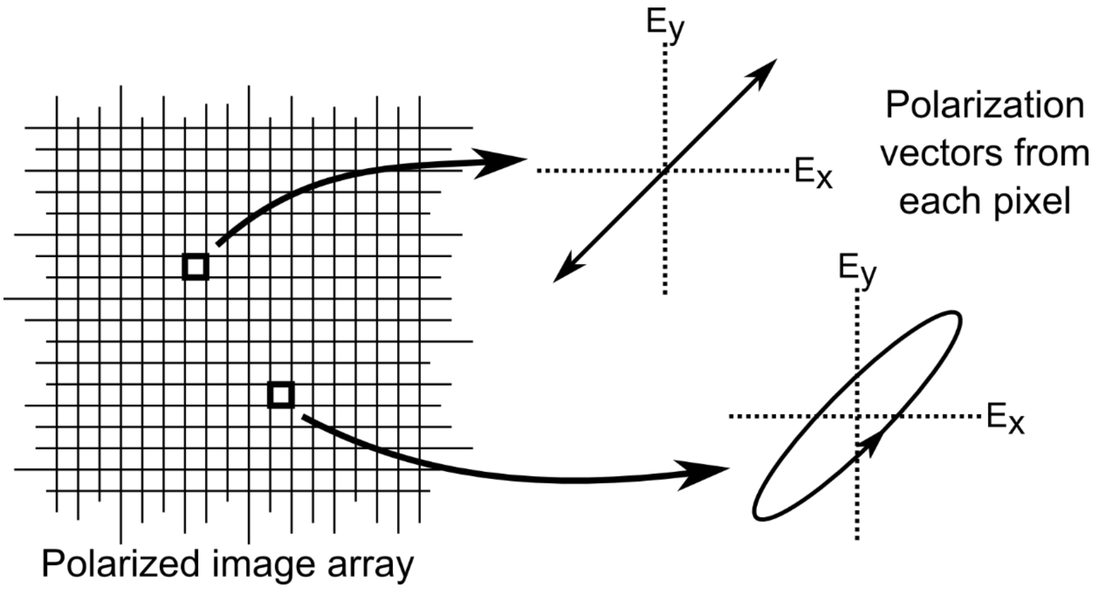

Figure 3.7: Diagram showing how a polarized image may be constructed from Jones vectors. The grid on the left represents an image of a polarized beam, where each pixel is a complex 2-D vector, representing the electric field at that point in the beam.

These images can be summed to model the interference of the two superposed wavefronts, such as the recombined beams from the FLDI system. This technique is used to develop some of the transfer functions presented later, and in simulations of the FLDI system's response.

Jones vectors share all of the properties of Euclidian vectors: they can be summed and subtracted or multiplied by scalars. The magnitude of a Jones vector describes its "length" in terms of the intensity of the light at that point, as in Eq. 3.10.

$$I = \langle E, E \rangle = E^{*} E = \begin{bmatrix} E_x^{*} & E_y^{*} \end{bmatrix} \begin{bmatrix} E_x \\ E_y \end{bmatrix} \tag{3.10}$$

It is worth noting that the phase difference between the x- and y-components of polarization does not affect the intensity of the light by itself: the ellipticity of light’s polarization is normally an invisible phenomenon. Passing the light through a polarizer, where the axis of the polarizer is aligned with the polarization vector, converts this phase difference into an intensity difference. Polarizers can be described mathematically using matrices, as demonstrated below.

Just as Euclidean vectors can be transformed using matrix algebra, states of polarization described by Jones vectors can be manipulated through Jones matrices. The effects of many optical elements on light intensity and phase can be modeled through these matrices, such as polarizers, waveplates, and the birefringent prisms used in this research. The simplest Jones matrices are those of polarizers aligned horizontally or vertically, represented by Eqs. 3.11a and 3.11b, respectively.

$$\begin{gathered} M_{\text{H-pol}} = \begin{bmatrix} 1 & 0 \\ 0 & 0 \end{bmatrix} \\ M_{\text{V-pol}} = \begin{bmatrix} 0 & 0 \\ 0 & 1 \end{bmatrix} \end{gathered} \tag{3.11a,b}$$

For polarizers with their axes mounted horizontally or vertically, the polarization component perpendicular to this axis is absorbed.

Another useful matrix is the rotation matrix. Rotation matrices for Jones vectors are identical to those for Euclidean vectors, and are described in Eq. 3.12.

$$M_{rot}(\theta) = \begin{bmatrix} \cos\theta & -\sin\theta \\ \sin\theta & \cos\theta \end{bmatrix} \tag{3.12}$$

Here, θ is the rotation angle of the matrix relative to the horizontal x-axis. Using this matrix, the Jones matrix for an arbitrarily-rotated polarizer may be formed. The Jones vector of the incoming light is first rotated into the plane of the polarizer, passed through a horizontal polarizer, and then rotated back into its original coordinate system. This process, and the resulting rotated polarizer matrix, is shown in Eq. 3.13.

$$\begin{aligned} M_{pol}(\theta) &= M_{rot}(\theta) \times M_{\text{H-pol}} \times M_{rot}(-\theta) \\ &= \begin{bmatrix} \cos(\theta) & -\sin(\theta) \\ \sin(\theta) & \cos(\theta) \end{bmatrix} \begin{bmatrix} 1 & 0 \\ 0 & 0 \end{bmatrix} \begin{bmatrix} \cos(-\theta) & -\sin(-\theta) \\ \sin(-\theta) & \cos(-\theta) \end{bmatrix} \\ &= \begin{bmatrix} \cos^2(\theta) & \cos(\theta)\sin(\theta) \\ \cos(\theta)\sin(\theta) & \sin^2(\theta) \end{bmatrix} \end{aligned} \tag{3.13}$$

Summing two beams with mutually perpendicular polarization will not result in interference, regardless of the relative phase between them, as the ellipticity of polarization does not affect the intensity of light. If a linear polarizer is applied to the combined beam, however, light that is in-plane with the polarizer axis will pass through unaffected, while the intensity of light with polarization that is out-of-plane with the polarizer will be attenuated.

Of equal importance to Jones matrices that affect polarization's amplitude are those that modify only its phase. The most basic Jones matrix of this kind is a simple phase retarder, described in Eq. 3.14.

$$M_{phase} = \begin{bmatrix} e^{i\phi_x} & 0 \\ 0 & e^{i\phi_y} \end{bmatrix} \tag{3.14}$$

In this matrix, the phases of the *x*- and *y*-components of polarization of an input electric field are delayed by ϕ_x and ϕ_y, respectively. As explained above, refractive index gradients along the light's path result in the phase difference $\Delta\varphi$. This would apply equally to both polarizations, resulting in the Jones matrix in Eq. 3.15, representing the phase retardance experienced by light integrated over its optical path, *s*.

$$M_{phase,s} = \begin{bmatrix} e^{i\Delta\varphi_s} & 0 \\ 0 & e^{i\Delta\varphi_s} \end{bmatrix} \tag{3.15}$$

Because both polarization components are delayed equally, this implies that a beam cannot be made to interfere with itself through phase delays from the density inhomogeneities examined here. The FLDI instrument, however, splits the input laser beam into two beams, separated by a short distance Δx, with mutually orthogonal polarization vectors. In this configuration, phase differences between the two beams due to density fluctuations will cause the initially-linear polarization of the input beam to become elliptical, proportional to the beam separation and the fluctuation strength. To model the FLDI instrument's response, it is necessary to have a model for the polarization vector at each point on the output of the interferometer. Here, only a single "pixel" at the output plane of the interferometer is considered, for the sake of simplicity, but the concept is easily expanded to a full two-dimensional case.

The laser used for this research is highly linearly polarized, and is oriented at 45 degrees to the beam separation axis. The input Jones vector for this polarization is shown in Eq. 3.16.

$$E_{in} = \frac{1}{\sqrt{2}} \begin{bmatrix} 1 \\ 1 \end{bmatrix} \tag{3.16}$$

This orientation is necessary because the birefringent prisms split incoming light into two beams, where one beam is polarized along the axis perpendicular to the resulting beam separation vector, and the other beam is polarized parallel to that beam separation vector. This is modeled by taking the output of multiplying the input Jones vector by horizontal and vertical polarizer matrices, respectively. Each of these beams encounters a slightly different phase shift, due to the separation of the beams, as they pass through the test volume. The phase-modulated beams are combined in the second prism through summation of their Jones vectors. Finally, the resulting beam passes through a phase compensator, which is used to take out any DC phase delay between the *x*- and *y*-components, leaving only the fluctuating component of the phase. The output polarization vector of this system for a ray passing through point (*x*, *y*) at the output is described by Eq. 3.17.

$$E = M_{compensator} \times \left(M_A + M_B\right) \times E_{input}$$

$$E(x,y) = \begin{bmatrix} e^{i\varphi} & 0 \\ 0 & 1 \end{bmatrix} \times \left(\begin{bmatrix} e^{i\phi_{s_A(x,y)}} & 0 \\ 0 & e^{i\phi_{s_A(x,y)}} \end{bmatrix} \begin{bmatrix} 1 & 0 \\ 0 & 0 \end{bmatrix} + \begin{bmatrix} e^{i\phi_{s_B(x,y)}} & 0 \\ 0 & e^{i\phi_{s_B(x,y)}} \end{bmatrix} \begin{bmatrix} 0 & 0 \\ 0 & 1 \end{bmatrix} \right) \times \frac{A(x,y)}{\sqrt{2}} \begin{bmatrix} 1 \\ 1 \end{bmatrix} \quad (3.17)$$

Here, φ represents the phase delay from the compensator, $s_A(x, y)$ and $s_B(x, y)$ are the optical paths of the two FLDI beams that arrive at point (*x*, *y*) at the output plane, and *A*(x, y) is the local amplitude of the input beam. In this research, the beam profiles are assumed to be Gaussian for simplicity.

The polarizing beamsplitter cube used for the FLDI instrument is oriented at 45° to the axis of beam separation, as seen in Fig. 2.3. In this orientation, the p-detector measures the polarization component parallel to the laser polarization vector ("p" for "parallel"). The s-detector measures the polarization component perpendicular to the laser polarization vector ("s" for "senkrecht", which is German for "perpendicular"). This is because the polarizing beam splitter cube behaves as a polarizer at 45° for light passing directly through the cube, and as a polarizer at 135° for light that is reflected to the side. The polarization vectors that pass through the polarizing beamsplitter cube and arrive at the photodiodes are described in Eq. 3.18:

$$E_P = \begin{bmatrix} 0.5 & 0.5 \\ 0.5 & 0.5 \end{bmatrix} \times E, \quad E_S = \begin{bmatrix} 0.5 & -0.5 \\ -0.5 & 0.5 \end{bmatrix} \times E \quad (3.18)$$

The intensities measured by the photodiodes of these two signals, I_P and I_S, are found using Eq. 3.10.

With the Berek phase compensator zeroed and with no disturbance present in the paths of the FLDI beams, all of the laser power should pass through to the p-detector, and none should pass through to the s-detector. However, if the FLDI beams do encounter a disturbance, the optical path length difference between the two beams causes a relative phase shift between the *p*- and *s*-components of the polarization vector. This phase shift, in turn, is measured as a change in the intensity measured by the two photodiodes. A diagram demonstrating this process is shown in Fig. 3.8.

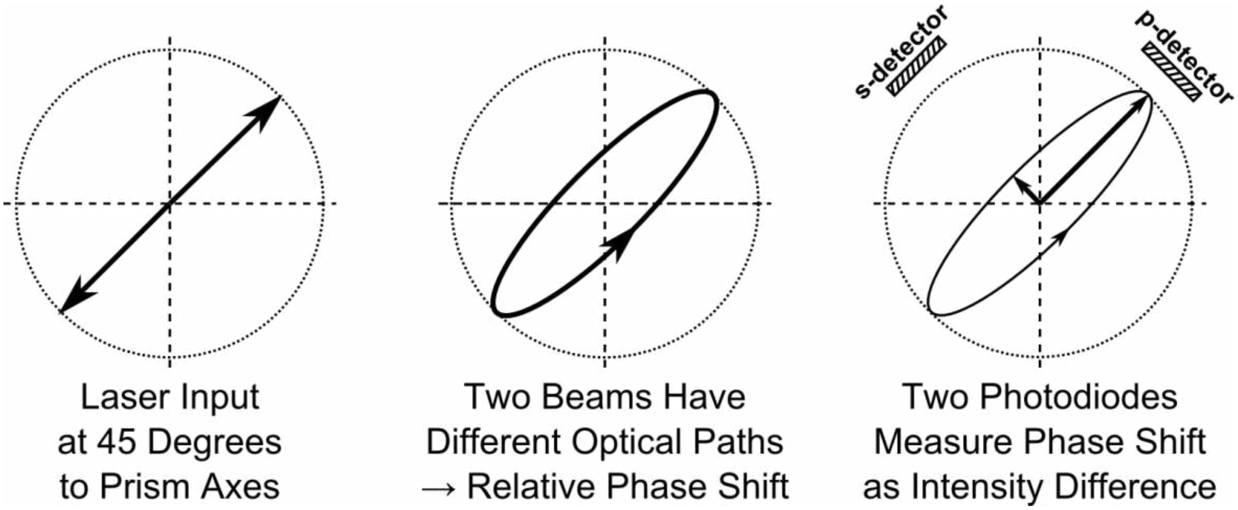

Figure 3.8: Measurement of polarization component phase shift from the interferometer. The laser beam entering the interferometer is aligned at 45 degrees to the beam displacement axis, which causes its intensity to be split evenly between the two beams. Each FLDI beam encounters a slightly different optical path, which causes a relative phase shift between the two beams. This phase shift results in the two photodiodes receiving different intensities of light. The change in beam intensity from the interferometer beam paths is used to calculate the strength of disturbances in the flow.

The phase shift of the (ideal) interferometer signal can be determined from the intensities measured by the two photodiodes using Eq. 3.19:

$$\Delta\varphi_A - \Delta\varphi_B = \sin^{-1}\left(\frac{I_P - I_S}{I_P + I_S}\right) \tag{3.19}$$

In practice, the intensity signals must be scaled to account for interferometer contrast effects, as detailed in Procedures section 4.6.

3.6.2 Sanderson Prisms

As described previously, the FLDI instrument presented in this research uses two stress-birefringent Sanderson prisms[53] to split the input laser beams of the interferometer into two perpendicularly-polarized beams in the test area of the instrument and then recombine them. The use of these prisms for differential interferometry was demonstrated by Biss et al.[54] and found to perform identically to a standard Wollaston prism.

Sanderson prisms rely on temporary birefringence that appears in glass-like polymers due to an applied stress, called the photoelastic or piezooptic effect. According to Maxwell's stress-optic law, the principal axes of stress in the prism correspond with the optical axes of polarized light[60]. Light with its polarization vector in the direction of the principal components of the stress, σ_j, encounters the refractive indices, n_j, along these axes by the relationship shown in Eq. 3.20.

$$n_j - n_0 = \frac{n_0^3}{2}\begin{bmatrix} q_{11} & q_{12} & q_{12} \\ q_{12} & q_{11} & q_{12} \\ q_{12} & q_{12} & q_{11} \end{bmatrix}\sigma \tag{3.20}$$

Here, n_j is the polarization-dependent refractive index, n_0 is the unstressed refractive index of the plastic material, q_{11} is the stress-optic coefficient for light polarized along the axis of the stress, q_{12} is the stress-optic coefficient for light polarized perpendicular to the axis of stress, and σ is a vector representing the principal stresses. The above relationship is often resolved into three equations using two coefficients, C_1 and C_2, in place of the stress-optic coefficients and unstressed refractive index:

$$\begin{aligned} n_1 - n_0 &= C_1\sigma_1 + C_2\left(\sigma_2 + \sigma_3\right) \\ n_2 - n_0 &= C_1\sigma_2 + C_2\left(\sigma_1 + \sigma_3\right) \\ n_3 - n_0 &= C_1\sigma_3 + C_2\left(\sigma_1 + \sigma_2\right) \end{aligned} \tag{3.21}$$

To match the behavior of a Wollaston prism, a Sanderson prism loads a rectangular prismatic polycarbonate bar in four-point bending to produce uniaxial stress in the bar. A free-body diagram for the prism in four-point bending is shown in Fig. 3.9.

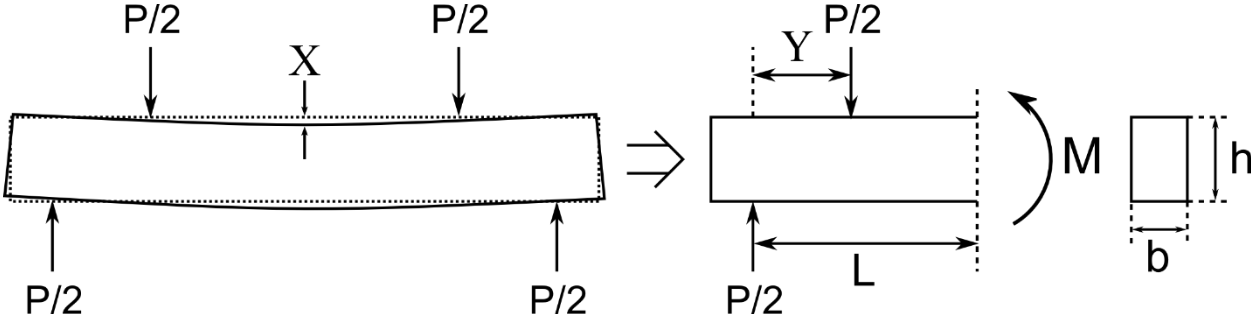

Figure 3.9: Four-point bending diagram for Sanderson prism. The applied force, *P*, results in a midspan deflection of the prism, *X*, and a corresponding bending moment in the prism, *M*. The beam separation from the prism is in the direction of the axis of the applied force.

X is the maximum deflection of the prism, which occurs at its center. *Y* is the distance between the two load points on each half of the prism, and *L* is the distance from the outer load points to the centerline of the prism. In cross-section, the thickness of the prism is *b*, and its height is *h*. Between the two pairs of load points, each applying a force equal to *P*/2, a bending moment, *M*, is generated in the prism which leads to a linear stress gradient from the bottom to the top of the prism. This stress gradient creates a refractive index gradient in the same direction, which is dependent upon the incoming polarization amplitude vector:

$$\sigma_1 = \frac{M_z x}{I_{zz}},\ \sigma_2 = \sigma_3 = 0$$
$$-\left(C_1 + C_2\right) = \frac{n^3}{2}\left(q_{11} - q_{12}\right) \tag{3.22a,b,c}$$
$$C_1 = q_{11}\frac{n^3}{2},\ C_2 = -q_{12}\frac{n^3}{2}$$

From these equations, the refractive indices for each polarization axis, forming a refractive index vector for light propagating through the birefringent medium, can be computed.

$$n_a - n_0 = C_1 \frac{M_z x}{I_{zz}}$$
$$n_b - n_0 = -C_2 \frac{M_z x}{I_{zz}} \tag{3.23a,b,c}$$
$$n_c - n_0 = -C_2 \frac{M_z x}{I_{zz}}$$

The refractive index vector here is three-dimensional, while the Jones polarization vector is only two-dimensional. To handle this, the three-dimensional refractive index vector must be projected onto the plane of the Jones vector. For uniaxial states of stress as used here, where the principal axis of stress is perpendicular to the propagation direction of the light, this case reduces to the polarization component in the same direction as the principal axis of stress encountering the refractive index n_a, while the other polarization component encounters refractive index n_b.

Thus the Sanderson prism behaves similarly to a gradient-index lens, with the gradient in the direction of the stress. Taking the derivative of the above three refractive indices with respect to x gives a description of this gradient, as shown in Eqs. 3.24a,b:

$$\frac{\partial n_a}{\partial x} = C_1 \frac{M_z}{I_{zz}}$$
$$\frac{\partial n_b}{\partial x} = \frac{\partial n_c}{\partial x} = -C_2 \frac{M_z}{I_{zz}} \tag{3.24a,b}$$

The derivative of the stress with respect to *x* gives the following relationship for a prism in four-point bending, using the dimensions shown in Fig. 3.9.

$$\frac{M_z}{I_{zz}} = \frac{6PY}{bh^3} \tag{3.25}$$

This can be expressed in terms of the midspan prism deflection, *X*:

$$\frac{M_z}{I_{zz}} = -\frac{3EX}{\left(3L^2 - Y^2\right)} \tag{3.26}$$

where *E* is the modulus of elasticity of the prism material. While the prism behaves like a gradient-index lens, the gradient is weak enough that it is possible to calculate a single beam divergence angle for the prism (Eq. 3.27).

$$\begin{aligned}\Delta\theta &\approx -\left[C_1 + C_2\right]\frac{M_z b}{I_{zz}} \\ &\approx \left[C_1 + C_2\right]\frac{3bEX}{\left(3L^2 - Y^2\right)}\end{aligned} \tag{3.27}$$

Note that this approximation is accurate only for rays that enter the prism at shallow angles to the normal vector of the prism surface. If the ray enters the prism at a steep angle, then the effects from refraction at the surfaces, due to the difference in refractive index between air and the prism, must be considered.

Rays propagating through a Sanderson prism follow a parabolic path inside it, due to the linear refractive index gradient in the *x*-direction from the stress birefringence. This path causes the apparent source of the two polarized beams, z_S, to be slightly forward of the center of the prism. A diagram illustrating this effect is shown in Fig. 3.10.

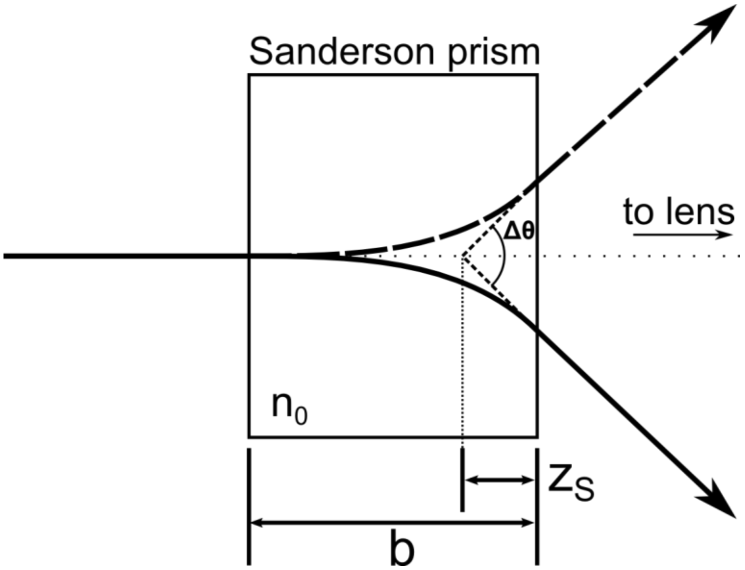

Figure 3.10: Effective focal point of the Sanderson prism and its related geometry. The angle Δθ is greatly exaggerated here for clarity. The effective focus of the prism must be used in alignment of the FLDI optics for the beams passing through the test section to be parallel.

The apparent source of the two beams is found using Eq. 3.28:

$$z_s = \frac{b}{2n_0} \tag{3.28}$$

This apparent source distance must be subtracted from the focal length of the FLDI field lenses when calculating the distance between the prisms and field lenses to achieve parallel beams through the test section.

Because the coefficients C_1 and C_2 from Eqs. 3.21-27 are not identical, the two beams are actually deflected at different angles from the incoming propagation direction. These angles are very small, so any difference between handling each angle separately and modeling the angles as being equal is unlikely to greatly affect the accuracy of the propagation modeling. The difference in angles will, however, manifest itself as a phase delay between the two beams, which must be compensated for, using the phase compensator mentioned above.

A figure comparing *Δx* estimated using Eq. 3.27 (with a field lens focal length of 50 mm) and the calculated *Δx* from a full optical model of the prisms used in this research is shown in Fig. 3.11a. Additionally, the relative phase delay between the two beams due to the C_1 and C_2 parameters being unequal is shown in Fig. 3.11b.

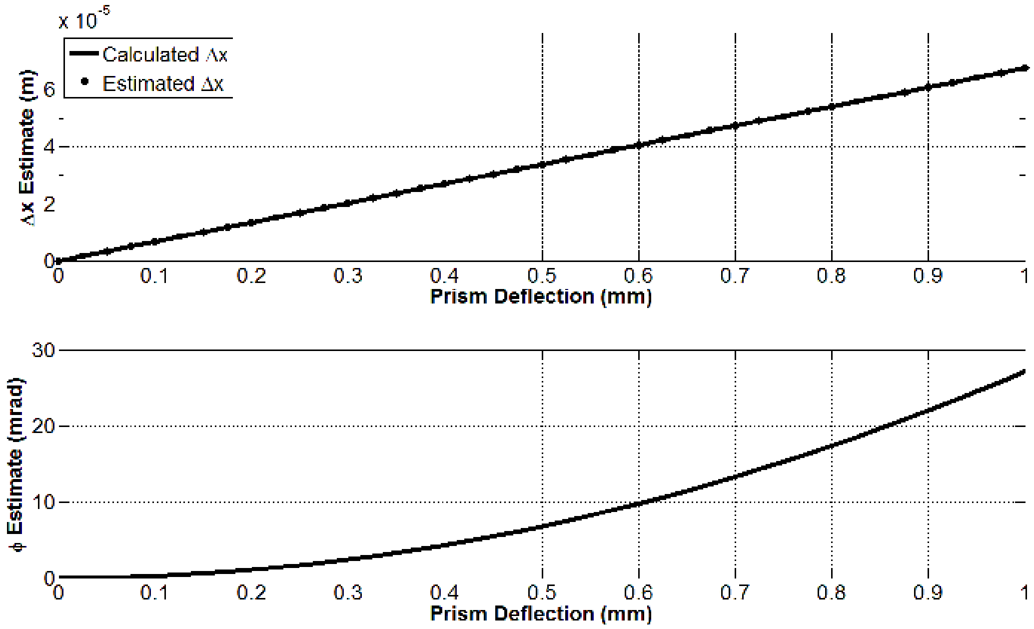

Figure 3.11a,b: Calculated and estimated Δx for the Sanderson prisms used in this research. The calculated phase difference between the two beams due to unequal C_1 and C_2 are shown in the bottom plot.

Here, the difference between the estimated *Δx* and the calculated *Δx* from theory is negligible, despite the calculated *Δx* taking the difference in C_1 and C_2 into account, which supports the use of the equal-angle approximation in general use. The relative phase shift of the two beams caused by this difference is small but demonstrates the need for the Berek phase compensator to “null” the interferometer.

These plots were calculated using the parameters of the Sanderson prisms used for the present research, where L = 38.8 mm, Y = 26 mm, b = 9.3 mm, and h = 11.6 mm. The prisms are made of Lexan polycarbonate, which has the following properties[60]: n_0 = 1.5816, E = 2.4 GPa, q_{11} = -4.6E-12 Pa^{-1}, and q_{12} = 24.6E-12 Pa^{-1}.

In what follows, it is necessary for the FLDI instrument to have small and continuously-adjustable beam separation Δx that is exactly the same for the two prisms in the system. This is possible with two inexpensive, adjustable Sanderson prisms. However, to do this with fixed Wollaston prisms would require an impractically-large and expensive collection of precisely-matched pairs of small-divergence-angle Wollaston prisms.

3.7 Spatial Filtering by the FLDI Instrument

In order to reject unwanted signals and get a point-like measurement at the focus of the interferometer, the FLDI technique relies upon spatial filtering of turbulence outside the region of interest. This spatial filtering can be broken down into two separate components: filtering due to finite beam separation, and filtering from the finite width of the beams. In order to model these effects theoretically, the approach used here is that of signal transfer functions, which are well-known measures of signal output from a sensor or optical system as a function of a given input[61]. Models for the transfer functions of these effects are presented here to better parameterize the behavior of FLDI systems. Comparison of these theoretical results to measurements of signal rolloff away from best focus will be presented in the Results chapter of this thesis.

3.7.1 Taylor's Hypothesis

When the two FLDI beams are separated by a sufficiently short distance Δx (Fig. 3.4), turbulence that passes through the beams will not change significantly in character from one beam to the other. Instead, it appears to simply convect through unchanged. In this case, it is reasonable to invoke Taylor's hypothesis of "frozen turbulence," where functions of time and functions of space are directly related to one another by the convective velocity of the field. This relationship is described in Eqs. 3.29a-n:

$$\begin{gathered} x = U_C t \\ \frac{d}{dx} = \frac{1}{U_C}\frac{d}{dt} \\ \cdots \\ \frac{d^n}{dx^n} = \frac{1}{U_C^n}\frac{d^n}{dt^n} \end{gathered} \tag{3.29a-n}$$

The instrument developed here relies heavily on understanding how the optics spatially filter turbulent signals, particularly those from wind-tunnel-wall boundary layers. The photodetectors used to measure the interference signals are sampled in the time domain. Because of this, maintaining a beam separation such that Taylor's hypothesis holds is crucial.

Much of the data shown in this thesis are in spectral plots, either of measured turbulence or of expected behavior of the instrument in the form of transfer functions. In most of these plots the spectra are plotted against wavenumber, rather than frequency, as this provides a more natural comparison between turbulent signals by removing the influence of flow velocity. Wavenumber is calculated by using Taylor's hypothesis above to transform frequency (Eq. 3.30):

$$k = \frac{2\pi f}{U_C} \tag{3.30}$$

Wavenumber, in units of m^{-1}, converts the time-domain signal, measured by the photodetectors, to a spatial frequency based on the apparent length scale of turbulent eddies. In doing so, turbulence generated from a given geometry, such as a round turbulent jet with a particular overall pressure ratio, is more easily compared with turbulence generated from the same geometry at different flow conditions.

What defines "sufficiently short" beam separation is dependent upon properties of the flow, particularly the Kolmogorov microscale of the turbulence and the mean flow velocity. Fundamentally, Taylor's hypothesis of frozen turbulence expects that the correlation between turbulence measured at two points will remain as high as possible, so that the relationship shown in Eqs. 3.31a,b holds.

$$\begin{gathered} f\left(\vec{r},t\right) = f\left(\vec{r}+\Delta\vec{r},t+\tau\right) \\ \tau = \frac{\left\|\Delta\vec{r}\right\|}{U_C} \end{gathered} \qquad (3.31\text{a,b})$$

Here, $\vec{r}$ and $\Delta\vec{r}$ are the position and velocity vectors of the turbulence signal, respectively, t is the initial time, and τ is the change in time between the initial and final samples of the signal. Ideally, the beam separation should be smaller than the smallest scales of turbulence, and a good target for this is the Kolmogorov microscale, η. Because most of the energy in the turbulence is present in much larger eddy scales than η, the correlation will remain high at larger beam separations than η, but in that case the frequency response of the instrument will suffer, and Taylor's hypothesis may no longer accurately relate frequency and wavenumber spectra for these larger eddy scales. Additionally, U_C may be a non-trivial function of the wavenumber of the turbulent disturbances, in which case the assumption of a constant convective velocity required by Taylor's hypothesis breaks down.

3.7.2 Effects of Varying Beam Separation

As discussed above, in the limit of beam separation approaching zero, the output of the FLDI instrument behaves as a true derivative in the direction of the beam separation. Because the two beams in a real instrument are necessarily separated by some finite distance, there are some spatial filtering effects that must be taken into account.

A simple model of how the system responds to a sinusoidal disturbance in one dimension is shown here in Eqs. 3.32a,b,c. The two FLDI beams, represented by the functions F_+ and F_-, encounter the same sinusoidal disturbance, but at different points along its curve due to their separation distance. The function h_{f0} represents the difference signal measured by the instrument for a given disturbance frequency, where f_0 is the frequency of the disturbance in Hz. U_C is the velocity at which the disturbance convects past the measurement points in the flow direction, while the beams are separated by the distance Δx.

$$\begin{aligned} F_+ &= \sin\left(2\pi f_0\left[t + \frac{1}{2}\frac{\Delta x}{U_C}\right]\right) \\ F_- &= \sin\left(2\pi f_0\left[t - \frac{1}{2}\frac{\Delta x}{U_C}\right]\right) \\ h_{f_0}(t) &= \frac{F_+ - F_-}{\Delta x / U_C} \end{aligned} \tag{3.32a,b,c}$$

At low disturbance frequency or small beam separation, the phase difference between the two signals is minor. At higher frequencies or larger beam separations, however, the phase difference may be large enough (greater than 90 degrees) that the signal will be subject to aliasing and will become ambiguous, as can be seen in Fig. 3.3 from the interferometry section above (Theory 3.5). These high frequency effects are easily seen in the frequency domain form of the function $h_{f0}(t)$, shown in Eq. 3.33.

$$H_{\Delta x}(k) = \frac{U_C}{\pi \Delta x} \sin\left[\frac{\pi \Delta x f}{U_C}\right] = \frac{2}{\Delta x} \sin\left[\frac{\Delta x k}{2}\right] \tag{3.33}$$

A demonstration of the behavior of this transfer function compared to that of a true derivative, which has a transfer function of *H*(*k*) = *k*, is shown in Fig. 3.12.

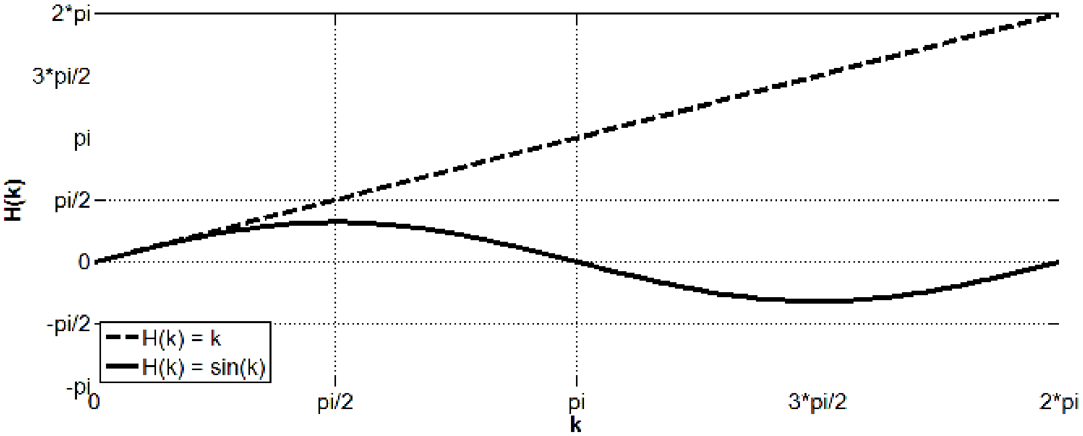

Figure 3.12: Transfer function magnitude of a true derivative compared to that of a finite difference. The finite difference gives a reasonable approximation of the derivative over only a small portion of the spectrum.

Here, the loss of the signal when the two beams see a disturbance at multiples of pi can be seen, as well as the general loss of signal amplitude at higher frequencies. To more easily see how the finite-difference scheme deviates from the behavior of a true derivative, additional transfer functions shown here for the finite-difference scheme will be normalized by dividing by *k*. They will also be presented with logarithmic frequency axes, and with the magnitude of the transfer functions in terms of decibels of attenuation from a true derivative. When normalized by k^{-1}, the system transfer function above becomes a sinc function, described in Eq. 3.34, and having the transfer function magnitude (for the case of Δx = 100 μm) shown in Fig. 3.13.

$$H_{\mathrm{sinc},\Delta x}(k) = \mathrm{sinc}\left(\frac{\Delta x k}{2}\right) = \frac{2}{\Delta x k} \sin\left[\frac{\Delta x k}{2}\right] \tag{3.34}$$

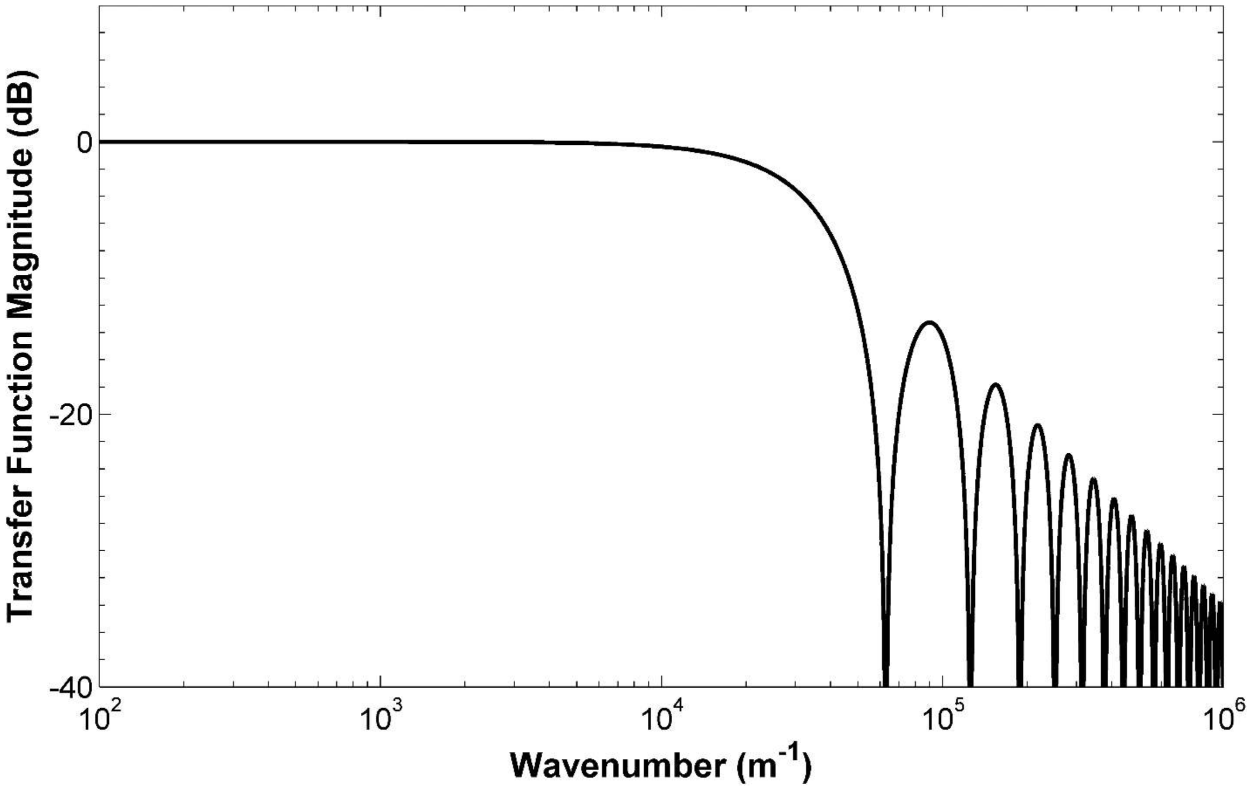

Figure 3.13: Transfer function of one-dimensional sinc filter, for $\Delta x = 100$ μm, using Eq. 3.34. For this case, the response of the filter is roughly flat out to a wavenumber of $1\text{x}10^4$ m^{-1}.

This basic sinc filter model is naïve, however, as we expect high wavenumber turbulence to behave generally isotropically. Under the isotropic assumption, a disturbance "wave" (i.e., a turbulent eddy) is equally likely to arrive at all angles to the beam separation axis. The apparent wavelength of a disturbance passing through the beams when it is off-axis is longer than the true wavelength, with a corresponding reduction in apparent wavenumber, as seen in Fig. 3.14.

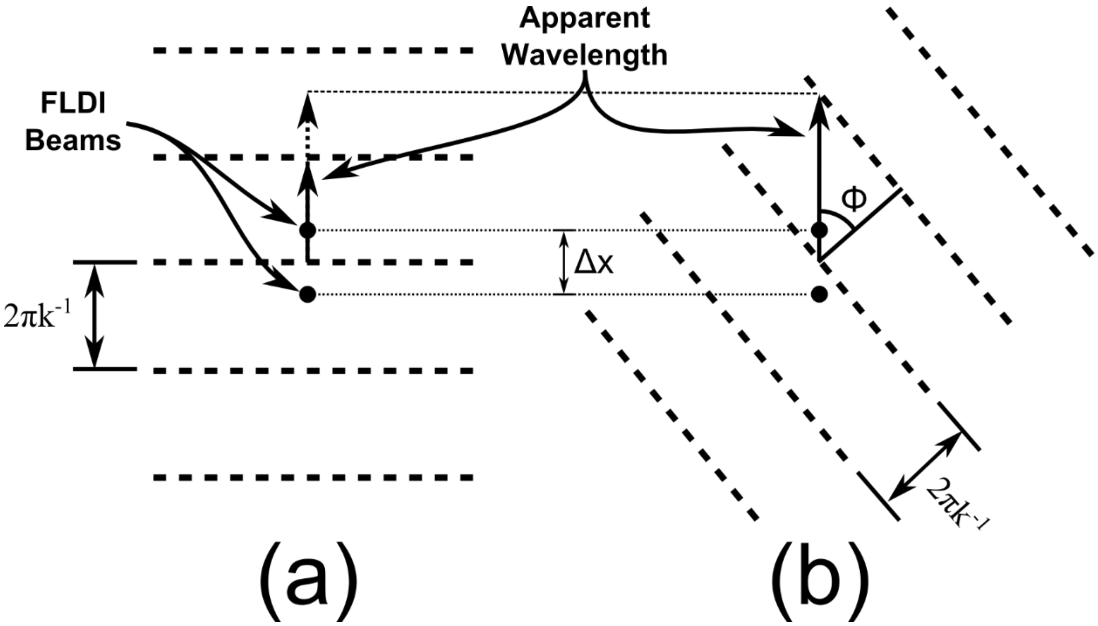

Figure 3.14: Effect of wave angle of incidence on apparent wavelength, looking down the optical axis. The points represent the two FLDI beams separated by a small distance. In a) the waves are propagating along the axis of the beam separation, while in b) the waves are propagating at angle Φ to the beam separation axis, appearing to the FLDI instrument as having longer wavelength because of this angle.

Here, the view is looking down the optical axis, z, and waves of wavelength $2\pi k^{-1}$ are convecting past the beams in both the x- and y-directions, with the dashed lines representing a period of the wave's oscillation. The FLDI instrument "sees" only in the direction of the beam separation, however. Waves that convect past the beams at an angle ϕ to the beam separation axis appear to the instrument to have longer wavelengths than the same waves propagating in the direction of beam separation. Since waves are equally likely to approach the FLDI beams at any angle ϕ, due to the isotropic assumption for the turbulence, the transfer function for the beam separation must take this angle of incidence into account.

At low wavenumbers, where the wavelength of a disturbance is large compared to the separation of the beams, the FLDI system output is almost exactly like a derivative. At higher wavenumbers, when the wavelength approaches and drops below the beam separation distance, this approximation is no longer appropriate, and the transfer function of the instrument becomes a function of both wavenumber and the angle of the wave relative to the beam separation axis. Taking angle of incidence into consideration in the transfer function of the system results in Eq. 3.35, and a plot of the resulting response curve is shown in Fig. 3.15.

$$H_{\Delta x}\left(k,\phi\right)=\frac{2}{\Delta x\,k}\sin\left[\frac{\Delta x\,k\cos\left(\phi\right)}{2}\right] \tag{3.35}$$

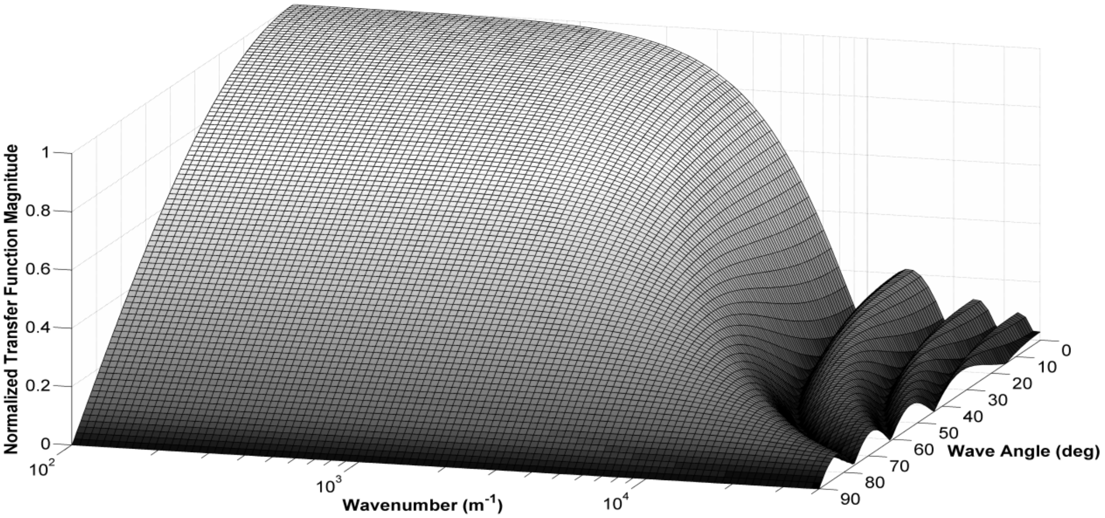

Figure 3.15: Effect of beam separation on signal magnitude as a function of wavenumber and wave angle. As seen in Fig. 3.14, increasing wave angle results in a longer apparent wavenumber to the finite difference.

Expressing the transfer function of the spatial filtering effect as a function of both wavenumber and wave angle is inconvenient, since with the current instrument it is not possible to actually measure the angle at which a disturbance arrives at the beam separation axis. The above equation does not describe the full situation, either, as the turbulence being interrogated by this instrument is a three-dimensional phenomenon, so it must be considered over a sphere, rather than just a circle. The coordinate system for this case is described in Fig. 3.16.

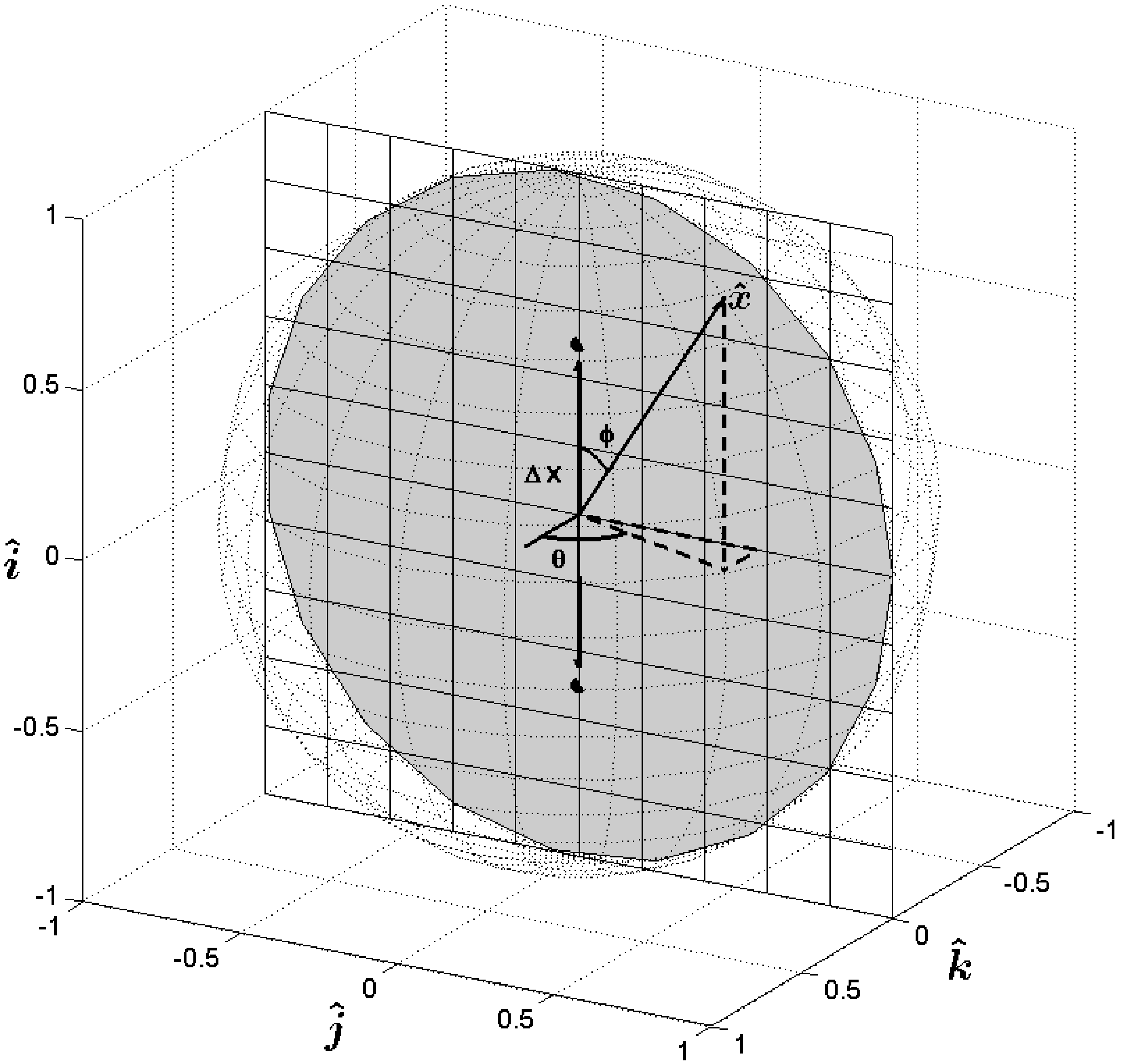

Figure 3.16: Spherical coordinate system used here, showing the two beams, separated by Δx, and the axis along which a disturbance varies, $\hat{x}$. The gray circle represents the cross-section of the FLDI beams, while the two dots show the separation of the beams.

Here, $\hat{x}$ is the propagation vector of the disturbance, θ is the angle between this vector and the propagation axis of the FLDI beams, and ϕ is the angle between the disturbance propagation vector and the beam separation axis. Using this coordinate system, where $\hat{\imath}$ is the axis of beam separation,

$\hat{k}$ is the FLDI beam axis, and the $\hat{\jmath}$-axis is perpendicular to both of these axes, the disturbance propagation vector is defined in Eq. 3.34.

$$\hat{x} = \begin{bmatrix} \cos(\phi) \\ \sin(\theta)\sin(\phi) \\ \cos(\theta)\sin(\phi) \end{bmatrix} \tag{3.34}$$

A Monte Carlo simulation was programmed to model the response of the FLDI instrument to sinusoidal disturbances due to the separation of the beams. Here, substitute coordinates, *u* and *v*, are introduced for the angles on the sphere, defined in Eqs. 3.35a,b,c.

$$\begin{aligned} &u, v \in (0,1) \\ &\theta = 2\pi u \\ &\phi = \cos^{-1}(2v-1) \end{aligned} \tag{3.35a,b,c}$$

Using these substitute coordinates, uniformly random samples of *u* and *v* in the range of 0 to 1 (as in Eq. 3.35a) result in uniformly distributed random disturbance propagation vectors of the following form:

$$\hat{x} = \begin{bmatrix} 2v-1 \\ 4v(1-v)\sin(2\pi u) \\ 4v(1-v)\cos(2\pi u) \end{bmatrix} \tag{3.36}$$

The simulation generates random sinusoidal disturbances with a characteristic wavenumber, *k*, propagating along the vector $\hat{x}$, and with random phase, *Φ*. These disturbances appear to the FLDI instrument as phase variations in the two beams as in Eq. 3.17:

$$\begin{aligned} \phi_x &= \pi \sin\left[\frac{\Delta x}{2} k\left(\hat{x} \bullet \hat{\imath}\right) + \Phi\right] \\ \phi_y &= \pi \sin\left[-\frac{\Delta x}{2} k\left(\hat{x} \bullet \hat{\imath}\right) + \Phi\right] \end{aligned} \tag{3.36}$$

Here, the ● represents the dot product (or inner product) between the disturbance propagation vector and a unit vector in the direction of the beam separation. This leads to the following polarization vector for the interferometer output:

$$E = \frac{1}{\sqrt{2}} \begin{bmatrix} e^{i\pi \sin\left[\frac{\Delta x}{2} k\left(\hat{x} \bullet \hat{\imath}\right) + \Phi\right] + i\frac{\pi}{2}} \\ e^{i\pi \sin\left[-\frac{\Delta x}{2} k\left(\hat{x} \bullet \hat{\imath}\right) + \Phi\right]} \end{bmatrix} \tag{3.36}$$

The amplitude response of the FLDI instrument to these disturbances is calculated using Eq. 3.19, and the root mean square (RMS) value of the amplitudes of all of the disturbance samples for a given wavenumber approximates the transfer function of the system at that wavenumber.

In this model, there is no preferred flow direction (i.e., effects due to the flow velocity vector are ignored), so the disturbance is equally likely to propagate in any direction. This can be seen in Fig. 3.17a, showing a random sampling of disturbance propagation vectors for this case. The result of the Monte Carlo simulation is plotted in Fig. 3.17b. A fit of the following form for the spatial filtering due to beam separation is applied to the simulation output:

$$H_{\Delta x}\left(k\right) = \frac{1}{\sqrt{1 + \left(k/k_c\right)^2}} \tag{3.37}$$

The cutoff wavenumber, k_c, for this case was found to be $0.54/\Delta x$.

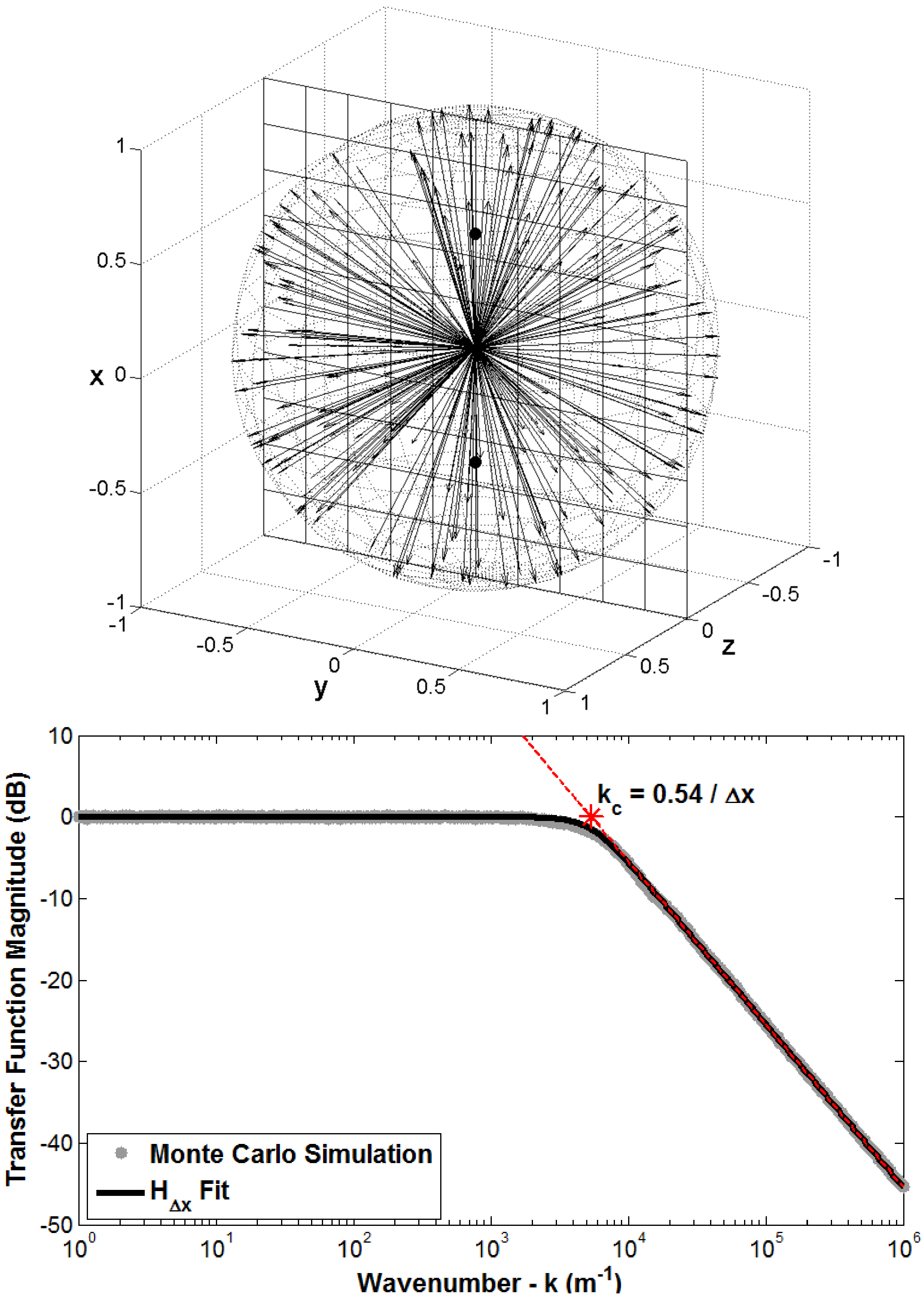

Figure 3.17a,b: Monte Carlo simulation of the FLDI instrument's transfer function due to beam separation, in the case that there is no preferred flow direction. Here, $\Delta x = 100$ µm. The two black dots in Fig. 3.17a represent the FLDI beam centroids.

A more comprehensive analysis of the FLDI instrument's response must take the flow velocity vector into account, to model the preferred direction of acoustic wave propagation. In this case, rather than modeling the amplitude of a disturbance's effect on the instrument's response as uniform across the sphere, the amplitude is instead equal to the dot product of the velocity vector, $\vec{U}$, and the disturbance propagation vector:

$$E = \frac{\left(\hat{x} \bullet \vec{U}\right)}{U_C \sqrt{2}} \begin{bmatrix} e^{i\pi \sin\left[\frac{\Delta x}{2} k\left(\hat{x} \bullet \hat{\imath}\right) + \Phi\right] + i\frac{\pi}{2}} \\ e^{i\pi \sin\left[-\frac{\Delta x}{2} k\left(\hat{x} \bullet \hat{\imath}\right) + \Phi\right]} \end{bmatrix} \tag{3.38}$$

Additionally, the output of the Monte Carlo simulation for this case is evaluated not at the original wavenumber, k, but at the effective wavenumber, k_{eff}, as defined in Eq. 3.39.

$$k_{eff} = \frac{2\pi f}{\hat{x} \bullet \vec{U}} = \frac{U_C k}{\hat{x} \bullet \vec{U}} \tag{3.39}$$

To calculate the RMS value for $H_{\Delta x}(k)$ in this case, the results from these simulations are binned according to the proximity of k_{eff} to k, such that if the value of k_{eff} is more than halfway between one bin for k and the next higher bin, it is rounded up, while if it is less than halfway between the two bins, it is rounded down.

A simulation showing the transfer function from the effect of beam separation when the flow is parallel to the axis of beam separation is shown in Fig. 3.18a,b. In this case, the cutoff wavenumber k_c was found to equal $0.42/\Delta x$. Finally, a simulation showing the transfer function from the effect of beam separation when the flow is perpendicular to the axis of beam separation is shown in Fig. 3.19a,b. In this case, the cutoff wavenumber k_c was found to equal $1.10/\Delta x$.

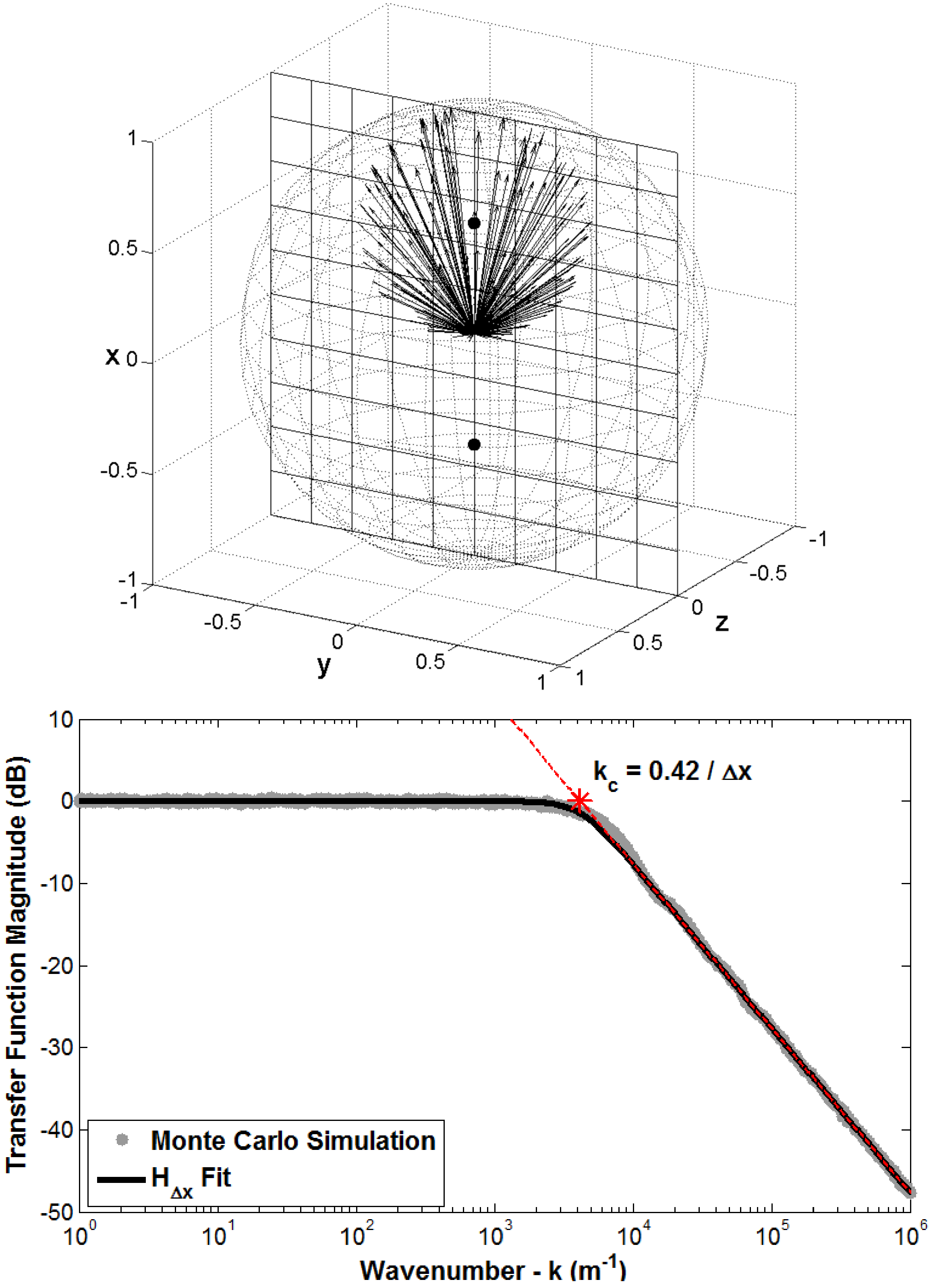

Figure 3.18a,b: Monte Carlo simulation of the FLDI instrument's transfer function due to beam separation, in the case that the flow is parallel to the axis of beam separation. Here, Δx = 100 μm. The two black dots in Fig. 3.18a represent the FLDI beam centroids.

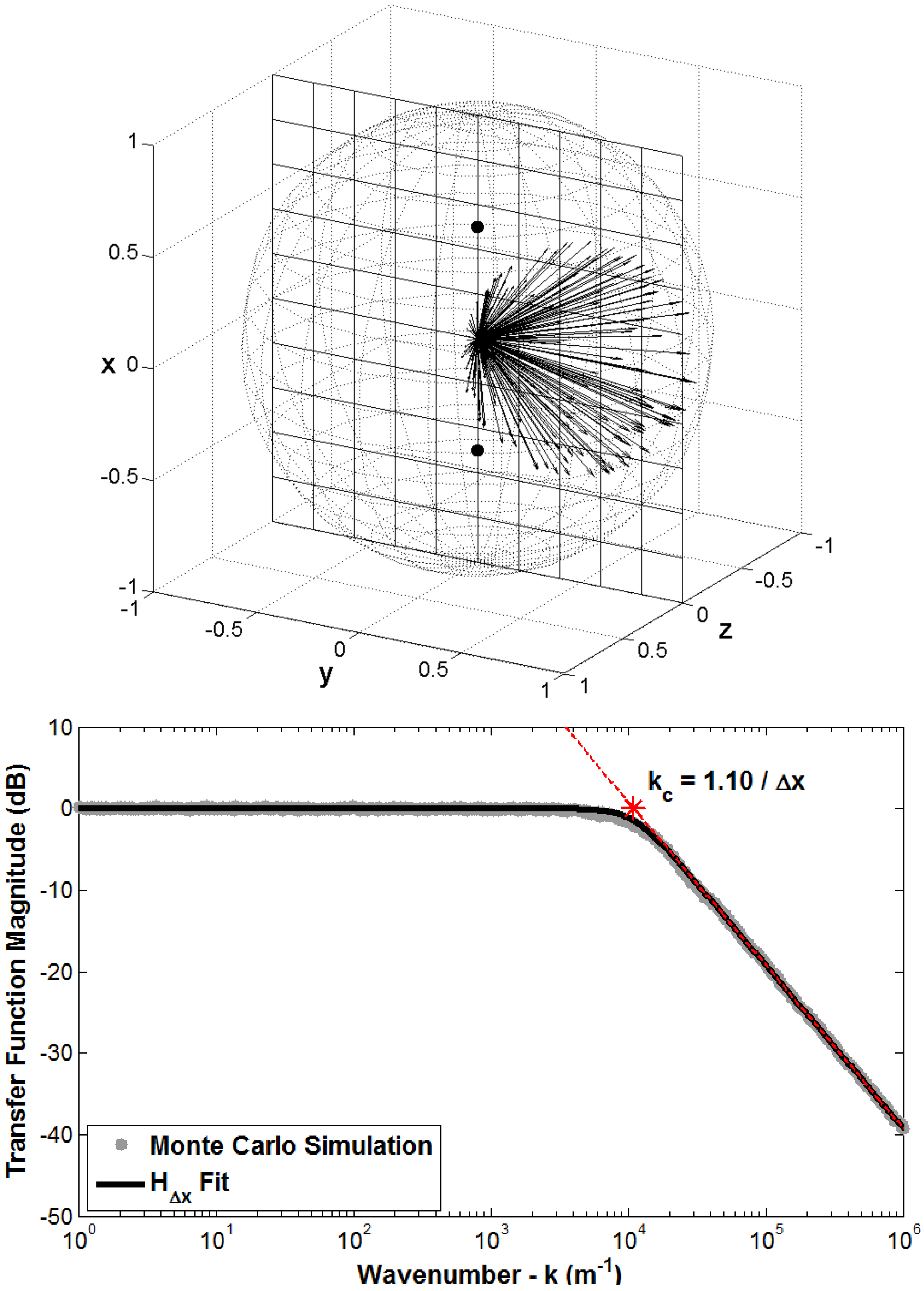

Figure 3.19a,b: Monte Carlo simulation of the FLDI instrument's transfer function due to beam separation, in the case that the flow is perpendicular to the axis of beam separation. Here, Δx = 100 µm. The two black dots in Fig. 3.17a represent the FLDI beam centroids.

While the transfer function from Eq. 3.37 can be deconvolved from acquired spectra for data analysis, a better practice is to adjust the instrument's Sanderson prisms so the cutoff wavenumber as calculated above is greater than the maximum wavenumber of interest. In this case, the influence of the beam separation on the frequency response of the instrument may be ignored, and the initial assumption that the instrument measures the true spatial derivative holds.

3.7.3 Frequency Response as a Function of Beam Size (f-number)

Propagation of the laser beam through the FLDI system is reasonably well approximated by a Gaussian beam model because of the high quality of the laser beam, particularly when spatially filtered through a pinhole. A Gaussian beam will focus to a minimum spot diameter related to the beam waist, w_0, calculated in Eq. 3.40, and the width at all other positions along the beam is dependent upon this minimum diameter. A diagram showing key parameters of the Gaussian beam geometry is shown in Fig. 3.20. An effective *f*-number of the FLDI optics may be defined by the ratio of the focal distance of the FLDI system, d, to the maximum diameter of the FLDI beams, $D_{4\sigma}$. This system *f*-number is a critical factor in the ability of the instrument to reject unwanted signals originating away from best focus, as the sensitivity of the instrument drops with increasing beam diameter.

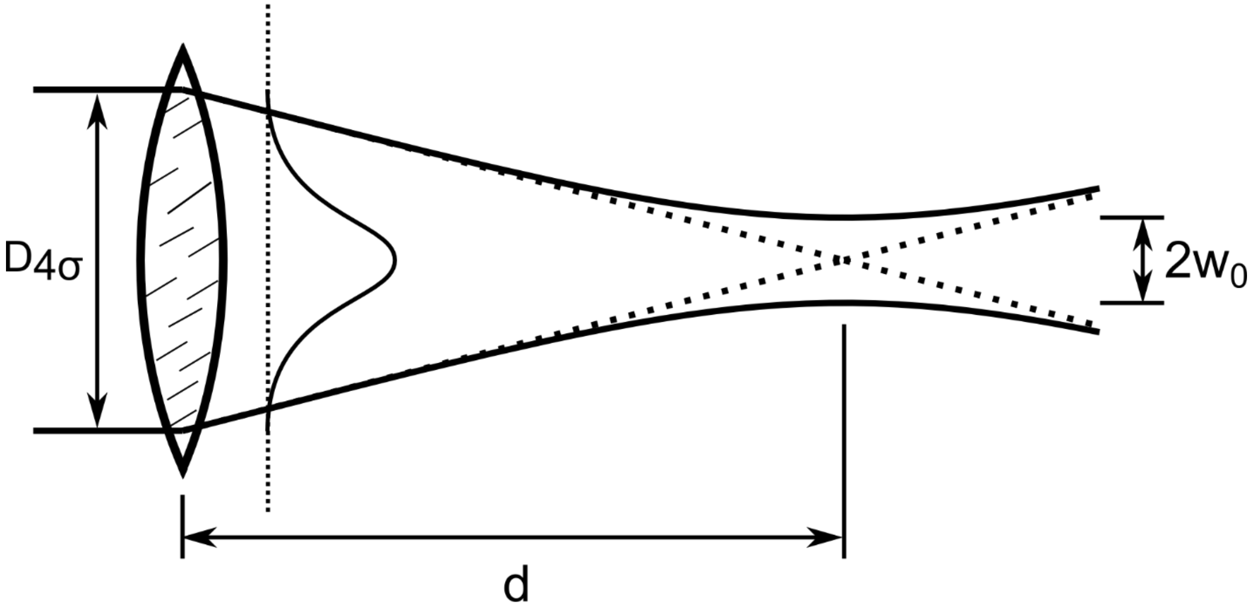

Figure 3.20: Gaussian beam geometry for the calculations presented here. *$D_{4\sigma}$* is the four sigma beam diameter of the FLDI beams at the field lenses, while w_0 is the Gaussian beam waist at best focus. The system *f*-number for the FLDI instrument may be defined as the ratio *$d/D_{4\sigma}$*.

$$\begin{gathered} w_0 = \frac{2\lambda d}{\pi D_{4\sigma}} \\ w(z) = \sqrt{w_0^2\left(1+\left[\frac{\lambda z}{\pi w_0^2}\right]^2\right)} \end{gathered} \tag{3.40}$$

Here, *d* is the distance from the focusing lens to the point of best focus, and $D_{4\sigma}$ is a standard measure of beam diameter representing the second moment of laser beam intensity, within which roughly 95% of the laser intensity is located. An approximation of the intensity of the beam in cross-section is shown in Eq. 3.41.

$$I(x,y,z)=\sqrt{\frac{1}{\pi w^2}}\exp\left(-\frac{2\left[x^2+y^2\right]}{w^2}\right)$$
$$=\sqrt{\frac{1}{\pi w_0^2\left(1+\left[\frac{\lambda z}{\pi w_0^2}\right]^2\right)}}\exp\left(-\frac{2\left[x^2+y^2\right]}{w_0^2\left(1+\left[\frac{\lambda z}{\pi w_0^2}\right]^2\right)}\right) \tag{3.41}$$

As the beam propagates through inhomogeneities, the wavefront phase is delayed at each point in the beam by the local refractive index. Because the FLDI instrument measures the mean phase of the entire beam at the output of the interferometer, fluctuations in phase across its width are averaged out to some extent, depending on the wavenumber of those fluctuations. This effect can be seen in Fig. 3.21.

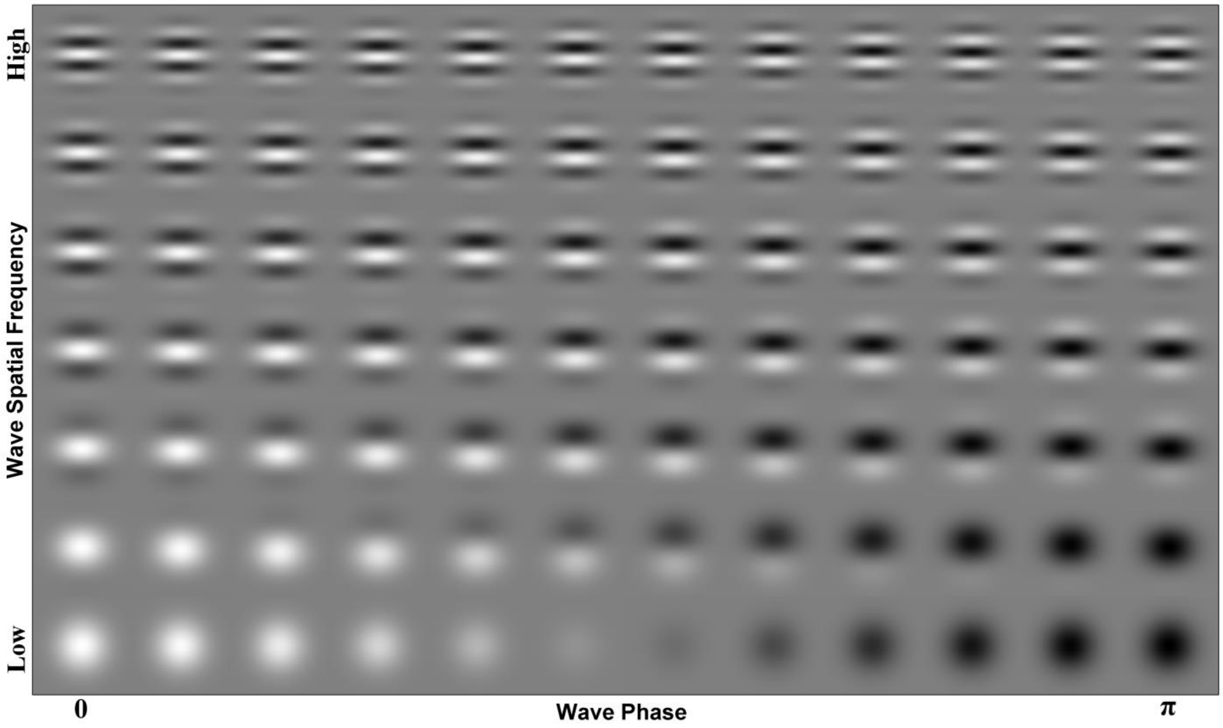

Figure 3.21: Spatially filtered phase difference signals showing the effect of a Gaussian beam profile on sinusoidal disturbances. The sinusoids vary along the vertical axis of the images, with the spatial frequencies of the images varying along the rows of the images, and the phase of the sinusoids varies along the columns. At low spatial frequencies, the change in phase between the images is obvious, while at high spatial frequencies they are almost indistinguishable due to spatial filtering.

At low wavenumbers, the contribution of a sinusoidal phase disturbance to the mean phase is clear, with good contrast. At higher wavenumbers, the contribution becomes indistinguishable, appearing almost exactly the same regardless of the phase of the disturbance.

The contribution of disturbances of a given wavenumber to the mean wavefront phase at each point along the beam is represented by a Gaussian function, with the transfer function given in Eq. 3.42.

$$\begin{aligned} H_w(k) &= \exp\left(-\frac{w^2k^2}{8}\right) \\ &= \exp\left(-\frac{w_0^2k^2}{8}\left(1+\left[\frac{\lambda z}{\pi w_0^2}\right]^2\right)\right) \end{aligned} \tag{3.42}$$

Away from best focus along the FLDI beam propagation axis, disturbances are heavily spatially filtered in the frequency domain. Because of this, the contribution to the mean FLDI phase of strong disturbances like turbulent boundary layers on wind tunnel windows is greatly diminished (see Fig. 3.22).

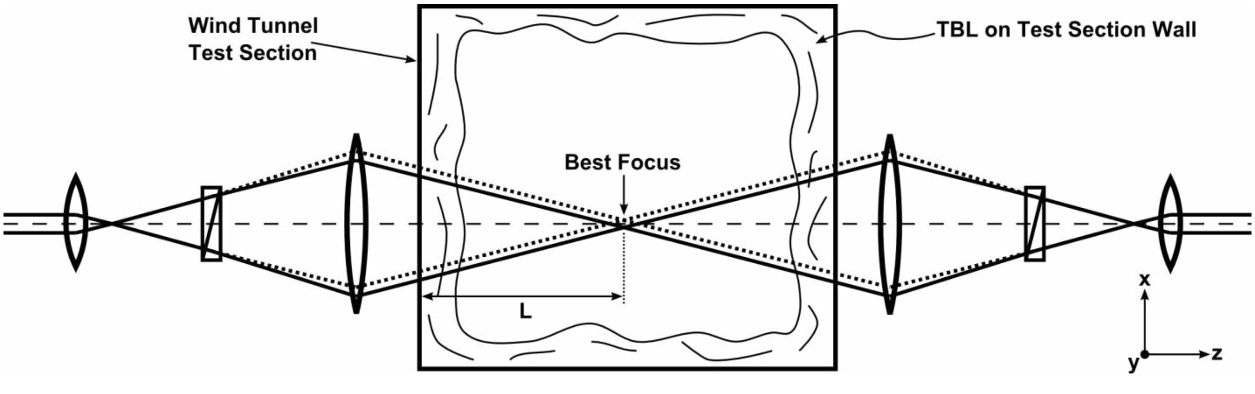

Figure 3.22: Diagram of the FLDI instrument used in a wind-tunnel test section with rectangular cross-section. Rejection of boundary layer signals from the FLDI output is best when the focus of the instrument is centered in the wind tunnel test section and with larger beam diameters inside the boundary layers.

Disturbances at best focus are largely unaffected with diffraction-limited beams, since the beam waist, w_0, is typically somewhat smaller than the turbulent scales of interest. Beam waists for clean Gaussian HeNe beams are typically in the range of 3-10 μm, while most energy-containing eddies are substantially larger than this. This 3-10 μm range is also typically smaller than the Kolmogorov scale of a turbulent flow, except in some cases where the flow is at very high speed (this scale is heavily dependent on Reynolds number), such that the maximum wavenumber resolved by the instrument is too small to resolve these smallest eddies[62].

3.7.4 Path-Integrated Spatial Filtering from Beam and Turbulence Profiles

Up to this point, all of the spatial filtering by the instrument has been considered at infinitesimally thick slices of the beam path perpendicular to the FLDI beam propagation axis, which only allows for turbulence to be treated as being essentially a two-dimensional disturbance that is perpendicular to the beam propagation axis. Because of the path-integrated nature of the instrument, however, the contribution to mean phase by disturbances along the full path must be considered. This means that the signal delivered by the FLDI system is necessarily a combination of the contribution of all of these slices. Unfortunately, modeling these contributions requires some degree of approximation of the spatial nature of the flow disturbances.

The simplest approximation is to consider the disturbances to be limited to an infinitely thin plane, perpendicular to the FLDI beam propagation axis. In this case, the response of the instrument is merely the convolution of the filter due to beam width and the filter from beam separation. An example of a transfer function due to the Gaussian beam width at best focus is shown in Fig. 3.23. This case demonstrates spatial filtering at best focus from a diffraction-limited spot given a $D_{4\sigma}$ of 20 mm and distance from lens to best focus, *d*, of 150 mm.

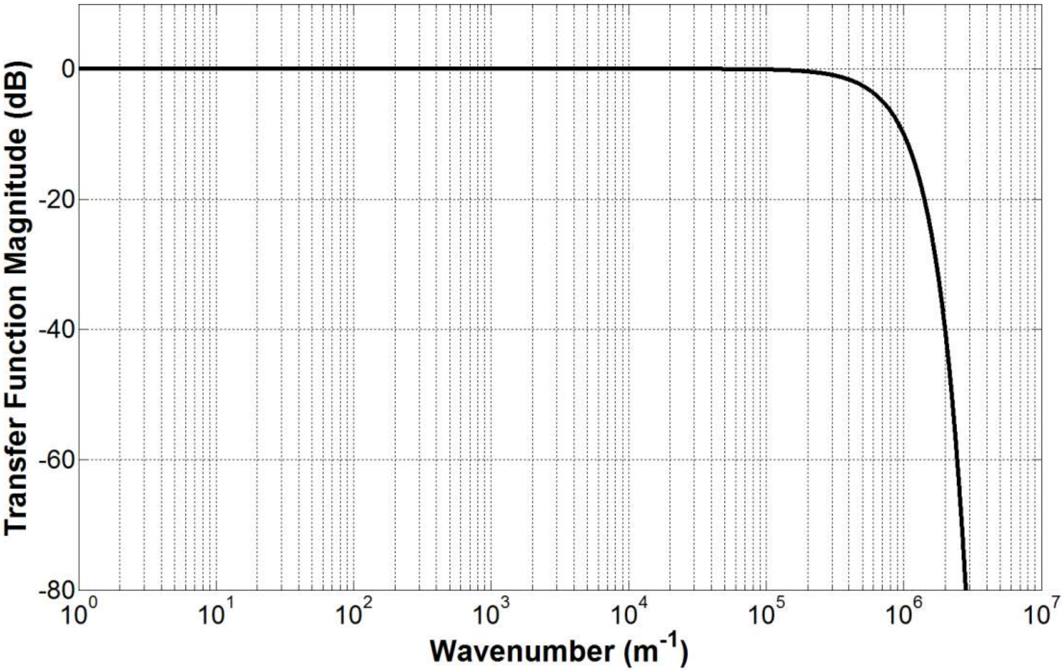

Figure 3.23: Simplest case for the beam size transfer function, where the turbulence is only present at the best focus, and is zero strength everywhere else.

In this simple case, the response of the instrument remains generally flat out to $k > 100000\ \mathrm{m}^{-1}$. This corresponds to a measurement frequency of roughly 10 MHz at a flow velocity of 600 m/s.

Another important case to consider is where the turbulent field is uniform across the test section, from one FLDI lens to the other. In this case, the transfer function of the instrument due to beam width is the RMS integral of beam width filters at all points along the beam in the test section. This transfer function is shown in Eq. 3.43, where L is the distance from the test section windows to the tunnel centerline, as diagrammed in Fig. 3.22.

$$\begin{aligned} H_z(k) &= \sqrt{\int_{-L}^{L} \exp\left(-\frac{w_0^2 k^2}{8}\left(1+\left[\frac{\lambda z}{\pi w_0^2}\right]^2\right)\right)^2 dz} \\ &= \sqrt{2\pi^{3/2}\frac{w_0}{\lambda k}\operatorname{erf}\left(\frac{L\lambda k}{2\pi w_0}\right)\exp\left(-\frac{w_0^2 k^2}{4}\right)} \end{aligned} \tag{3.43}$$

Using the same properties as the previous case, and a test section width L = 75 mm, is shown in Fig. 3.24:

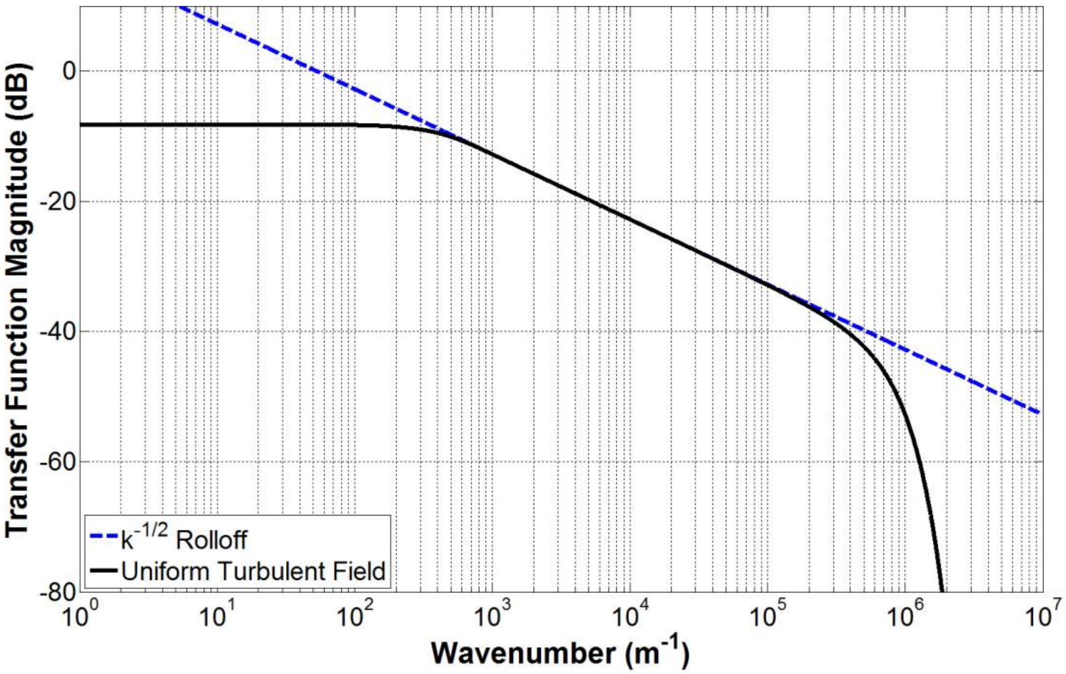

Figure 3.24: System transfer function when the disturbance is of uniform strength through the test section.

The straight dashed line has a slope of one decade per decade, and represents the rolloff due to the error function from the transfer function in Eq. 43. This model is most appropriate for modeling the FLDI beams' response to freestream turbulence, as the turbulence should be relatively consistent in strength and spectral characteristics throughout the core flow of a wind tunnel.

As L is increased, the wavenumber at which the error function begins to roll off decreases. In the limit as L approaches infinity, representing an infinitely wide test section, the rolloff starts immediately, and the resulting transfer function is shown in Eq. 3.44.

$$
\begin{aligned}
H_z(k) &= \sqrt{\int_{-\infty}^{\infty} \exp\left(-\frac{w_0^2k^2}{8}\left(1+\left[\frac{\lambda z}{\pi w_0^2}\right]^2\right)\right)^2 dz} \\
&= \sqrt{2\pi^{3/2}\frac{w_0}{\lambda k}\exp\left(-\frac{w_0^2k^2}{4}\right)}
\end{aligned}
\tag{3.44}
$$

The last approximation considered here is one in which the turbulent field follows a Gaussian strength profile, with standard deviation width σ_{jet} and centered at a distance along the beam relative to best focus, z_0. An illustration of the geometry for this case is given in Fig. 3.25.

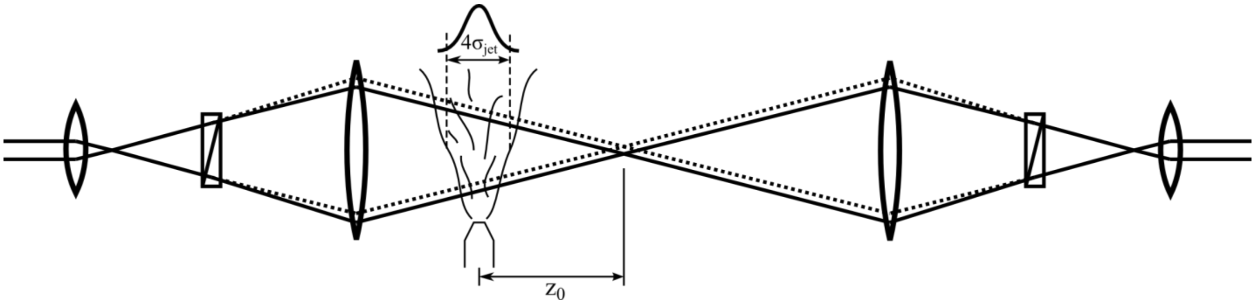

Figure 3.25: Geometry for the model of FLDI response to a Gaussian profile disturbance. Here, the jet is centered on the beams along the *y*-axis, and decentered from best focus by the distance *z₀* along the *z*-axis.

The transfer function for this case is shown in Eq. 3.45.

$$
\begin{aligned}
H_\sigma(k) &= \sqrt{\int_{-\infty}^{\infty}\left[\left[\exp\left(-\frac{w_0^2k^2}{8}\left(1+\left[\frac{\lambda z}{\pi w_0^2}\right]^2\right)\right)\right]\exp\left(-\frac{\left[z-z_0\right]^2}{\sigma_{jet}^2}\right)\right]^2 dz} \\
&= \sqrt{\frac{2\pi^{3/2}\exp\left(-\frac{k^2}{4}\left[w_0^2+\frac{8\lambda^2z_0^2}{k^2\lambda^2\sigma_{jet}^2+8\pi^2w_0^2}\right]\right)}{\sqrt{\frac{8\pi^2}{\sigma_{jet}^2}+\frac{k^2\lambda^2}{w_0^2}}}}
\end{aligned}
\tag{3.45}
$$

A plot of this model, using the same properties as above, with a Gaussian signal σ_{jet} of 1 mm, is shown in Fig. 3.26.

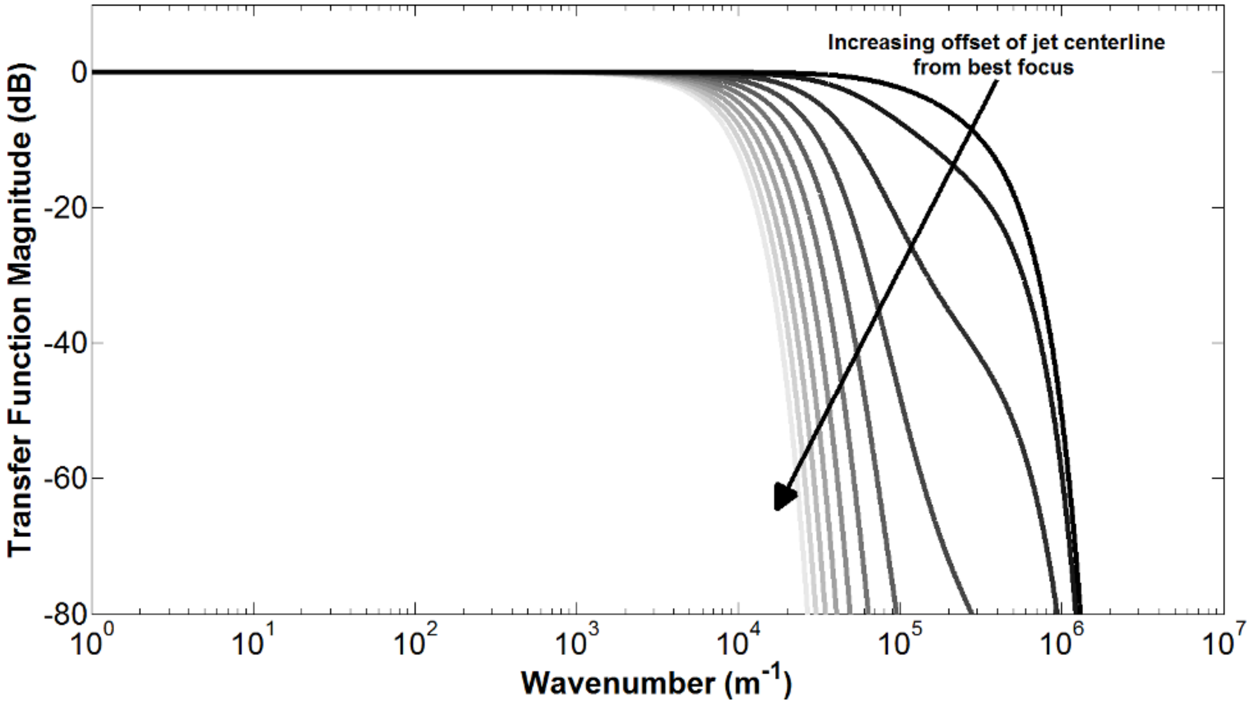

Figure 3.26: System transfer function when the disturbance follows a Gaussian profile. Lighter line shades indicate decentering of the disturbance ($|z_0 - z| > 0$).

This approximation can be used to model generally Gaussian signals, such as the signal from a turbulent jet[63]. As a small turbulent jet is used as a reference signal to characterize the rolloff of the FLDI instrument in later results, it is important to have a realistic model for how the instrument should behave in this case.

3.8 Turbulence Intensity

A standard diagnostic in turbulence research is the measurement of turbulence intensity, which relates RMS velocity fluctuations to the local freestream velocity. This is shown in Eq. 3.46, based on fluctuations in the freestream *u*-direction only.

$$TI\% = \frac{u'_{RMS}}{U_\infty} \times 100\% \tag{3.46}$$

Measured turbulence intensity is heavily dependent on the kind of flow under consideration. Combustion events are often very turbulent, with turbulence intensities of twenty percent or greater, while "quiet" wind tunnels achieve freestream turbulence intensities of small fractions of one percent.

According to Parseval's theorem, the total energy of a signal in time is identical to the energy of the signal in frequency (Eq. 3.47a). Using this relationship, it follows that the RMS value can be calculated from either a sampled signal or from its Fourier transform. Parseval's theorem requires an infinite integral which is not possible with a discrete, sampled signal. However, as long as the bandwidth of the signal is large enough that it encompasses all of the signal's meaningful energy, the discrete approximation in Eq. 3.47b is essentially exact.

$$\begin{gathered} \int_{-\infty}^{\infty} \left|h(t)\right|^2 dt = \int_{-\infty}^{\infty} \left|H(f)\right|^2 df \\ h_{rms} = \sqrt{\frac{1}{N}\sum_N h^2(t)} = \sqrt{\frac{1}{N^2}\sum_N \left|H(f)\right|^2} \end{gathered} \tag{3.47a,b}$$

Despite the ubiquity of turbulence intensity measurements, their utility is very limited. Turbulent kinetic energy couples between freestream turbulence and other aspects of flows, such as boundary layers, based on the frequency response of the flow feature. For example, boundary layer stability theory shows that boundary layers are generally receptive to turbulence disturbances only in particular frequency bands. Turbulence intensity, by the nature of the RMS calculation, is dominated by energy from the low-wavenumber “energy containing” eddies of the turbulence and gives no information on how that energy is distributed in frequency. This disconnect limits the usefulness of turbulence intensity as a diagnostic for these frequency-dependent phenomena. Still, baseline descriptors of turbulence like TI are necessary.

Thus, in terms of the present FLDI instrument, increasing the beam separation causes the measured turbulence spectrum to roll off at a lower frequency, but it might not significantly reduce the measured turbulence intensity. An example of this, using a simulated turbulence spectrum, is shown in Figs. 3.27a,b. Here, the effect of increased beam separation is obvious in the spectral plots, but the calculated turbulence intensities are only marginally reduced, retaining about 94% of the true turbulent energy at Δx = 100 μm, 90% at Δx = 200 μm, and around 87% at Δx = 300 μm.

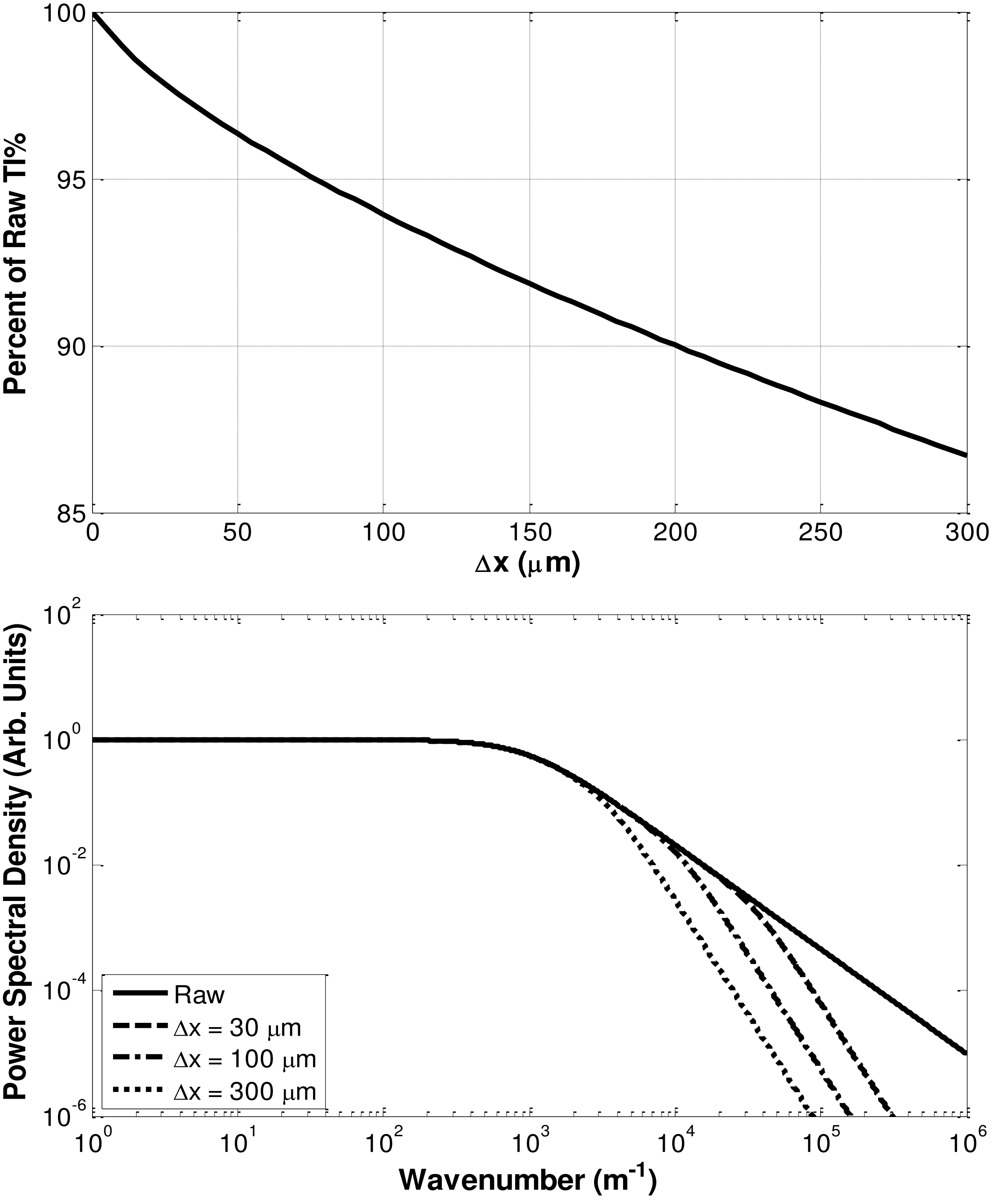

Figure 3.27a,b: Effect of FLDI beam separation spatial filtering on simulated turbulence spectra, showing RMS turbulence intensity (a) and the filtered spectrum (b). While the effect on the measured turbulent intensity from spatial filtering is relatively small, its effect on turbulence spectra is significant. This effect can be problematic when the signal strength is low compared to electronic noise, as the signal may fall below the noise floor in the high-frequency range of the spectrum, which is very important for turbulence characterization.

3.8.1 The Strong Reynolds Analogy

The FLDI instrument senses density fluctuations, not the velocity fluctuations required for the turbulence intensity measurement as written above. Corrsin claims that the spectral behavior of a passive scalar like weak density fluctuations should follow the same frequency behavior (e.g., spectrum) as does velocity[64], however he gives no simple theory for the relationship of their relative turbulence intensity amplitudes. The Reynolds analogy, given in Eq. 3.48, relates the fluctuating thermodynamic and kinematic variables in a compressible flow.

$$\left(1+\frac{\gamma-1}{2}M^2\right)\frac{T_0'}{\overline{T}_0}=\frac{P'}{\overline{P}}-\frac{\rho'}{\overline{\rho}}+\left(\gamma-1\right)M^2\frac{u'}{U_\infty} \tag{3.48}$$

Here, M is the local Mach number of the flow, γ is the ratio of specific heats in the gas, T_0 is the local stagnation temperature of the flow, P is the local pressure, ρ is the local density, and u is the local velocity. Terms with overbars represent Reynolds-averaged values, and primed variables represent the fluctuating components of that variable.

It would be extremely difficult to measure all of these terms simultaneously, so instead some assumptions must be made about the behavior of some of the terms. The FLDI instrument measures local density fluctuations that occur over a very short distance. In the time required for the signal to convect through the measurement volume it is very unlikely that the local stagnation temperature and pressure will vary significantly, at least in the absence of moving shock waves or other fine flow structures. After neglecting the T_0 and P terms, the direct relationship between the strength of density and velocity fluctuations shown in Eq. 3.49, known in the literature as the "strong Reynolds analogy," results.

$$\frac{\rho'}{\overline{\rho}}=\left(\gamma-1\right)M^2\frac{u'}{U_\infty} \tag{3.49}$$

This relation is used to calculate approximate velocity-based turbulence intensity from the density-based turbulence intensity measured by the FLDI instrument, for comparison with results in the literature.

3.9 Turbulence Spectra

Turbulence is an extremely broadband phenomenon: in a single turbulent flow, the scales of turbulent eddies range from the size of the largest features of the flow all the way down to dissipative scales. The importance of turbulent eddy scales in the behavior of turbulence and its interactions with flows lends itself naturally to Fourier analysis, where the frequency spectrum of the signal, rather than the time-domain signal itself, is the most useful representation of the data.

3.9.1 Importance of High Frequency Response

Of crucial importance to the behavior of turbulence is the cascade of energy from its largest scales, where most of the energy is present, to smaller scales and ultimately to viscous dissipation as heat. Being able to resolve this full range of scales is necessary to truly characterize the turbulence present in a flow, and it requires extremely-high frequency response from measurement instrumentation.

Traditionally, the most common instrument used for measurement of turbulence spectra is the hot-wire anemometer. The frequency response of hot-wire anemometry is limited by the size of the wire probe and the relative temperature of the probe to that of the surrounding fluid, and is typically in the tens to low hundreds of kHz. With very-fine-wire probes and high overheat ratios, manufacturer specifications state that a 3 dB bandwidth of 250 kHz may be possible. However, these probes are extremely fragile and may not be suitable for use in a high-speed flow due to breakage.

On the other hand, the FLDI instrument presented here should be capable, in principle, of many MHz of bandwidth with careful beam conditioning. As a non-intrusive technique it is also capable of being used in flows unsuitable for hot-wire anemometry, especially compressible flows. In fact, some hypersonic compressible flows have such high stagnation enthalpy that the concept of a hot-wire in the flow is fundamentally unreasonable.

3.9.2 Normalization of FLDI Signal

The relationship between the measured phase difference signal from the FLDI instrument and turbulent density fluctuations is shown in Eq. 3.50.

$$\lim_{\Delta x \to 0} \frac{\Delta\varphi_A - \Delta\varphi_B}{\Delta x} = \frac{2\pi K_{GD}}{\lambda} \int_{z_1}^{z_2} \frac{\partial \rho'}{\partial x} dz \tag{3.50}$$

Here, $\Delta\varphi_A$ - $\Delta\varphi_B$ is the raw phase signal from data, while the ultimate goal is to extract the density fluctuations due to turbulence, ρ', which is done by deconvolving the spatial filtering from the FLDI instrument from the signal. This filtering manifests itself in the right hand side of the above equation as a convolution of the fluctuating density field with the finite difference operator, $h_{\Delta x}$, and the spatial filtering due to finite beam width, h_z (Eq. 3.51).

$$\begin{aligned} \Delta\varphi_A - \Delta\varphi_B &= \frac{2\pi K_{GD}\Delta x}{\lambda} \int_{z_1}^{z_2} \frac{\partial \rho'}{\partial x} dz \\ &= \frac{2\pi K_{GD}\Delta x}{\lambda} \int_{z_1}^{z_2} \left[\rho' * h_{\Delta x}\left(\Delta x\right) * h_z(z)\right] dz \end{aligned} \tag{3.51}$$

Note that the derivative of the density field comes from the convolution (denoted by the * operator) of the fluctuating density with the finite difference operator, which is why it does not appear above.

Convolution is difficult to handle in the time/space domain, but is easily done in the frequency domain, where it is simply the multiplication together of the Fourier transform of the functions $f(x)$ and $g(x)$ (Eq. 52a). Simple derivatives and indefinite integrals can also be handled through Fourier transforms, by Eqs. 3.52b,c

$$\begin{gathered}
f(x) * g(x) \underset{\mathrm{F}^{-1}}{\overset{\mathrm{F}}{\rightleftarrows}} \mathrm{F}\left\{f(x)\right\} \mathrm{F}\left\{g(x)\right\} \\
\frac{d^n f(x)}{dx^n} \underset{\mathrm{F}^{-1}}{\overset{\mathrm{F}}{\rightleftarrows}} (ik)^n \, \mathrm{F}\left\{f(x)\right\}(k) \\
\int_{-\infty}^{\infty} f(x)\, dx \underset{\mathrm{F}^{-1}}{\overset{\mathrm{F}}{\rightleftarrows}} \frac{1}{ik} \mathrm{F}\left\{f(x)\right\}(k)
\end{gathered} \qquad (3.52a,b,c)$$

Using the above identities, the convolution from Eq. 3.51 is expressed in terms of Fourier transforms in Eq. 3.53. The impulse responses of the filters $h_{\Delta x}$ and h_z are replaced by their transfer functions, $H_{\Delta x}$ and H_z, which are convolved with the fluctuating density signal. Note that the multiplication of $H_{\Delta x}$ by k, omitted for clarity in the spatial filtering section above, 3.7.3, is reintroduced here (see the description for Fig. 3.12).

$$\mathrm{F}\left\{\rho'(t) * h_{\Delta x}(\Delta x) * h_z(z)\right\} = \mathrm{F}\left\{\rho'(t)\right\}\left[ik \cdot H_{\Delta x}(k)\right] H_z(k) \qquad (3.53)$$

Because the turbulence is assumed to be isotropic, integration and differentiation in the x- direction can be handled identically to integration and differentiation in any other direction. This allows the integration over z to be handled using a Fourier transform, using Eq. 3.52c. Substituting the convolution above into the result gives Eq. 3.54.

$$\begin{aligned}\mathcal{F}\left\{\Delta\varphi_A-\Delta\varphi_B\right\}&=\mathcal{F}\left\{\frac{2\pi K_{GD}\Delta x}{\lambda}\int_{z_1}^{z_2}\left[\rho * h_{\Delta x}\left(\Delta x\right) * h_z(z)\right]dz\right\}\\&=\frac{2\pi K_{GD}\Delta x}{\lambda}\left(\frac{1}{ik}\mathcal{F}\left\{\rho'\left(t\right)\right\}\left[ik\cdot H_{\Delta x}\left(k\right)\right]H_z\left(k\right)\right)\\&=\frac{2\pi K_{GD}\Delta x}{\lambda}\mathcal{F}\left\{\rho'\left(t\right)\right\}H_{\Delta x}\left(k\right)H_z\left(k\right)\end{aligned}\tag{3.54}$$

The multiplication by *k* from the finite difference is cancelled out by the division by *k* from the integration, resulting in a much simpler calculation. Isolating the ρ' term on the left-hand side, and taking the inverse Fourier transform of the result, gives the desired relationship between the measured signal and the fluctuating density (Eq. 3.55).

$$\rho'\left(t\right)=\frac{\lambda}{2\pi K_{GD}\Delta x}\mathcal{F}^{-1}\left\{\frac{\mathcal{F}\left\{\Delta\varphi_A-\Delta\varphi_B\right\}}{H_{\Delta x}\left(k\right)H_z\left(k\right)}\right\}\tag{3.55}$$

The density-based turbulence intensity of the measured signal, TI_ρ, is found by calculating the RMS value of the power spectrum of the density fluctuations and dividing by the freestream density. An approximation of the velocity-based turbulence intensity, TI_U, can be calculated by applying the strong Reynolds analogy from Eq. 3.49 to this calculation.

$$\begin{aligned}TI_\rho\%&=\frac{\rho'}{\bar{\rho}}=\frac{1}{\bar{\rho}}\sqrt{\frac{1}{N^2}\sum_N\left|\frac{\lambda}{2\pi K_{GD}\Delta x}\frac{\mathcal{F}\left\{\Delta\varphi_A-\Delta\varphi_B\right\}}{H_{\Delta x}\left(k\right)H_z\left(k\right)}\right|^2}\times 100\%\\TI_U\%&=\frac{u'}{U_\infty}\approx\frac{1}{\bar{\rho}\left(\gamma-1\right)M^2}\sqrt{\frac{1}{N^2}\sum_N\left|\frac{\lambda}{2\pi K_{GD}\Delta x}\frac{\mathcal{F}\left\{\Delta\varphi_A-\Delta\varphi_B\right\}}{H_{\Delta x}\left(k\right)H_z\left(k\right)}\right|^2}\times 100\%\end{aligned}\tag{3.56}$$

3.9.3 Turbulence Models

In order to better understand the turbulent density spectra measured by the FLDI instrument, it is useful to first perform the analysis discussed in this Theory section on simulated "model" turbulence spectra as an example. As mentioned above, turbulence is a very complicated, broadband phenomenon, but there are properties of turbulence spectra that are shared between many different flows which the following turbulence models attempt to represent. Three models of turbulence spectra that are common in the literature are presented here: the Kolmogorov spectrum, the von Kármán spectrum, and the Tatarski spectrum.

The most commonly-referenced model for turbulence spectra is the Kolmogorov model, named after the Soviet mathematician Andrey Kolmogorov, who in 1941 published his theory of the turbulent energy cascade of very-high-Reynolds-number turbulence. Through dimensional analysis he established that, in the "inertial range" of the turbulence spectrum (where inertial effects are much greater than viscous effects), turbulent kinetic energy must be transferred from larger eddies to smaller eddies such that the three-dimensional kinetic energy spectrum, $E(k)$, is proportional to $k^{-5/3}$. When considering the vector decomposition of turbulent energy (the turbulent field), $\Phi(\vec{k})$, this corresponds to a slope of $k^{-11/3}$, as in Eq. 3.57[65].

$$\Phi(\vec{k}) \sim k^{-11/3} \tag{3.57}$$

The Kolmogorov spectrum shows up in almost all turbulent flows, from microchannel turbulence to the motion of the interstellar medium, and is as close to a universal theory of turbulence as currently exists. Nevertheless, as mentioned before, this theory holds only in the inertial range of the turbulence spectrum, and is not meaningful elsewhere. At low wavenumbers (the so-called "energy-containing region" of turbulence) energy is fed into the turbulence cascade from the mean flow, such that the energy level of the spectrum actually increases with wavenumber. At very high wavenumbers, corresponding to eddies smaller than the Kolmogorov length scale, η, viscous effects dominate, and the turbulent energy spectrum rolls off much faster than $k^{-5/3}$.

To deal with the low wavenumber discrepancy, the von Kármán spectrum introduces an "outer scale" length term, L_o, which represents the maximum size of turbulent eddies in a flow. The inclusion of this term limits the spectrum at low wavenumbers, and is especially important in constrained flows like the ones considered in this research. The turbulent field for the von Kármán spectrum is given by Eq. 3.58.

$$\begin{gathered} k_0 = \frac{2\pi}{L_0} \\ \Phi(\vec{k}) \sim (k^2 + k_0^2)^{-11/6} \end{gathered} \tag{3.58}$$

The faster rolloff from viscous effects at high wavenumbers (the dissipation range) is handled by the Tatarski spectrum (Eq. 3.59), which adds an exponential term that begins to roll off around the "inner scale" length, L_i.

$$\begin{gathered} k_0 = \frac{2\pi}{L_0}, k_i = \frac{5.92}{L_i} \\ \Phi(\vec{k}) \sim (k^2 + k_0^2)^{-11/6} exp\left[-\left(\frac{k}{k_i}\right)^n\right] \end{gathered} \tag{3.59}$$

The empirical n term determines how much faster the spectrum rolls off in the dissipation range, and it is usually taken to be equal to 2.

In isotropic turbulence, as considered here, the turbulent field can be collapsed into a function of a single variable, k, rather than needing the vector, $\vec{k}$. This is called the three-dimensional turbulent spectrum, $E(k)$. It represents the power spectral density of waves with the same wavenumber vector magnitude, $k = \|\vec{k}\|$, and is found by taking the spherical integral of the turbulent field for all wavenumbers. For scalar turbulence, the one-dimensional spectrum, $F(k_l)$, is obtained by integrating $E(k)/k$ over all wavenumbers greater than k_l[66]. These calculations are given in Eqs. 3.60a and 3.60b, respectively.

$$\begin{gathered} E(k) = 2\pi k^2 \Phi(k) \\ F(k_1) = \int_{k_1}^{\infty} k^{-1} E(k)\, dk \end{gathered} \tag{3.60a,b}$$

Example one- and three-dimensional spectra calculated from a basic Tatarski spectrum are shown in Fig. 3.28, normalized to highlight the agreement between $E(k)$ and $F(k)$ in the interial region of turbulence. The outer scale wavenumber, k_o, and inner scale wavenumber, k_i, are labelled, and n is set to 2 as is common in the literature. The $k^{-5/3}$ rolloff from Kolmogorov's theory is overlaid.

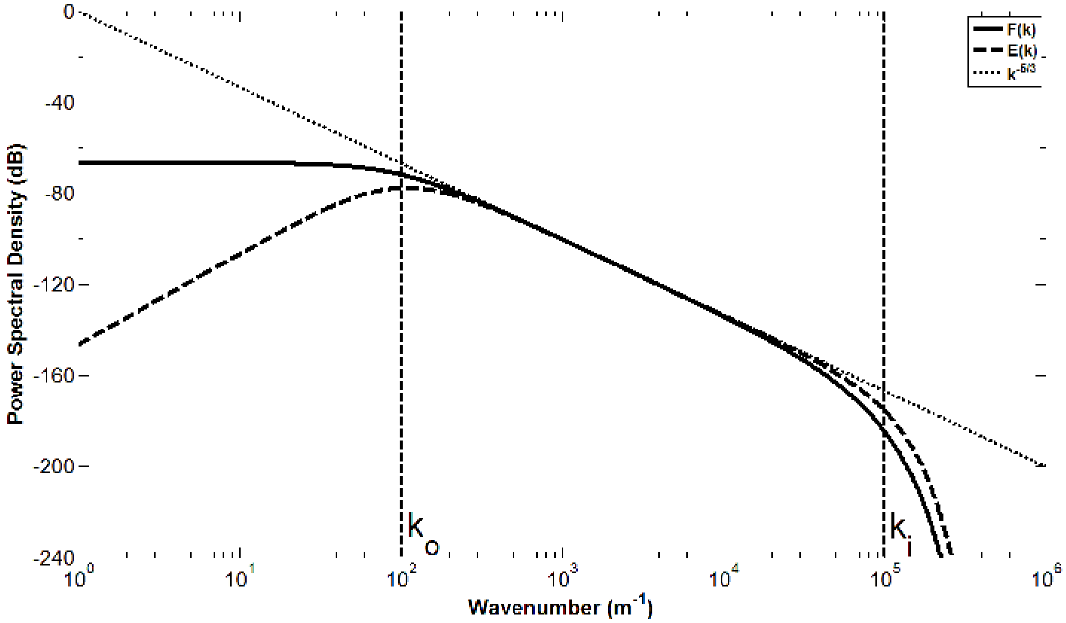

Figure 3.28: Simulated 3-D and 1-D turbulence spectra for density as a passive scalar.

The FLDI instrument operates on the three-dimensional spectrum of turbulence, but the output follows the one-dimensional form, similar to the output of a hot-wire anemometer, due to the spatial derivative from the two interferometer beams. Deconvolution of the FLDI system transfer function from the measured signal results in spectra that are qualitatively similar to the Tatarski spectrum. This allows fitting of the above spectrum models to the calculated density spectra for turbulence parameterization, which is much more meaningful than simple measurements of turbulence intensity.

Although it is best to perform a least-squares fit of a turbulence model to the data, it is also useful to simply estimate the inner and outer scale lengths of the turbulent signal. A simple calculation for the outer length scale using numerical integration is given in Eq. 3.61. This represents the average scale of the highest energy eddies.

$$L_o \approx 4\pi \frac{\int_0^\infty k^{-1} E(k)\,dk}{\int_0^\infty E(k)\,dk} \tag{3.61}$$

A calculation for the inner scale length is shown in Eq. 3.62. This represents the average scale of eddies at which viscosity begins to significantly affect the turbulent spectrum, marking the transition between the inertial and dissipative ranges of the turbulence, and is called the Taylor microscale.

$$L_i \approx \sqrt{\frac{\int_0^\infty E(k)\,dk}{\int_0^\infty k^2 E(k)\,dk}} \tag{3.62}$$

Both of these estimates are heavily susceptible to noise on the FLDI signal, particularly the inner length scale calculation due to the derivative in the denominator. Because of this, the signal-to-noise ratio of the signal must be quite high in order to get reasonable estimates of the turbulent length scales. Better practice is to use these estimates as initial guesses for least-squares fit parameters.

3.10 Numerical Simulations of FLDI Measurements

The response of the theoretical FLDI instrument to model cases may give some insight into how well an actual instrument will suit a given situation. Two such models are presented here. One models the response of the instrument to a round turbulent jet. The other examines the influence of boundary layers on tunnel windows on the calculated turbulence intensity and spectra of a uniform turbulent field (see the diagram of an FLDI instrument applied to a wind-tunnel test section in Fig. 3.22).

3.10.1 Jet simulation

Round turbulent jets are a well-characterized turbulence source that are standard in the literature. They are used in this research to provide a reference turbulence signal to compare with published data, and also to characterize the sensitive region of the FLDI instrument. Since the turbulence intensity profile of round turbulent jets is known, how fast the signal from the FLDI instrument rolls off as the jet is translated away from best focus along the FLDI beam propagation axis, z, compared to the true rolloff of the jet signal, provides a simple estimate of the ability of the instrument to reject unwanted signals occurring away from best focus. For this reason, a simulation of the FLDI response to a model round turbulent jet was developed to verify the transfer function models above.

For this simulation, round turbulent jets are modeled as fully developed, with Gaussian turbulence intensity profiles of standard deviation length σ_{jet}, as in Fig. 16. The turbulence is assumed to follow a von Kármán spectrum with the outer length scale, L_o, equal to two times the standard deviation length of the jet profile. Using this approximation, the largest-scale energy-containing turbulent eddies are on the same scale as the half-width of the jet.

The FLDI transfer function from Eq. 45 is calculated for a range of z_0 values. At each point, this system transfer function is convolved with the jet's turbulent spectrum. The RMS level of the spectrum data at each z_0 point represents the unprocessed signal that would be measured by the FLDI instrument, if the jet centerline were to be placed at that distance from the FLDI beam focus.

A plot of the simulated response of the instrument is shown in Fig. 3.29, where $\sigma_{jet} = 2$ mm, $d = 150$ mm, and $D_{4\sigma} = 20$ mm. The true Gaussian profile of the jet turbulence is also shown for comparison.

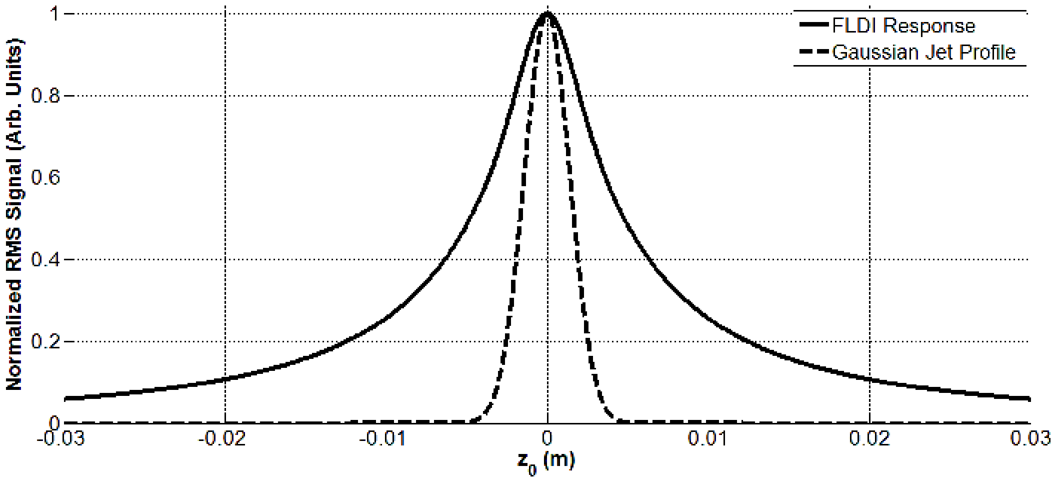

Figure 3.29: Simulation of a jet with a Gaussian turbulence profile, centered at distance z_0 relative to best focus, as diagrammed in Fig. 3.25.

As the maximum beam diameter of the FLDI instrument is increased, its response becomes more "point-like" due to spatial filtering of signals away from best focus. In the limit as the maximum beam diameter approaches infinity, the measured turbulence profile of the jet matches the true turbulence intensity profile. This is seen in Fig. 3.30, where the response of the instrument is modeled with the same system properties as above, but with a range of $D_{4\sigma}$ values, spaced logarithmically from 5 mm to 1 m.

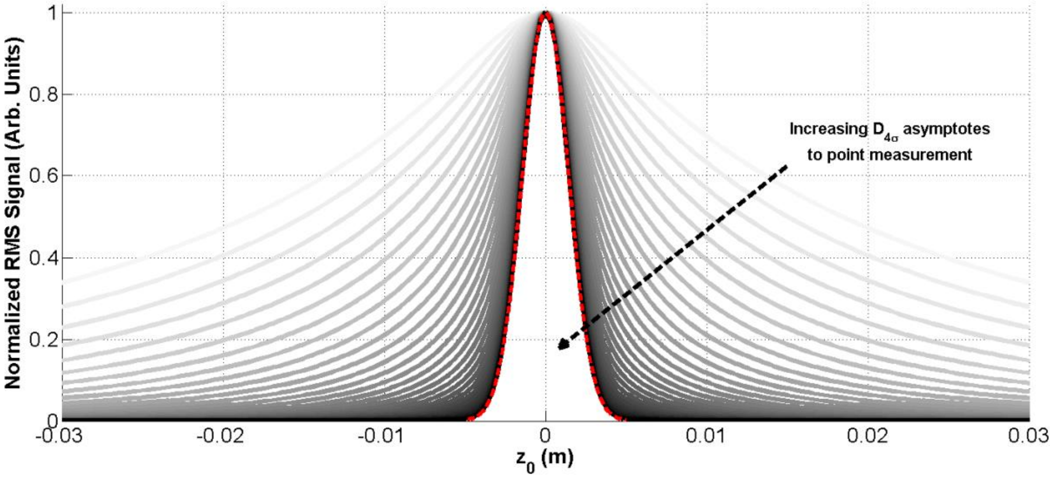

Figure 3.30: Simulation of a jet with a Gaussian turbulence profile, centered at distance z_0 relative to best focus, with increasing maximum FLDI beam diameters. In the limit as $D_{4\sigma}$ goes to infinity, the response of the instrument becomes exact.

Clearly, focusing a one meter diameter beam to a point in the span of 150 mm is not feasible. This would correspond to a system *f*-number of 0.15 (see Fig. 3.21), while the practical limit on f-number is approximately *f*/1 to avoid severe aberrations in the beam from the focusing optics. This model serves, however, to point out the asymptotic behavior of the FLDI optics towards a “point” measurement from a path-integrated optical system with increasing beam angle (reduced system f-number).

Scaling functions for the distance from best focus and the amplitude of the turbulence were developed, using the FLDI optics parameters d and $D_{4\sigma}$ and jet width standard deviation, σ_{jet}. These scaling functions are given in Eqs. 3.63a and 3.63b, respectively.

$$
\begin{aligned}
z_{scaled} &= \frac{z_0 D_{4\sigma}}{\sigma_{jet} d} \\
\varphi_{scaled} &= \varphi_{RMS}\sigma_{jet}^{1/6}
\end{aligned}
\tag{3.63a,b}
$$

These functions are used to scale the simulated response of the FLDI instrument to modeled turbulent jets, where d = 150 mm, $D_{4\sigma}$ = 30 mm, and with σ_{jet} varying from 1 to 11 mm. The unprocessed simulations are shown in Fig. 3.31a, while the scaled data are seen in Fig. 3.31b.

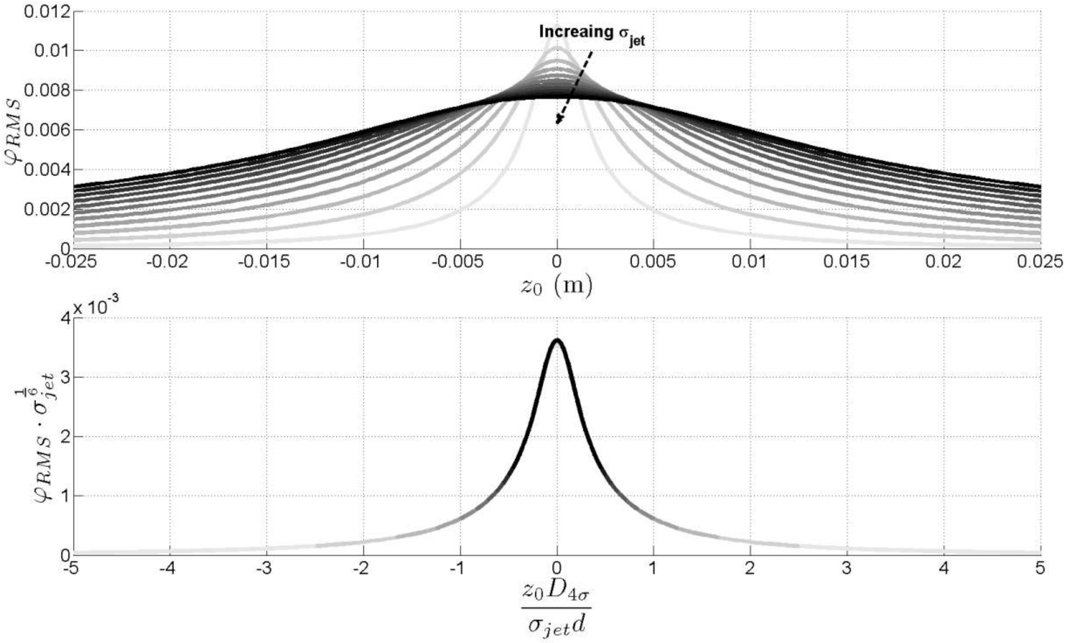

Figure 3.31a,b: Simulation of a jet with a Gaussian turbulence profile, centered at z_0 relative to best focus, for a range of σ_{jet} values from 1 to 11 mm. The top plot is unprocessed, while the bottom plot is scaled using the functions above.

Here, darker lines represent jets modeled with higher values of σ_{jet}. Using these scaling functions, the data for different values of σ_{jet} appear to align well with one another. Data calculated with different values of d / $D_{4\sigma}$, which serves as the effective *f*-number of the FLDI system, have nonlinear effects on the response of the instrument to turbulent jets. This is seen in Fig. 3.32.

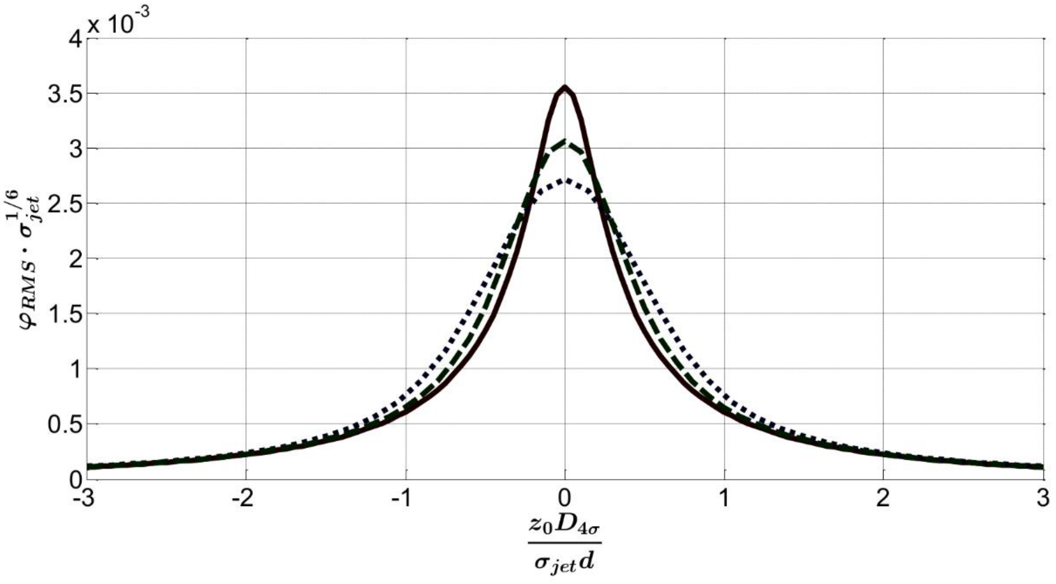

Figure 3.32: Simulation of a jet with a Gaussian turbulence profile, centered at z_0 relative to best focus, scaled using the scaling functions from above, with different values of $d/D_{4\sigma}$ (the system f-number).

Here, the solid line data are calculated using $D_{4\sigma} = 30$ mm, the dashed line data are calculated using $D_{4\sigma} = 40$ mm, and the dotted line data are calculated using $D_{4\sigma} = 50$ mm. When more than around one scaled distance from focus, the curves for each data set follow the same exponential decay, but within this range the response behaves quite nonlinearly.

3.10.2 Freestream turbulence simulation

An important application of the FLDI instrument is in wind tunnel testing, where the quantity of interest is the freestream turbulence level and spectrum, or a local turbulence level in a flow being surveyed by the FLDI instrument along the tunnel centerline. Boundary layers on the test section windows, that develop along the nozzle wall, corrupt the optical path of the instrument. These boundary layers are typically much stronger than the freestream turbulence level, and for typical path-integrated optics, where each point along the beam path is equally weighted, they present a significant problem for analysis of core-flow features. The FLDI instrument, due to its spatial filtering effects, "sees through" much of this boundary layer noise. While the signal from the boundary layers is still present in the output of the instrument, only the very low frequencies of the boundary layer turbulence pass through, and the effect of the boundary layer noise on the measured turbulence intensity is greatly attenuated. This contribution is reduced even further by deconvolution of the expected system transfer function from the signal, such as by using an assumption that the freestream turbulence is a uniform field across the test section, as in Eq. 3.44.

A simulation was developed that models this uniform turbulent field throughout a test section, with turbulent boundary layer signals at both edges of the optical path. As with the turbulent jet model, the turbulence spectra of the freestream and the boundary layers are modeled as being identical von Kármán spectra, where the outer scale length of the turbulence is equal to the boundary layer thickness. A more realistic simulation would model the freestream turbulence as having a smaller outer scale length, equal to the boundary layer thickness from some upstream point on a de Laval nozzle wall from which the turbulence is radiated into the flow. For the purposes of demonstration, however, the model used here should be adequate. The strength of the turbulence in the boundary layers is modeled as a linear decay from a maximum turbulence intensity, Tu_{BL}, to the freestream turbulence level, Tu_{∞}. Although simplistic, this model is a reasonable analogue of how turbulence intensity behaves in a real turbulent boundary layer. Klebanoff's measurements of turbulence intensities in an incompressible turbulent boundary layer on a flat plate along the x-, y-, and z-directions are reproduced in Fig. 3.33 to support this model[67].

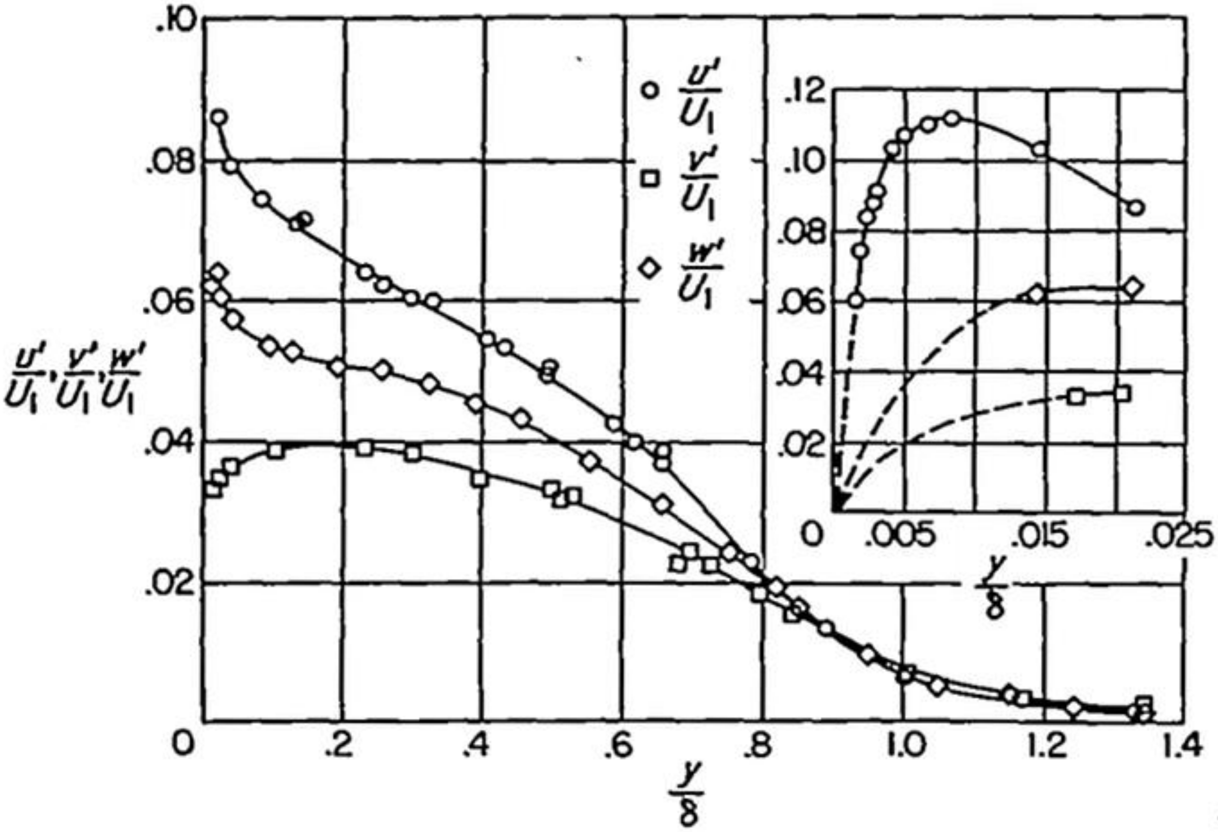

Figure 3.33: Measured turbulence intensities in incompressible turbulent boundary layers on a flat plate, from Klebanoff (1955) [67]

The simulation calculates the increase in measured turbulence intensity with increasing boundary layer strength, starting from the case of no boundary layers. A plot of example boundary layer turbulence intensity profiles as a function of distance from the test section centerline is shown in Fig. 3.34. The dimensions used for this simulation are a test section width of 6 inches (152.4 mm) with 1 inch thick sidewall boundary layers identical to those of the Penn State Supersonic Wind Tunnel where some of the testing for this research was performed.

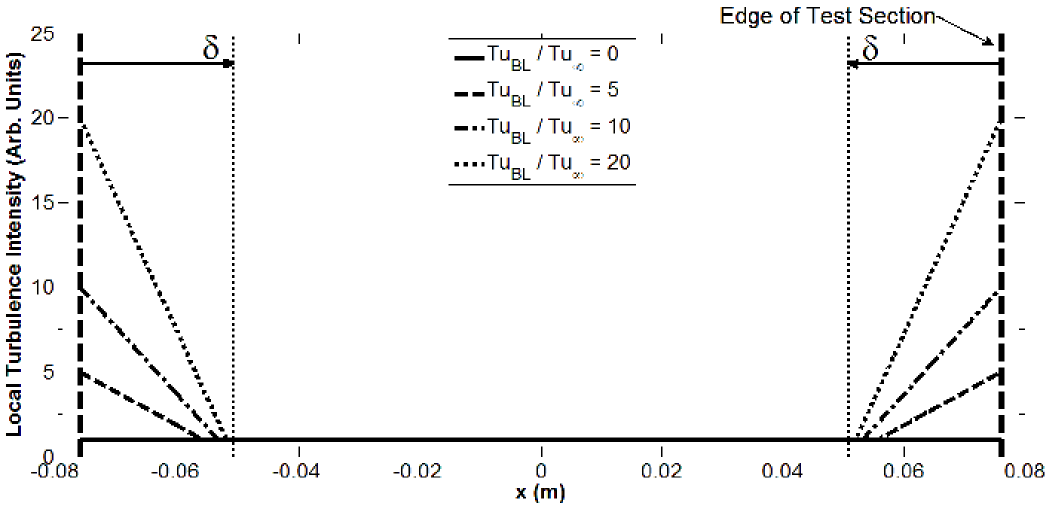

Figure 3.34: Simulated turbulence intensity, as a function of distance x from test section centerline, for uniform freestream turbulence with added turbulent boundary layers outside the core flow in the PSUSWT.

The turbulent boundary layer signals manifest themselves as “humps” in the low-frequency range of the “true” FLDI system transfer function, compared to the expected transfer function for a uniform turbulent field. This is shown in Fig. 3.35, where the solid line represents a uniform field with no turbulent boundary layers, and the other lines represent increasing boundary layer strength.

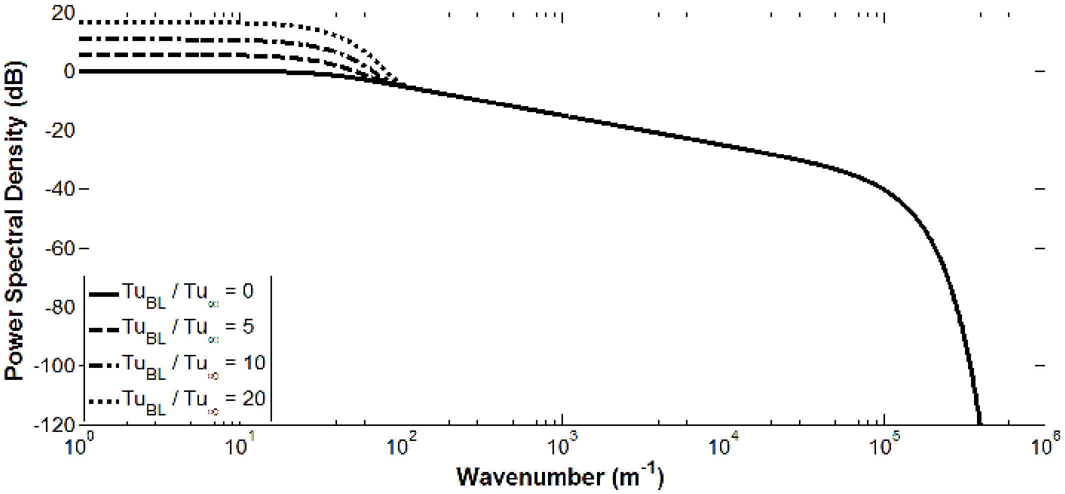

Figure 3.35: Simulated spectra for uniform freestream turbulence with turbulent boundary layers outside the core flow in the PSUSWT.

As can be seen here, the effect of introducing boundary layer turbulence to the edges of the test section is limited almost exclusively to low wavenumbers. For the parameters given above, wavenumbers above about 100 m^{-1} are essentially unaffected, even with boundary layers twenty times the strength of the freestream turbulence. This result implies that, while boundary layer “noise” may be much stronger than the freestream turbulence signal, the spectrum measured by the FLDI instrument is for the most part an accurate representation of the spectrum of interest.

This is a crucial theoretical result regarding the use of the FLDI instrument to make optical turbulence measurements on a wind-tunnel centerline while looking through thick turbulent boundary layers on both sidewall windows. This theoretical result shows that it is possible to do that, but that the low-frequency end of the resulting spectrum is likely to be contaminated by sidewall boundary layer influences. In practice, FLDI users will ignore this low-frequency spectrum and concentrate on the uncontaminated higher-frequency results provided by FLDI.

Transfer functions like those shown in Fig. 3.36 are applied to the von Kármán turbulent spectrum described above, for a range of boundary layer strengths from 0 to 100 times the turbulence intensity of the freestream. The raw turbulence intensity at each boundary layer strength is calculated, along with the turbulence intensity where the system transfer function (which assumes the field is uniform across the test section) is deconvolved. This is demonstrated in Fig. 3.36, along with a plot of the integrated turbulent energy across the entire test section.

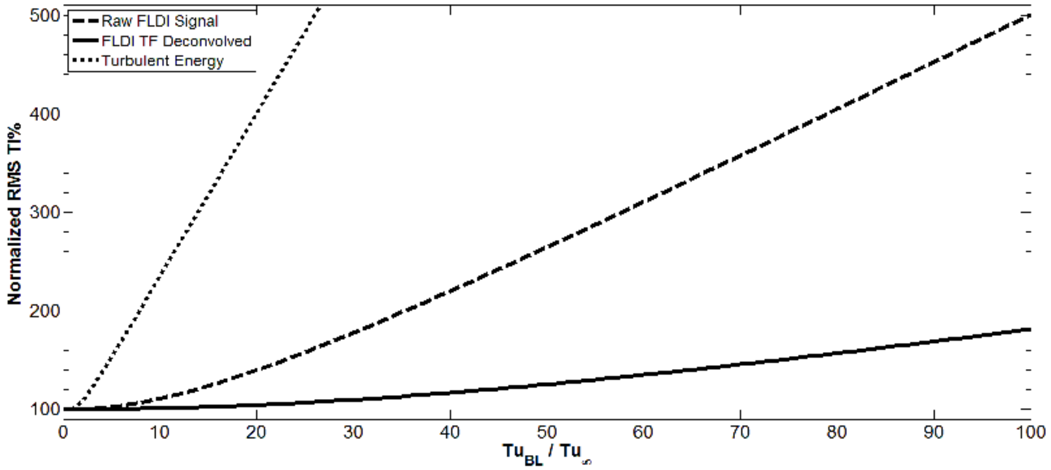

Figure 3.36: Normalized turbulence intensities for the model of uniform freestream turbulence with added turbulent boundary layers.

The spatial filtering from the FLDI instrument dramatically reduces the influence of boundary layer signals on the measured turbulence intensity, compared to the turbulent energy as would be seen by an unfiltered beam, as demonstrated in Fig. 3.37. Deconvolution of the FLDI transfer function from the signal reduces their effect even more. The measured turbulence intensity is within 10% of the correct result with boundary layers up to about 10 times the strength of the freestream turbulence for the raw signal, and up to approximately 35 times for the processed signal. This supports the statement that the response of the FLDI instrument, while still using path-integrated optics, gives a point-like measurement. There is no other known optical instrument that can make useful turbulence measurements under such conditions.

Chapter 4: Procedure

4.1: Setup of Instrument

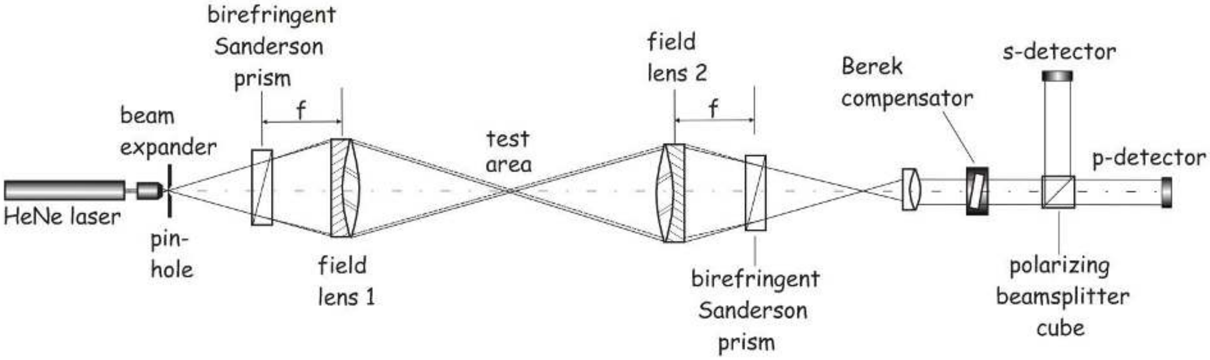

Figure 4.1: Layout of FLDI instrument.

The first components of the focusing laser differential interferometer to be installed are the field lenses used to focus the beam, for example, within a wind tunnel test section. They should be evenly spaced and as close as possible to the intended measurement volume in order to maximize the convergence angle of the beam, thus minimizing the sensitive volume. One can determine the back focal length of these field lenses by projecting onto card stock a bright light source such as a candle or LED placed far from the lens. The distance from the surface of the lens to the point where the image of the light source is sharpest on the card stock is the back focal length.

The Sanderson prisms are installed next, placed at the back focal lengths of the field lenses measured previously. Due to the gradient-index nature of these prisms, their effective focal point is slightly off center, as described by Eq. 3.28, and this must be taken into account when aligning the optics to ensure that the FLDI beams will be parallel through the test area. The first prism should be equipped with a dial indicator reading the deflection at the center of the base of the prism. This deflection measurement is reasonably accurate for predicting the beam separation Δx after the prisms have been calibrated.

The laser and microscope-objective beam expander are installed next, placed appropriately to achieve the desired focal point in the test section. It is necessary to check that the beam is the same size going through both prisms at this point since if this is not the case, then it is likely that the second field lens is not placed at the same distance from the focal point as the first lens. A "clean" beam is very important for achieving high sensitivity with the FLDI instrument, so the smallest pinhole that still allows adequate light transmission should be used in the beam expander. A 5 µm pinhole was used for the present research.

The laser beam should next be collimated to a thin beam after the second prism. It is helpful to use a high-quality lens designed for a small camera, such as a security camera lens, in order to avoid introducing aberrations. The beam must be collimated for the Berek phase compensator used here, since its phase retardation is heavily dependent on illumination angle-of-incidence.

The final components in the instrument are the polarizing beamsplitter cube and the two photodiodes. The beamsplitter cube should be tilted in the axis of the incoming beam so that the two photodiodes are at +/- 45 degrees from the axis of beam-separation as seen in Fig. 2.3. This aligns the polarizing beamsplitter cube with the polarization axes of the laser beam and maximizes the difference signal between the two photodiodes when the Berek compensator is reset to zero compensation.

4.2: Adjustment of Sanderson Prisms

For the initial setup, the strain on both Sanderson prisms should be relaxed and the Berek compensator should be set to zero retardance. The first prism should then be adjusted to the needed deflection, depending on test conditions and desired sensitivity as described in section 3.6.2. Using a multimeter with peak-holding capability or an oscilloscope, the second prism should next be adjusted until the absolute difference between the outputs of the s- and p-polarization photodiodes is maximized. In this case the two prisms are balanced, and no further adjustment of the prisms is required. The number of surfaces and stray light reflections in the optical path makes achieving 100% interference contrast between the two photodiodes challenging. However, with careful adjustment and alignment, a contrast of 80% or greater is possible, and is adequate.

With the prisms properly adjusted, the next step is to adjust the Berek phase compensator to balance the interferometer response. The goal is to shift the phase variations, measured by the two photodiode signals, so that they are nominally centered about the 0 and 180 degree points on the sine curve response of the interferometer. This results in the most closely linear response and largest dynamic range possible for the instrument. First, one adjusts the Berek compensator until one of the signals is maximized and the other is minimized. Next, the voltages of both beams and the compensator setting are recorded. Then the compensator is adjusted for the opposite condition, in which the second signal is maximized and the first is minimized, and the resulting values are recorded as was done previously. Finally, one adjusts the compensator until the signals are at the average of their maximum and minimum voltages. This should occur close to the average value of the two compensator settings, but since the Berek compensator does not respond linearly, this guidance is approximate. A Soleil-Babinet compensator can be used instead. It responds linearly to adjustment, but is significantly more expensive. The extra accuracy is not necessary for the instrument, so it does not justify the expense.

When the Berek compensator is properly adjusted, the sensitivity of the FLDI instrument's electronics is maximized, as seen below in Fig. 4.2 where a helium jet was used to give a demonstration of sensitivity.

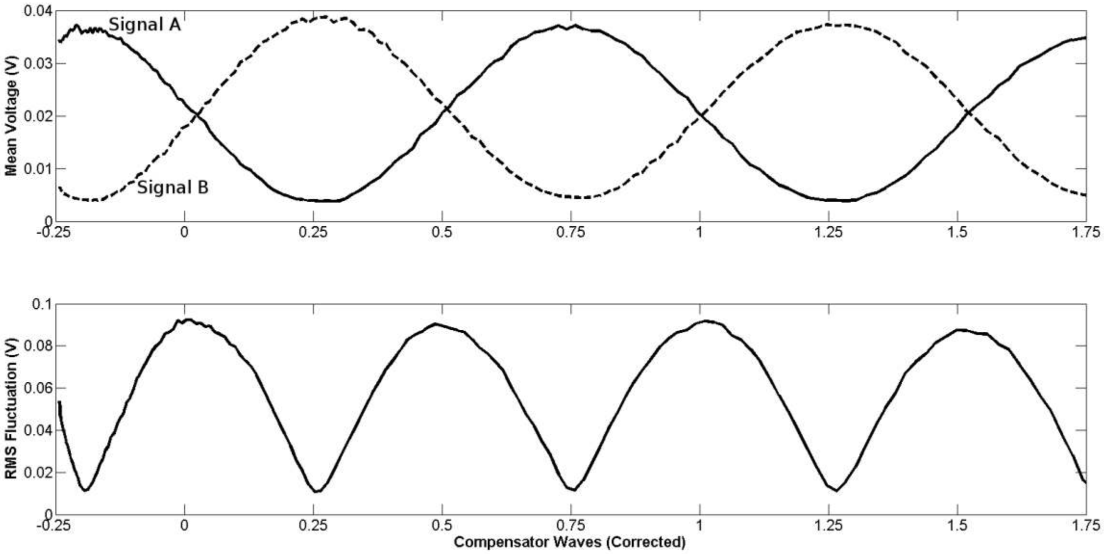

Figure 4.2: Outputs of both photodiodes as Berek compensator is adjusted. A helium jet provided a refractive disturbance to show the RMS signal response of the instrument as shown.

Here, the top plot shows the mean voltage from the outputs of the two photodiodes, while the bottom plot shows the RMS variation of the FLDI signal at each compensator setting. The horizontal axes of these plots is the compensator setting in units of wavelengths of retardance for the HeNe laser light used in this research. When one signal is adjusted so that its average phase corresponds to the 0 degree point on a sine curve, the other signal must correspond to the 180 degree point on a sine curve. The linearity of the interferometer's output is maximized at this setting, and the RMS fluctuation response to the refractive signal is also maximized, as expected from the theory from section 3.6.1.

4.3: Measurement of Beam Separation

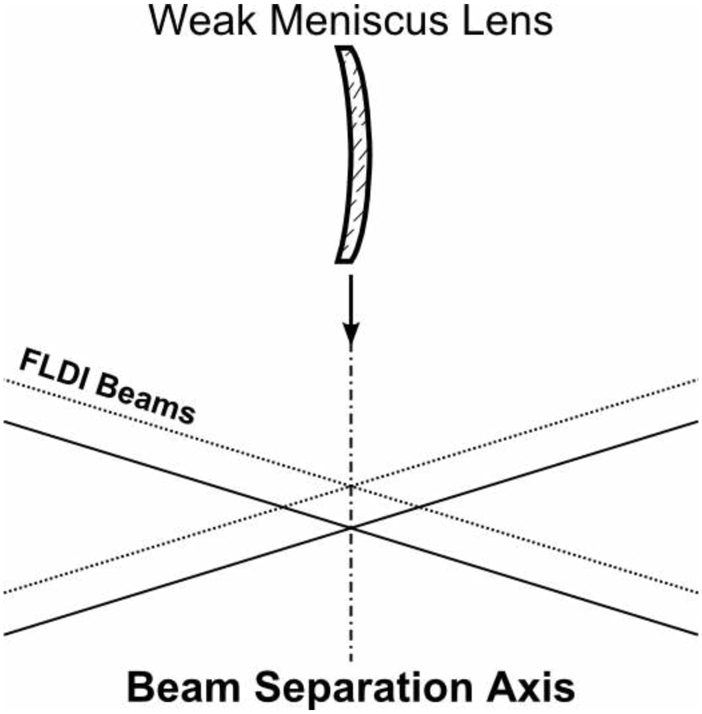

Figure 4.3: Beam separation measurement using a weak lens. The lens is translated through the point of best focus along the beam separation axis.

In order to quantify the output of the FLDI instrument, it is necessary to have a good estimate of the separation distance between the two beams as they pass through the test section. To measure this separation, a long focal length positive meniscus lens (10 m or longer) is used here as a "reference refraction." With such a long focal length the optical path difference of the lens is approximately parabolic. Since the interferometer behaves as a first-difference operator, the phase difference that it measures from the weak meniscus lens is a linear function with its zero point at the center of the lens. The response of the instrument is the sine of this phase difference signal.

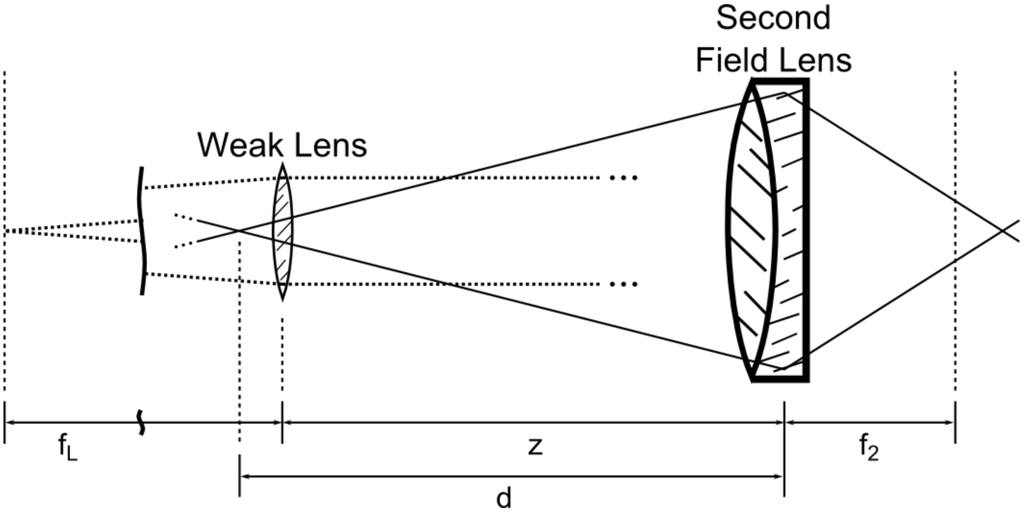

Figure 4.4: Geometry of calibration optics.

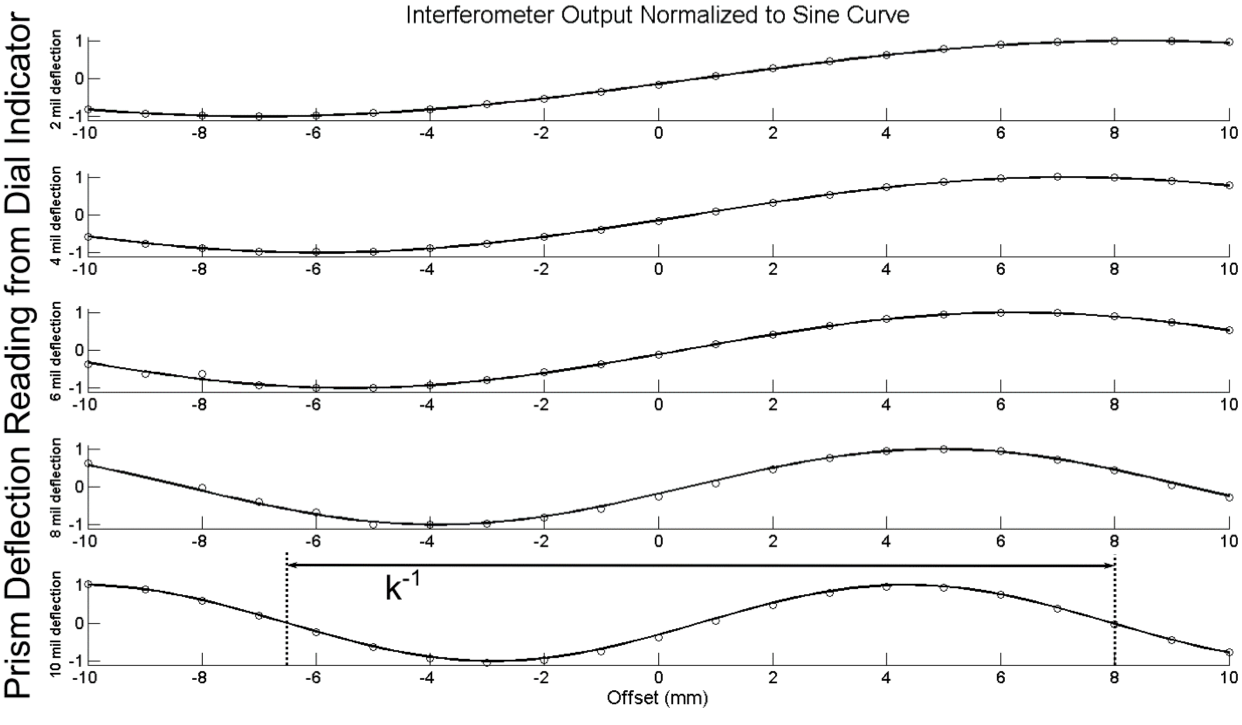

Figure 4.5: Interferometer calibration measurements using a 2 m focal length meniscus lens at various prism deflections. The result gives sine curves where their spatial frequency, *k*, is dependent on the focal length of the lens.

Measuring the output of the FLDI instrument as the weak meniscus lens is traversed along the beam separation axis results in a sinusoidal output. This sine wave's spatial frequency is proportional to the beam separation according to the following relationship:

$$\Delta x = \frac{k\lambda f_2 f_L^2}{z\left(f_2 + f_L - z\right)} \tag{4.1}$$

Here, Δx is the beam separation in meters, k is the spatial frequency of the sine wave, f_L is the focal length of the meniscus lens, f_2 is the focal length of the field lens, z is the distance from the second field lens to the meniscus lens, and λ is the wavelength of the laser beam. Note that when f_L is much greater than f_2, the above equation reduces to:

$$\Delta x = \frac{k\lambda f_2 f_L}{z} \tag{4.2}$$

This result is not exact, but from computer simulations in the ZEMAX optical modeling package it is found to be within a few percent of the correct value. The result of this modeling is shown in Fig. 4.6.

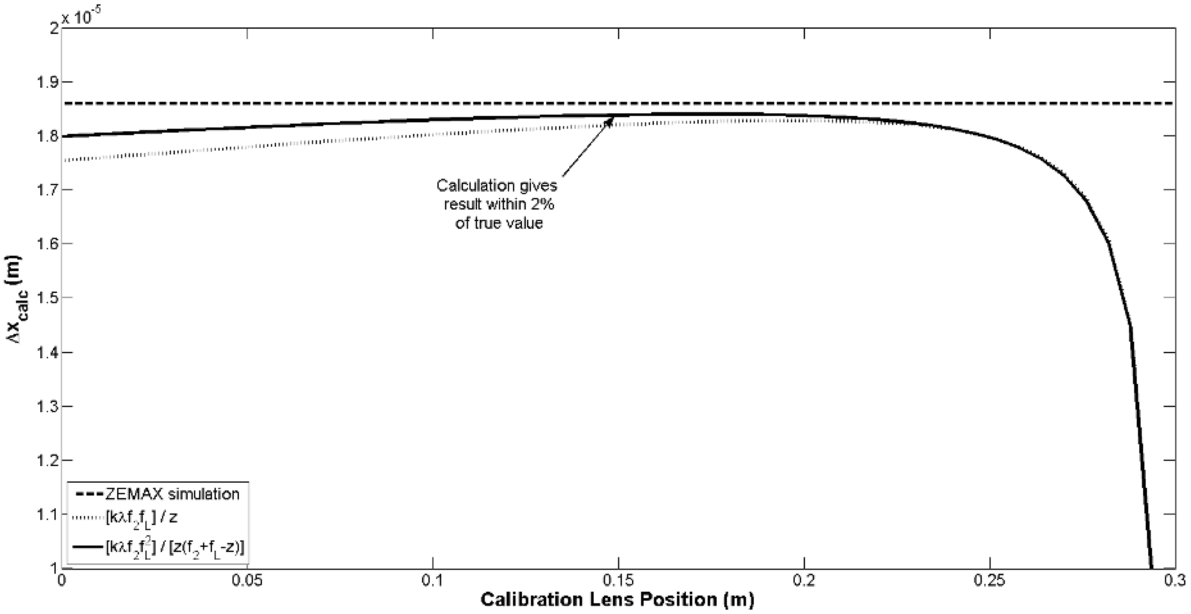

Figure 4.6: Comparison of true and approximate beam separation Δx using ZEMAX model for a 10 m focal length meniscus lens, with 50 mm focal length field lenses and a distance from the field lenses to best focus of 150 mm.

With very small beam separations and very long focal length meniscus calibration lenses used for the reference refraction, the frequency of the resulting sine wave may be too small to calculate accurately. Even with the 2 m focal length lens in Fig. 4.5 above, at 2 mils of prism deflection the interferometer does not sample a full cycle of the sine wave over the lens offset range used there. With a 10 m focal length meniscus lens at this setting the same offset range will give an approximately linear response, so the frequency of the resulting sine wave will be ambiguous and may not fit correctly. To eliminate this ambiguity the phase measurements can be performed at a range of Berek compensator settings. By sampling the FLDI output phase in a grid of compensator settings and lens positions, a sinusoidal surface results that can be easily fit to get an accurate measurement of the spatial frequency, as shown below in Fig. 4.7.

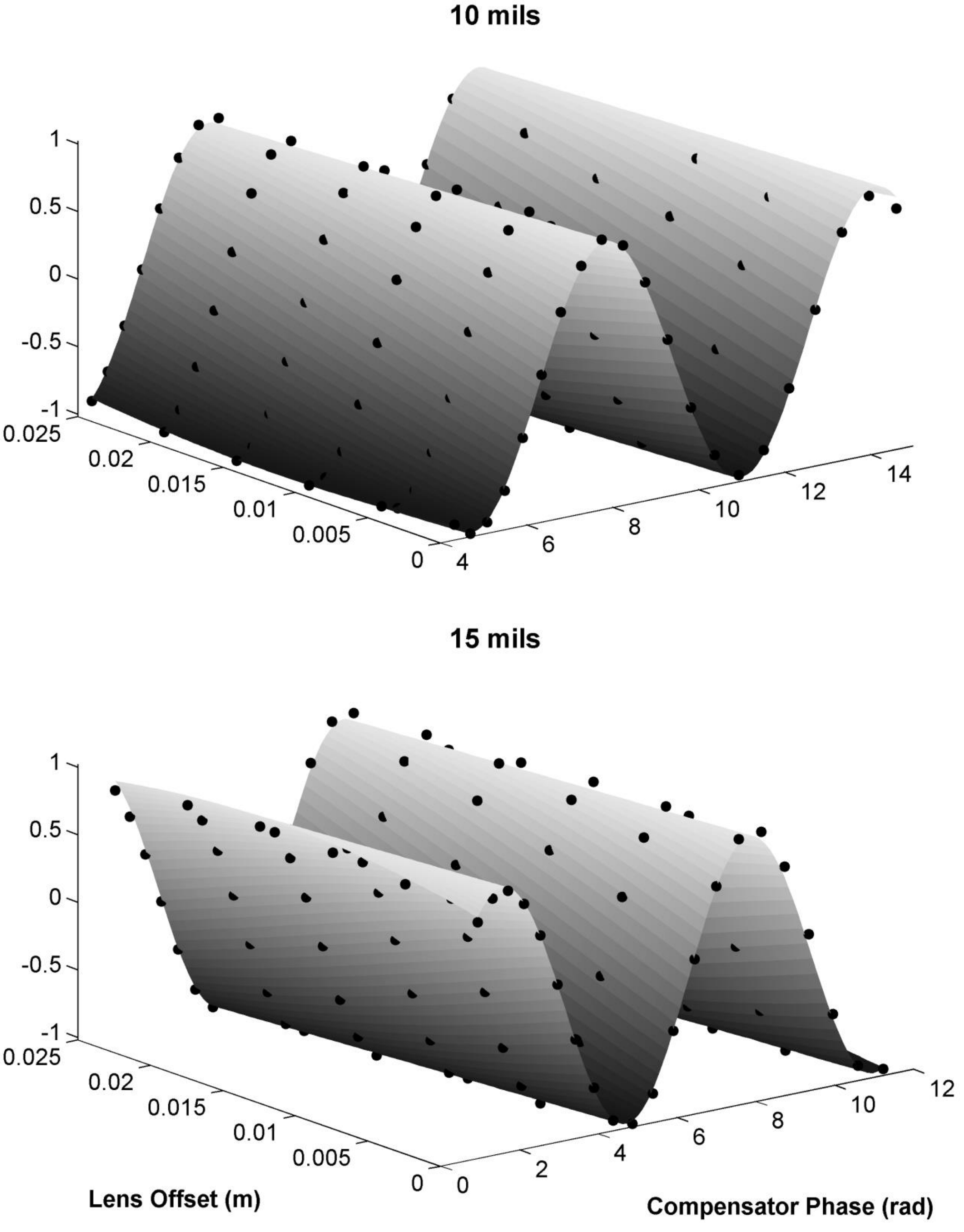

Figure 4.7: Grid sampling of lens offsets and phase compensator settings (in radians of phase retardation) showing reduction in frequency ambiguity, despite small prism deflections of 10 and 15 mils (1 mil = 0.001").

Despite the low spatial frequency of the result from the combination of the long-focal-length meniscus calibration lens and the small prism deflection, the grid method of calibration gives a repeatable and accurate measurement of the beam-separation distance, while sampling at a single Berek compensator setting fails to accomplish this goal.

A calibration of prism deflection to beam separation can be produced by performing this analysis across the full range of prism deflections of interest. Results from the calibration of the Sanderson prisms used for this research are shown in the Results section 5.22, with a fit of prism deflection to beam separation plotted in Fig. 5.9.

4.4: Data Acquisition

The data acquisition system of the FLDI instrument is set up to measure the output from both s- and p-polarization photodiodes on two separate channels. The sample rate should be at least 2 megasamples per second per channel (2 MS/s-ch) in order to benefit from the inherently-high frequency response of the FLDI optical instrument, as this allows measurement of turbulence spectra up to 1 MHz bandwidth. Benchtop tests with the FLDI instrument have shown frequency response to exceed 4 MHz with proper photodiode and termination resistance choice, as explained in section 4.5 below.

Additionally, the bit depth of the measurement should be as high as possible in order to maximize the dynamic range of the digitizer. While the analog signal is continuous, discretization of this signal by digitization restricts it to a limited number of possible values, and this may introduce quantization noise if the bit depth is too small. Small-amplitude fluctuations may not appear in the sampled signal in this case. Because quantization is performed over the gain range of the data acquisition system, this range should also be set as close as possible to the maximum and minimum voltages expected from the *s*- and *p*-polarization photodiodes. A good baseline approach is to use the voltages at the maximum and minimum of the sine curves measured when the Sanderson prisms are adjusted. Neglecting the noise floor of the electronics, the quantization-limited dynamic range of the digitizer (signal to quantization noise ratio, *SQNR*) is defined by the equation

$$SQNR = 20\log_{10}\left(2^{Q}\right) \tag{4.3}$$

where *SQNR* is in dB, and Q is the bit depth of the digitization. This means that the smallest amplitude fluctuation that the digitizer can adequately measure is *SQNR* dB below the maximum amplitude of the gain range of the digitizer. Quantization error can also be reduced by oversampling, where the sample rate of the data acquisition is increased, but the extra samples are averaged with the original samples to regain the original sample rate. Multiplying the sample rate by a factor of 2^{2n} achieves an increase in effective bit depth by n bits per sample. This method requires much more sample memory for a relatively-small improvement in quantization noise, so it should be avoided if possible.

It is important to ensure that the electronics and any preamplification used for the *s*- and *p*-polarization detectors produce as little noise as possible. At some point the gains in dynamic range from improving quantization error encounter the electronic noise floor, after which no further improvement can be made in the data acquisition. High-quality shielded coax cables should be used between the photodiodes and data acquisition system, and everything that can be run from battery power instead of AC mains should do so. Particularly when the interference signal is very low amplitude, the electronic noise floor can significantly reduce the quality of frequency spectra calculated from the instrument.

4.5: Measurement of Photodiode Frequency Response

In addition to the frequency response effects of the FLDI optics, the frequency response of the photodiodes used to measure the interferometer signals must also be considered. The voltage generated by a photodiode is directly proportional to the termination resistance, R_L, used to convert the photodiode current to a measurable voltage. The frequency response, on the other hand, is inversely proportional to this resistance. Both of these effects must be balanced to make successful measurements, as using too low a termination resistance to avoid frequency response problems may not provide adequate signal amplitude over the electronic noise floor. Meanwhile, too high a termination resistance will give a high signal amplitude, but the low frequency response of the photodiodes may limit the maximum signal frequency detectable above the noise floor in measured spectra.

The junction capacitance of photodiodes, stray capacitance in cabling and the measurement equipment, and impedance mismatch between the cables and termination resistor all reduce the frequency response of the photodiodes. As with the FLDI spatial filtering, the frequency response effects from the photodiodes may be deconvolved from the measured signals if they are known.

A simple method to measure the transfer functions of the photodiodes is to pulse an LED with a square wave input and measure the voltage of the photodiodes in response to this LED. Reduced frequency response manifests itself as rounded off corners from the original square wave in the photodiode response signal. A diagram of how this calibration is performed is shown in Fig. 4.8.

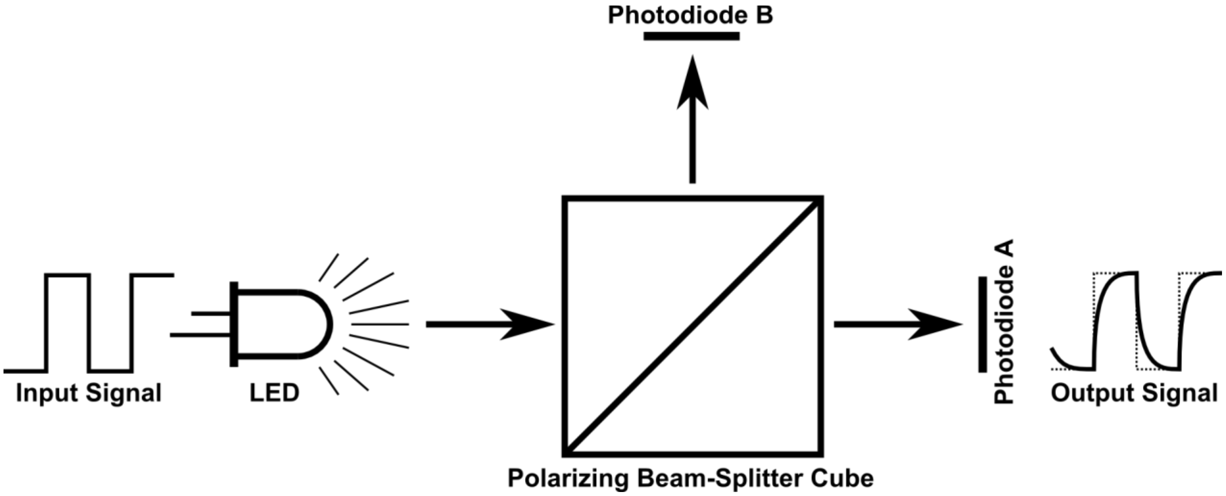

Figure 4.8: Diagram of the photodiode calibration method using square-wave testing.

The Fourier transform of a square wave is an infinite series of delta functions at odd multiples (harmonics) of the square wave's fundamental frequency. These peaks continue on infinitely because very-high frequencies are needed to achieve the sharp edges of a square wave. Low-pass filtering due to reduced photodiode frequency response causes the high-frequency content of the square wave input to roll off, causing the rounded-off signal seen in the above diagram.

To perform this calibration, a square wave of a known frequency (such as 1 kHz) is applied to the LED, and the voltage at the LED and the output signals from the two FLDI photodiodes are measured by the data acquisition system. Fourier transforms of both signals are then calculated, and the amplitudes of the Fourier transforms at each odd multiple of the square wave frequency are extracted from the resulting spectra.

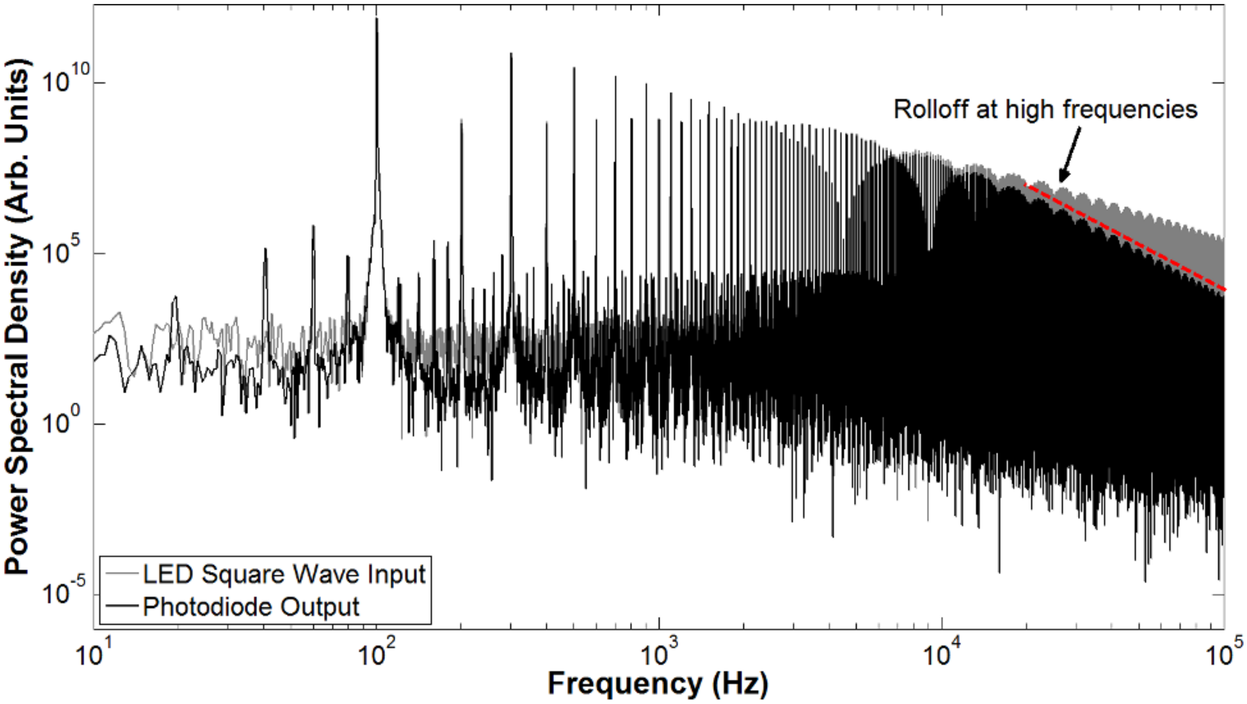

Figure 4.9: Example power spectral density plot for square wave testing of the photodiodes used in this research. The square wave frequency used for this plot was 100 Hz, and the photodiode was terminated at R_L = 50 kΩ to dramatically limit frequency response.

The ratio of the output signal to the input signal at each harmonic represents the transfer function of the photodiode at that frequency. Unamplified, reverse-biased photodiode transfer functions are typically well modeled by simple first-order low pass filters, so the method used for this research fits this form of transfer function (Eq. 4.4) to the spectra produced by this square-wave testing.

$$H(f) = \frac{1}{\sqrt{1+[f/f_c]^2}} \tag{4.4}$$

Here, $H(f)$ is the transfer function of the photodiode, f is the frequency of the signal in Hz, and f_c is the cutoff frequency of the filter estimated by the fitting process. Multiple tests at several different square wave frequencies are combined to improve the accuracy of the fitting. The results of these fits to square wave tests of both FLDI photodiodes used in this research are shown in Figs. 4.10-14. The effect of termination resistance on frequency response is easily visible beyond

1 kΩ, while there is essentially no frequency response loss in the frequency range of interest at a termination resistance of 50 Ω. The effect of the limited frequency response of the photodiodes can be removed by filtering the photodiode signals by the inverse of the first-order low pass filter described above.

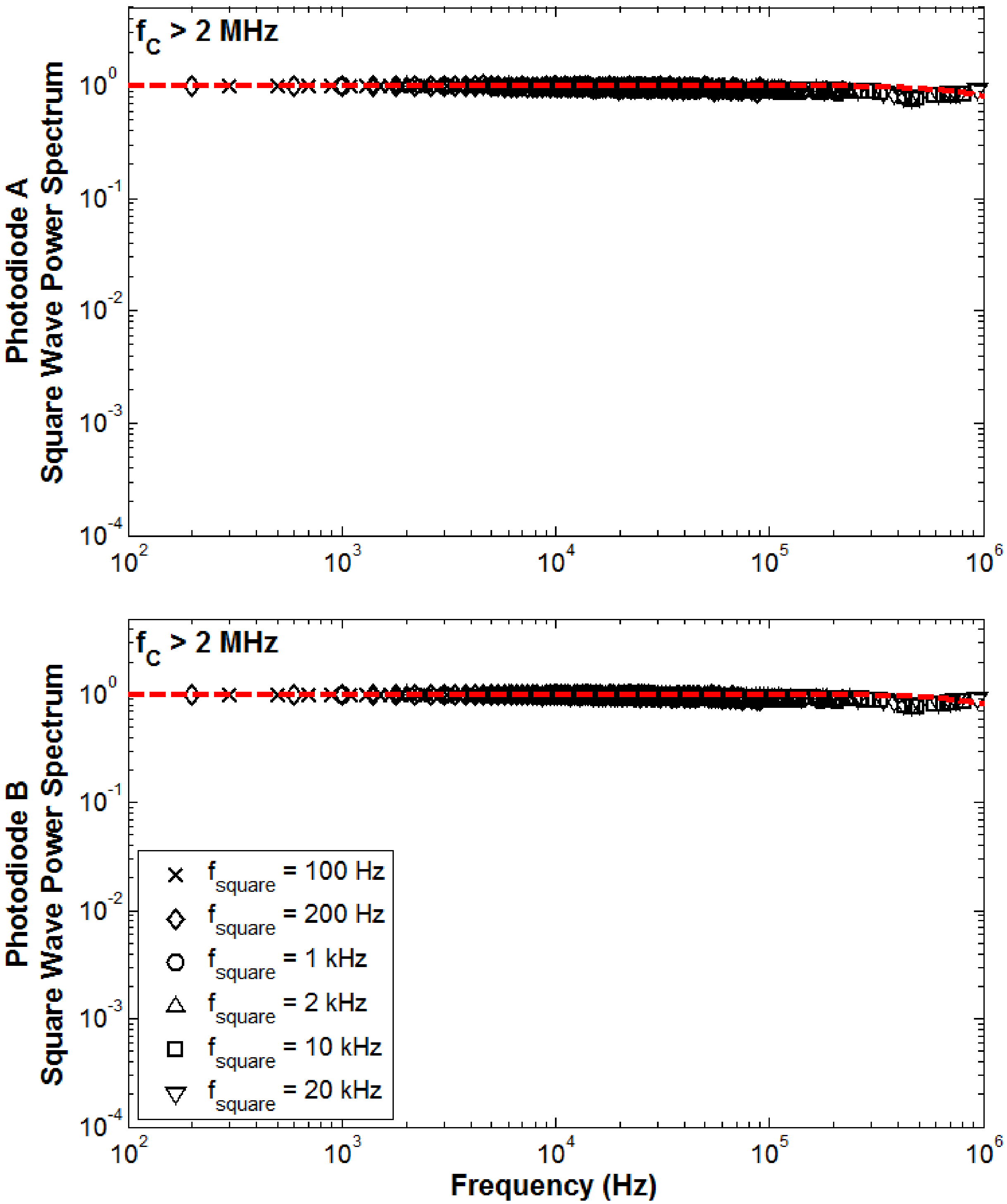

Figure 4.10: Square wave testing of FLDI photodiodes at R_L = 50 Ω. Data from tests at 100 Hz to 20 kHz are shown, with the dashed line showing the transfer function fit to these data using Eq. 4.4.

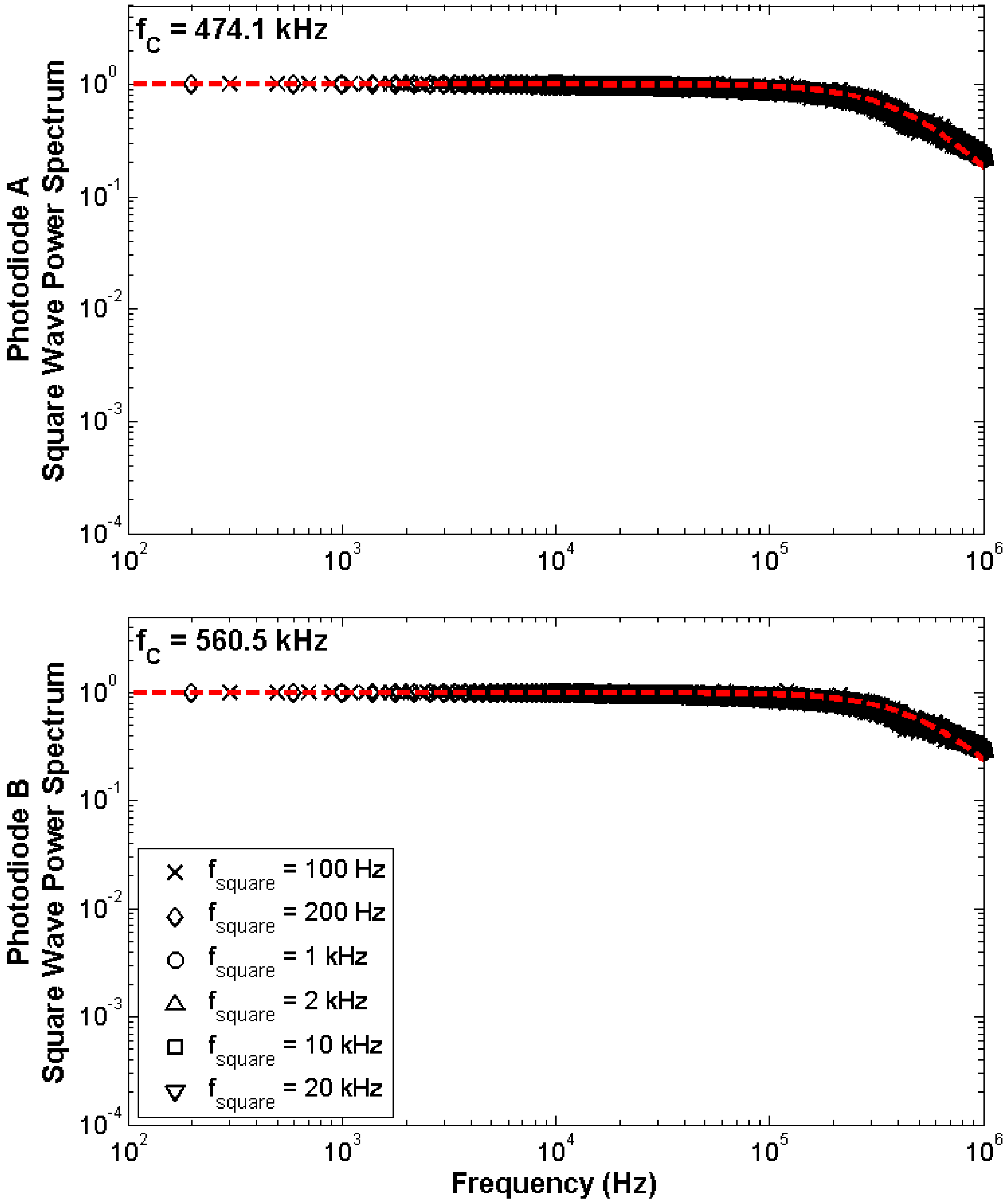

Figure 4.11: Square wave testing of FLDI photodiodes at R_L = 1 kΩ. Data from tests at 100 Hz to 20 kHz are shown, with the dashed line showing the transfer function fit to these data using Eq. 4.4.

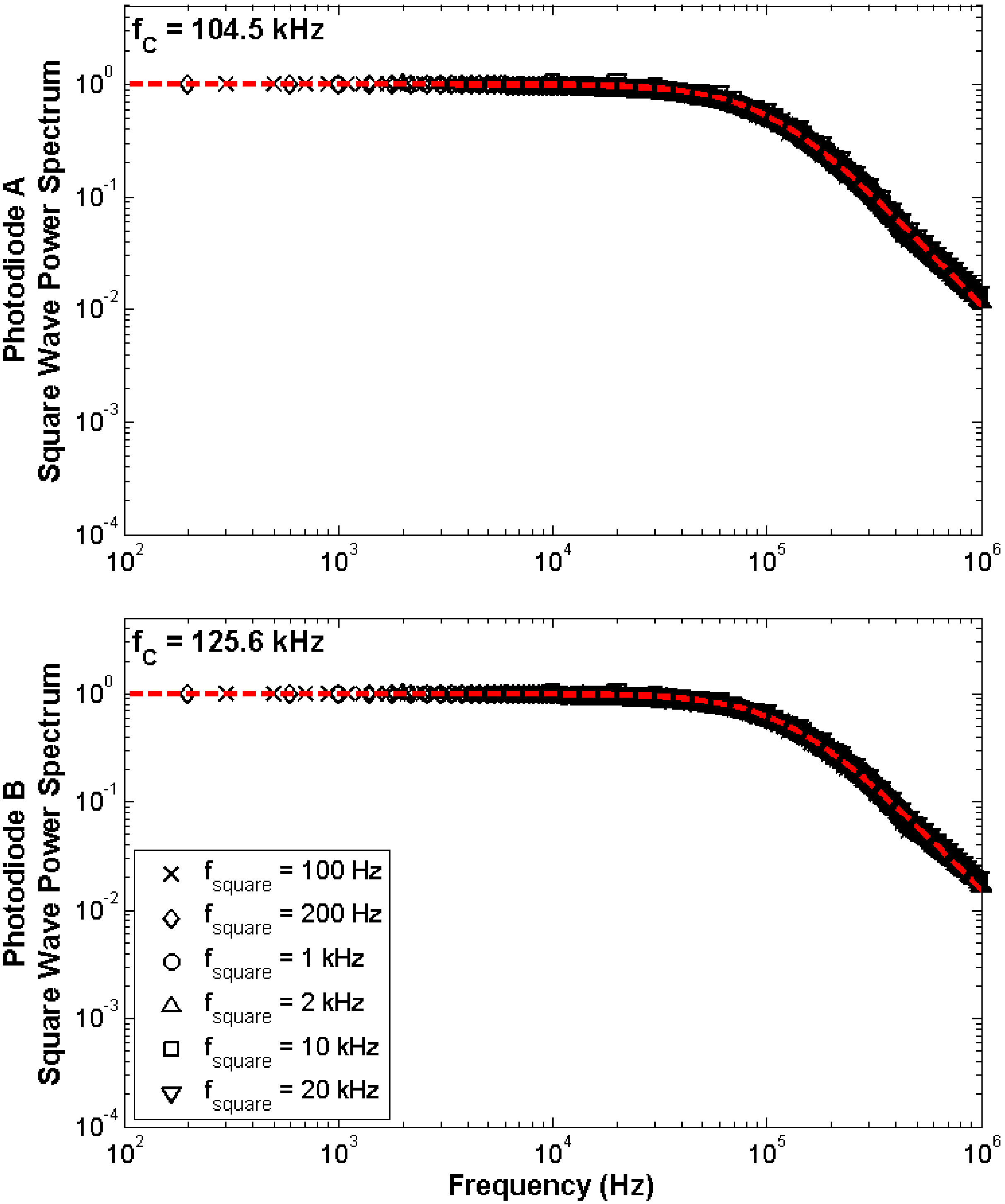

Figure 4.12: Square wave testing of FLDI photodiodes at R_L = 5 kΩ. Data from tests at 100 Hz to 20 kHz are shown, with the dashed line showing the transfer function fit to these data using Eq. 4.4.

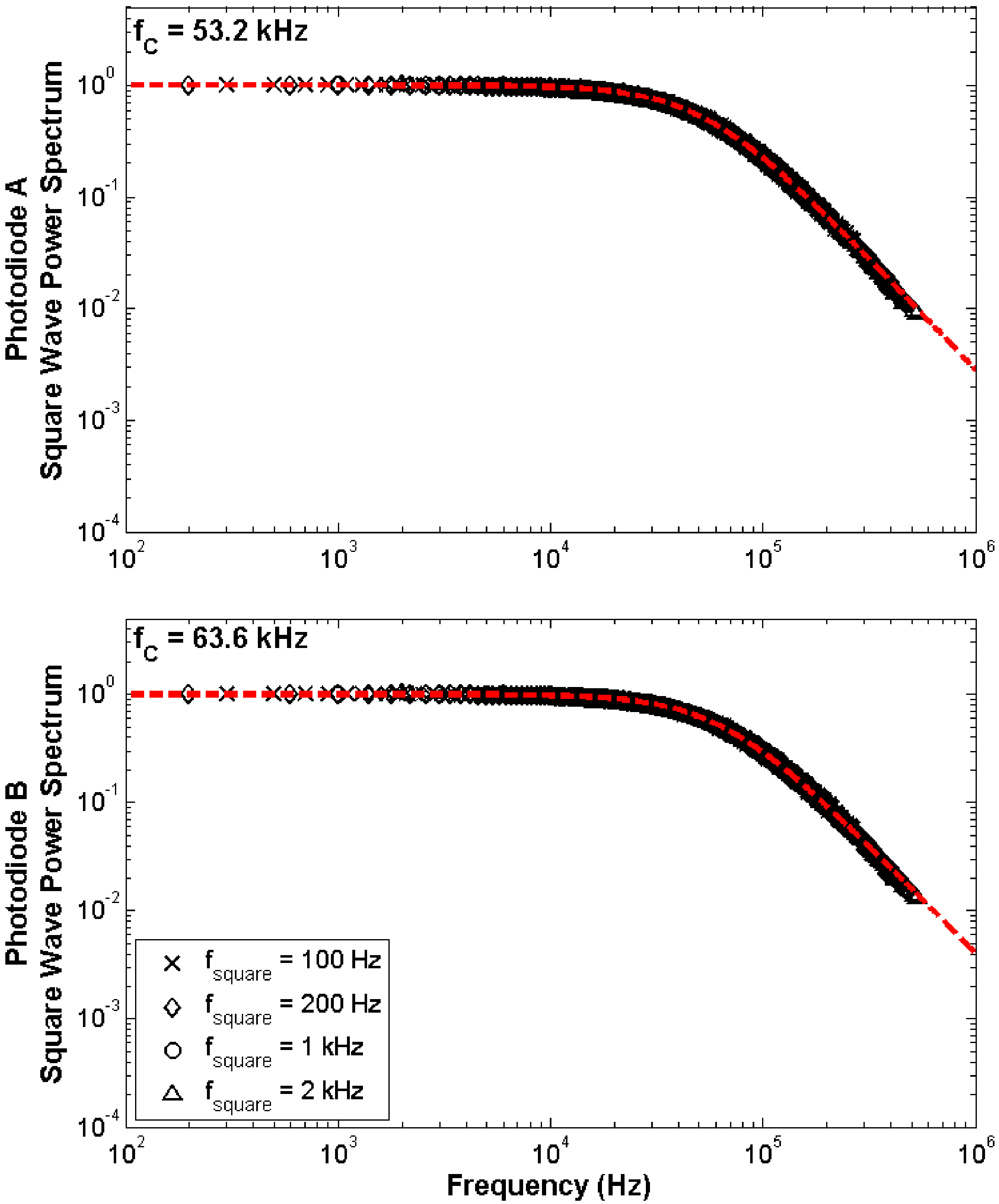

Figure 4.13: Square wave testing of FLDI photodiodes at R_L = 10 kΩ. Data from tests at 100 Hz to 20 kHz are shown, with the dashed line showing the transfer function fit to these data using Eq. 4.4.

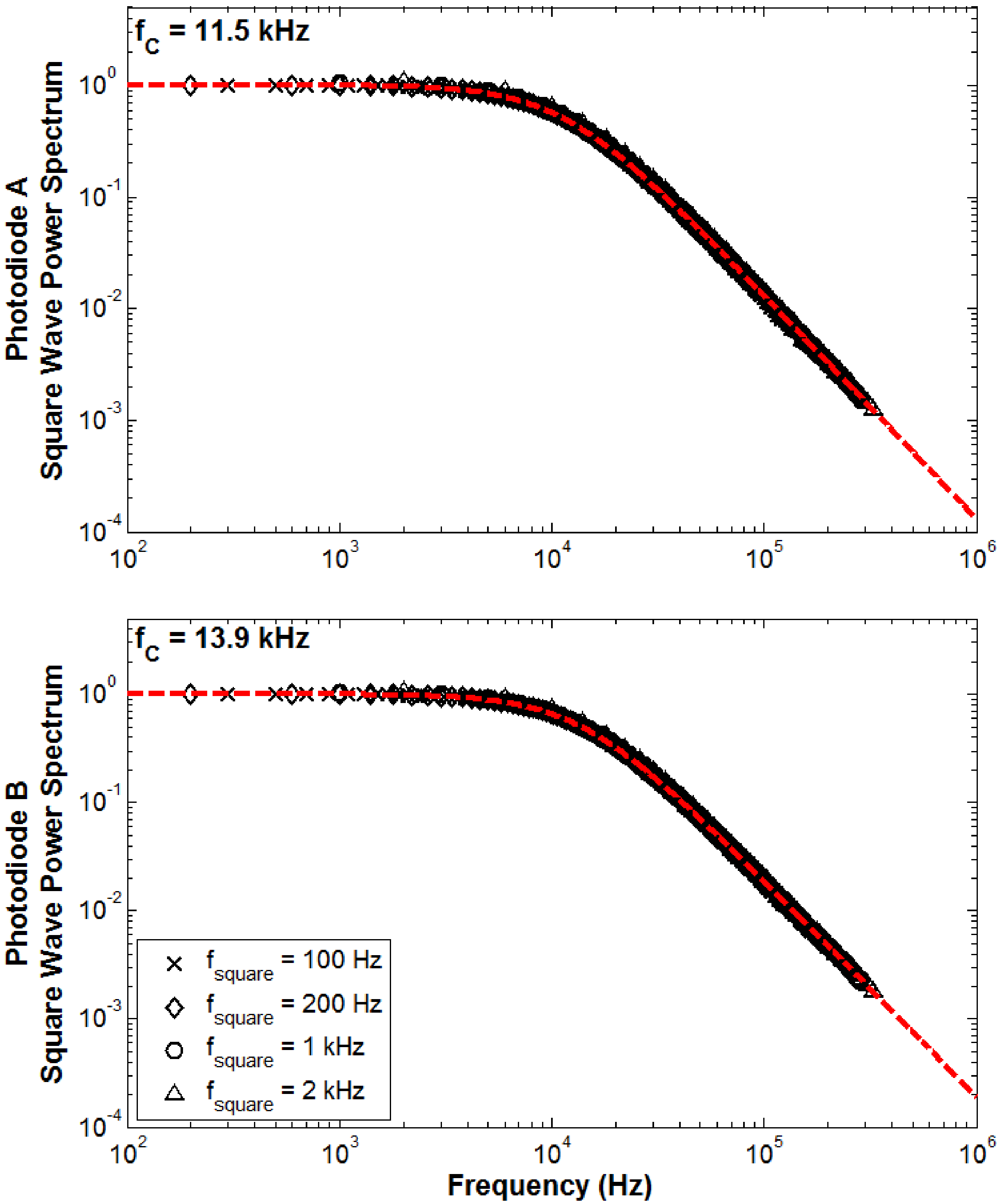

Figure 4.14: Square wave testing of FLDI photodiodes at R_L = 50 kΩ. Data from tests at 100 Hz to 20 kHz are shown, with the dashed line showing the transfer function fit to these data using Eq. 4.4.

4.6: *Processing of FLDI Instrument Data*

Raw data from the data acquisition system are imported into MATLAB, with the *s*- and *p*-polarization photodiode channels saved as data streams A and B. As the signals are 180 degrees out of phase of one another, it is arbitrary which channel is saved as what variable.

The FLDI photodiode difference signal is found by calculating $F_{AB} = (A - B) / (A + B)$. This result must then be normalized by the maximum and minimum limits of the interferometer's response. These limits are found by adjusting the Berek compensator in either direction from the setting used for testing and noting the maximum and minimum values of $(A - B) / (A + B)$ attained, which are a measure of the interferometer contrast mentioned in section 4.2. This normalization is calculated as follows:

$$F_{AB,norm} = 2\left(\frac{F_{AB} - F_{AB,min}}{F_{AB,max} - F_{AB,min}}\right) - 1 \tag{4.5}$$

The result of this normalization is a signal clamped within a range of -1 to 1, representing the sine of the measured phase difference between the two FLDI beams. Ultimately, the desired signal from the FLDI instrument (from Eq. 3.55), $\Delta\varphi_A$ - $\Delta\varphi_B$, is calculated by Eq. 4.6.

$$\Delta\varphi_A - \Delta\varphi_B = \sin^{-1}\left[2\left(\frac{F_{AB} - F_{AB,min}}{F_{AB,max} - F_{AB,min}}\right) - 1\right] \tag{4.6}$$

This phase difference signal is then processed, using the technique explained in the Theory section of this thesis, to get estimates for RMS density fluctuation levels and estimates of the spectra of density turbulence in surveyed flows.

Chapter 5: Results

In this chapter, the methods developed in this thesis to characterize the FLDI instrument and its components are validated experimentally. The performance of the instrument is compared with published data from the literature as well as with hot-wire anemometry and crossed-beam schlieren measurements.

5.1 Signal/Noise Ratio Issues with Crossed-Beam Schlieren

As discussed in the introduction, early research for this thesis considered the crossed-beam schlieren (CBS) technique for optical turbulence measurements in a core flow despite irrelevant turbulence in a surrounding boundary layer. As the research progressed, however, it became clear that the CBS instrument did not have adequate rejection of undesired signals, and its performance suffered dramatically when trying to detect small density fluctuations, resulting in the switch to the FLDI technique.

This is seen in Figs. 5.1a,b & 5.2a,b, where multiple-beam-displacement CBS cross-correlations were performed at a range of displacement distances downstream of a 1.83 mm diameter nozzle producing a helium jet at stagnation pressure P_0 = 30 psia (207 kPa). The blue lines are the raw cross-correlation signals at each displacement location. The red lines are a Gaussian fit to the correlation peaks, giving uncertainty values. The black lines show the point of maximum correlation. In Fig. 5.1a, which is fairly close to the nozzle exit (x/D = 8.2), the correlation signal at each beam displacement is quite strong, with easily discernable, sharp peaks. In this case, the convective velocity has a small uncertainty, and is found to be 271.2 +/- 9.7 m/s, an uncertainty of about 4%. In Fig. 5.2a, which is relatively far from the nozzle exit (x/D = 54.7), the helium has mostly mixed out with the surrounding air, significantly reducing the refractive index difference between the jet and the ambient conditions. This results in weak correlation signals, giving a high uncertainty: the convective velocity is found to be 33.8 +/- 9.3 m/s, an uncertainty of around 28%.

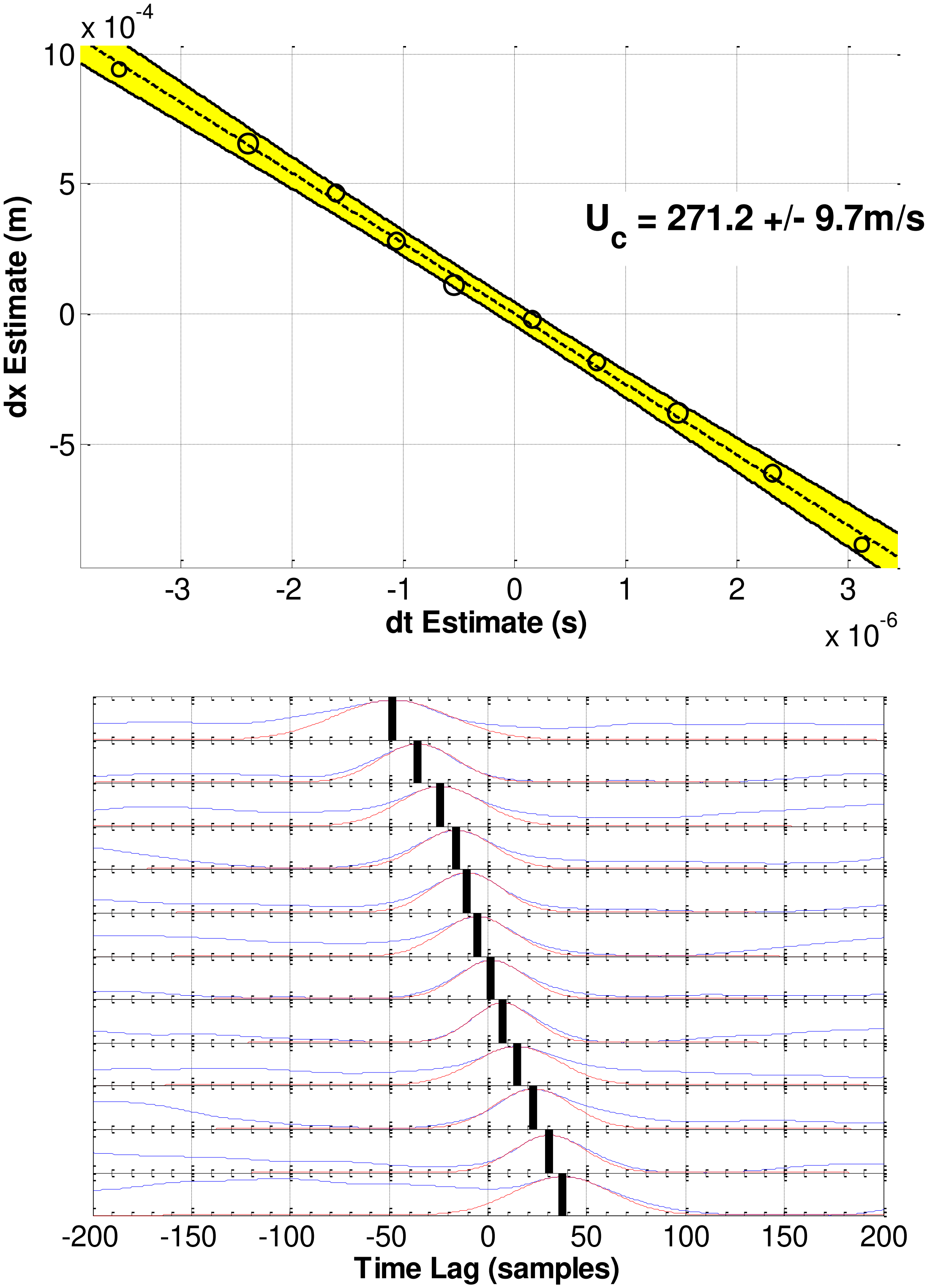

Figure 5.1a,b: Example of multiple-beam-displacement correlation measurements in a P_0 = 30 psia helium jet at 8.2 diameters downstream of the nozzle exit.

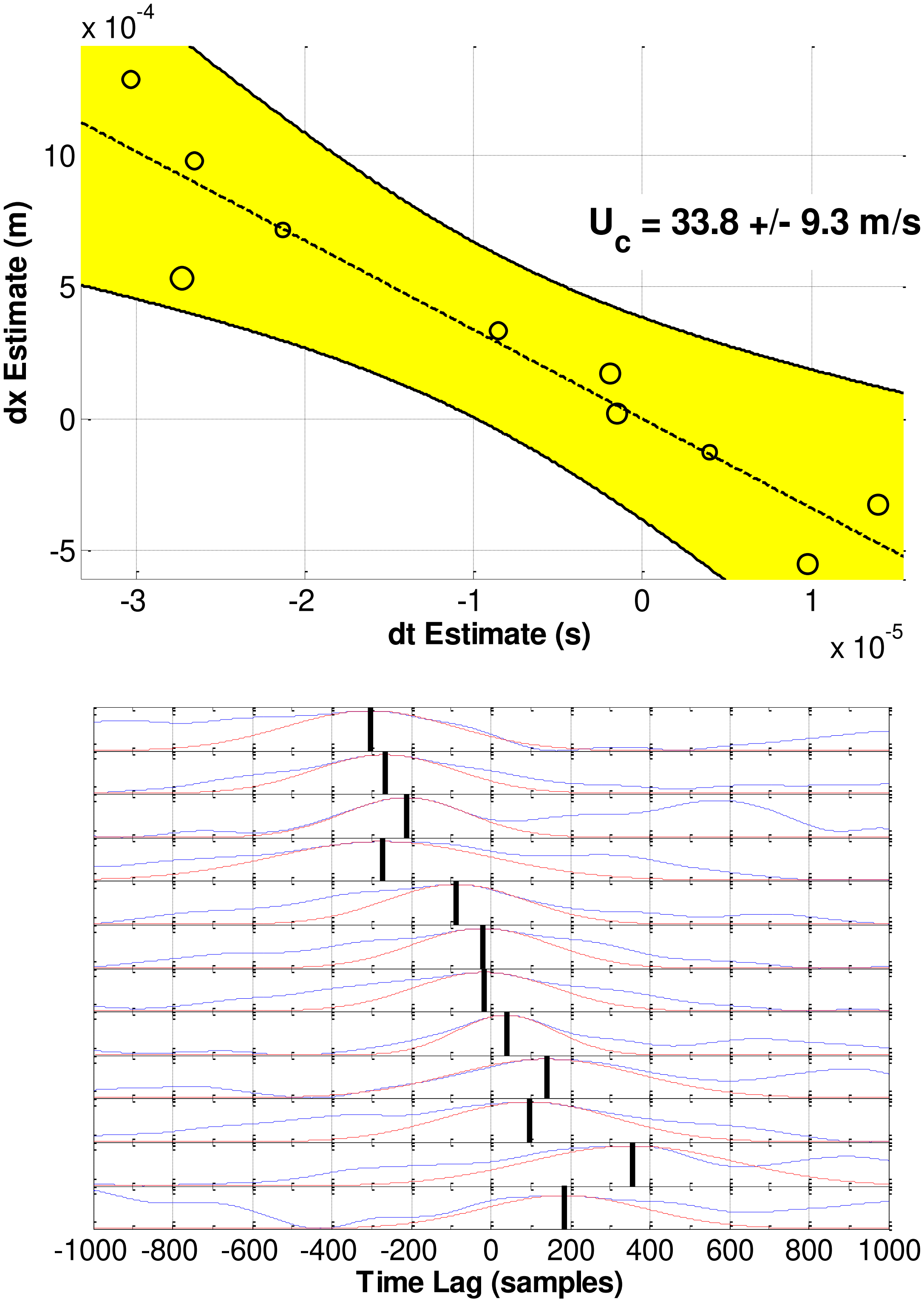

Figure 5.2a,b: Example of multiple-beam-displacement correlation measurements in a *P_0* = 30 psia helium jet at 54.7 diameters downstream of the nozzle exit.

The refractive index of helium at 0 °C and $\lambda = 632.8$ nm is 1.000035, substantially smaller than the refractive index of air at the same conditions: 1.000277. With such a large difference in refractive indices, the failure of the CBS instrument to achieve adequate correlation signals in the downstream region of the jet, even accounting for mixing out of the helium gas into the surrounding air, cast doubt on its chances of success for significantly weaker signals.

A related difficulty arises if one attempts to use hot-wire anemometry to independently measure helium-jet turbulence in air. Because of the large difference in thermodynamic properties between helium and air, a helium-air jet is difficult for hot-wire anemometry, where the difference in heat transfer properties of the gases causes significant deviations in the spectral behavior of the anemometer. An air jet in air is much better to use for this reason, however it must be heated or cooled by a large amount to match the refractive index difference between helium and air, to the point where the temperature is likely no longer a passive scalar quantity in the jet. For this reason, no CBS/HWA comparison is given here.

Tests of the CBS instrument were performed, however, at Mach 3 in the PSUSWT, both with crossing the beams within the core flow of the wind-tunnel test section as well as crossing them in the tunnel sidewall boundary layer at approximately $y/\delta \approx 0.5$. Images of windowed correlations (correlograms) for both of these cases are shown in Figs. 5.3a,b.

Note that, after the helium jet testing and before the PSUSWT testing of the CBS instrument, the windowed correlation scheme was changed to segment the data sets into many more ensembles than the scheme used to produce Figs. 5.1 and 5.2, thus improving the time resolution of the correlation scheme. Also, the visual representation of the cross-correlation result has been adapted to better present the data: the horizontal axis of the correlograms directly displays the lag time between the two beam signals, while the vertical axis shows the relative displacement of the two crossed beams in the flow direction. If a strongly-correlated convecting signal appears in the measurement, the speed at which it convects downstream can be found by fitting a line to the visible trace of this signal, where the slope of the line represents its convective velocity.

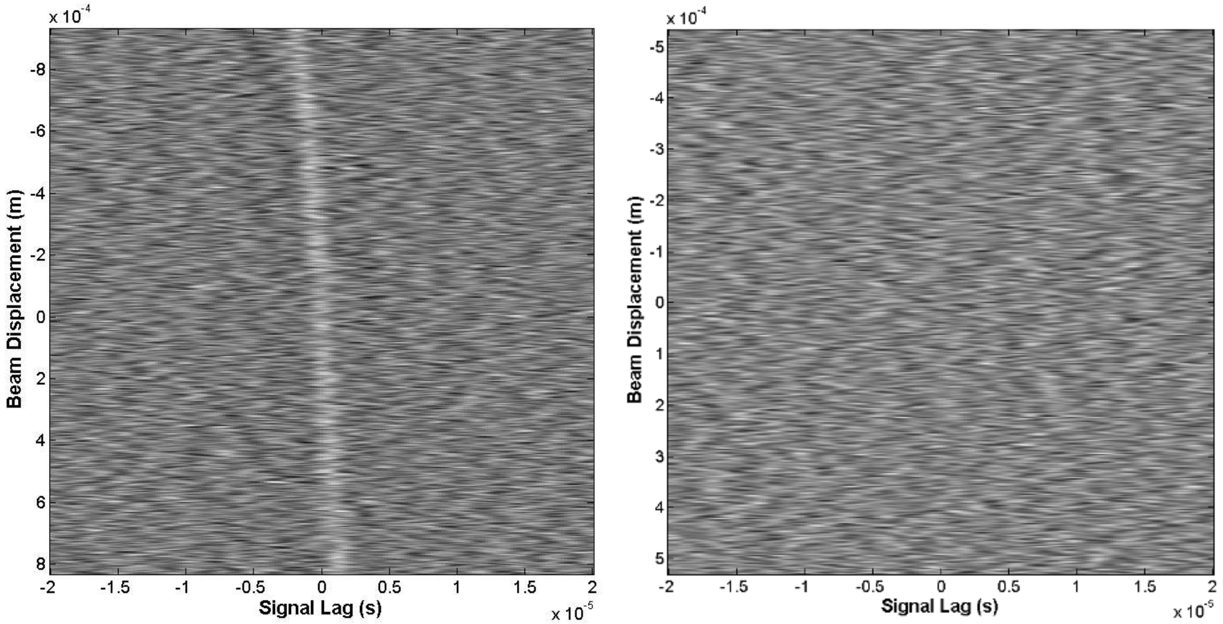

Figure 5.3a,b: Windowed correlations of crossed-beam signals in the core flow of the test section (on the right, Fig 5.3b) and in the boundary layer (on the left, Fig. 5.3a). Noise in the correlations can be clearly seen in the background. The instrument was not able to resolve a correlated signal in the core (a), while it was able to resolve a signal in the sidewall boundary layer (b).

A strong correlation was observed in the CBS signal when the beams were crossed in the sidewall boundary layer, but not in the test section core flow. The signal in the core proved to be weaker than the crossed-beam schlieren instrument is able to resolve, and its ability to reject the unwanted signal in the correlation from sidewall boundary layer “noise” is inadequate, as evidenced by the lack of any discernable slope above the noise in the freestream correlogram (Fig. 5.3b).

The sensitivity of the correlation scheme is improved somewhat by “pre-whitening” the spectra of the input signals from the detectors through a numerical differentiation scheme for the first derivative. By doing this, the autocorrelation of each signal becomes more like a delta function typical of uncorrelated white noise, thus reducing incidental correlation between the two signals while maintaining spectral content that truly is correlated between both signals.

Additionally, the integral time scale of the undisplaced beam's autocorrelation (an example of which is shown in Fig. 5.4) is calculated and used as a measure of the maximum time lag between the two signals within which the signals can be expected to remain correlated, which by Taylor's hypothesis of frozen turbulence is related to the maximum relative beam displacement over which they will remain correlated.

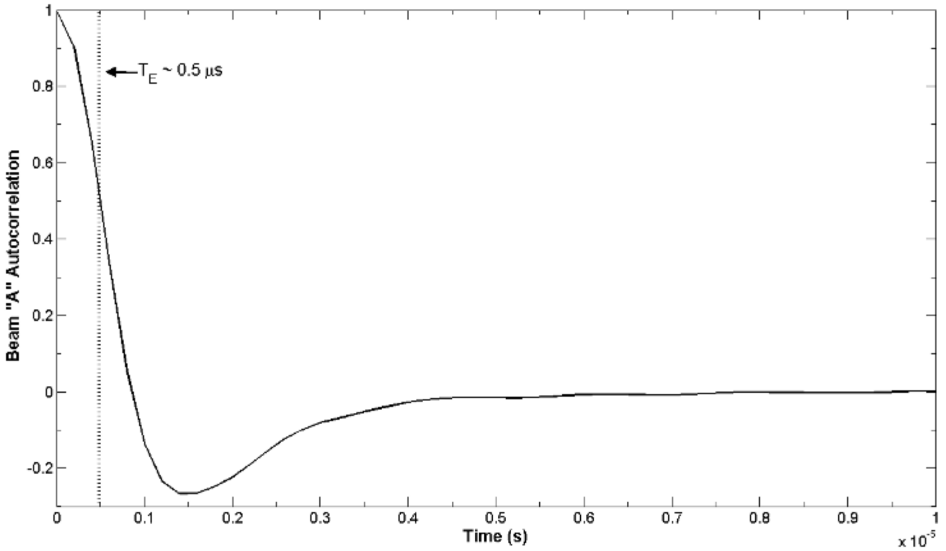

Figure 5.4: Autocorrelation of the undisplaced beam showing the calculated integral time scale of the boundary layer turbulence.

For the signals encountered in testing in the PSUSWT, the typical integral time scale is around 0.5 μs, which at a typical sampling rate of 10 MHz corresponds to a window of +/- 5 samples of lag within which the two beams' signals are expected to correlate strongly, and with no correlation expected beyond +/- 10 samples of lag. Knowledge of this window is used to filter the correlograms produced by the CBS data reduction scheme, since the integral time scale of the autocorrelation sets an upper bound for when the code should expect the signals to remain correlated. The magnitude of the correlation outside of this window is due to partially-correlated noise and ringing of the signals due to their periodicity.

First, a guess is made at the convective velocity of the signals. This guess is used to convert the beam displacement of each segment to an estimated time lag between the signals. A filter is produced by centering a Gaussian window with standard deviation equal to the integral time scale at the estimated time lag for each segment. The correlogram is then multiplied by this filter, and the best fit for the convective velocity to the data is found by maximizing the sum of the resulting image, as shown in Figs. 5.5a,b.

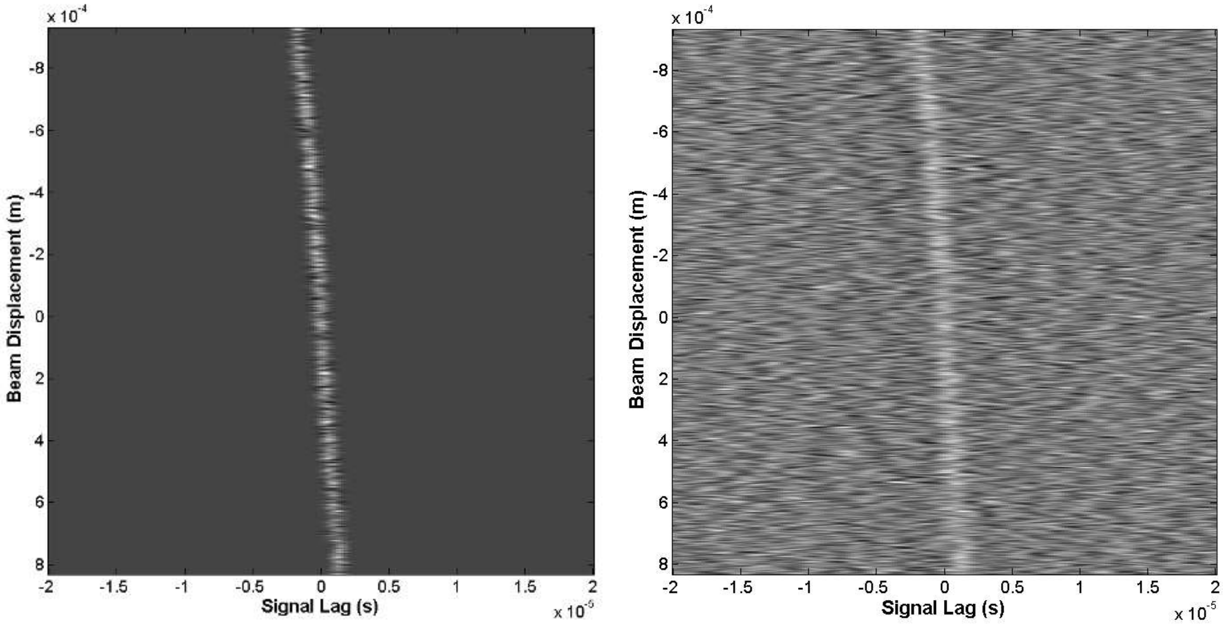

Figure 5.5a,b: Filtered correlation signal from Figure 5.3a (reproduced here on the right) where the background noise has been significantly reduced, clearly showing the correlated signal underneath the noise.

The convective velocity measurements of three runs at $M = 3.0$ using the CBS method yields U_c = 601, 611, and 574 m/s, in excellent agreement with the value of U_∞ = 598 m/s, based on M_∞ and

$\sqrt{\gamma R T_\infty}$. This shows that the CBS instrument is adequately sensitive to small-scale turbulent structures in the outer part of the boundary layer, which are convected at approximately the freestream velocity. The instrument is not, however, adequate for rejecting uncorrelated noise from the underlying signal for measuring properties in the freestream of a flow. This, ultimately, led to abandonment of the CBS technique in favor of the FLDI instrument which, as a "focusing" technique, by its nature rejects signals outside of a small depth-of-focus.

5.2 FLDI Characterization

To successfully implement the FLDI instrument, it is necessary to accurately measure the separation between the two interferometer beam foci and to quantify the "active" size of the FLDI instrument's focal volume. The adjustable Sanderson prisms used in this research, while significantly increasing the versatility of the instrument, further require careful calibration of prism deflection, or of prism strain, to the induced beam separation.

5.2.1 Calibration of Berek Compensator

For the beam separation measurement using the method presented in the Procedures chapter, the Newport 5540 Berek Polarization Compensator, used to shift the phase of the interferometer signal, must be carefully calibrated, or else the sinusoidal surface fit to the prism calibration data will be inaccurate. This would cause errors in the measurement of density fluctuations, ρ', thus precluding the accurate sensing of turbulence intensity by the FLDI instrument.

The phase shift of the compensator is set using the indicator wheel on the compensator. However, its response is highly nonlinear: the phase difference between settings 9 and 10 on the compensator, for example, is much less than the phase difference between settings 10 and 11.

The phase difference induced by the compensator is given by Eq. 2.1 from the Apparatus chapter of this thesis, and the tilt angle of the compensator window is calculated from the indicator setting on the compensator. According to the manual supplied with the compensator, this tilt angle can be found using the following equation, where I is the indicator setting.

$$\theta = \frac{\pi}{4} - \sin^{-1}\left(\frac{50.22 - I}{71}\right) \tag{5.1}$$

Using this calibration results in Fig. 5.6, where the dashed line represents the expected phase delay, while the open circles are the actual phase delay measured at indicator settings from 0 to 17 in steps of 0.1.

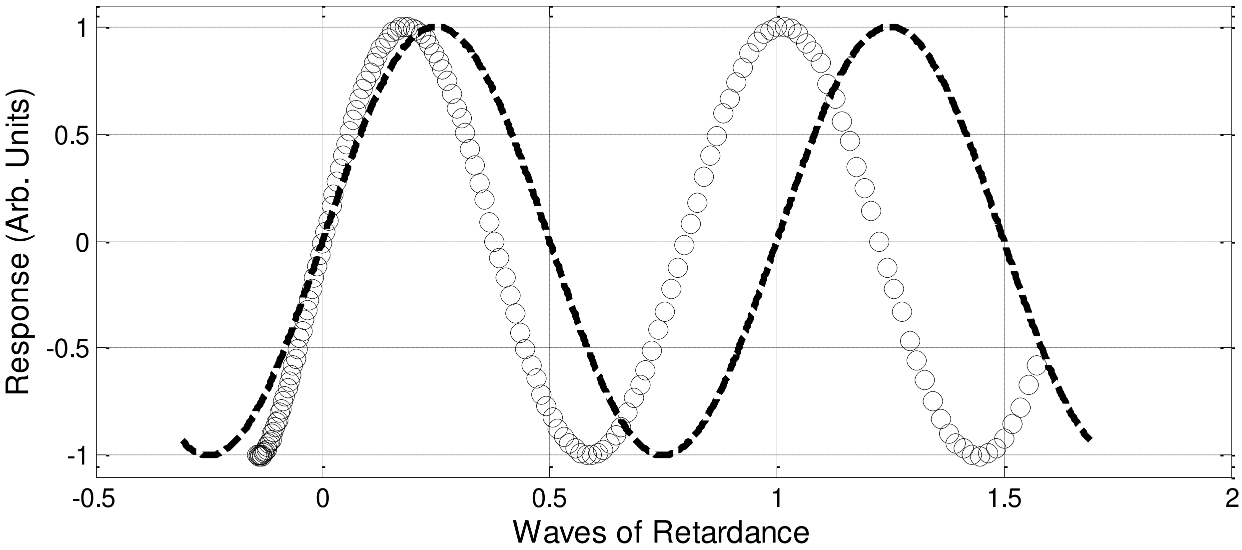

Figure 5.6: Compensator phase retardance using the supplied fit from Newport for the relationship of compensator setting to polarization retardance.

For unknown reasons, using the parameters supplied by Newport results in an extremely poor match between the expected and actual optical phase. This calibration must be corrected in order to use the lens calibration method for the birefringent prisms of the FLDI instrument presented here.

A least-squares minimization was performed to correct these parameters in order to get an accurate calibration of compensator setting to phase retardance, as shown in Fig. 5.7. The tilt angle calculation used to get this calibration follows the same form as that supplied by Newport, but with corrected parameters:

$$\theta = \frac{\pi}{4} - \sin^{-1}\left(\frac{46.89 - I}{69.19}\right) \tag{5.2}$$

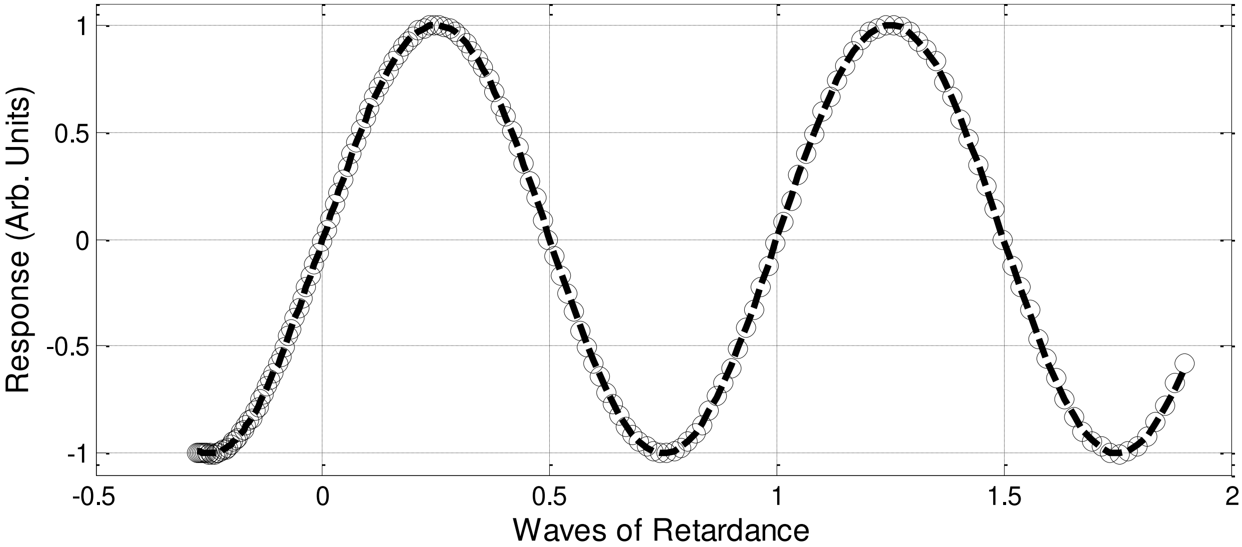

Figure 5.7: Calibration curve fit for Berek compensator using measured data, showing good agreement.

The corrected compensator calibration given above results in a very good match between expected and actual phase retardance.

5.2.2 Measured Beam Separation Compared to Simulation

A calibration of the Sanderson prisms used for this research was performed using a 10 m focal length positive meniscus lens as a standard refraction and two Nikon 50 mm *f*/1.2 camera lenses for the field lenses of the FLDI instrument. The prism deflection was varied from 0 to 45 mils (1 mil = 0.001" = 0.0254 mm) in steps of 5 mils, covering the full range of beam deflections that are practical with the prisms used here. The deflection is read directly from a Starrett dial gage indicator in units of mils.

Sinusoidal surface fits to the measured data are shown in Figs. 5.8a and 5.8b, and show excellent agreement between the measured points and the expected behavior of the prisms. The angles that the sinusoidal surface peaks follow between the lens position and compensator phase axes are used in the calculation from the Procedures chapter to determine the beam separation distance Δx in the test volume.

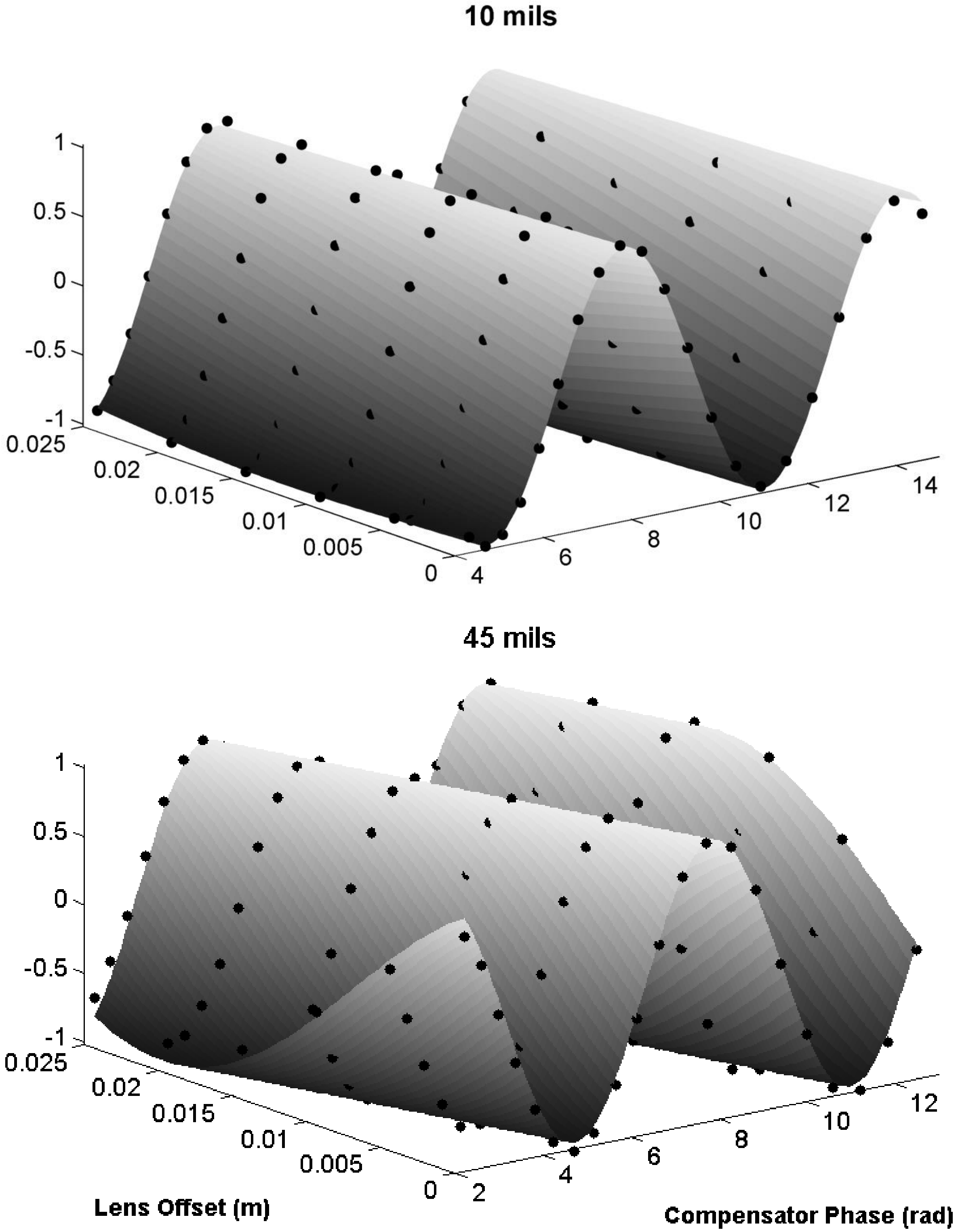

Figure 5.8a,b: Sinusoidal surface fits to prism calibration data at 10 and 45 mils deflection. The angle of the surface isocontours is used to estimate the beam separation, *Δx*.

A plot of the calculated beam separations as a function of prism deflection is shown in Fig. 5.9. A linear fit to these data is also shown, along with a fit using a slope calculated from theory using the parameters of the prisms given in the Apparatus chapter.

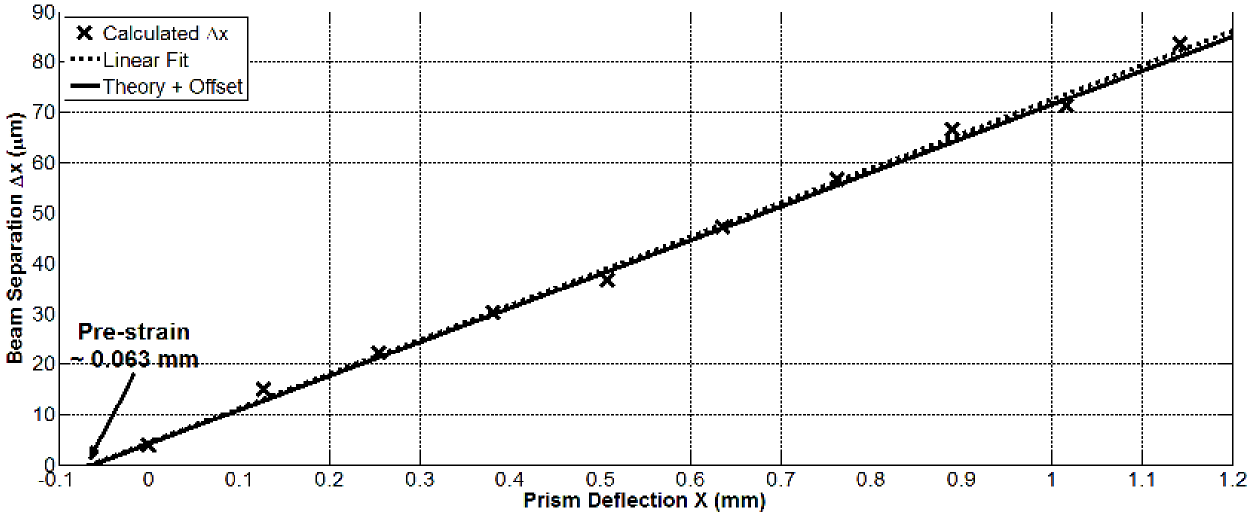

Figure 5.9: Beam separation as a function of prism deflection as calculated using the lens calibration method. The slope of the measured beam separations agrees well with the slope predicted by theory, although a small "pre-strain" is needed to adequately fit the data. There is likely a small permanent stress in the prisms from plastic deformation that cannot be removed by removing the adjustment screw.

The beam separation fit for these prisms is given in Eq. 5.3, where beam separation Δx is in meters, while prism deflection X is in millimeters:

$$\Delta x = 68.9 \times 10^{-6} \cdot X + 4.5 \times 10^{-6} \tag{5.3}$$

As evident in Fig. 5.9, the beam separation at zero prism deflection is nonzero. This could either be a result of residual strain in the prisms, or it could be from improper adjustment of the dial-gage indicator "feeler" on the base of the prism. Regardless of its source, this error highlights the need for calibration of the prisms for accurate calculation of beam separation. Ideally, the lens calibration method described in this thesis would be used prior to each test, or at least at the start of the day on which the instrument is used, however this is somewhat time consuming and should not be necessary if the ambient conditions of the lab room are consistent. Because of variation in the properties of the prism material due to environmental conditions, however, the prisms should be reset to zero strain and then loaded to the desired deflection if exposed to large changes in ambient temperature. This should reduce any effect of thermal expansion on the measured prism deflection.

Sanderson prisms are not yet available commercially, so they must be fabricated by the user. If they do become a commercial product, they should certainly be supplied with a detailed calibration like the one shown here.

The lens calibration method was also verified by comparison with beam deflections measured using the position-sensitive diodes used previously for the CBS instrument. The two polarized beams from one of the Sanderson prisms used for the FLDI instrument were split using a polarizing beam splitter cube mounted six inches from the prism, while the two position-sensitive diodes were mounted six inches farther from the prism, giving an optical path length of one foot (304.8 mm). This ensured that the beam deflection measured at the detectors was significantly larger than the noise. Measured angular deflections of the two beams are shown in Fig. 5.10 along with linear fits to these data.

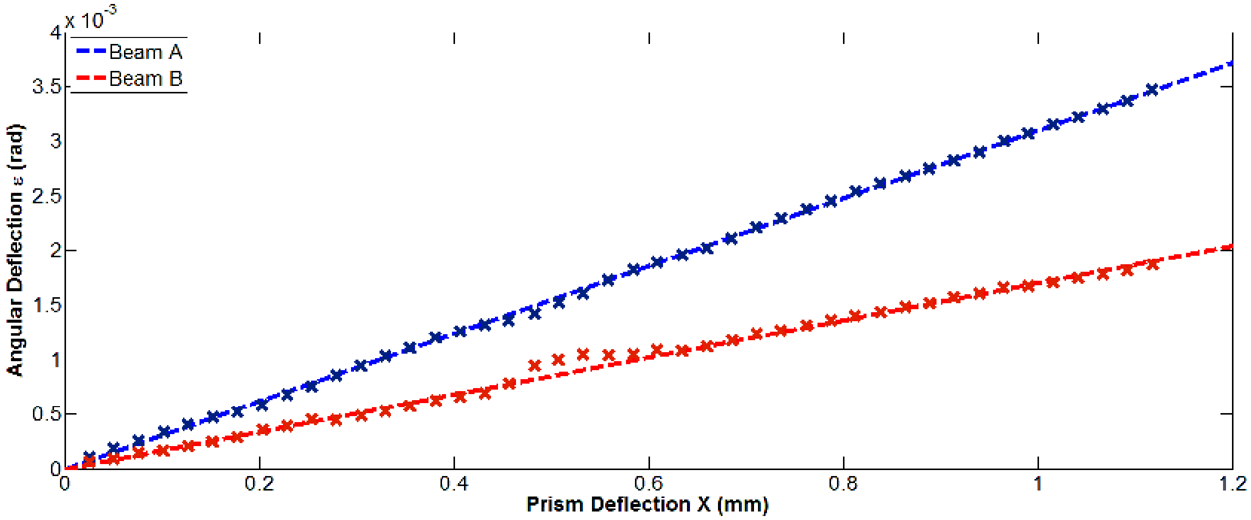

Figure 5.10: Angular deflection of the two polarized beams from one of the Sanderson prisms of the pair used in the FLDI instrument for this research, as measured by a position-sensitive diode.

Because it was not possible to take baseline beam separation measurements using this method, it is not possible to determine if any pre-strain is present in the prisms, however the relative angle of the beams can be used to estimate the beam separation as a function of prism deflection. Using the position-sensitive diode calibration, the beam separation Δx was found to scale as in Eq. 5.4:

$$\Delta x = 69.9 \times 10^{-6} \cdot X + C \tag{5.4}$$

Here, *C* is an undetermined constant. The slope of this fit, 69.9E-6 m/mm is very close to the slope found using the lens method, 68.9E-6 m/mm, further supporting the above calibration procedure. While this procedure was performed only for one of the two FLDI prisms used for the FLDI instrument, they were produced to identical dimensions and are made of the same material, so they should behave identically to one another.

The beam separation Δx is used not only for normalization of the FLDI signal, but also in determining the effect of beam separation on the measured turbulent spectrum, as detailed in the Theory chapter. The transfer function of the beam separation spatial filtering can be deconvolved from the measured spectra to get an estimate of the “true” turbulent spectrum. If the estimate of the beam separation is accurate, then the deconvolved spectrum from tests performed at any prism deflection should be identical to any other deflection for the same flow conditions.

Turbulence spectra from a 1 mm diameter round jet at P_0 = 20 psia (138 kPa) are presented in Figs. 5.11a and 5.11b, where Fig. 5.11a shows raw (but normalized) spectra, and Fig. 5.11b shows these spectra after deconvolution of the beam separation spatial filtering. The beam separations were calculated using the above fit for prism deflections of 10, 20, 30, and 40 mils. For these tests, the jet axis was perpendicular to the axis of beam separation, so the beam separation spatial filtering transfer function for the case shown in Fig. 3.19 was used here. The resulting spectra show excellent agreement with one another, and demonstrate the concept of deconvolution of the spatial filtering transfer functions.

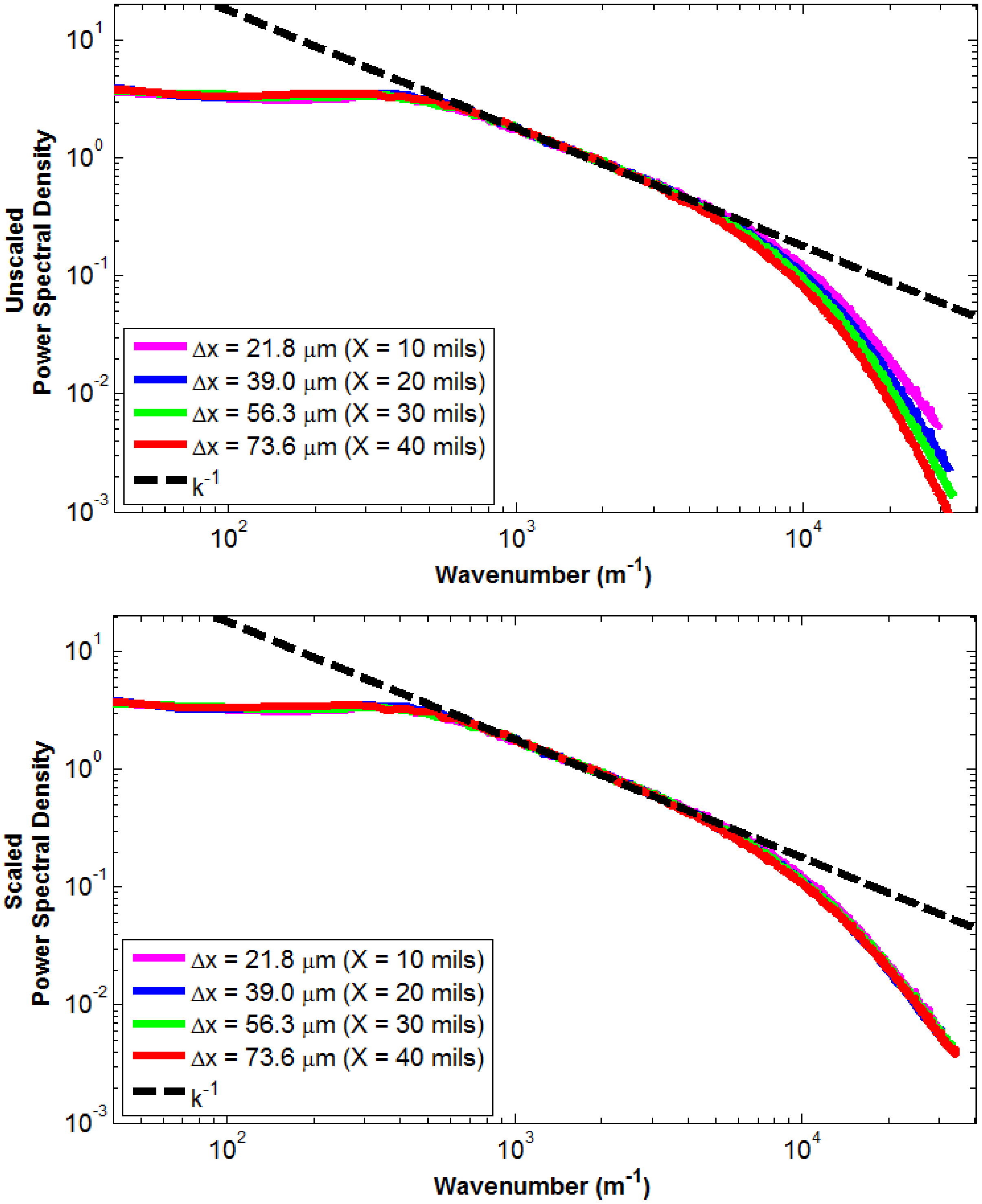

Figure 5.11a,b: Round turbulent jet testing at 20 psia (138 kPa) at 10, 20, 30, and 40 mils prism deflection, showing raw spectra and spectra where the prism deflection spatial filtering has been deconvolved. The close match between the spectra after deconvolution supports the use of the transfer function model from Theory section 3.7.2.

5.3 *Air Jet*

As discussed previously, round turbulent jets are a well-characterized turbulence source that are often found in the literature, and as such they provide an excellent test case to demonstrate the behavior of the FLDI instrument and to compare with the theory for FLDI response developed in this thesis.

5.3.1 Rolloff of FLDI Signal Intensity Along the y-Axis

A baseline measurement for the response of the FLDI instrument to a turbulent jet is the measurement of the radial turbulence profile of the jet. For these measurements, the jet is set to a given distance downstream of the nozzle exit, *x*, and the FLDI output is measured at a series of points where the jet is traversed along the *y*-axis, which is perpendicular to both the FLDI beams (*z*-axis) and jet (*x*-axis). The measurement is performed with the jet placed at best focus in the *z*-axis. The geometry of this measurement is shown in Fig. 5.12.

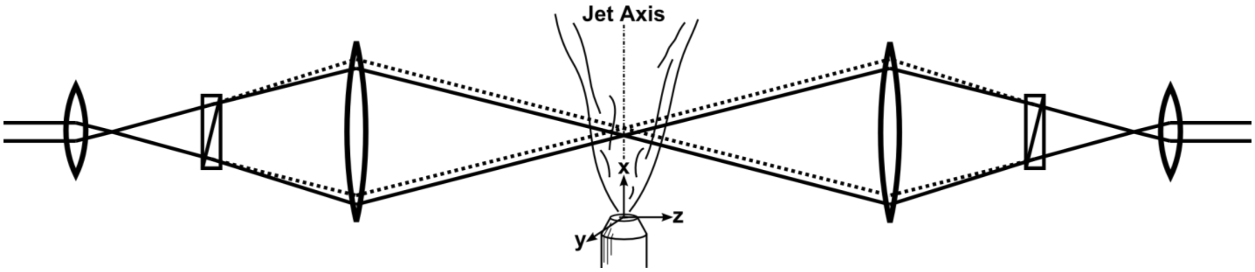

Figure 5.12: Diagram of FLDI measurement of a round turbulent jet, with coordinate system centered at nozzle exit.

In the following results, the helium jet used earlier is replaced by an air jet exiting a round nozzle orifice of diameter *D* with stagnation pressure P_0 = 30 psia (207 kPa). This is approximately a sonic air jet at the converging nozzle exit, so that isentropic flow at $\gamma = 1.4$ can be used to show that the jet static temperature is ~ 0.83 T_0, where T_0 is taken to be approximately the ambient stagnation temperature of the jet. In other words, if T_0 is 298 K, then the static temperature of the jet is ~247 K. This temperature difference is more than enough to provide an ample FLDI turbulence signal for the instrument performance diagnostics reported here.

A series of measurements with downstream distances of 1 to 30 diameters is shown in Fig. 5.13, which displays RMS signal normalized by the integrated signal across the jet profile. Initially, the FLDI response to the jet has a kind of top-hat profile, but as the jet develops downstream, this develops into a generally Gaussian profile, especially past the end of the potential core of the jet. The cumulative distribution functions of these jet profiles are calculated (shown in Fig. 5.14) and a normal distribution CDF is fit to these data. This gives an estimate of the standard deviation width, σ_{jet}, of a best-fit Gaussian profile to each profile.

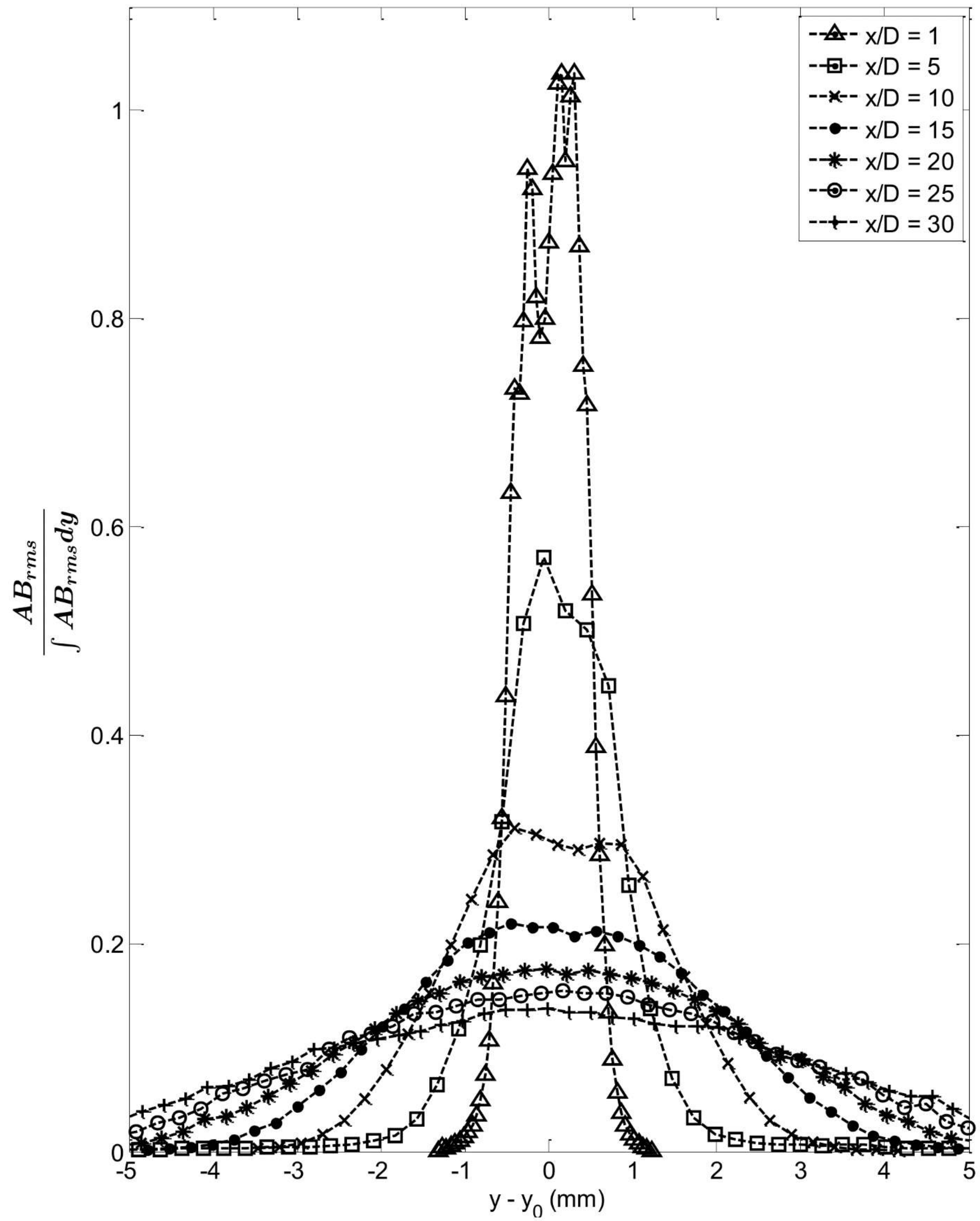

Figure 5.13: Turbulent jet profiles measured using the FLDI instrument for a 1 mm diameter nozzle, using compressed air at 30 psia. The signals are normalized for clarity by the numerically integrated area under the curve.

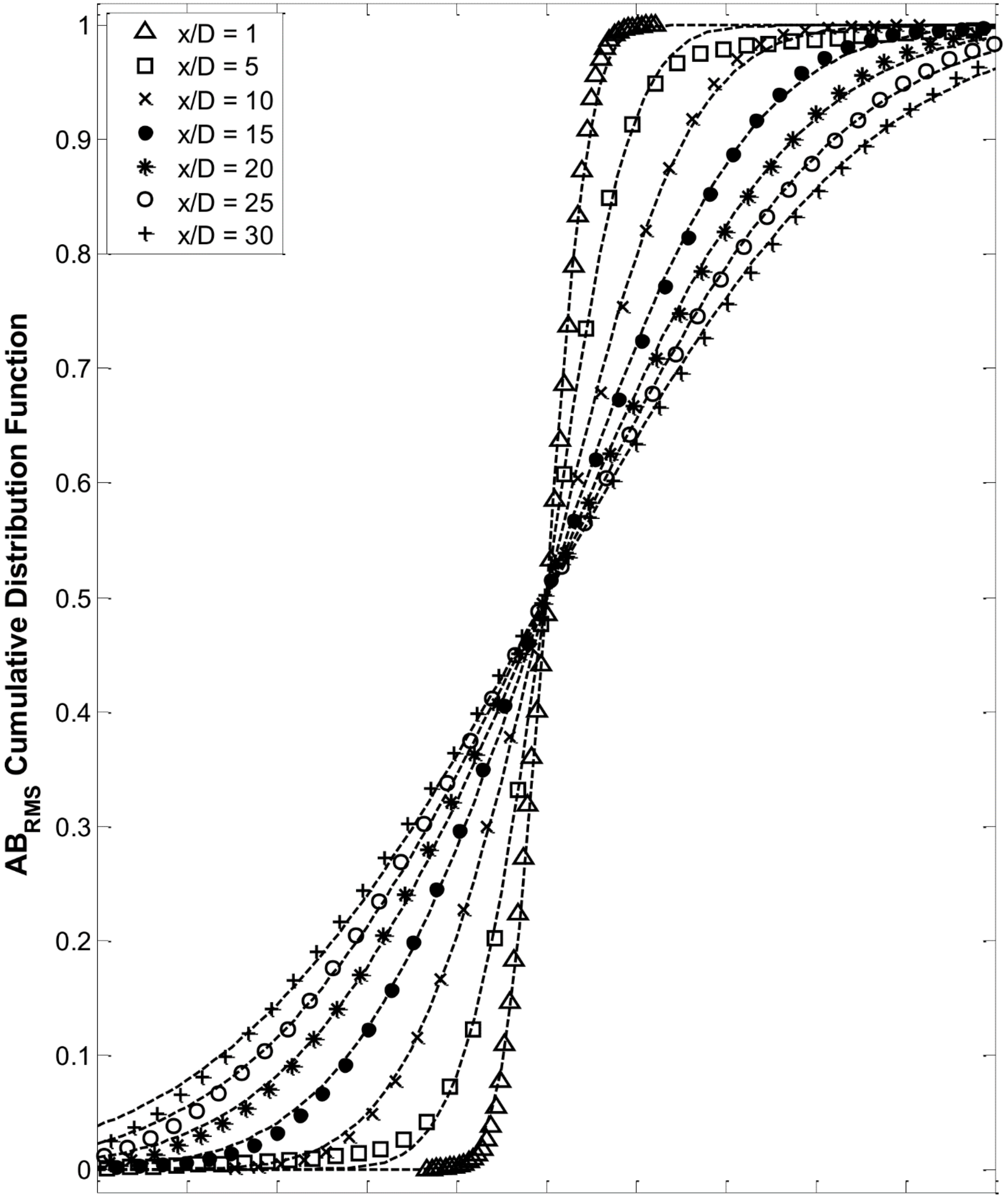

Figure 5.14: Best-fit Gaussian cumulative distribution functions for each of the turbulent jet profiles measured by FLDI. As y_0 is calculated using these CDFs, the median value of each profile is found at 0 mm offset on this plot.

The standard deviation widths of these Gaussian fits are plotted in Fig. 5.15. A linear fit to these data gives the following result, where σ_{jet} is the jet width in millimeters:

$$\sigma_{jet} = 0.0864 \cdot \frac{x}{D} + 0.3309 \tag{5.5}$$

The spreading angle of the jet, 0.086 rad (4.9 degrees), is identical to the angle measured by Wygnanski and Fiedler[68], Rodi[69] and Hussein et al.[70]. This illustrates the ability of the FLDI instrument to yield experimental turbulent round-jet data in agreement with historical benchmark experiments.

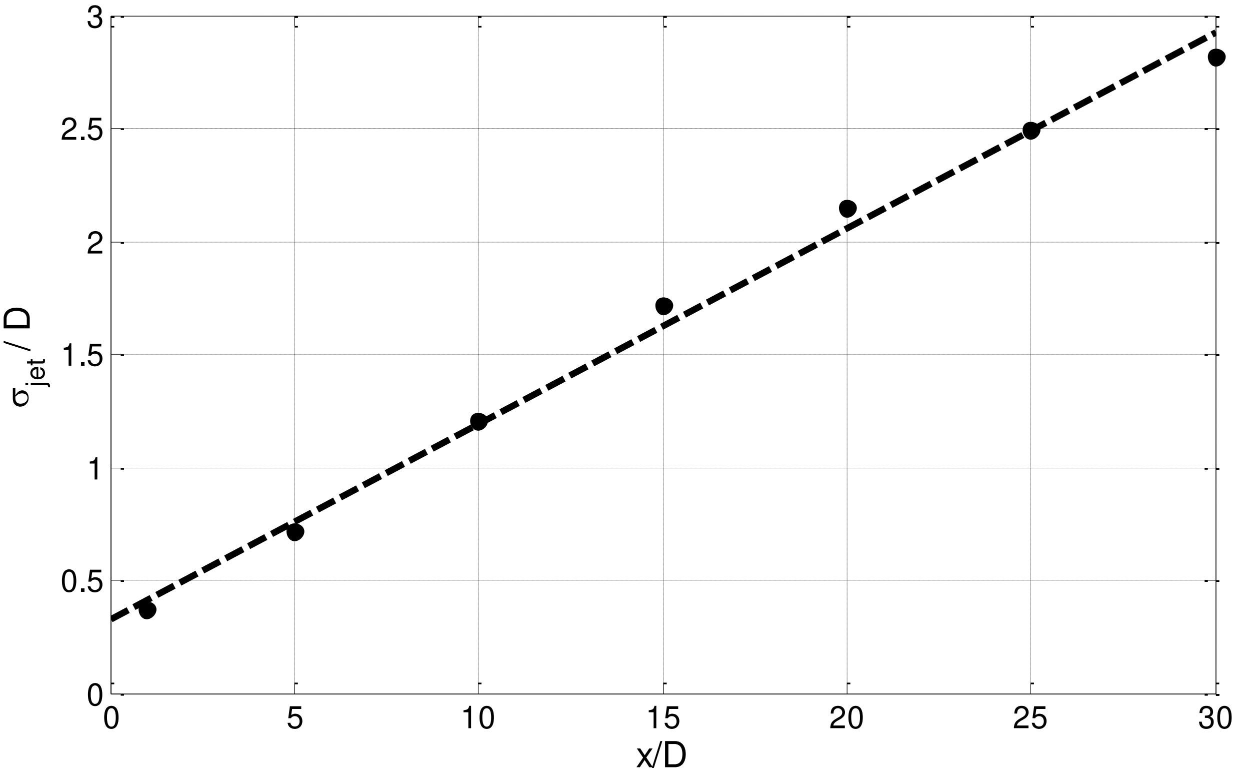

Figure 5.15: ~4.9 degree spreading angle measured from FLDI jet profiles for FLDI data shown previously. This spreading angle is commonly quoted in the literature for the spreading rate of density in turbulent round jets.

The Gaussian CDFs from Fig. 5.14 are normalized by these measured-jet-width standard deviations in Fig. 5.16. The jet turbulence profiles from Fig. 5.13 are also normalized by the jet width standard deviation, shown in Fig. 5.17.

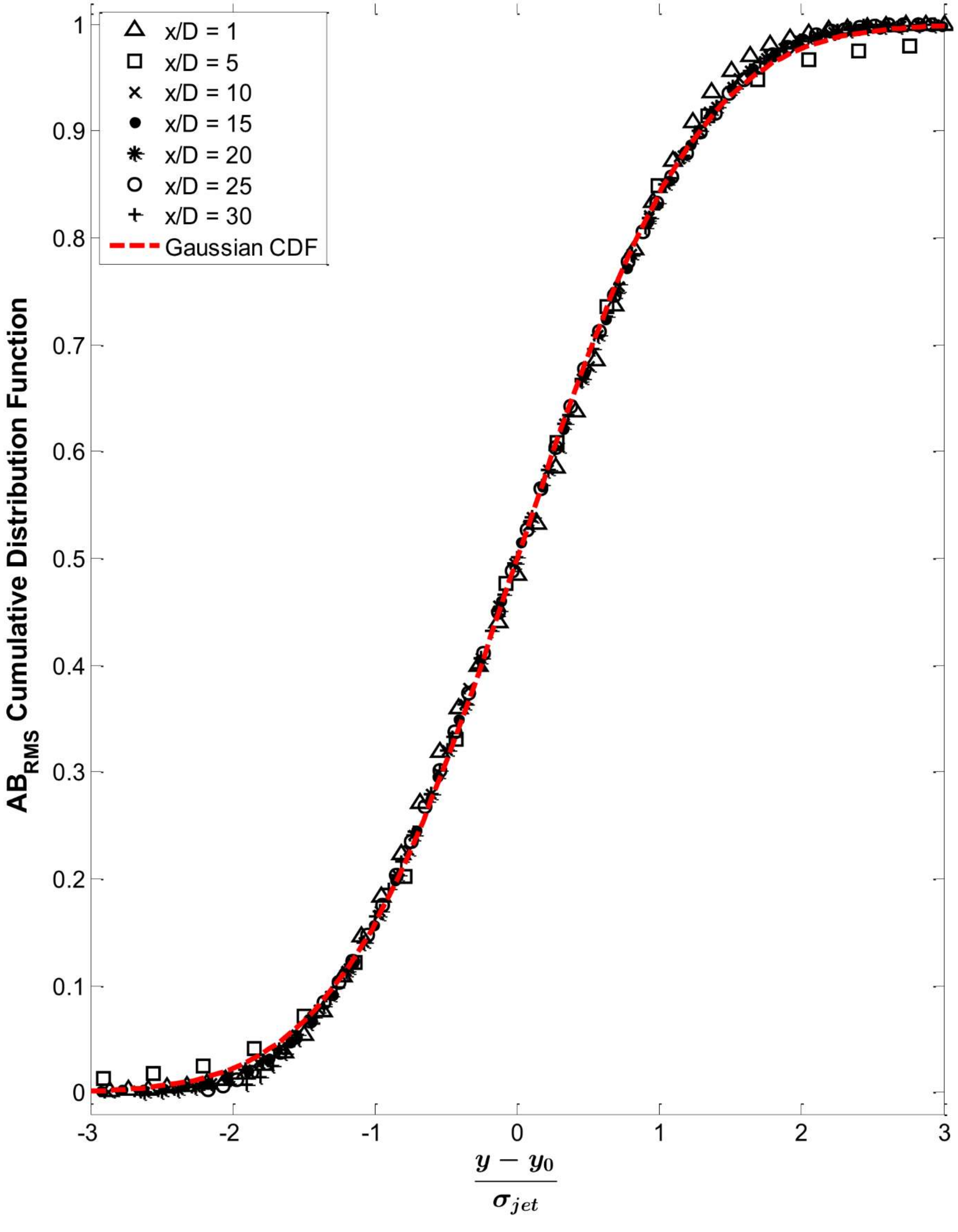

Figure 5.16: Turbulent jet profile cumulative distribution functions (CDF) normalized by jet width standard deviation. A dashed line represents a true Gaussian CDF, showing good agreement with the data, which supports the use of the Gaussian jet approximation used in this research.

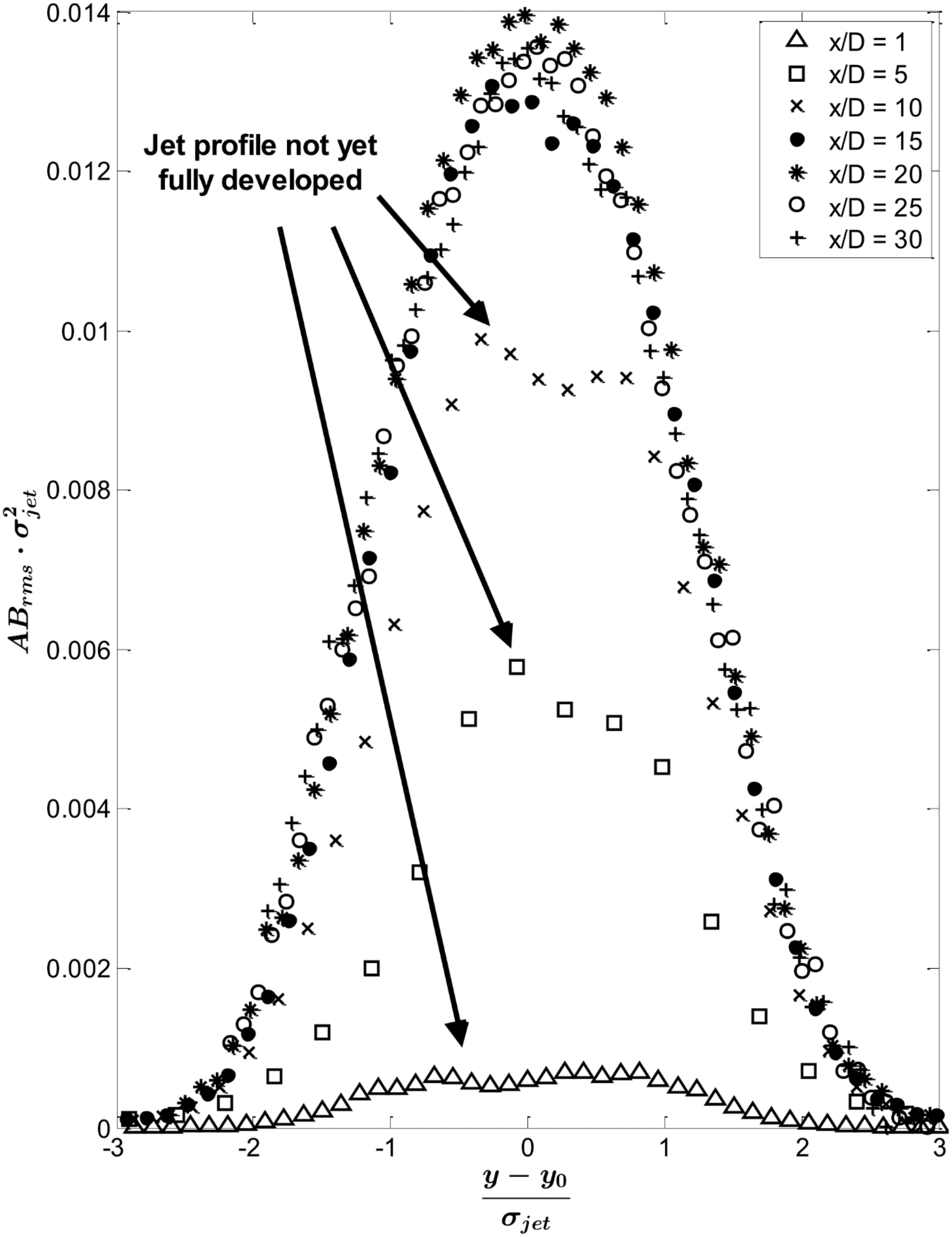

Figure 5.17: Turbulent jet profiles from Fig 5.13 normalized by the jet width standard deviations calculated using Eq. 5.5. While the jet width normalization works well, amplitude normalization fails for downstream distances less than 15 nozzle diameters from the jet origin, as the jet profile is not yet fully developed at these distances.

The RMS turbulence profiles of the turbulent jet at $P_0 = 30$ psia do not appear to be fully developed until around 20 nozzle diameters downstream, based on present FLDI data. After this point, the jet profiles are well-approximated by a Gaussian model.

As will be demonstrated next, the jet width standard deviation is a critical length scale for determining how fast the FLDI signal rolls off when the jet is offset along the *z*-axis away from best FLDI focus. It is used, along with the $1/e^2$ diameter of the FLDI beams, $D_{4\sigma}$, and the distance from the field lens to the focal point of the system, d, to find a non-dimensional length scale of the FLDI system:

$$Z = \frac{z_0}{\sigma_{jet}} \tan^{-1}\left(\frac{D_{4\sigma}}{d}\right) \tag{5.6}$$

If the angle of the beam focus is shallow, then the small-angle assumption can be used to simplify the above relationship:

$$Z = \frac{z_0 D_{4\sigma}}{\sigma_{jet} d} \tag{5.7}$$

Although it is applied in this thesis only to round jet turbulence, the form of Eq. 5.7 for a non-dimensional length should be applicable to other geometries, replacing σ_{jet} with the relevant characteristic lengths in those cases.

5.3.2 Rolloff of FLDI Signal Intensity Due to Focusing of Twin Laser Beams

The signal measured by the FLDI instrument rolls off when disturbances occur away from the focus of the twin laser beams due to spatial filtering, as described previously. As seen in the non-dimensional length scale above, the rolloff of the system response as a disturbance traverses along the *z*-axis of the FLDI instrument is governed by the optical angle at the beam focus.

To verify that this length scale is valid, the angle of the beams was varied by stopping down the apertures of the 50mm *f*/1.2 Nikon camera lenses used as FLDI field lenses in benchtop testing. The total power detected by the photodiodes was measured, and the RMS fluctuation level from the jet turbulence described above was measured from -30 mm to 30 mm z-axis displacement relative to the focus. The lens was stopped down in one-stop increments from *f*/2 to *f*/16, giving a large variation in the effective *f*-number of the FLDI system, defined as $N_{FLDI} = d/D_{4\sigma}$.

First, it is necessary to determine the maximum diameter of the beam before it is reduced by stopping down the lens aperture. At each lens stop, the total power measured by both photodiodes was summed to determine the beam power transmitted through the system, and the radius of the clear aperture of the lens was calculated by dividing the focal length of the lens by the *f*-number. Then, a function (Eq. 5.8) describing the transmitted power of a Gaussian beam clipped by a circular aperture was fitted to the resulting curve.

$$T = 1 - e^{\frac{-2r^2}{w^2}} \tag{5.8}$$

Here, T is the transmitted power fraction, r is the radius of the clear aperture of the lens, and w is the $1/e^2$ radius of the beam (half of the four-sigma diameter, $D_{4\sigma}$). This fit results in an estimate of the maximum beam diameter that could be achieved with no clipping from the lens aperture. A plot of the measured photodiode voltages (directly proportional to incident laser power) compared to clear aperture diameter is shown in Fig. 5.18, with the above fit superimposed as a dashed line.

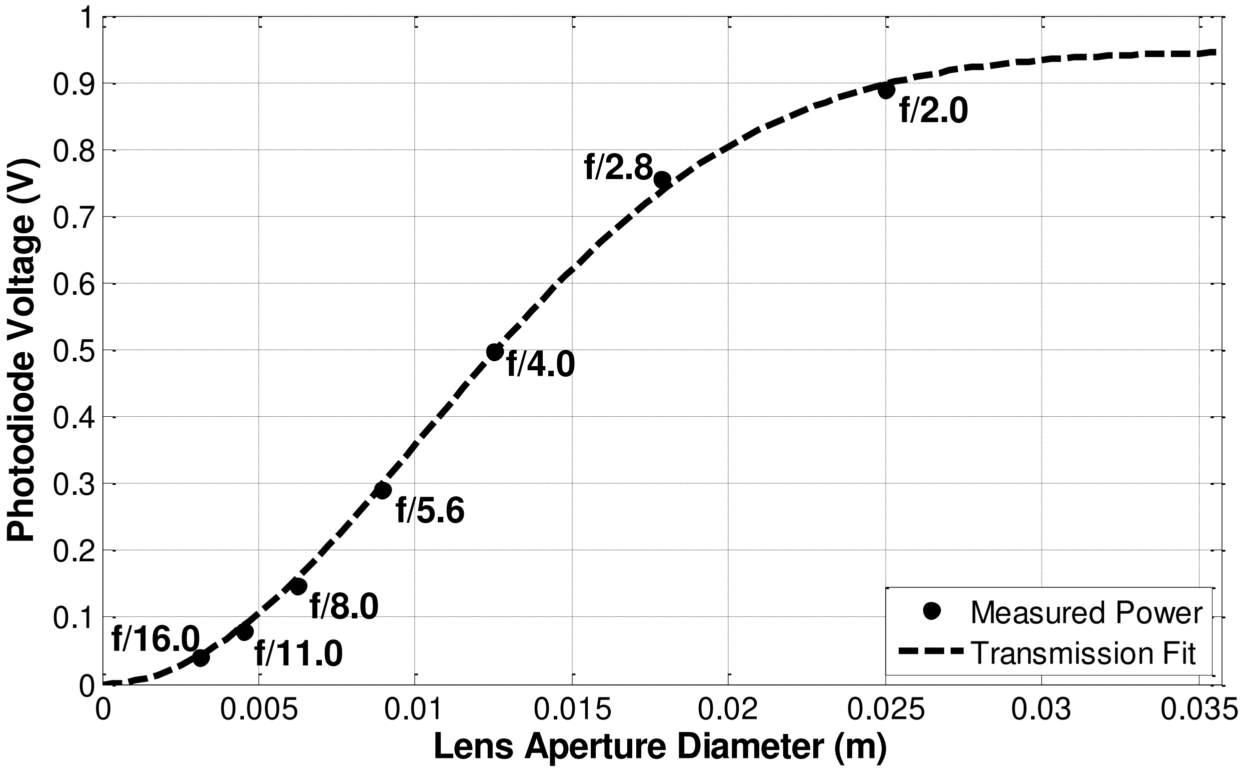

Figure 5.18: Beam profile fit to measured photodiode voltages at different camera lens *f*-stops using Eq. 5.8. The maximum four-sigma diameter of the beam, $D_{4\sigma}$, is found to be 20.5 mm.

The unclipped four-sigma diameter of the beam from the testing above was found to be 20.5 mm.

Due to stopping down the lenses, the clipped beams are no longer Gaussian in profile, and become more like top-hat beams as the aperture is further restricted. For the normalization used here, it is necessary to calculate the equivalent Gaussian beam diameter from this clipped profile. This is done by taking the square root of the ratio of measured beam power at a given *f*-stop to the maximum beam power calculated from the fit above (Eq. 5.8).

$$D_{4\sigma} = 2w\sqrt{\operatorname{erf}\left(\sqrt{2}\left[1-\exp\left(\frac{-2r^2}{w^2}\right)\right]\right)} \tag{5.9}$$

Here, erf is the error function, which is the integral of a Gaussian from its center to the argument of the function.

The results of this test, both raw and normalized by the calculated four-sigma diameters of the beam at each *f*-stop, are shown in Figs. 5.19a,b. Despite assuming that the clipped beams are Gaussian, using the effective diameter described above, the normalization appears to be reasonably effective.

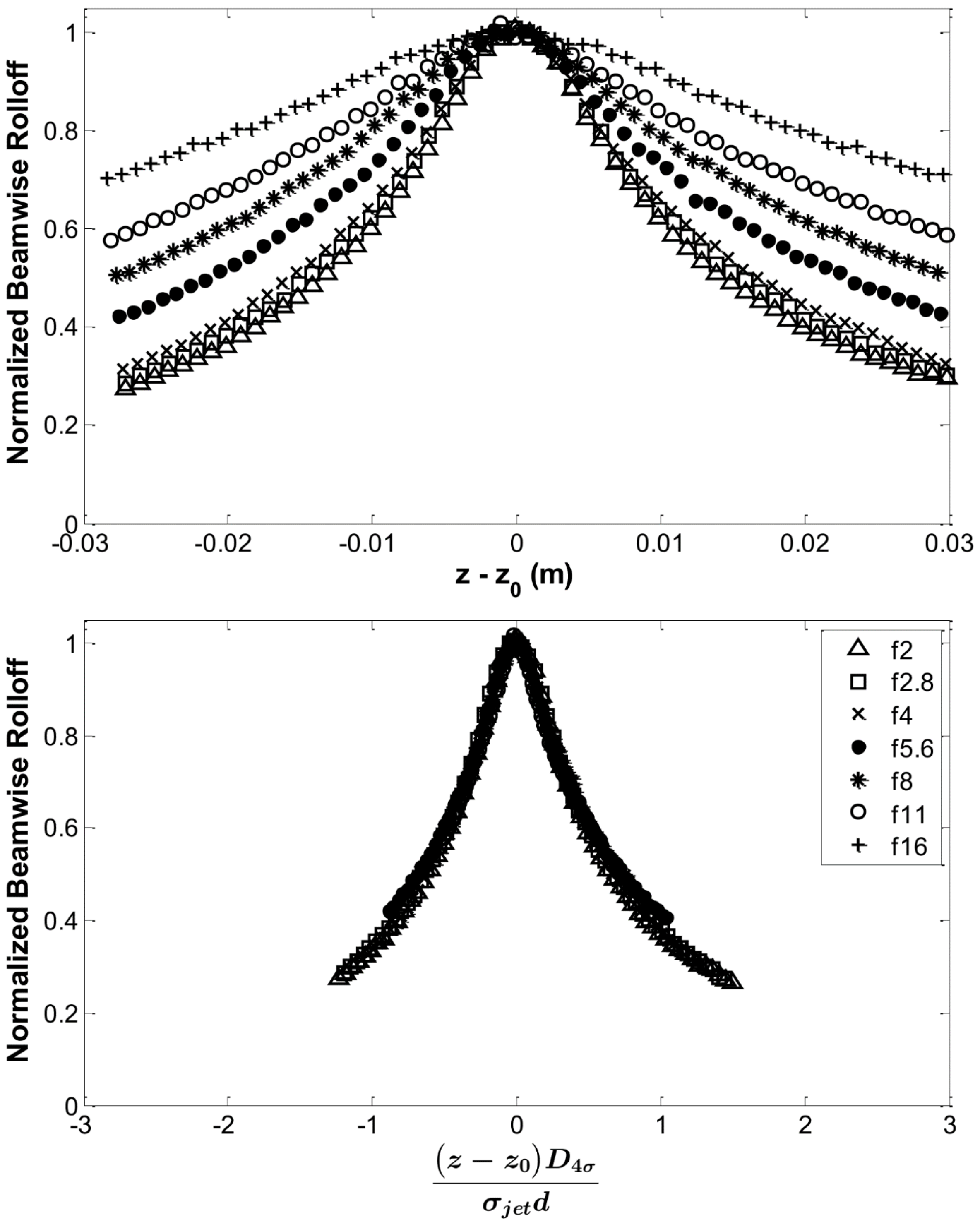

Figure 5.19a,b: Beamwise (z-axis) rolloff of jet turbulence results due to reduction of FLDI system angle by stopping down the field lenses. The f-numbers at aperture setting of the Nikon field lenses used for this testing are shown in the legend.

5.3.3 Beamwise Rolloff of Signal Intensity as a Function of Jet Diameter

The other term in the non-dimensional length scale is the jet width standard deviation, σ_{jet}, which was measured earlier. As the jet nozzle is moved away from the focus along the jet axis (x), the size of the disturbance that the FLDI instrument sees increases due to jet spreading, so it is expected that the rolloff of the signal will be slower as the jet is moved along the beam axis, z (see Fig. 5.12).

Tests were performed with the $D = 1$ mm round jet supplied with air at $P_0 = 30$ psi. It was positioned so as to cross the z-axis at 10 to 30 nozzle diameters D downstream of the nozzle exit. The FLDI response to the jet was measured when the jet was located at points along the beam axis, z, from -30 mm to 30 mm relative to best focus (see diagram). The results of these tests are shown in Figs. 5.20a,b, showing both the raw data and the normalized points. As with the testing at different beam diameters, the result shows excellent agreement.

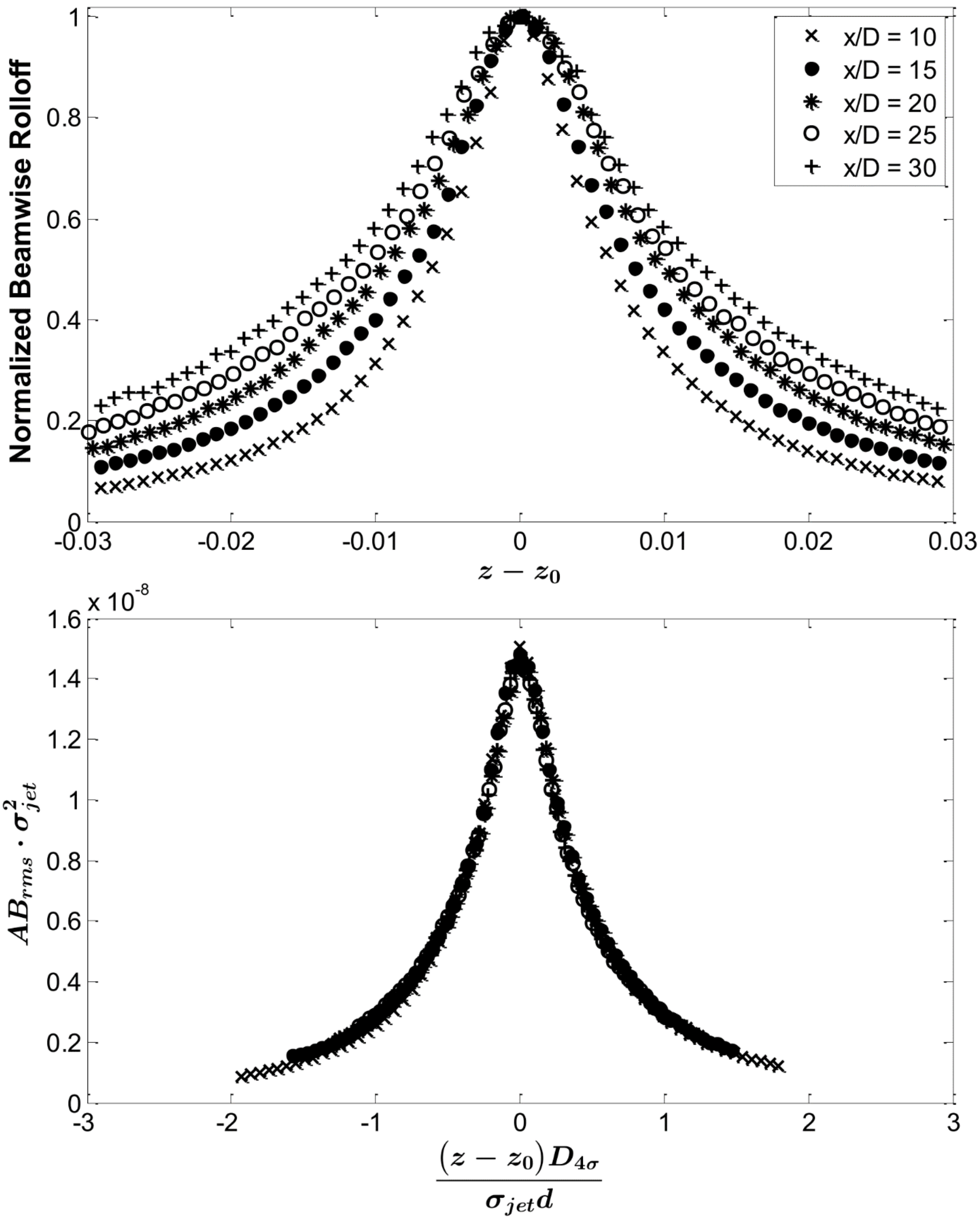

Figure 5.20a,b: Normalized rolloff of turbulence intensity signal away from best focus in the z-direction at varying distances downstream of the jet, with increasing jet diameter further downstream of the nozzle.

5.3.4 CBS Fit to Velocity Profile

The crossed-beam schlieren (CBS) instrument developed for this research was used to measure convective velocities in a round turbulent jet as a function of distance downstream of the nozzle exit. The nozzle was 1.83 mm in diameter and supplied with helium at 30 psi (207 kPa) absolute. Measurements were performed from 7.5 to 75 nozzle diameters downstream. The measured velocities are compared with the theoretical fit developed by Witze[71]. The result of this testing is shown in Fig. 5.21.

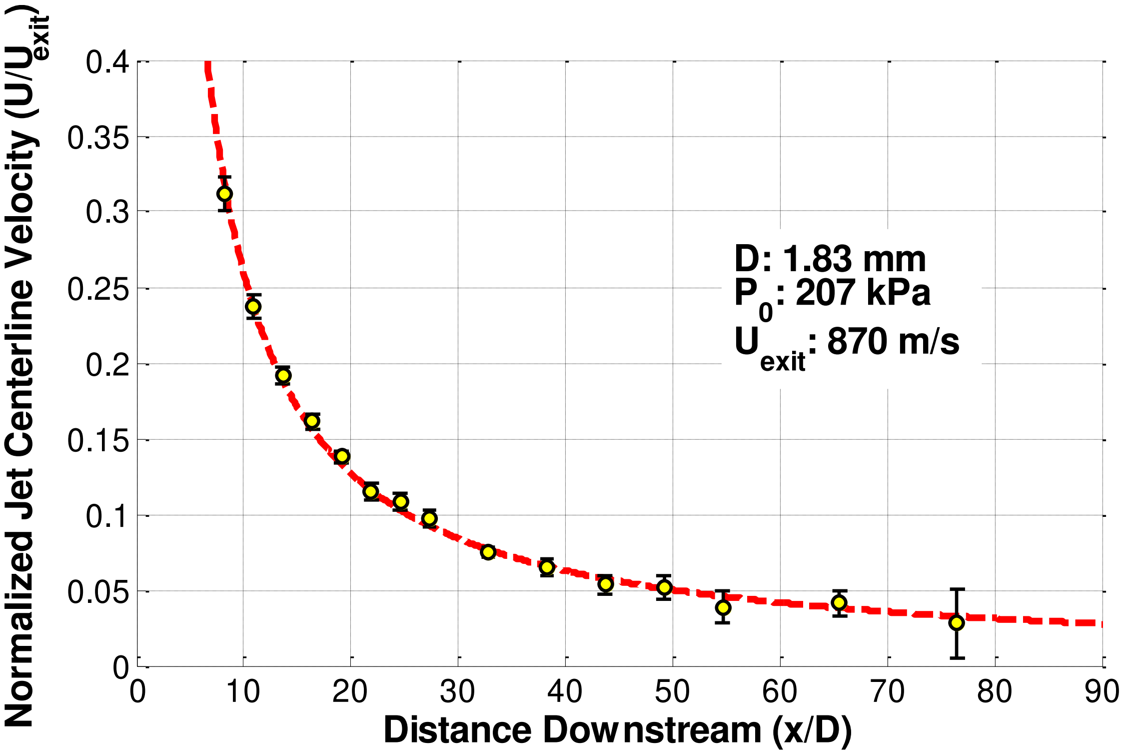

Figure 5.21: Crossed-beam schlieren measurements of convective velocity in a high-speed helium jet in air, compared with theory developed by Witze[71]. The dashed line shows Witze's model for centerline velocity decay using the listed flow properties.

The form of Witze's fit is given in Eq. 5.10:

$$f(\bar{x}) = 1 - \exp\left(\frac{-1}{\kappa\bar{x}(\overline{\rho_e})^{0.5} - X_c}\right) \tag{5.10}$$

In this fit, $f(\bar{x})$ is the flow property of interest, which decays with distance downstream along the centerline of the jet, $\bar{x}$, which is the distance from the nozzle divided by the nozzle radius. $\overline{\rho_e}$ is the ratio of the density of the surrounding fluid to the density of the fluid at the jet exit. X_c is a non-dimensional core length, which has a universal value of 0.70 according to Witze. Finally, κ is a proportionality constant which is different for each flow property.

The proportionality constant κ that provided a best fit to the data collected above was found to be 0.075, while the theoretical universal proportionality constant for centerline velocity decay found by Kleinstein[72] is $\kappa = 0.074$. The proportionality constant for fluid enthalpy is 0.102, and the constant for centerline decay of concentration/temperature/density is 0.104. Ultimately, this means that the rolloff of density occurs sooner after the nozzle exit than does the rolloff of velocity, due to a shorter potential core for density, and it also rolls off faster toward ambient conditions.

It was not possible to measure the velocity of the jet closer to the nozzle exit because turbulent density fluctuations within the potential core are very weak, leading to failure of the correlation results. Uncertainty in the calculated convective velocity was found to be at a minimum just beyond the potential core, increasing gradually as the helium in the jet mixes out with the surrounding air. Beyond approximately 75 nozzle diameters downstream it was found that the helium had mixed out of the jet too far to allow consistent measurement, test to test.

The results of this experiment are important because they show that the correlating CBS signal in the jet convects at almost the same velocity as the jet centerline velocity, although U_C is typically a little lower than U on tunnel centerline. This means that the convective velocity may be used for a reasonable approximation of mean flow velocity to calculate wavenumber for the turbulent density spectra measured by the CBS instrument. Although the FLDI instrument developed during this research was not equipped to perform these cross-correlation measurements, it is possible to do so, and because of the similarity in the form of the output of deflectometry and differential interferometry, it should provide a similar result. Simultaneous measurement of convective velocity and the single-point fluctuating FLDI signal would greatly reduce the uncertainty of spectra and of the calculated spatial filter transfer functions for each run. This, however, is left for future work.

5.3.5 Electronic Noise Spectra

There is a significant amount of noise present at low frequencies in the signals measured by the FLDI instrument: so-called “flicker” noise which follows a $1/f$ slope in measured spectra, fluctuations in laser power, changes in room air temperature from ventilation air currents, etc. This can be seen in Fig. 5.22, where such noise is visible above the electronic noise floor of the data acquisition system out to around 500 Hz.

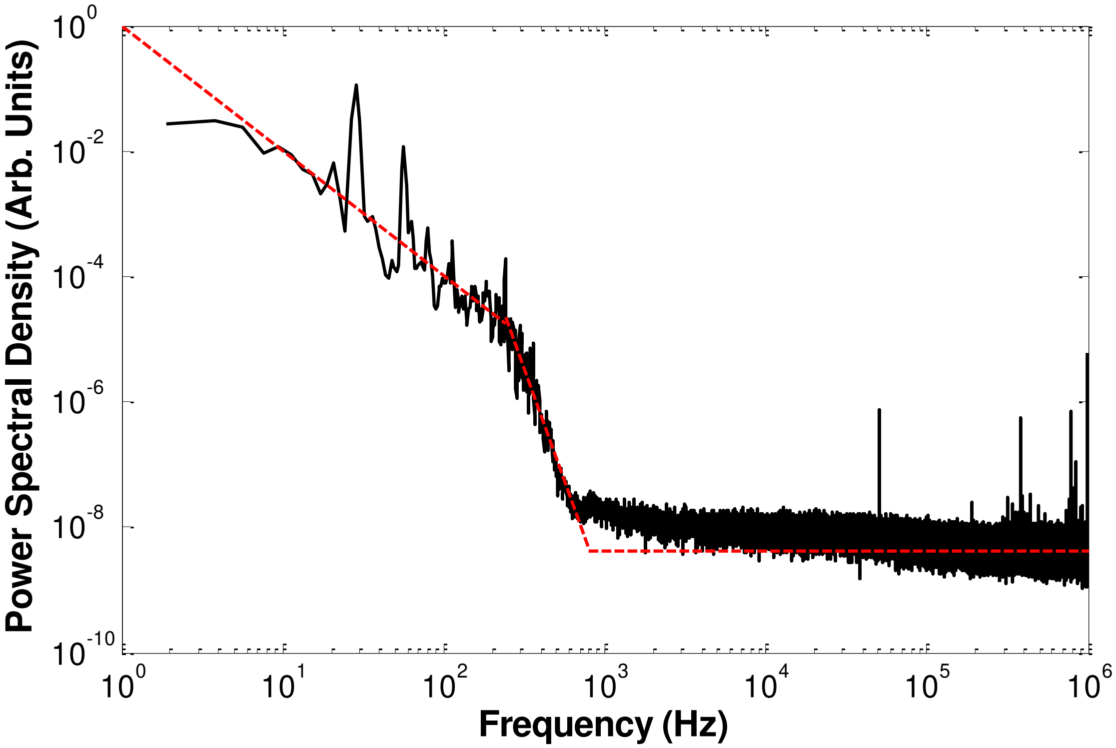

Figure 5.22: Baseline electronic noise present in FLDI measurements when no jet or other flow is present. The dashed red line follows an approximate "noise floor" of measured spectra.

Despite the relatively high strength of this noise compared to turbulence spectra measured by the FLDI instrument, the noise detected by the two photodiodes is uncorrelated, thus the coherence of the two signals is low. Meanwhile, as the photodiodes measure essentially the same signal, but 180 degrees out of phase to one another, the photodiode signals from to the interferometer should be very coherent, while electronic noise on top of those signals should not. This provides a useful method for rejecting artifacts on measured turbulence spectra that are not actually due to the turbulent flow under study, but rather come from random noise entering the system.

Coherence is calculated from the spectra of two signals using Eq. 5.11:

$$C_{AB} = \frac{|S_{AB}|^2}{S_A \cdot S_B} \tag{5.11}$$

Here, A and B are the two FLDI photodiode signals, C_{AB} is the coherence signal of the spectrum, S_{AB} is the cross-correlation of signals A and B, and S_A and S_B are the autocorrelations of each signal. Direct measurement of the coherence of the full spectrum is extremely noisy, so instead it must be calculated over many ensembles of the FLDI signals and then averaged. A plot of the coherence signal from a sample turbulent jet signal is shown in Fig. 5.23, annotated to show how external noise appears in the spectrum.

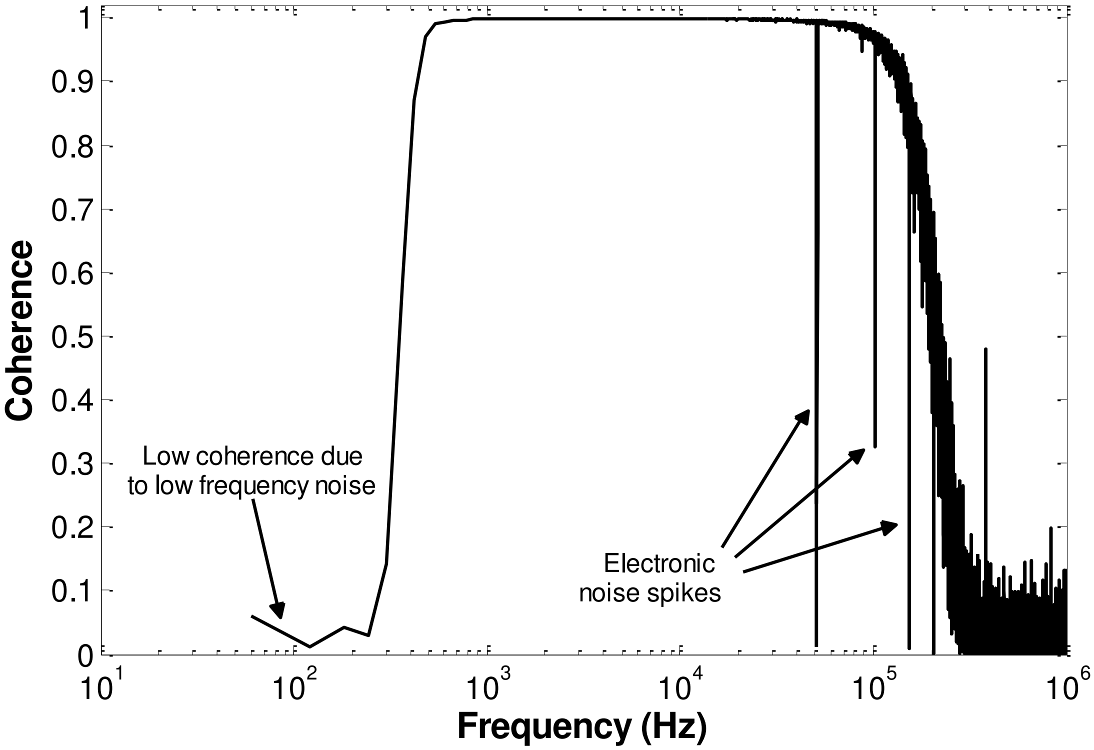

Figure 5.23: Example coherence plot from a turbulent air jet test, showing strong coherence from the turbulent signal, and low coherence at frequencies corrupted by electronic noise.

Here, the effect of the noise from 0 Hz to ~500 Hz, shown in the baseline spectrum above, appears as a very-low-coherence signal. Ignoring all points below a given threshold, such as 90% coherence, limits the influence of electronic noise on FLDI turbulence spectra. The spectrum to which the above coherence plot corresponds is shown in Fig. 5.24, where the full spectrum is plotted in black, and the portion of the spectrum where the coherence is above 90% is overlaid.

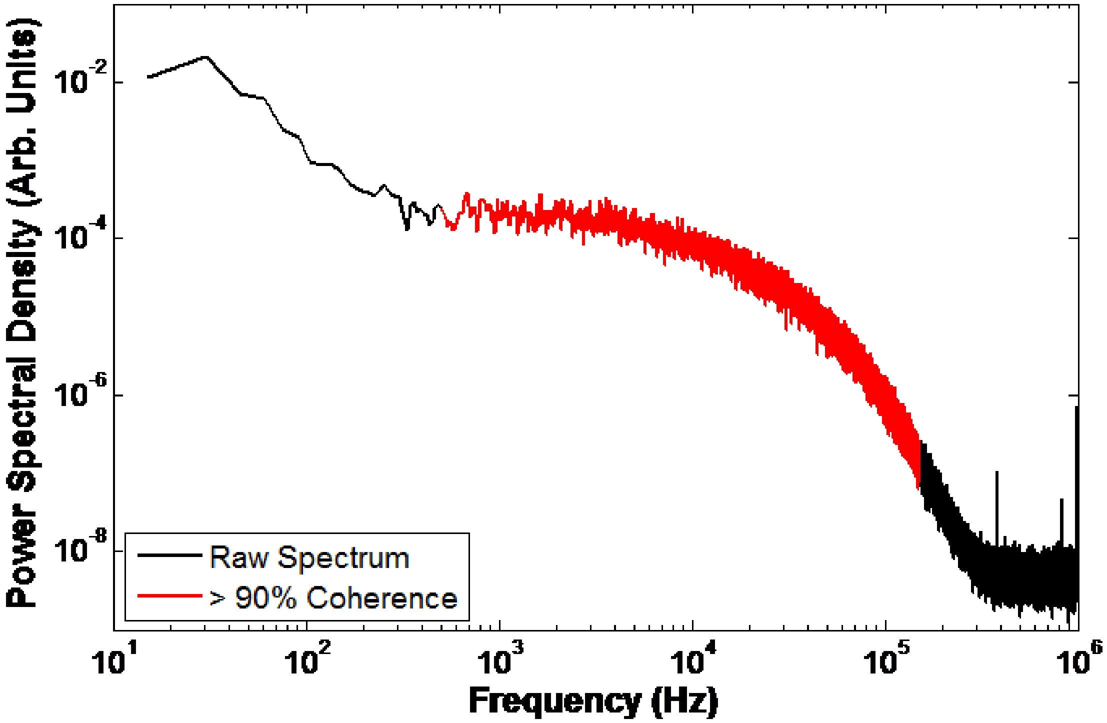

Figure 5.24: Turbulent jet spectrum showing the full spectrum and the spectrum clipped to only those points having greater than 90% coherence.

The background noise seen in Fig. 5.22 can be clearly seen superimposed upon the raw spectrum in Fig. 5.24. Limiting the spectrum to just the signal above 90% coherence trims this noise out, leaving behind only the signal that can be strongly attributed to the interferometer response to the turbulent flow under study.

In addition to the ability to eliminate the effect of laser power fluctuations on the FLDI signal, the ability to perform this coherence analysis is another benefit from using two photodiodes for FLDI phase quadrature, instead of using a single photodiode and measuring the ratio of photodiode voltage fluctuations to mean voltage. This technique appears to be novel in the literature. Many papers show turbulence spectra contaminated with electronic noise at low frequencies and crossing the noise floor at high frequencies, but have no way to discriminate between spectra of interest and noise on the spectra.

5.3.6 Measurement of Fluctuating and Mean FLDI Phase

The FLDI instrument is capable not only of measuring fluctuations in density, but can also be used to measure differential phase between the foci of the two beams. This can be seen in Fig. 5.25, which shows the fluctuating and mean phase measured in a round turbulent jet from a $D = 1.83$ mm nozzle, supplied with air at $P_0 = 70$ psia (480 kPa). At this stagnation pressure, sonic flow at the nozzle exit is followed by expansion to supersonic flow and a series of "shock diamonds[73]." Here, the jet axis, x, is in the same direction as the axis of beam separation, so the mean phase measured by the instrument represents the density gradient along the x-axis of the jet (see Fig. 5.12).

The effect of shock diamonds in the potential core of the jet is clearly visible in both the fluctuating and mean component plots. These shock diamonds exist until around 12 diameters, *D*, downstream of the nozzle exit, which can be determined by finding the point that the mean component stops oscillating. The fluctuating component is at a maximum at the peaks of the mean phase plot, as this is where the density of the flow is greatest, and it is at a minimum at the valleys of the mean phase plot, where the density is at a local minimum.

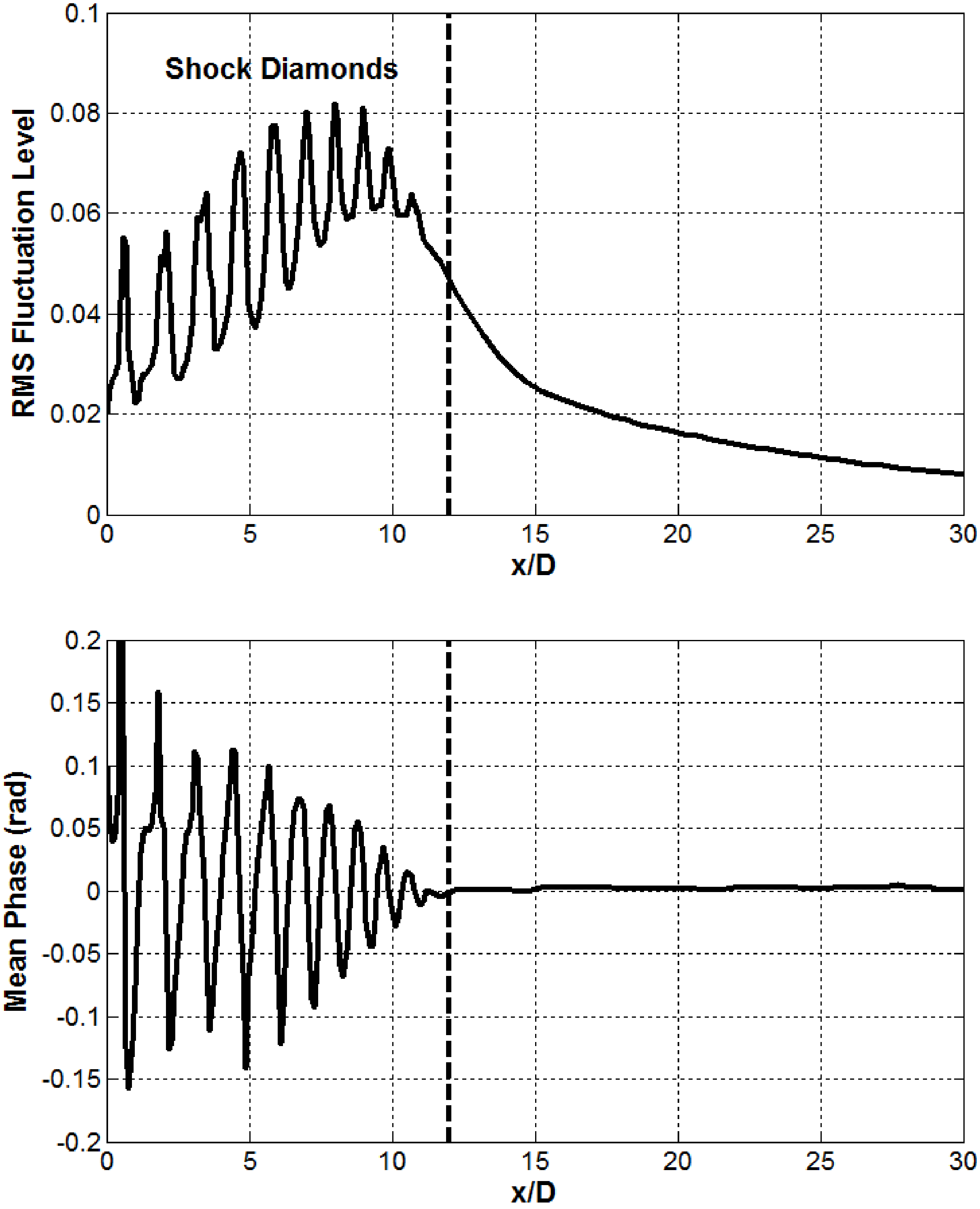

Figure 5.25: Fluctuating and mean phase in a P_0 = 70 psia (480 kPa) turbulent air jet. Shock diamonds in the jet are clearly visible out to around 12 diameters downstream of the nozzle.

5.3.7 Comparison with Literature and HWA Data

Measurements were made of turbulent intensity and spectra in the turbulent air jet using both hot-wire anemometry and the FLDI technique, for direct comparison as well as validation from data from the literature. The data shown here were all taken with a jet stagnation pressure of P_0 = 30 psia (207 kPa), using the 1 mm diameter nozzle described earlier. This may be described as approximately a sonic jet with few if any shock diamonds.

One difficulty with hot-wire anemometry (HWA) is that its response is highly non-linear. The Wheatstone bridge voltage measured by the anemometer must be calibrated against a known velocity, at the desired wire operating resistance, in order to measure velocity and its fluctuating component. For the present experiments, this was done by making measurements at a range of distances x downstream of the nozzle exit. The average wire voltage, minus the voltage of the wire with the jet turned off, was related to the centerline velocity predicted by Witze's model (described earlier) with a 6th-order polynomial fit.

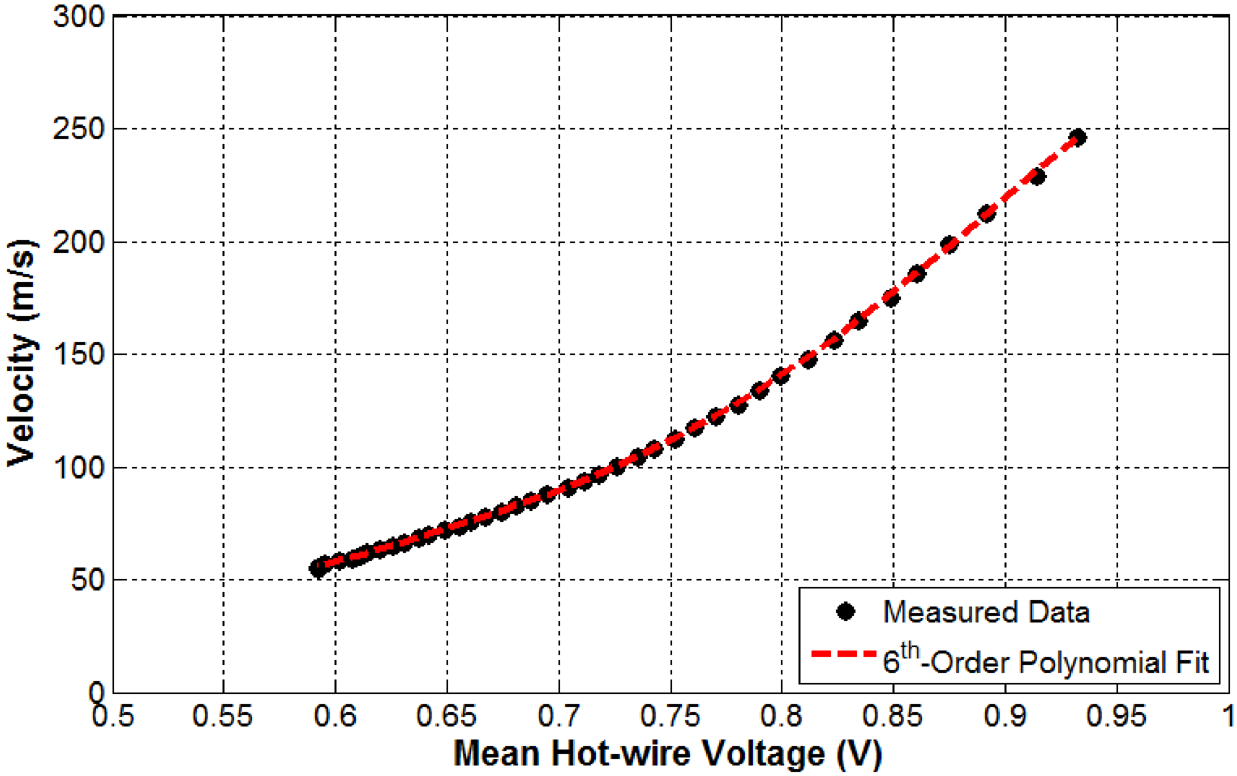

Figure 5.26: 6th-order polynomial fit of hot-wire anemometer mean voltage to jet centerline velocity, as per the hot-wire anemometer system documentation.

To avoid issues from jet geometry and possible misalignment of the jet, only points well outside the potential core of the jet ($x/D > 10$) were used.

Using this calibration, the velocity turbulence intensity along the centerline of the jet was measured using HWA, and the density turbulence intensity was measured using FLDI. The results are compared with data published in Chen & Rodi[74]. The published data refer to ρ_a/ρ_o, which is the ratio of ambient density to the density of the jet at the nozzle exit. This density ratio was calculated for the turbulent jet used in this research using the compressible isentropic relationship for density:

$$\frac{\rho_a}{\rho_o} = \frac{P_\infty}{P_0}\left(1 + \frac{\gamma - 1}{2} M^2\right)^{\frac{1}{\gamma - 1}} \tag{5.12}$$

Here, M is the nozzle-exit Mach number of the jet, γ is the ratio of specific heats in the gas, P_∞ is the pressure of the surrounding fluid, and P_0 is the stagnation pressure of the jet. For the 30 psia jet at lab conditions, $M = 0.96$, and ρ_a/ρ_o is approximately 0.75.

The measured HWA centerline velocity turbulence intensity of the jet is shown in Fig. 5.27b. It peaks around 20 diameters downstream, which is approximately where the jet profile was found to be fully developed to a Gaussian profile in the profile testing described earlier. Past this point, the turbulence intensity appears to flatten out to around 20%.

The centerline density turbulence intensity of the jet, measured by the FLDI instrument, is shown in Fig. 5.28b. It rapidly rises to a peak at around 10 diameters downstream of the nozzle exit, and then rolls off slowly, also flattening out to around 20%. Note that the decay of density along the jet centerline occurs sooner and is more rapid than the velocity decay, accounting for the difference in the location of peak turbulence intensity measured by both instruments.

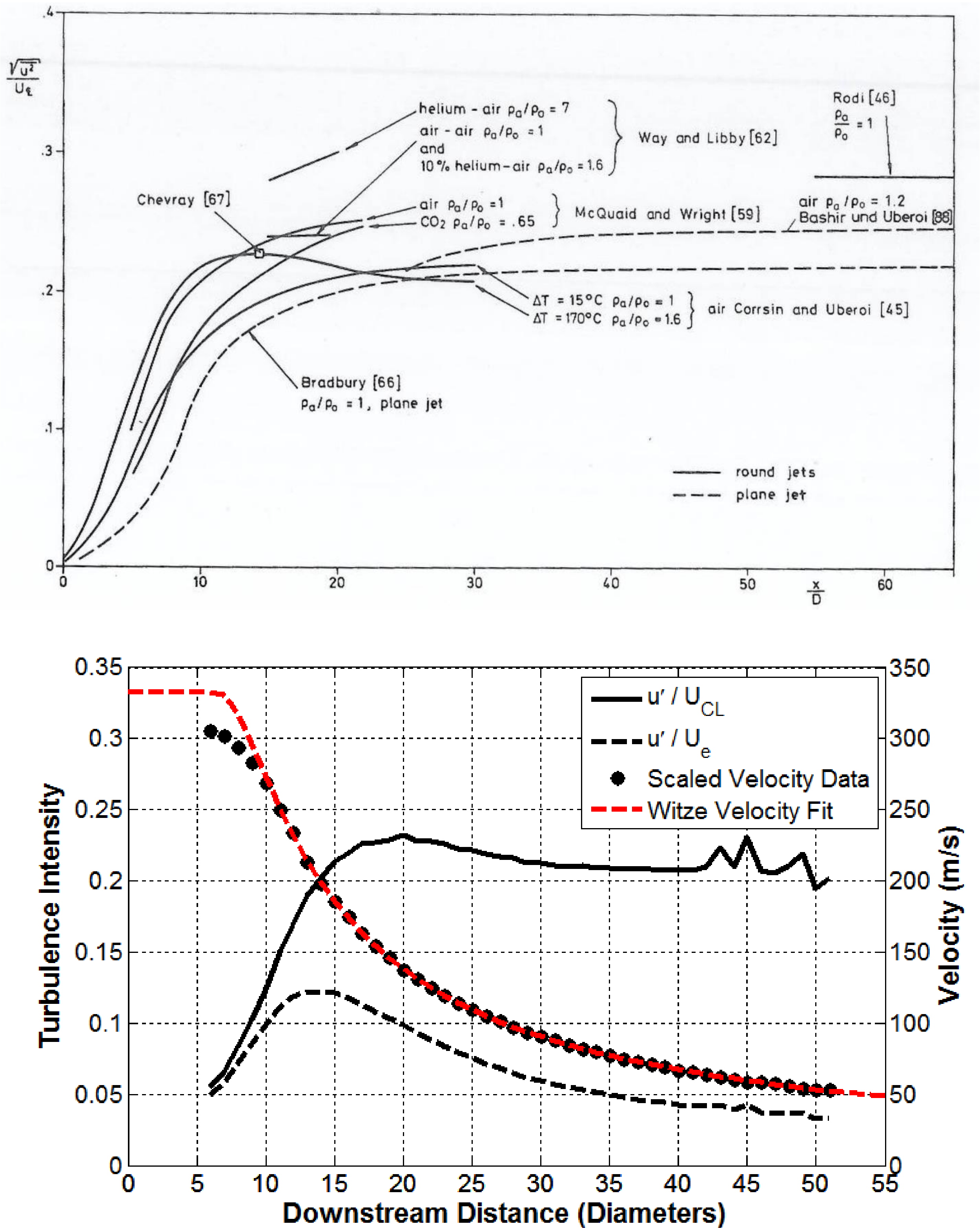

Figure 5.27a,b: Measured velocity turbulence intensity in the turbulent jet from hot-wire anemometry, compared to published data from Chen & Rodi[74].

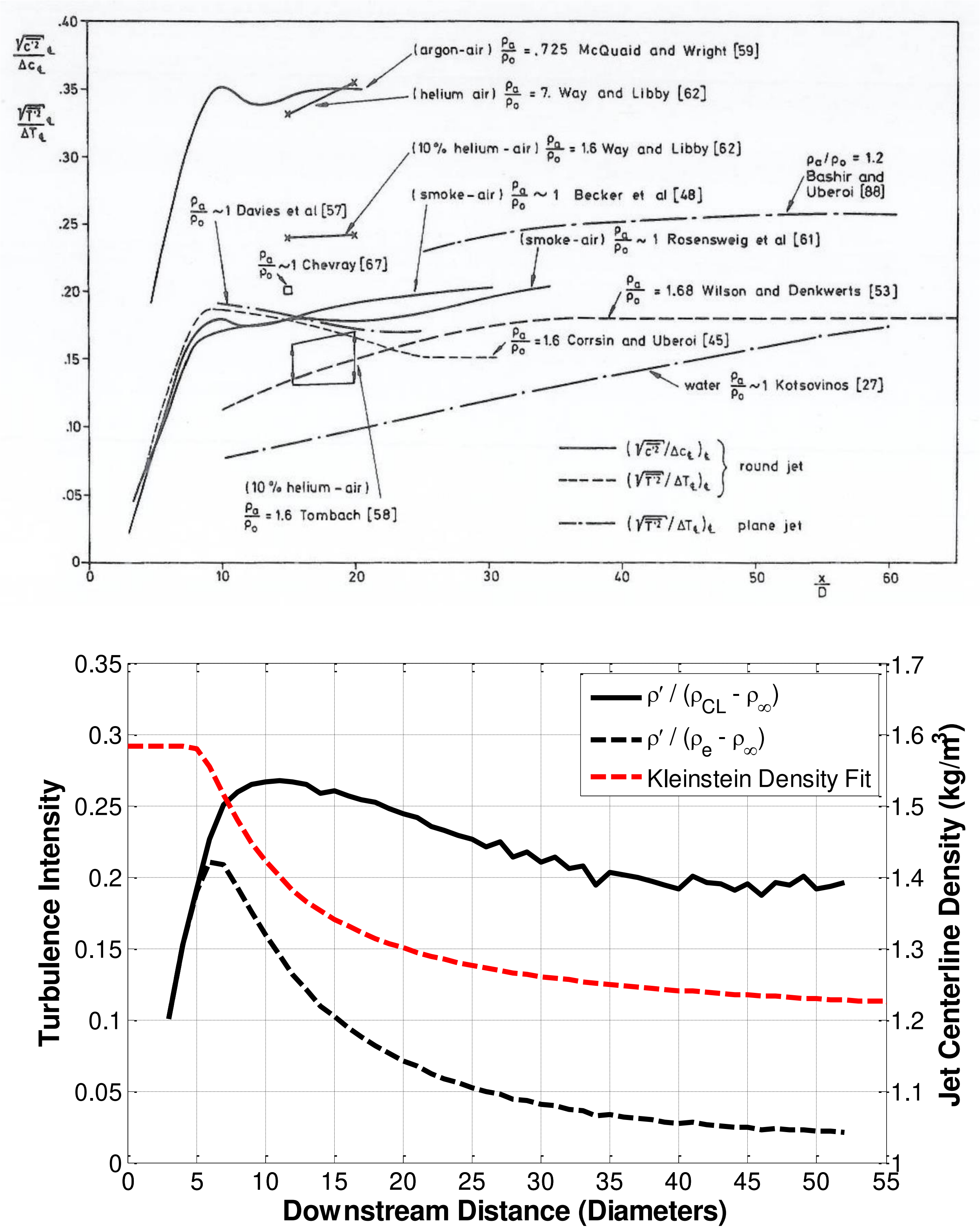

Figure 5.28a,b: Measured density turbulence intensity in the turbulent jet from the FLDI instrument, compared to published data from Chen & Rodi[74].

The turbulence intensity measurements from both instruments are overlaid on one another in Fig. 5.29. Despite *ρ* and *u* being fundamentally different properties of the flow, the turbulence intensity profiles for velocity and density turbulence are quite similar in terms of general shape.

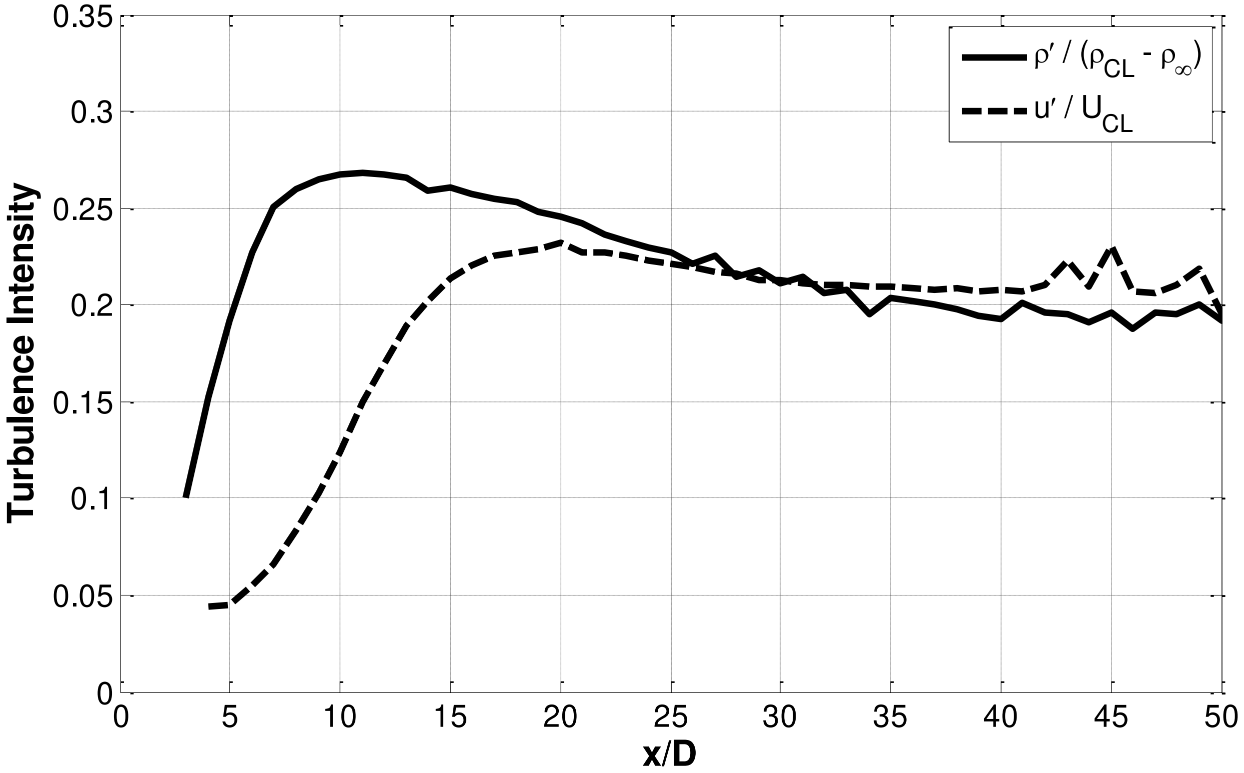

Figure 5.29: Turbulence intensity measured by HWA (velocity TI%) and FLDI (density TI%) instruments.

Because of this similarity between the two turbulence intensities, it should be possible to directly compare measurements of density and velocity turbulence in a wind tunnel facility. This would allow use of the FLDI instrument to measure disturbance levels in flow conditions unsuitable for other techniques, but would still give results comparable to those published in the literature.

Some testing was also performed at higher jet speeds. The data from Fig. 5.30 were taken at P_0 = 70 psia (480 kPa), giving a peak Mach number of around 1.3. The density turbulence intensity calculated for this case compares favorably with P_0 = 321.7 kPa, M = 1.4 data by Panda[75], which were gathered using the Rayleigh scattering technique.

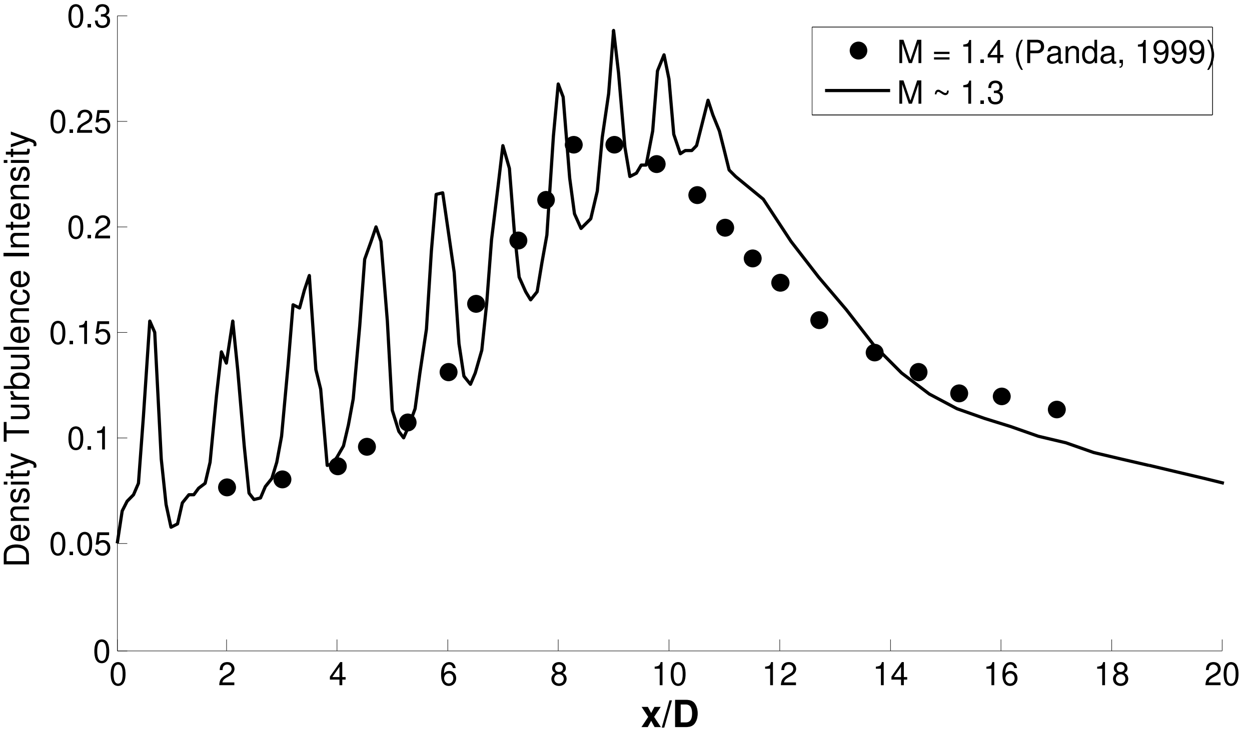

Figure 5.30: Comparison of density turbulence intensity measured by FLDI in a Mach ~1.3 turbulent jet and by Rayleigh scattering in a Mach 1.4 jet measured by Panda[75].

As mentioned above, the spikes in the measured density fluctuations occur due to large changes in the local density at the jet centerline from shock diamonds in the potential core of the jet. Without a method of directly measuring the local density level, the FLDI method must rely on estimates of local density: in this case, the fit described by Witze was used. Even with this drawback, the data show reasonable quantitative agreement. The shift in the location of peak turbulence intensity may be due to Panda's use of a converging-diverging nozzle, while the jet used for this research is produced by a converging nozzle. The jet in Panda's research leaves the nozzle perfectly expanded at $M_{exit} = 1.4$, while the jet from the nozzle examined here is choked at $M_{exit} = 1$ and is underexpanded, achieving its maximum Mach number some distance downstream.

5.3.8 Turbulence Spectra

In addition to turbulence intensity measurements, measurements of turbulence spectra were made at downstream locations in the turbulent jet, with the flow directed perpendicular to the axis of beam separation. Raw spectra from the jet experiments already cited at $P_0 = 30$ psia are shown in Fig. 5.31 for a range of diameters downstream of the nozzle exit. Spectra processed by deconvolution of the system and beam separation transfer functions are shown in Fig. 5.32. The spectra are normalized and spaced in two-decade intervals for clarity. The lightest dots in each plot show the full power spectrum of the signal. Darker spots highlight the meaningfully-coherent signal, selected using the method described earlier. The dark line is a smoothed power spectrum from each data set. Finally, for the processed spectra, the dashed line represents a Von Kármán spectrum fit to the data (as described in the Theory section of this thesis), which is initially flat, but rolls off to a slope of -5/3, representing the Kolmogorov spectrum, and this rolloff occurs around the wavenumber k_0, the outer scale of turbulence.

Note that very few turbulence spectra are found in the literature for turbulent jets, because of the difficulty of the measurement, especially before modern digital data acquisition and processing capabilities became available.

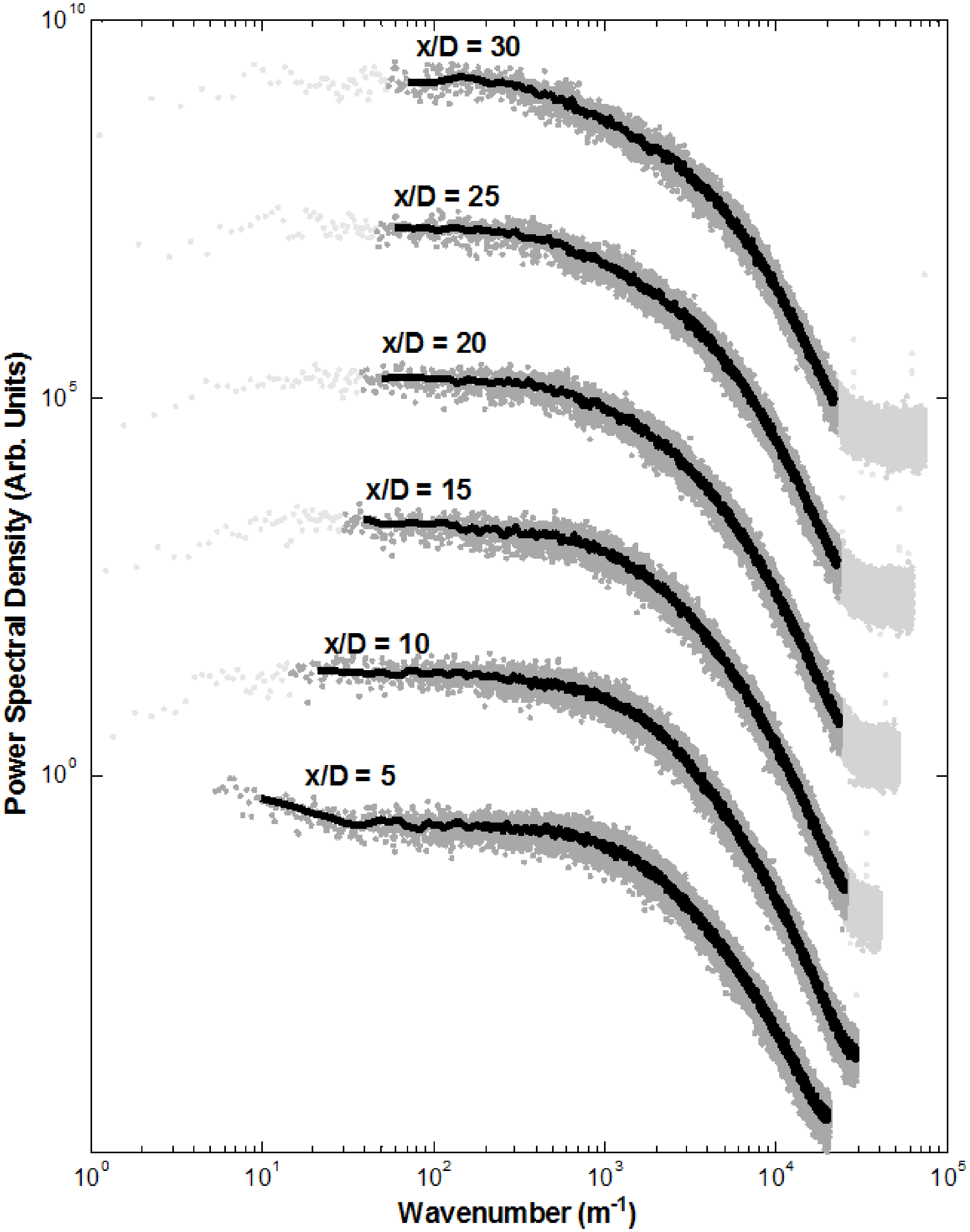

Figure 5.31: Raw turbulent jet spectra from FLDI measurements of P_0 = 30 psia jets. D = 1 mm, at a variety of distances downstream of the nozzle exit. The light gray points represent all of the measured points on the spectra, while the darker gray points correspond to the portions of the spectra where the two photodiode signals are highly coherent. The solid lines shows these spectra after smoothing.

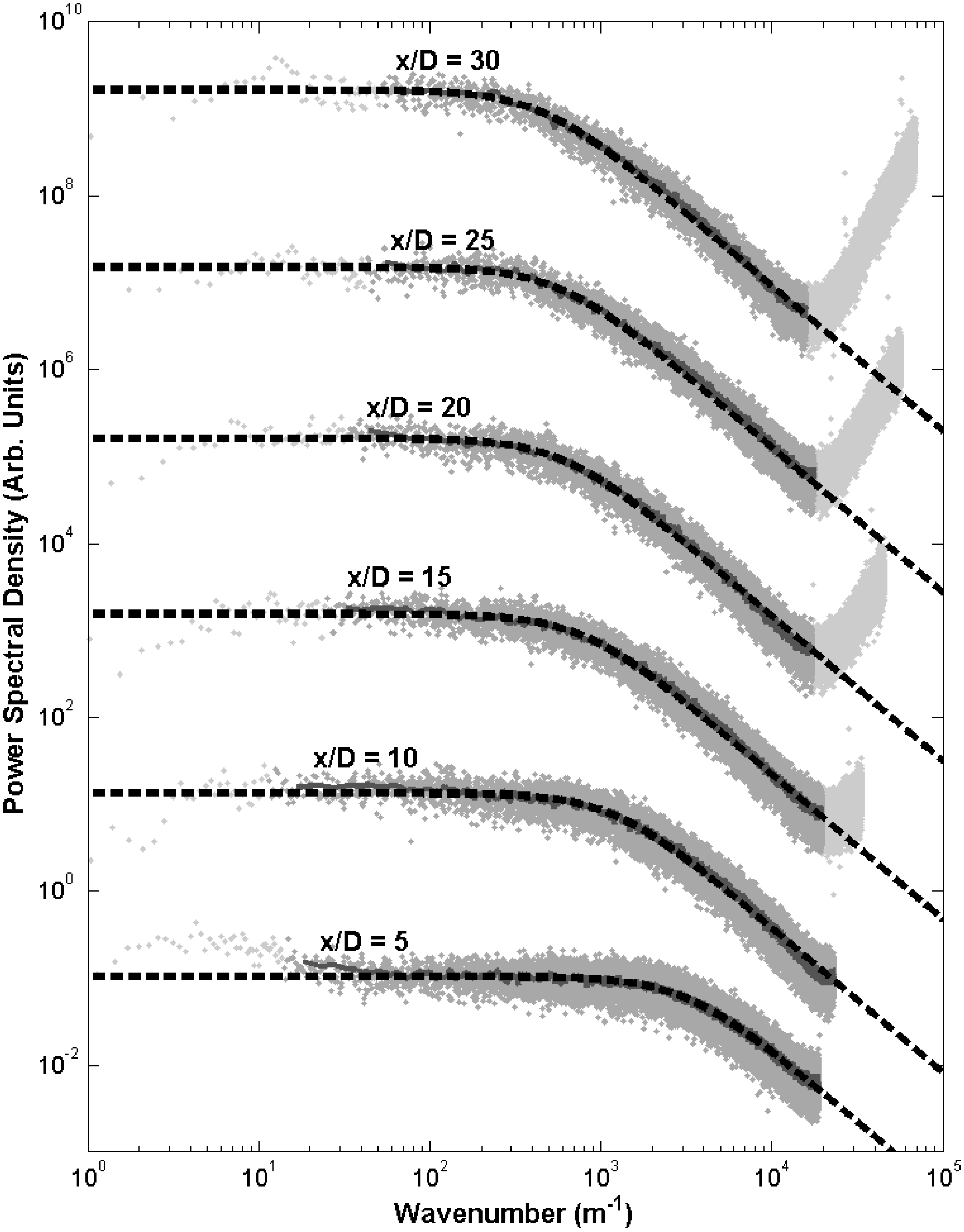

Figure 5.32: Processed turbulent jet spectra from FLDI measurements of P_0 = 30 psia jets. D = 1 mm, at a variety of distances downstream of the nozzle exit. The light gray points represent all of the measured points on the spectra, while the darker gray points correspond to the portions of the spectra where the two photodiode signals are highly coherent. The solid gray lines shows these spectra after smoothing. The dashed lines are Von Kármán spectrum fits to these spectra.

Measurements were made with hot-wire anemometry for comparison with these turbulent density spectra. Compared to FLDI, however, limitations upon the frequency response of hot-wire anemometers are quite dramatic. This is due to the natural frequency response of the hot-wire/amplifier combination, which is necessarily low in order to maintain stability of the hot-wire Wheatstone bridge and amplifier transfer functions.

The transfer function of the hot-wire bridge and amplifier is measured by applying a square-wave signal to one leg of the hot-wire bridge and measuring the resulting spectrum (Fig. 5.33). The Fourier transform of a square wave gives a series of delta functions at odd harmonics of the square wave frequency, rolling off as 1/*f*. For a square wave at 1024 Hz, the first spike will occur at 1024 Hz, the second spike at 3072 Hz, and so on. These frequencies are sampled from the measured square-wave test spectrum of the hot-wire anemometer to find the system response.

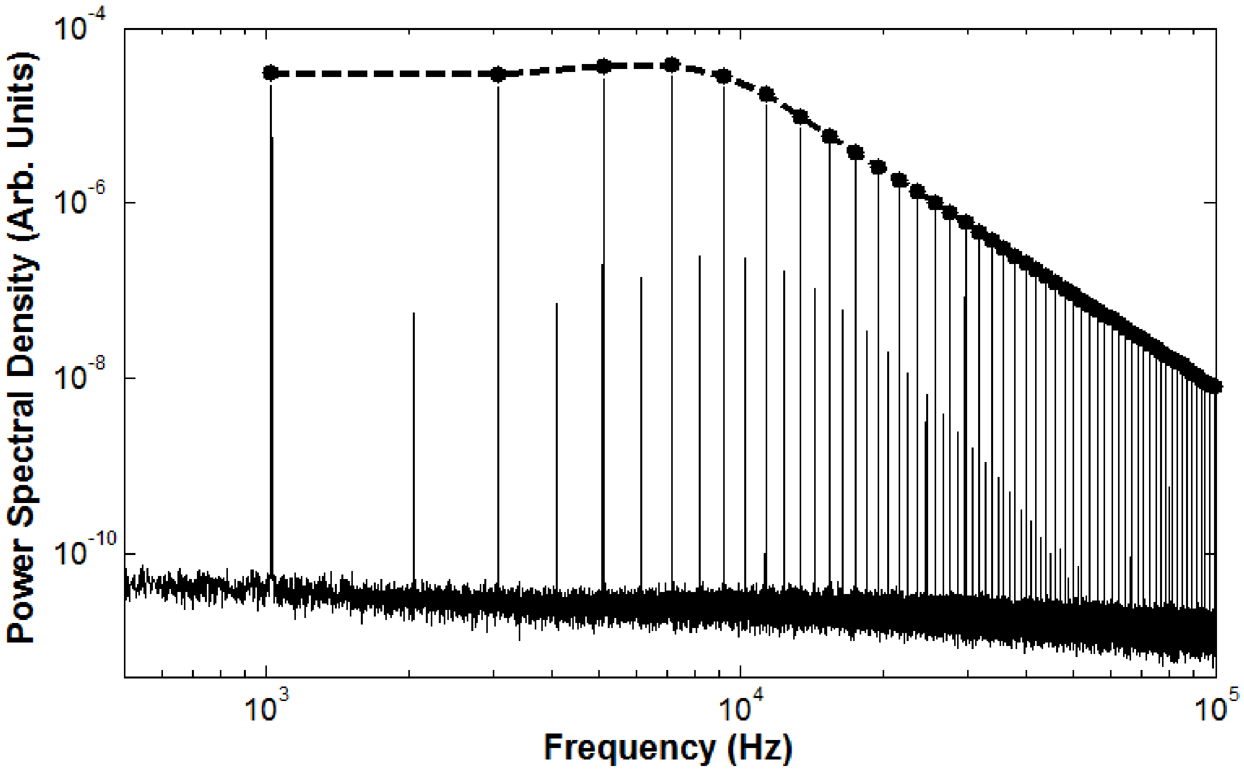

Figure 5.33: Square-wave test of the TSI IFA300 hot-wire anemometer equipment used in this research. There is no flow for this particular spectrum. The points represent the square-wave delta functions, and the dashed line is a fit to these data.

Because the hot-wire anemometer fundamentally measures heat transfer from the hot-wire probe, rather than directly measuring velocity as is desired, the wire's transfer function changes based on the convective heat transfer coefficient of the flow around the wire. This coefficient is a function of the Nusselt number of the flow, which is itself a strong function of Reynolds number. As a result, the system transfer function is heavily dependent on the velocity of the flow. The transfer function of the wire must be found for a range of flow velocities that covers the velocities encountered in the experiment.

For the testing presented here, this calibration was performed in a similar manner to the velocity calibration above: square-wave tests were performed at a range of distances downstream of the jet nozzle exit, from x/D = 10 to 50. A fit to the measured square-wave points on the spectra of these tests was performed to estimate the system transfer function. The results of these tests are shown in Fig. 5.34.

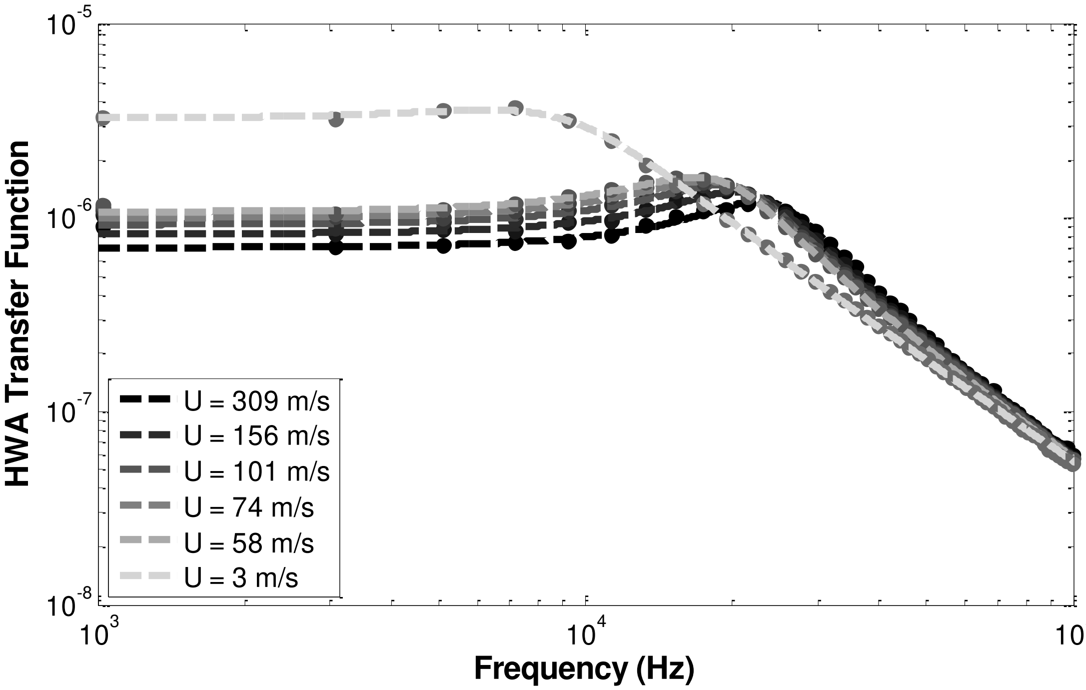

Figure 5.34: HWA transfer function fits for the calibration testing from *x/D* = 10 (*U* = 309 m/s) to *x/D* = 50 (*U* = 58 m/s) in steps of 10 diameters, with baseline (*U* = 3 m/s, due to natural convection from hot-wire).

The fit used for these results is of the following form (Eq. 5.13):

$$\mathrm{H}(f)=\mathrm{A}\left[\frac{1}{\left(1-\left(\frac{f}{f_c}\right)^2\right)^2+\frac{1}{\mathrm{Q}^2}\left(\frac{f}{f_c}\right)^2}\right]^{\frac{\mathrm{B}}{2}} \tag{5.13}$$

Unlike the standard first-order transfer function described in the TSI anemometer documentation, the fit used here takes the form of a second-order low-pass filter with an added term, *B*. This term accounts for the effect of the turbulence rolloff on the apparent slope of the system transfer function, and it is ignored during deconvolution by being set to 1. *A* is the amplitude of the filter, and it is also ignored during deconvolution by setting it to 1, so the resulting filter is of unity gain. f_c is the cutoff frequency of the filter. *Q* is a factor related to the damping of the filter, and defines how "peaky" the filter is. This accounts for the hump seen in the transfer functions near the cutoff frequency in Fig. 5.34, which cannot be corrected using a first-order transfer function model. The factors ultimately used in the deconvolution process, f_c and *Q*, were found to vary as semilogarithmic functions of flow velocity. Plots of these factors are shown in Fig 5.35.

Deconvolution of this transfer function from measured spectra is a simple process, described in Eq. 5.14:

$$\begin{aligned}\mathrm{H}(f)&=\sqrt{\frac{1}{\left(1-\left(\frac{f}{f_c}\right)^2\right)^2+\frac{1}{\mathrm{Q}^2}\left(\frac{f}{f_c}\right)^2}}\\ \mathrm{S}_{filt}(f)&=\frac{\mathrm{S}(f)}{\mathrm{H}(f)^2}\\ &=\mathrm{S}(f)\left[\left(1-\left(\frac{f}{f_c}\right)^2\right)^2+\frac{1}{\mathrm{Q}^2}\left(\frac{f}{f_c}\right)^2\right]\end{aligned} \tag{5.14}$$

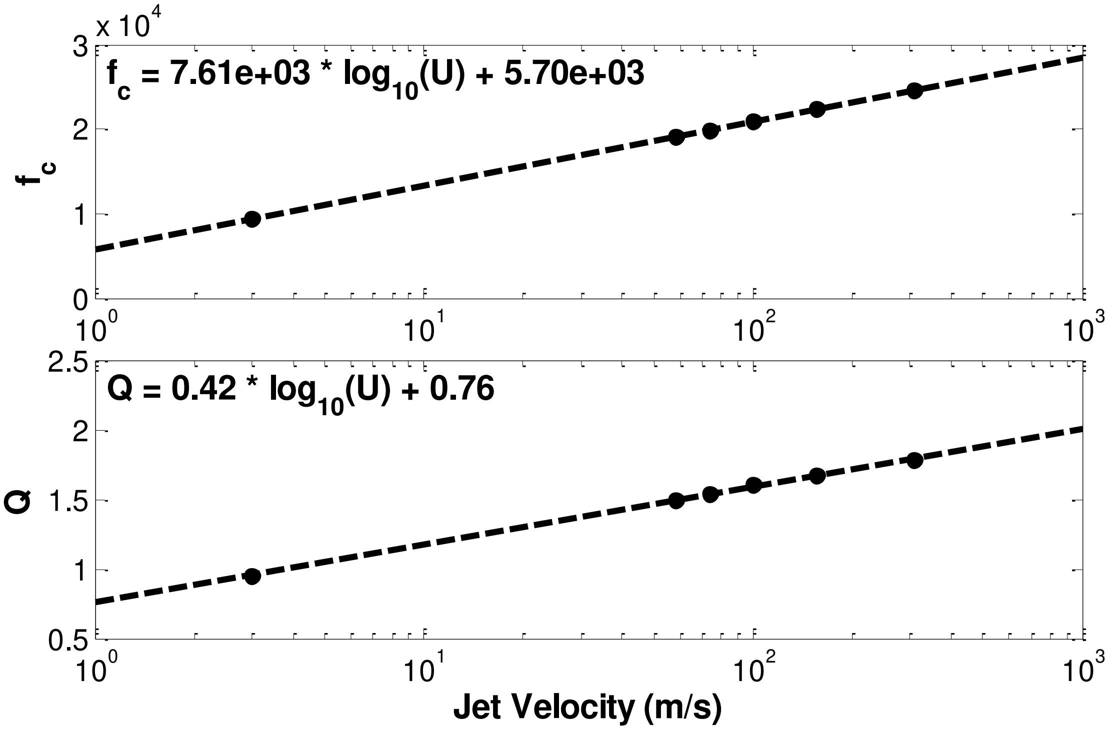

Figure 5.35: Hot-wire anemometer transfer function factors. The jet velocity shown here is the centerline velocity of the jet calculated at each distance downstream of the nozzle exit.

An example of this deconvolution process is seen in Fig. 5.36a, which shows the raw hot-wire spectrum with the square-wave signal superimposed, and in Fig. 5.36b, which shows the same spectrum with the estimated system transfer function deconvolved from the signal. Note that while this method can compensate for the effect of the hot-wire system's transfer function on the slope of the turbulence rolloff, it cannot overcome limitations on the maximum frequency visible above the noise floor. If the signal falls below the noise floor at 100 kHz, then even with the deconvolution presented here, the signal will be meaningless above this frequency. This poses a fundamental limit on the maximum frequency observable in a signal by a given anemometer setup. Only methods which directly improve the frequency response of the HWA instrument, such as using finer hot-wire probes or moving to higher overheat ratios, can raise this frequency limit.

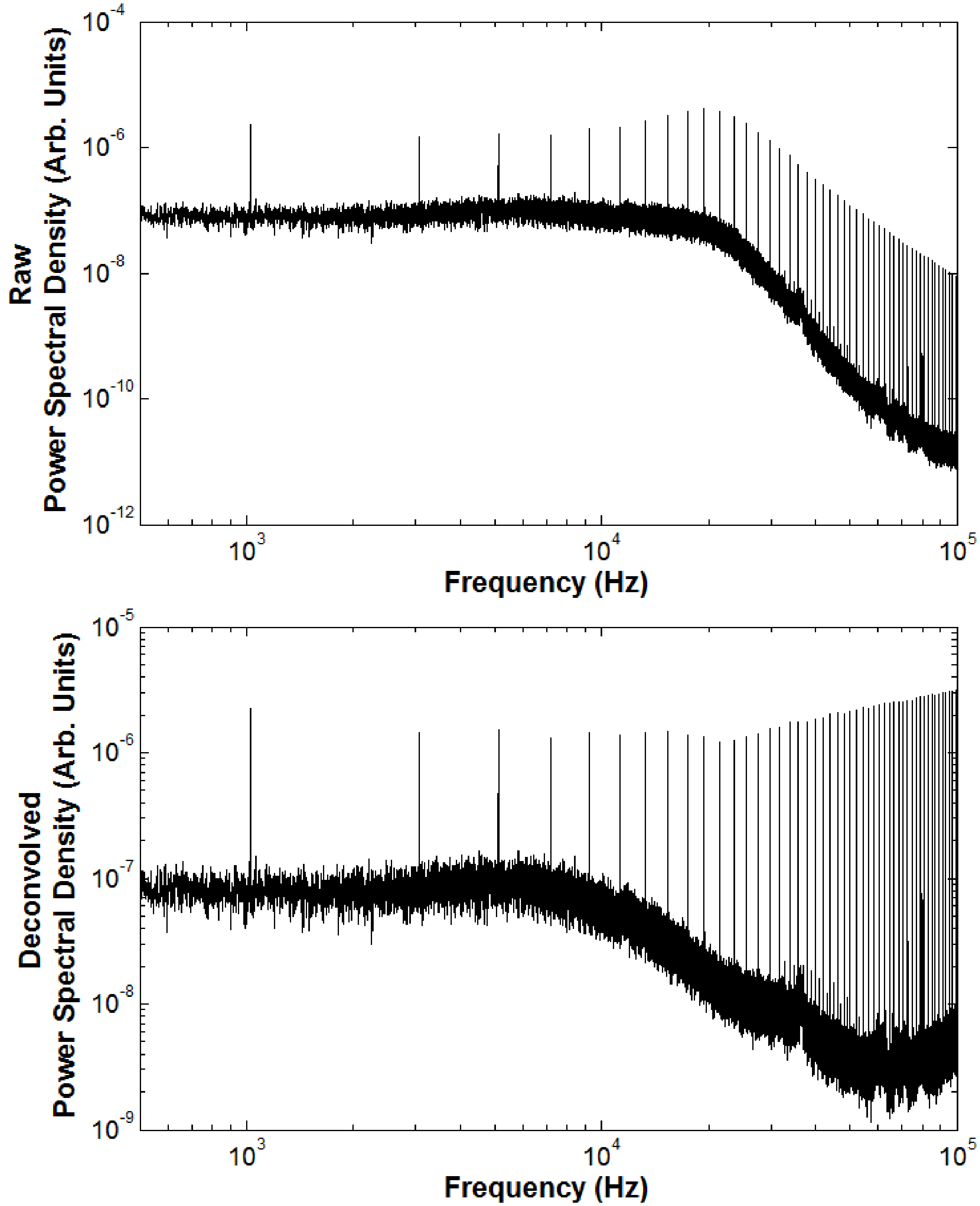

Figure 5.36a,b: a) Raw HWA spectrum of the turbulent air jet at *x/D* = 20, and b) the same spectrum with the estimated transfer function deconvolved. After deconvolution, the response of the system to the square-wave excitation is generally flat across the processed spectrum, while it peaks around 20 kHz and then rapidly rolls off at higher frequencies in the raw spectrum.

As with the FLDI instrument, measurements of turbulence spectra were made downstream in the turbulent jet by hot-wire anemometry. Raw spectra are shown in Fig. 5.37, and spectra processed by deconvolution of the hot-wire anemometer transfer function are shown in Fig. 5.38. The spectra are normalized and spaced in two-decade intervals for clarity. The lightest dots for each plot show the full power spectrum of the signal. Darker spots highlight the signal of interest. The dark line is a smoothed power spectrum from each data set, and the dashed line represents a Von Kármán spectrum fit to the data as with the FLDI tests.

Note the rapid rolloff of the raw HWA signal, which severely restricts the maximum resolvable wavenumber in the spectrum. Additionally, electronic noise spikes that are close to the noise floor "leak" into the deconvolved signal. This can be seen clearly in the x/D = 15 case, where noisy spikes cover much of the spectral range of interest.

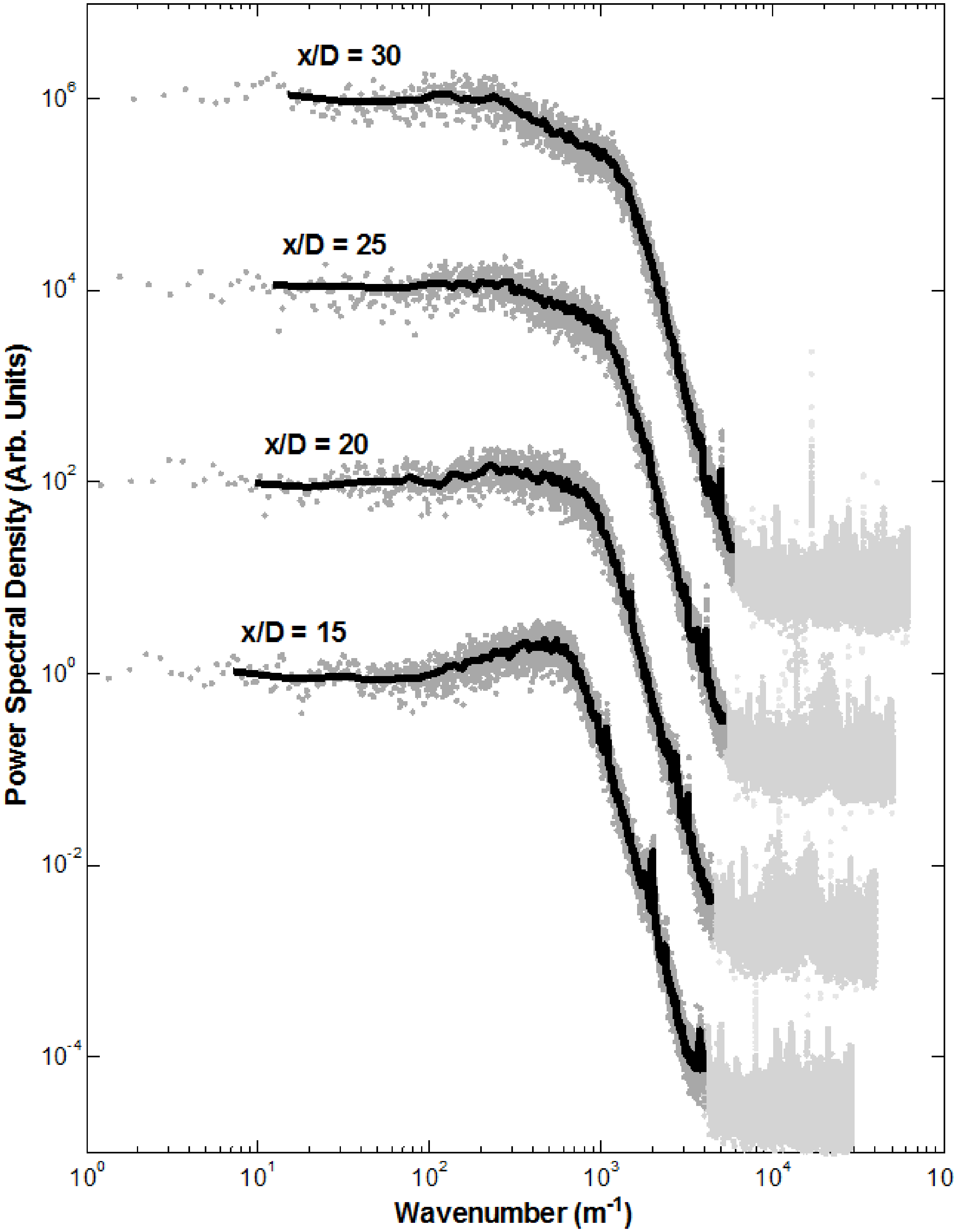

Figure 5.37: Raw HWA spectra measured in the round turbulent jet. D = 1 mm, P_0 = 30 psia. The light gray points represent all of the measured points on the spectra, while the darker gray points correspond to the portions of the spectra which are above the electronic noise floor prior to processing of the spectra. The solid gray line shows these spectra after smoothing. The dashed lines are Von Kármán spectrum fits to these spectra.

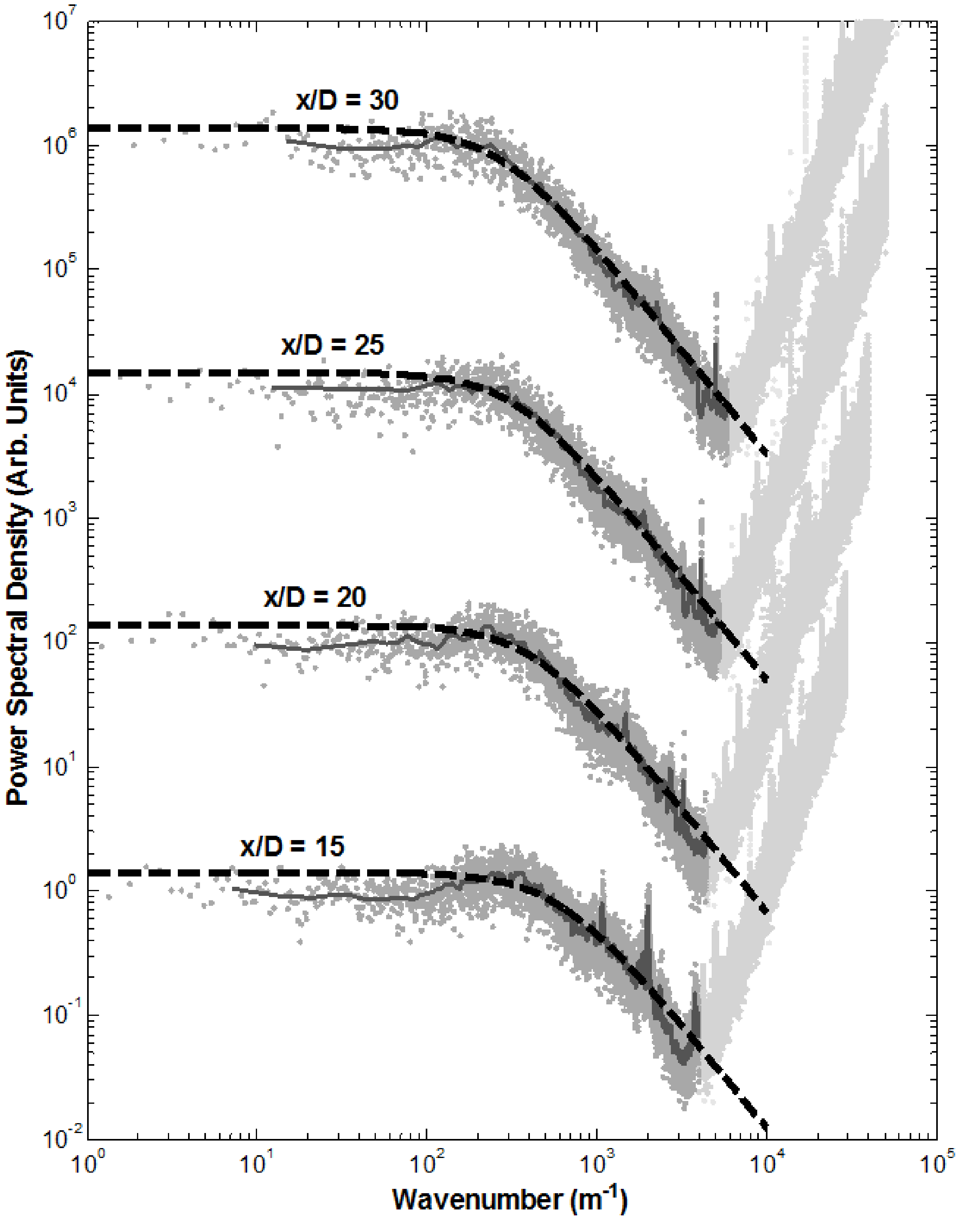

Figure 5.38: Processed HWA measurements of spectra in the round turbulent jet. *D* = 1 mm, *P_0* = 30 psia. The light gray points represent all of the measured points on the spectra, while the darker gray points correspond to the portions of the spectra which are above the electronic noise floor prior to processing of the spectra. The solid gray line shows these spectra after smoothing. The dashed lines are Von Kármán spectrum fits to these spectra.

Jet turbulence spectra measured by hot-wire anemometry and the FLDI instrument are compared in Figs. 5.39-42, with Von Kármán spectrum fits overlaid. Both spectra appear to roll off similarly to Kolmogorov's -5/3 spectrum. The outer scale wavenumber at which this rolloff occurs, k_0, seems to happen earlier for the hot-wire anemometry data, however, while the outer scale wavenumber for the FLDI spectra does not change much. In both cases, the outer scale wavenumber lies between $1/\sigma_{jet}$, a wavenumber that corresponds to the diameter of the jet plume at that location downstream, and $1/D$, a wavenumber corresponding to the diameter of the nozzle exit.

In the spectra from x/D = 15 to 25, beyond a wavenumber of around 10^4 m^{-1}, the FLDI spectra deviate from the -5/3 slope, rolling off faster. This may be the turbulence entering the dissipation regime, or perhaps incorrect assumptions about the FLDI system transfer function for the jet. Unfortunately, the spectrum reaches the noise floor shortly beyond this wavenumber, so it is not possible to determine the cause of this deviation with these data.

The higher frequency limit of the FLDI instrument is seen in the much-higher wavenumbers it can measure compared to the hot-wire anemometer. In the high-speed case at x/D = 15, the FLDI instrument sees a full order of magnitude higher wavenumber spectrum than does the HWA, seeing out to k = 30,000 m^{-1} compared to the 3,000 m^{-1} limit of the hot-wire. At x/D = 30, the maximum wavenumber measured by FLDI is 20,000 m^{-1}, compared to the hot-wire at 5,000 m^{-1}. Using higher-power lasers to achieve greater signal-to-noise ratios, the FLDI instrument should be capable of measuring even higher wavenumbers if necessary.

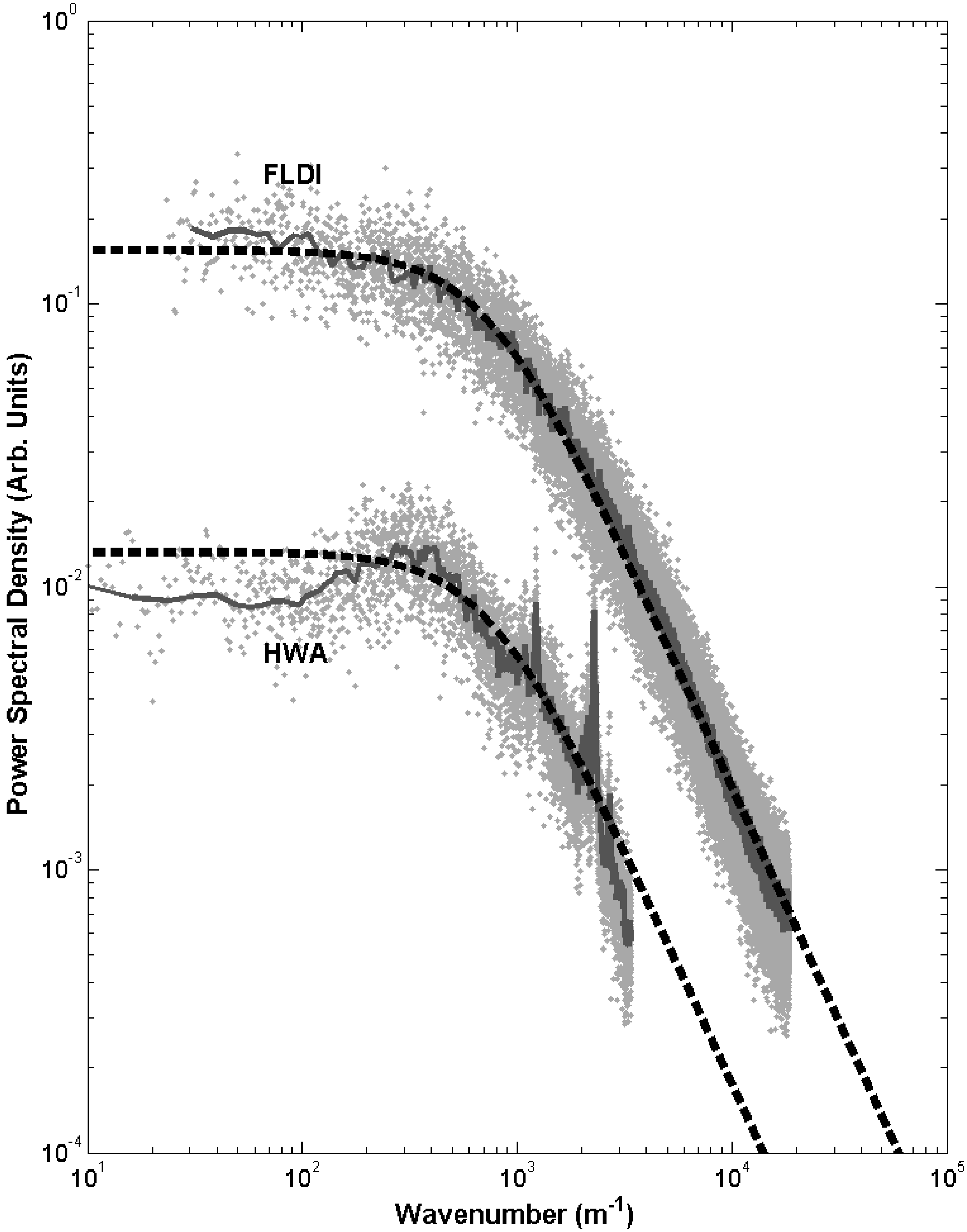

Figure 5.39: Comparison of HWA and FLDI results at *x/D* = 15. The gray points represent the actual measured points on the spectra, while the solid gray line shows these spectra after smoothing. The dashed lines are Von Kármán spectrum fits to these spectra.

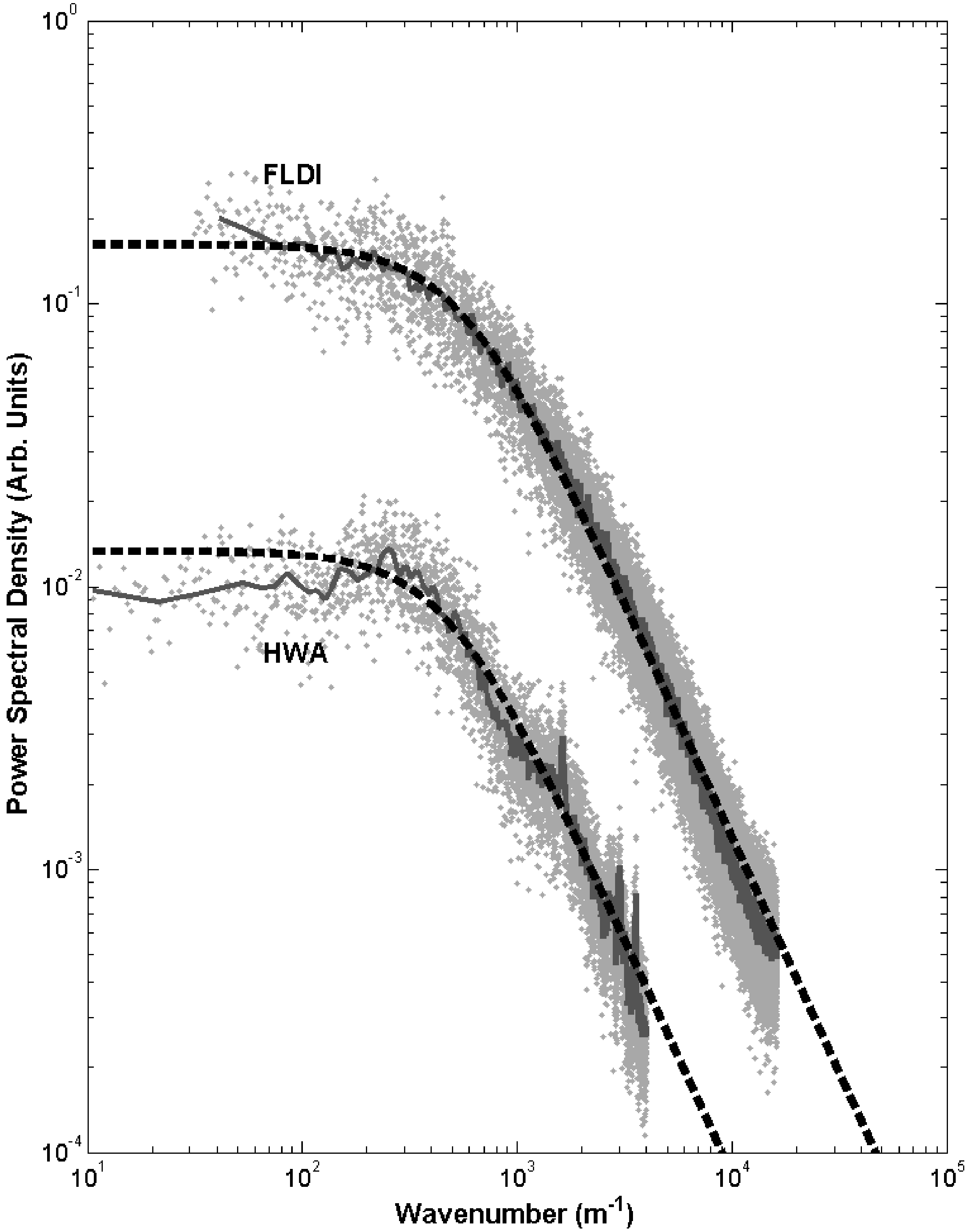

Figure 5.40: Comparison of HWA and FLDI results at *x/D* = 20. The gray points represent the actual measured points on the spectra, while the solid gray line shows these spectra after smoothing. The dashed lines are Von Kármán spectrum fits to these spectra.

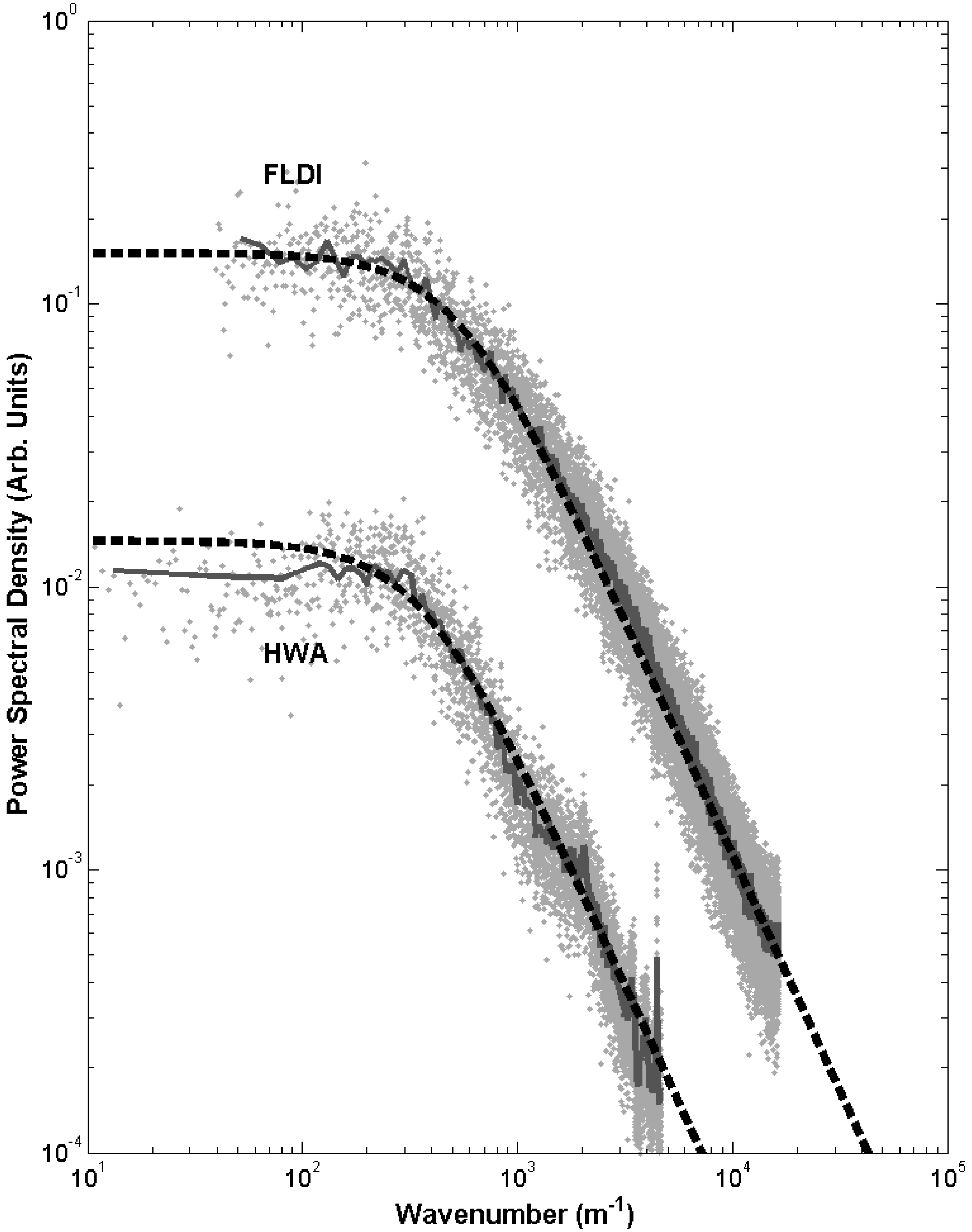

Figure 5.41: Comparison of HWA and FLDI results at *x/D* = 25. The gray points represent the actual measured points on the spectra, while the solid gray line shows these spectra after smoothing. The dashed lines are Von Kármán spectrum fits to these spectra.

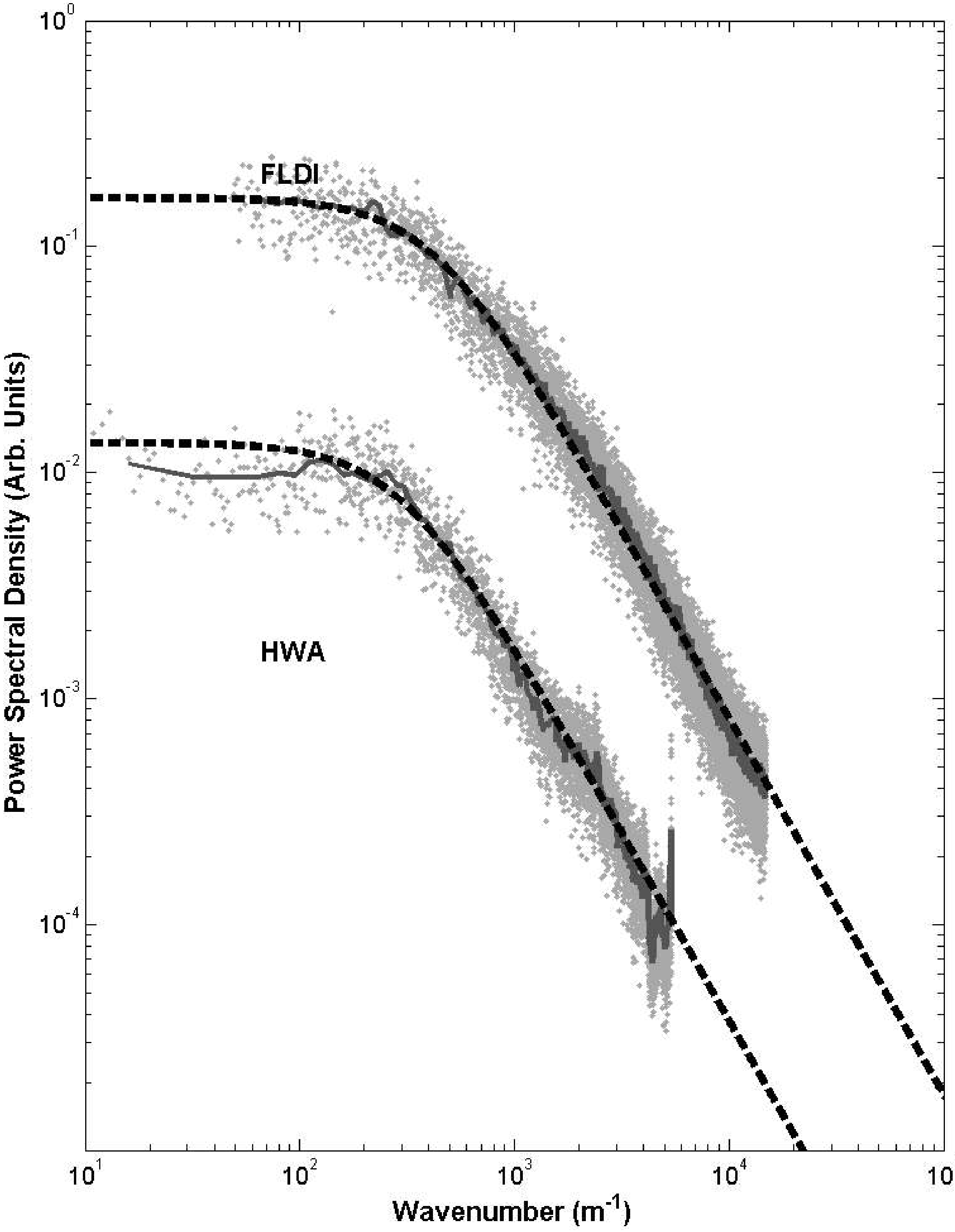

Figure 5.42: Comparison of HWA and FLDI results at $x/D = 30$. The gray points represent the actual measured points on the spectra, while the solid gray line shows these spectra after smoothing. The dashed lines are Von Kármán spectrum fits to these spectra.

5.4 PSUSWT & Hypervelocity Tunnel 9 FLDI Experiments

Measurements of turbulence intensity and spectra were taken in both the Penn State supersonic wind tunnel (PSUSWT) and the AEDC Hypervelocity Tunnel 9. For both cases, rather than using a Von Kármán spectrum fit, a more general spectrum fit of a similar form was used, allowing for changes in the slope of the spectrum, rather than assuming the -5/3 Kolmogorov rolloff. This spectrum is described in Eq. 5.15:

$$E(k) = \frac{A^2}{(k^2 + k_0^2)^{-B/2}} \tag{5.15}$$

Here, A is the amplitude of the spectrum fit and B is the slope of the spectrum at high wavenumber. In the case that $B = -5/3$, this fit is identical to that provided by the Von Kármán spectrum.

5.4.1 PSUSWT Testing

Testing in the Penn State supersonic wind tunnel was performed at Mach 3, and the optics were moved along the beam axis such that the best focus of the beam occurred at various distances from the tunnel centerline to the windows. Spectra are presented in Figs. 5.44-47, showing data taken at tunnel centerline (3 inches from the window), 2.5 inches, 2 inches, and finally 1.5 inches from the window. The boundary layer thickness for the run conditions used here is approximately 1 inch. A diagram of the FLDI system shifted from tunnel centerline into the boundary layer is shown in Fig. 5.43. The beam diameter is exaggerated here for clarity.

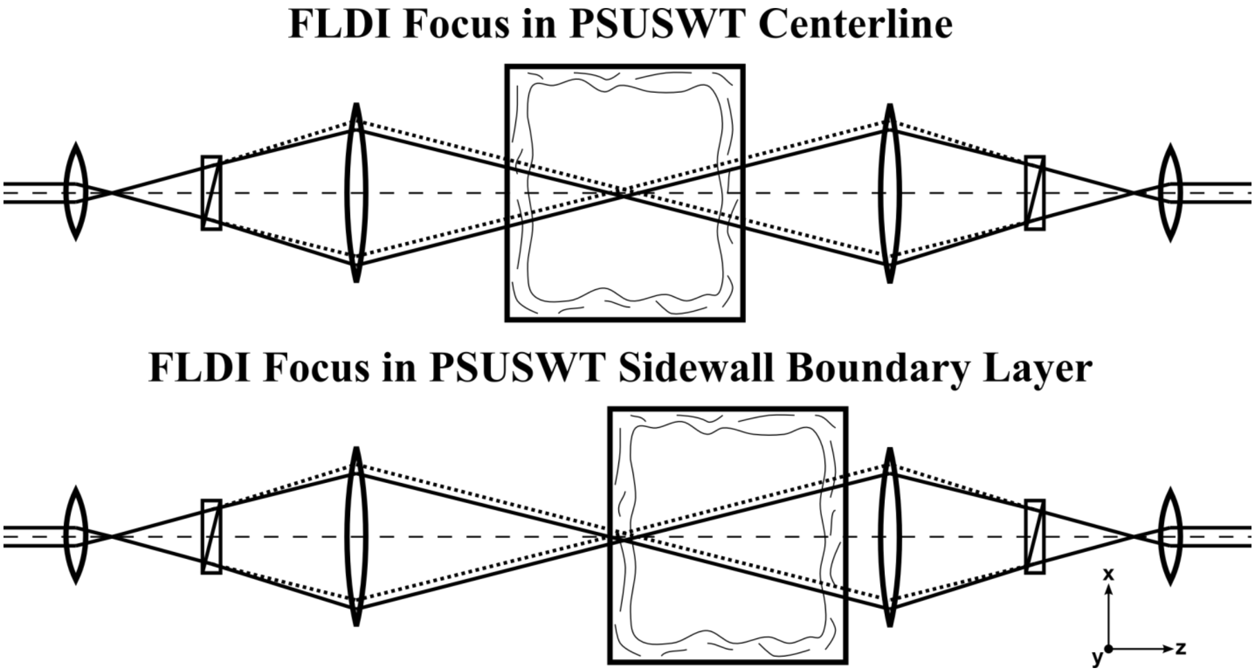

Figure 5.43: Diagram of FLDI system in PSUSWT with FLDI focus shifted between tunnel centerline and into the boundary layer. Translation of the FLDI system along the optical axis shifts the focus of the system from the tunnel centerline towards the tunnel wall boundary layers, resulting in reduced rejection of boundary layer signals.

As the beam focus approaches the window, the signal from the tunnel sidewall boundary layer becomes much more distinct, which is seen in the steepening slope of the spectrum fit, and the increase in the amplitude of the signal over the noise floor. The spectrum fits shown in the scaled power spectra are marked with a + symbol at the outer scale wavenumber, k_0, predicted by the fitting routine.

The difference in the shape of the spectrum from tunnel centerline to the edge of the tunnel sidewall boundary layers is quite small. This implies that the instrument, in the embodiment used for these experiments, does not reject the boundary layer noise enough to easily differentiate any differences that might exist between the shape of the boundary layer and freestream turbulence spectra. However, a small hump is visible above a wavenumber of 1000 m^{-1} in the spectrum measured at the tunnel centerline. This hump is not large enough to reliably resolve using the general spectrum fit from above, however a Von Kármán fit to it is shown in Fig. 5.48.

The density of the flow in the PSUSWT at the Mach 3 run conditions used in these tests is 0.6 kg/m^3, or ~50% of atmospheric density. The density-based freestream turbulence intensity calculated using the data taken at tunnel centerline is about 0.3%. This leads to a velocity-based freestream turbulence intensity of less than 0.1% based on the Strong Reynolds Analogy discussed in section 3.8.1 of this thesis.

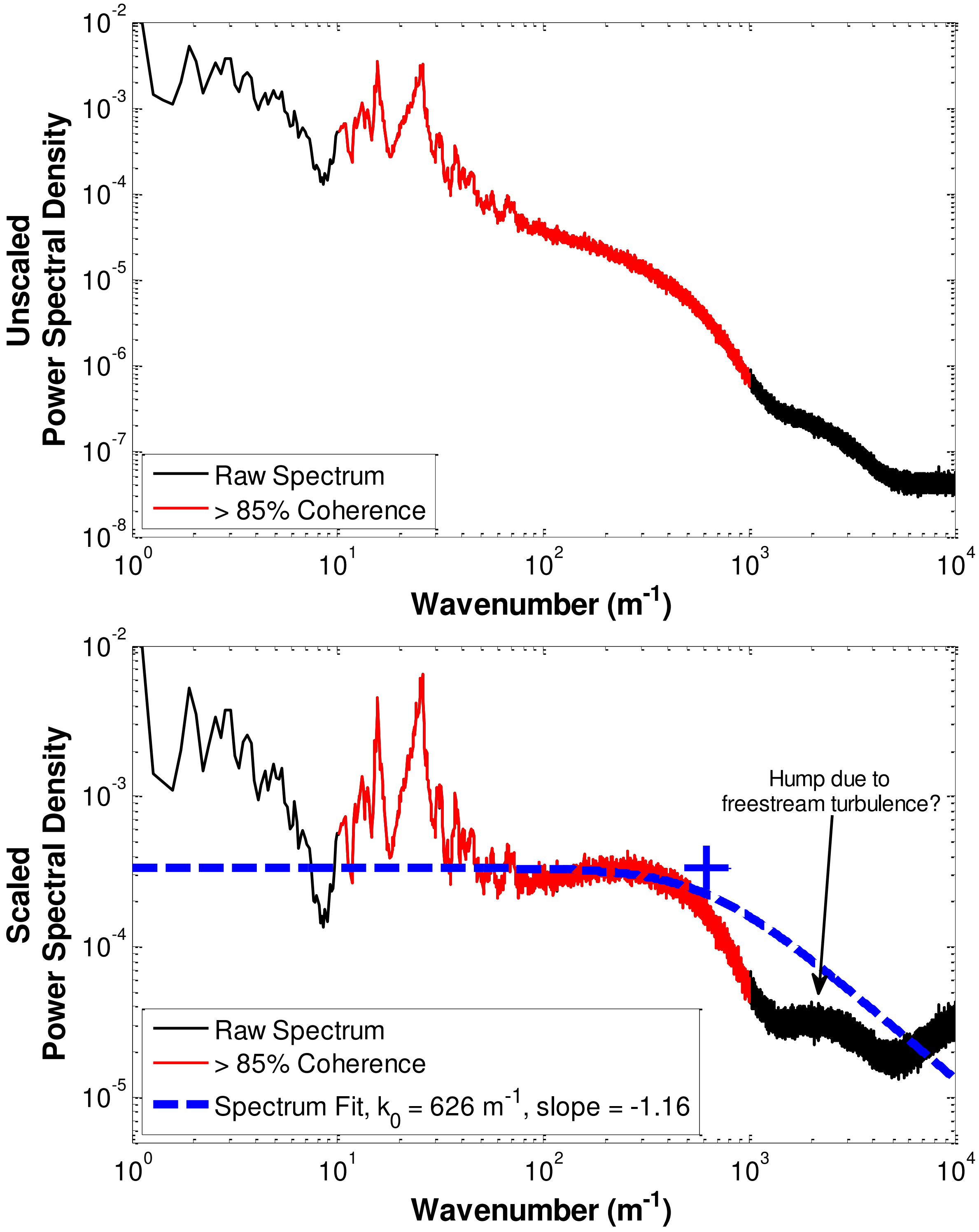

Figure 5.44: PSUSWT Mach 3 testing, with the FLDI focus at tunnel centerline (3 inches from window)

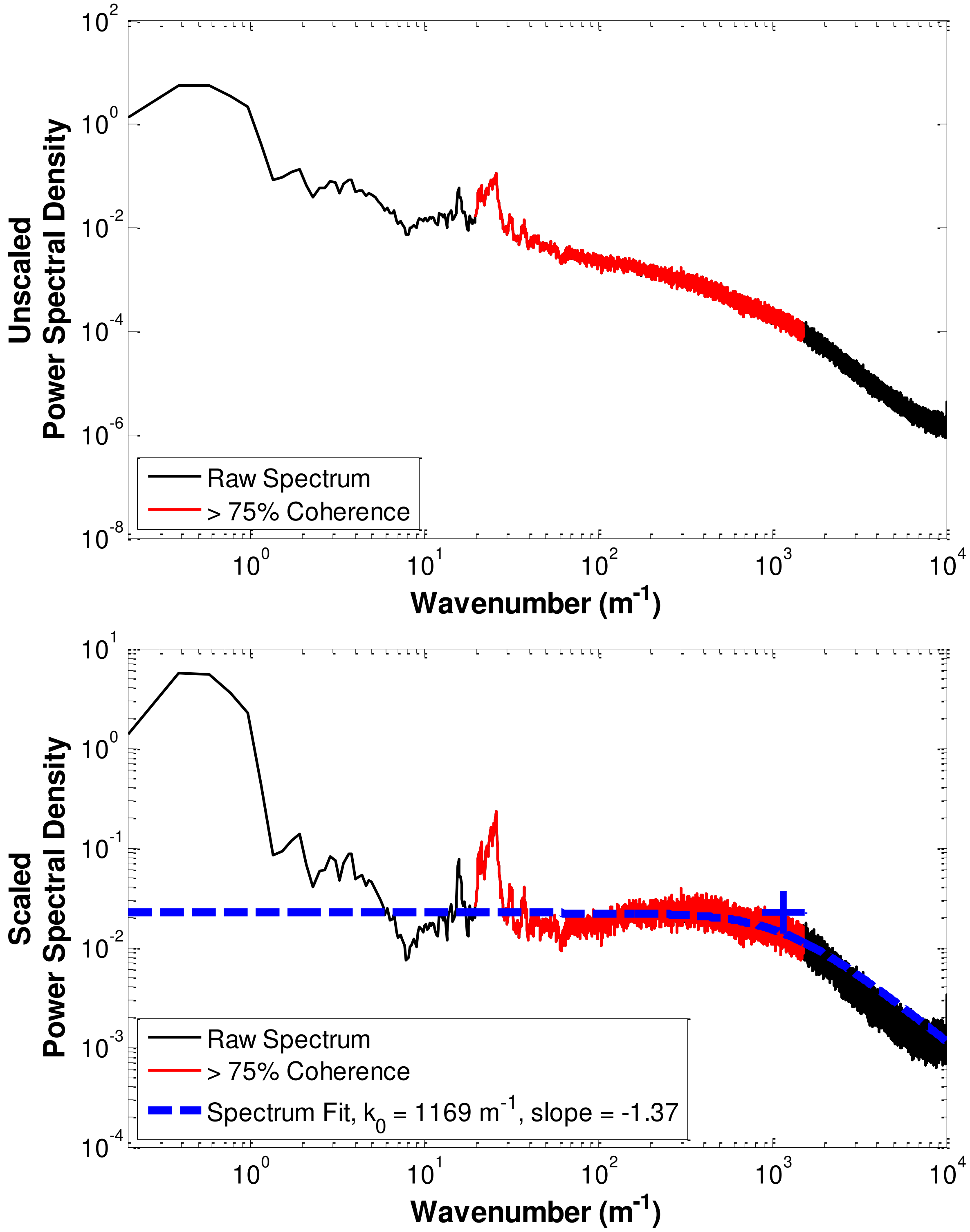

Figure 5.45: PSUSWT Mach 3 testing, with the FLDI focus at 2.5 inches from window

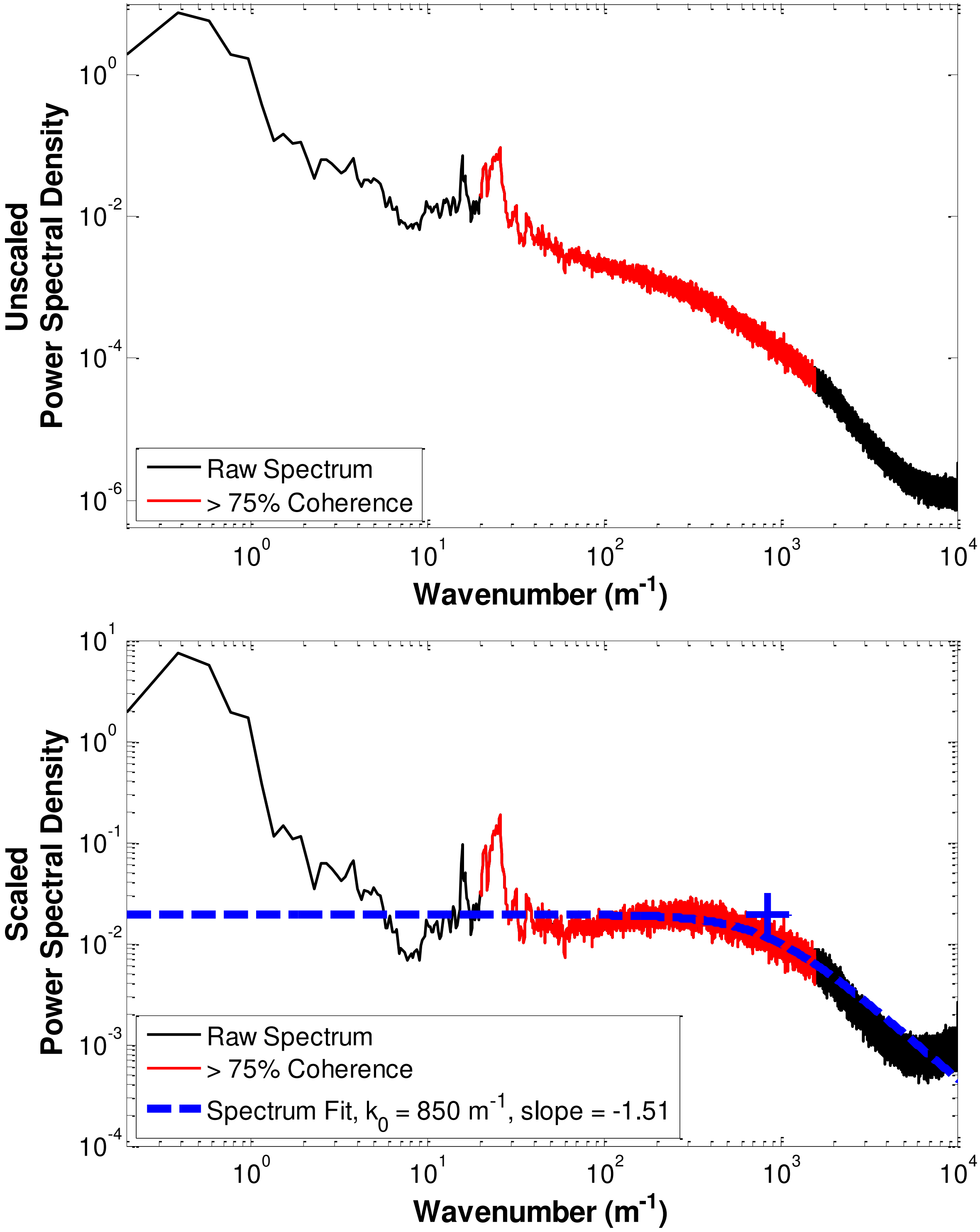

Figure 5.46: PSUSWT Mach 3 testing, with the FLDI focus at 2 inches from window

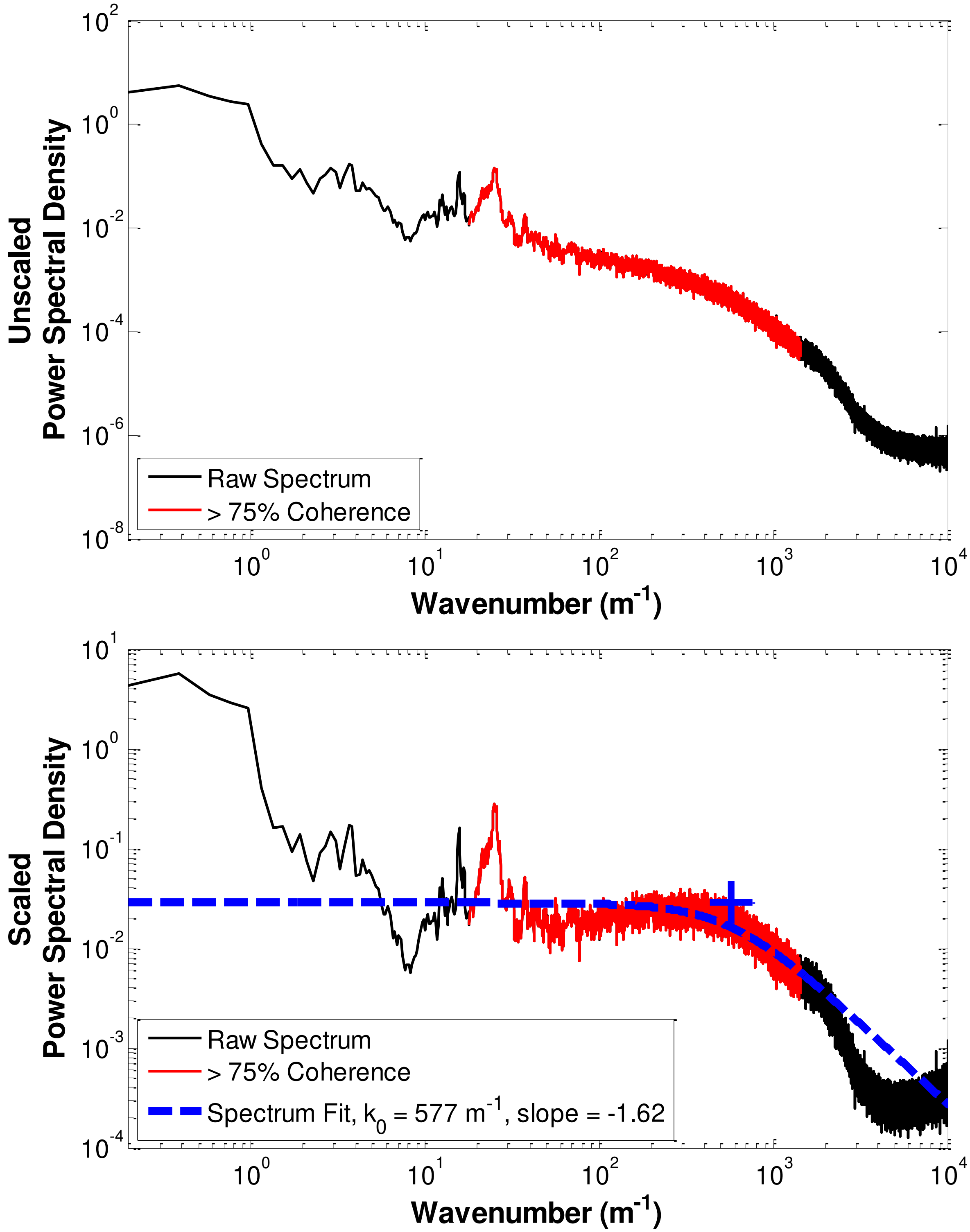

Figure 5.47: PSUSWT Mach 3 testing, with the FLDI focus at 1.5 inches from window

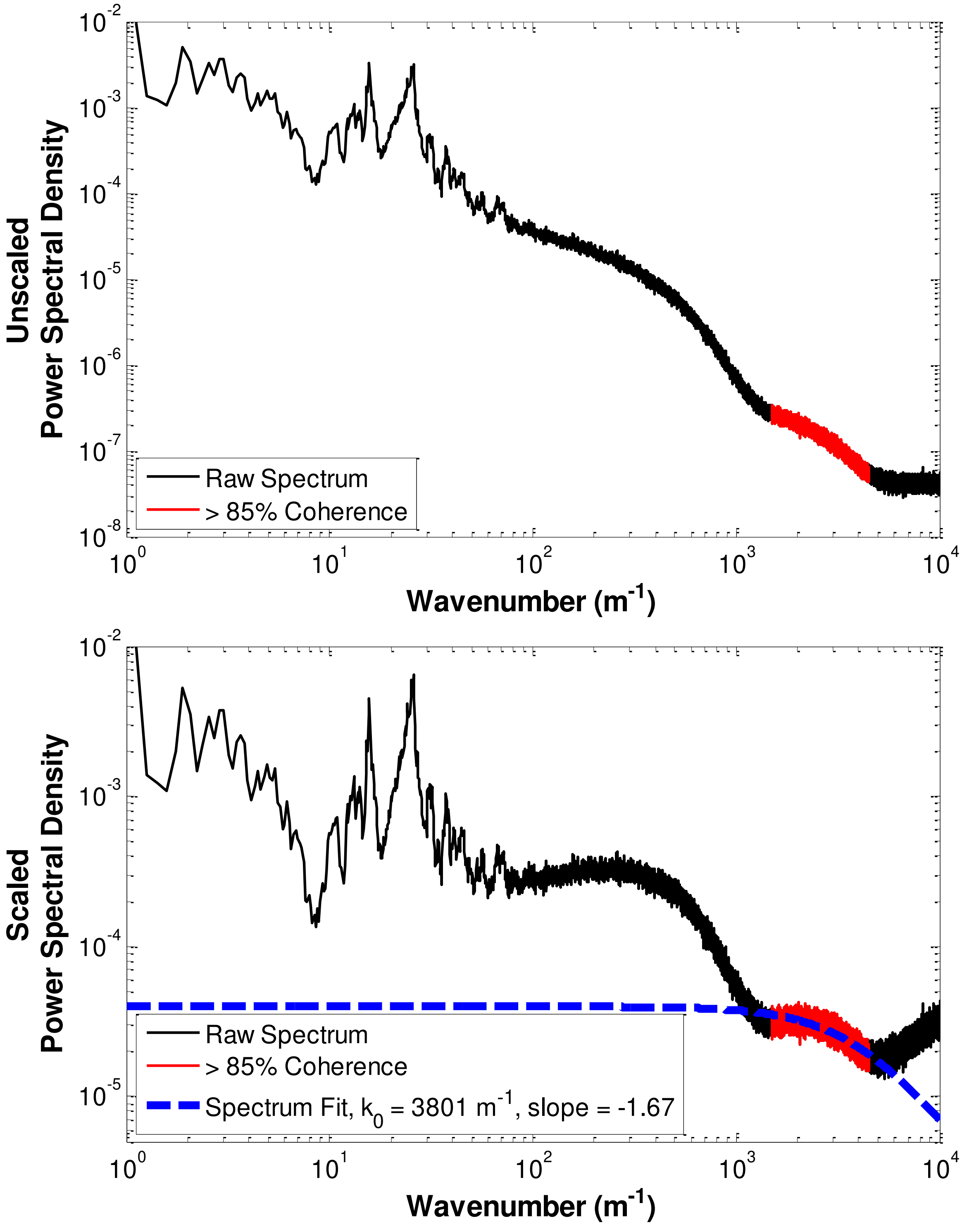

Figure 5.48: PSUSWT Mach 3 testing, along tunnel centerline, Von Kármán fit to second hump in spectrum, potentially related to freestream turbulence.

5.4.2 AEDC Hypervelocity Tunnel 9 Tests

Four tests of the FLDI instrument were conducted in Hypervelocity Tunnel 9 in October 2013. Unfortunately, of these, only one run successfully acquired data. This successful run was at Mach 10, with a unit Reynolds number of 5×10^6 ft^{-1} (16.4×10^6 m^{-1}). The FLDI Sanderson prism was set to 20 mils deflection, and with the 200 mm focal length field lenses used in the Tunnel 9 testing, this corresponds to a beam separation of 156 μm. The raw output voltage of the FLDI instrument from this run is shown in Fig. 5.49.

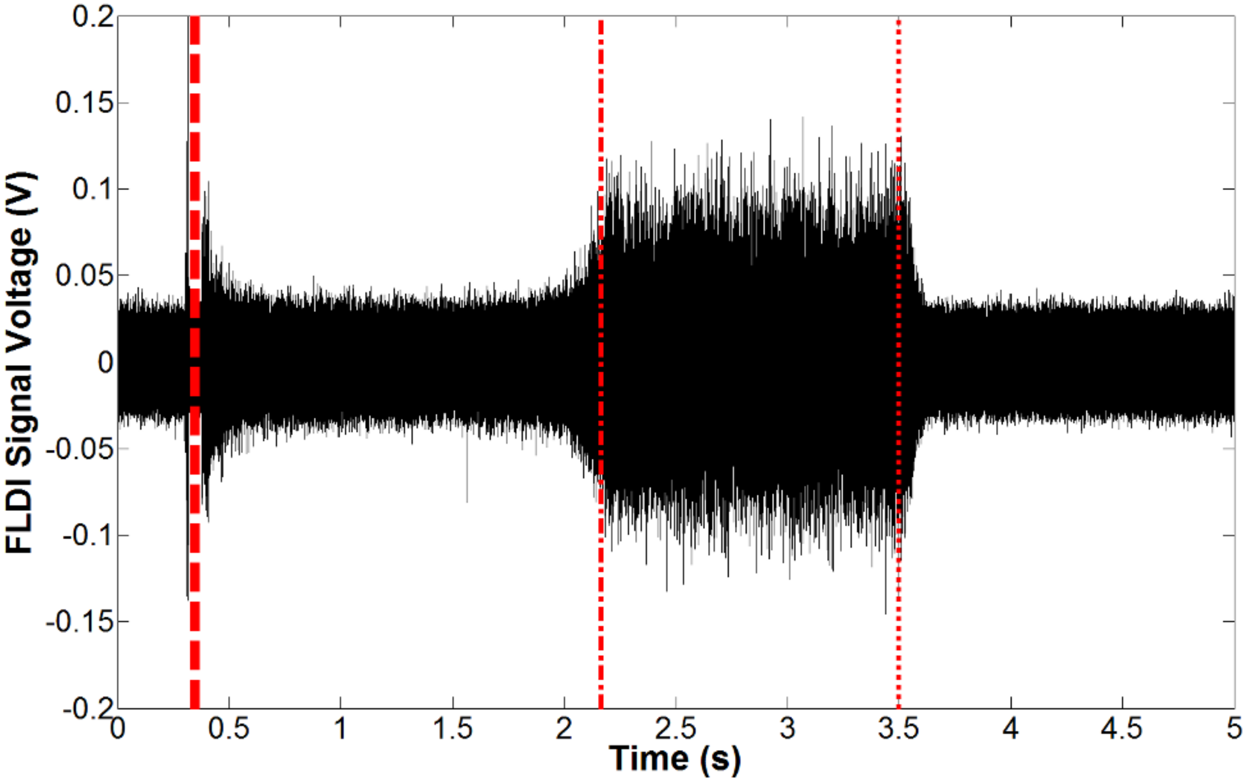

Figure 5.49: Raw FLDI signal from Tunnel 9 run 3738. The thick dashed line on the left of the plot is just before tunnel startup, the dash-dotted line is where the flow transitions from the pre-burst flow to the run condition, and the dotted line is at the end of the useful flow, where the shutdown shock passes through the tunnel.

Here, the startup shock can be seen passing the beams at the first dashed line. The signal before this line demonstrates the relative amplitude of the electronic noise compared to the rest of the signal. After the starting shock passes through, the tunnel undergoes what Tunnel 9 personnel call the “ablator” or “pre-burst” flow, where a set of plugs in the tunnel erodes away to ramp the tunnel up to its run condition. The dash-dotted line shows the start of the full Mach 10 run-condition flow of the tunnel. This lasts for slightly less than one and a half seconds. Finally, the dotted line shows when the tunnel shuts down, and the FLDI beams become obscured, reducing the signal back to the level of the electronic noise floor.

Spectra measured in each of these conditions are shown in Fig. 5.50. The wavenumber calculated for these spectra uses the freestream velocity at full run speed, which is approximately 1470 m/s at the run conditions described above.

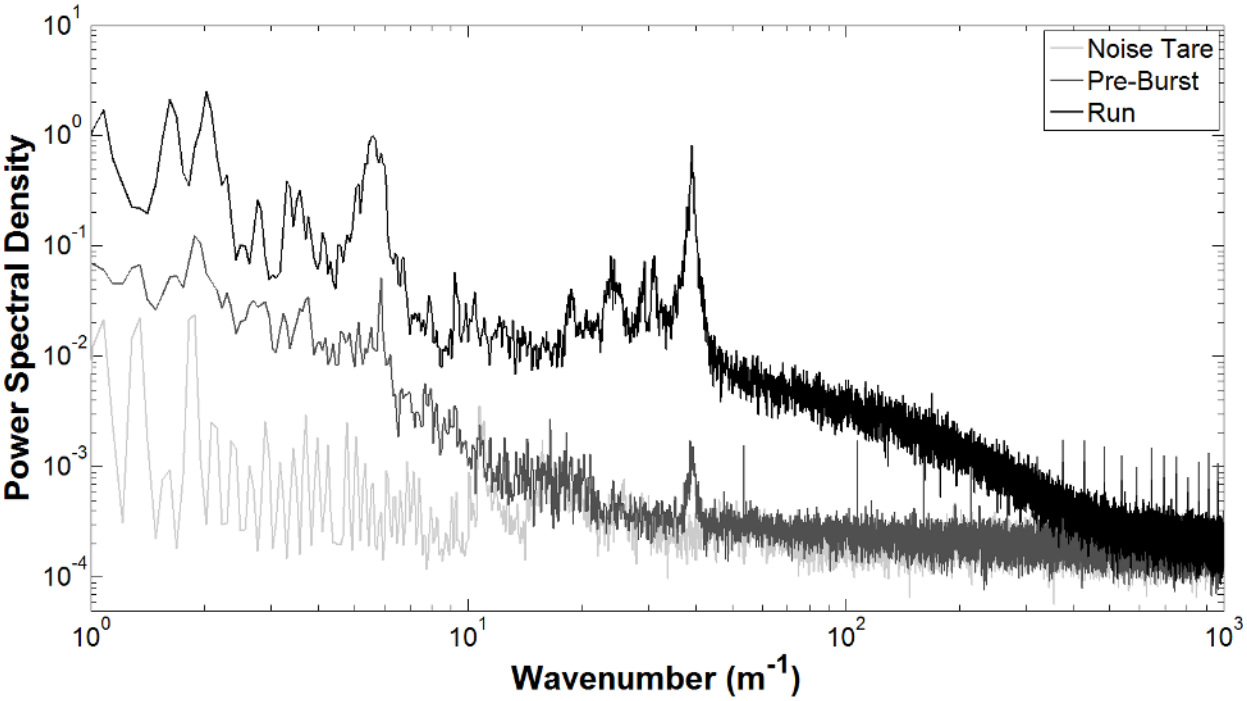

Figure 5.50: Raw Tunnel 9 spectra, run 3738, showing the background noise, a spectrum calculated from the pre-burst portion of the flow, and a spectrum calculated at full run conditions. The run condition spectrum is at least an order of magnitude above the background noise for most of the spectrum.

The raw and processed spectra from the ablator flow are shown in Fig. 5.51, while the raw and processed spectra from the run-condition flow are shown in Fig. 5.52. The power spectrum of the electronic noise in the Tunnel 9 data is shown in Fig. 5.53. In both the ablator flow and run-condition spectra, a distinct, dominant spike is seen at a wavenumber around 40 m^{-1} ($f \sim 9.4$ kHz), however it is not seen in the electronic noise spectrum. This spike may be due to a resonance in the tunnel or other source of flow noise. A turbulent spectrum shape can be seen in the run-condition spectrum, which appears to roll off as a Kolmogorov spectrum or perhaps slightly faster. Further testing is necessary, with higher signal-to-noise ratio, to determine the nature of both of these phenomena.

The turbulence in the tunnel is extremely weak during the ablator flow, as the freestream density is very low. Even at full run-condition flow, the freestream density is approximately 0.0385 kg/m^3, which only about 3% of atmospheric density. This significantly restricts the expected signal level, which is proportional to freestream density. To compensate for the low levels, Stanford Research SR560 battery-backed preamplifiers were used to amplify the FLDI signals. For run 3738, the preamps were set to 2000x gain and were DC-coupled to allow normalization of the signal using the method described in the Procedures section of this thesis.

The turbulence intensity calculated from the coherent portion of the run-condition spectrum is 7.7%, which is comparable to the pitot pressure fluctuation level of 4.9% measured by Bounitch[76] at a unit Reynolds number of 2×10^6 ft^{-1} (6.6×10^6 m^{-1}). The FLDI test was performed at a higher unit Reynolds number, accounting for the higher turbulence level. Converted to a velocity turbulence intensity by the strong Reynolds analogy, this gives a velocity turbulence intensity of approximately 0.2%. When the density TI% is normalized by the dynamic pressure factor $\gamma M^2/2$, this gives a value of 0.11%, comparable to data listed by Lafferty and Norris for Tunnel 9[77].

These very limited results for AEDC Hypervelocity Tunnel 9 comprise more of a feasibility demonstration for the FLDI instrument than actual wind-tunnel calibration data. The FLDI instrument was "piggy-backed" with another wind-tunnel experiment, and the available time was heavily constrained by circumstances. Nevertheless, it was demonstrated that an FLDI turbulence signal could be obtained despite low-freestream-density conditions. There is little doubt, given enough time to improve the signal-to-noise ratio of the instrumentation and run more tests, that freestream turbulence data of wind-tunnel-calibration quality can be measured using FLDI. There is much room for improvement in the boundary-layer rejection ability of the FLDI instruments used in both the PSUSWT and Tunnel 9, as the system *f*-numbers for these tunnels were around *f*/9.8 and *f*/14.4 respectively.

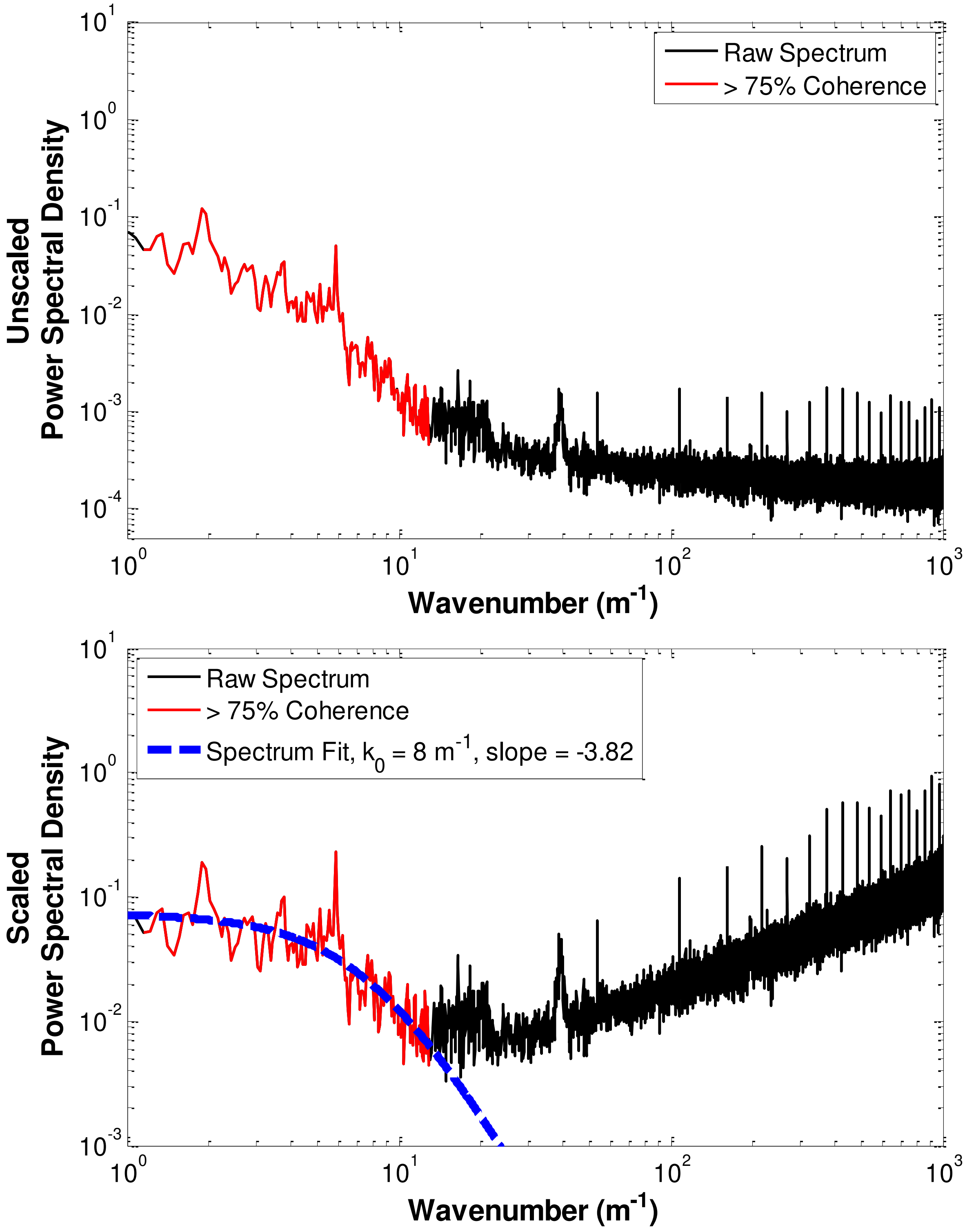

Figure 5.51: Tunnel 9, run 3738 pre-burst spectrum

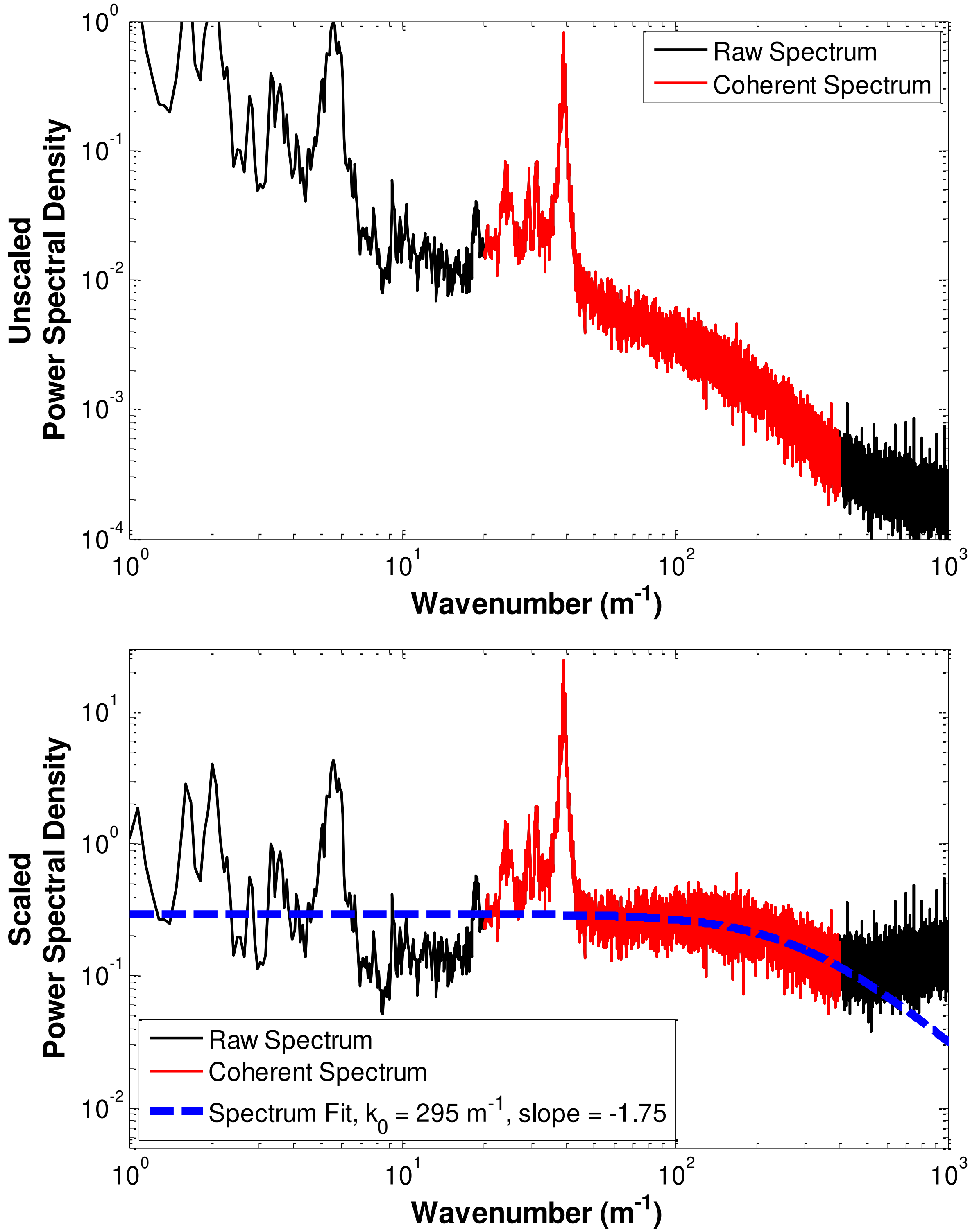

Figure 5.52: Tunnel 9 run 3738 run-condition spectrum

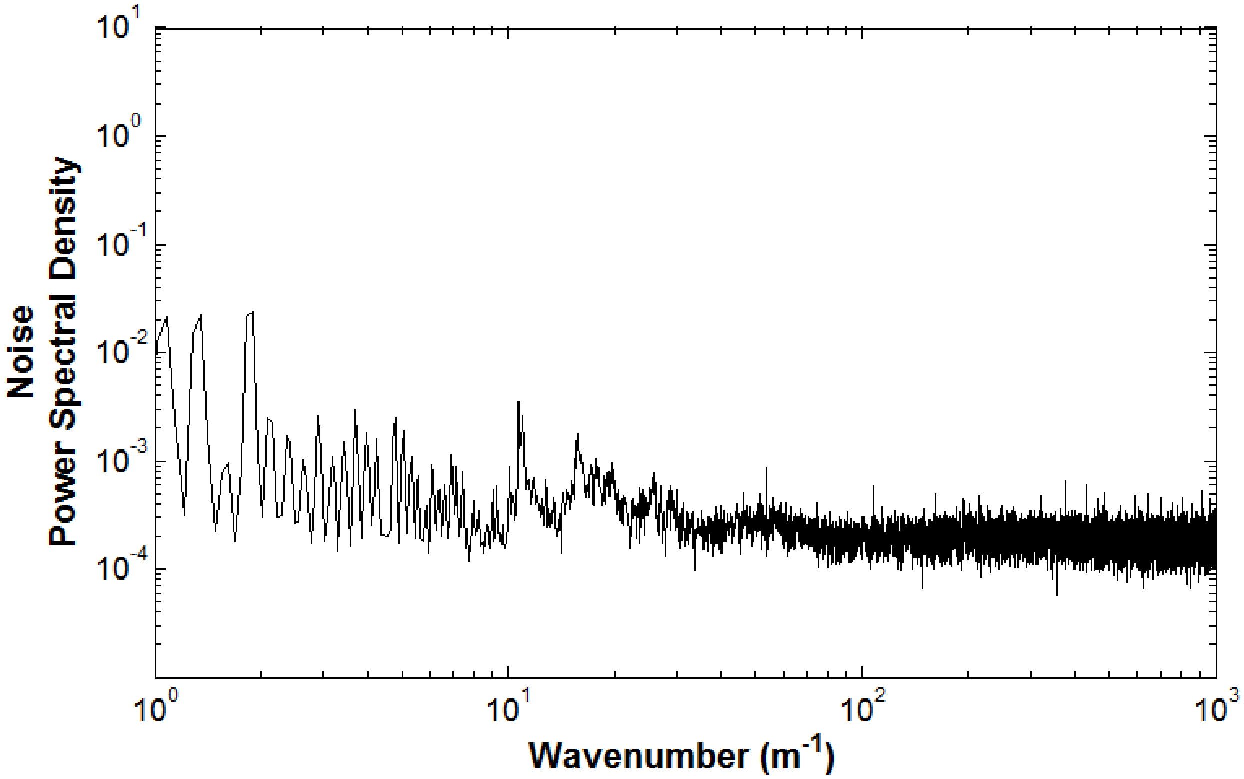

Figure 5.53: Tunnel 9 run 3738 noise spectrum

Chapter 6: Conclusions and Recommendations for Future Research

6.1 Summary and Conclusions

The issue examined in this thesis is the optical, non-intrusive measurement of turbulence in the core flow of high-speed wind tunnels, despite having to look through thick turbulent boundary layers on both wind tunnel windows. High-speed turbulent flows naturally produce density fluctuations that can, in principle, be detected by the optical phase shift they cause. (In low-speed flows, seeding by way of temperature or injection of a different gas can have the similar effect of a passive scalar.)

Popular flow diagnostics like PIV and LDV, which depend upon particle seeding of the flow, lack the frequency response to yield meaningful high-frequency spectra in high-speed flows. Thus an optical instrument that can make such measurements in a wind tunnel, despite sidewall boundary-layer "noise," is an important addition to the available tools for measuring turbulence.

There are known optical instruments that already attempt to do this, for example the crossed-beam schlieren (CBS) technique. This approach succeeds for turbulent flows not having additional surrounding turbulent noise. However, the CBS approach was examined here for the wind-tunnel core flow measurement of interest, and was found unable to sufficiently reject sidewall boundary-layer turbulence.

A little-known interferometer instrument that also competes to make this measurement is the Focusing Laser Differential Interferometer (FLDI). It is a type of shearing interferometer whose twin coherent light beams are focused to a small "sampling volume." Invented in the 1970s but not well developed, it has been the subject of only a handful of recent studies, however it was successfully used by Parziale to measure the tunnel freestream disturbance levels in the Caltech T5 reflected shock tunnel[50].

In this thesis, the FLDI is seen as the best-available candidate to measure turbulence in high-speed wind tunnels. An attempt is therefore made to build a firm theoretical basis for this instrument using polarization-interferometry theory and optical transfer-function analysis.

It was discovered that FLDI measures turbulence spectra that are convolved with transfer functions related to the small separation distance between the twin coherent FLDI light beams, and to the effective f/number or beam convergence angle of these beams. This convergence to a sharp focus in the turbulent flow being measured allows the FLDI to perform spatial filtering on the flow, thus rejecting contributions to the measured signal away from a small focal volume. Deconvolution of the FLDI's optical transfer function then allows an estimate of the true turbulent spectrum and turbulence intensity of a flow under investigation.

Numerical simulations of the FLDI response to "simple" turbulent flows demonstrated the roll-off of the instrument's response to turbulence with distance away from the focal volume, an essential feature for measurements in a wind-tunnel core flow. This response was found to be a strong function of the type of turbulent flow under investigation.

Next, experiments were performed. These experiments primarily used a small round turbulent air-jet to gauge the actual response of a real FLDI instrument. Results compared well with the theoretical prediction, for example, of the shape and rate of signal roll-off as a function of non-dimensional distance from the instrument's focal volume.

The FLDI instrument yielded measurements of turbulence intensity and spectra of the round turbulent air-jet that are comparable to published data for such jets. However, since few turbulent air-jet spectra exist in the literature, hot-wire anemometry was used to measure new spectra for comparison with the FLDI results.

The straightforward ability of the FLDI to measure turbulence spectra up to at least the MHz frequency range is a powerful feature of the instrument. While the energy at these frequencies is typically low, resolving the profile of the turbulence spectra at high frequencies is important for accurate modeling of its decay. Traditional instruments such as hot-wire anemometry and particle-based diagnostics (PIV and LDV) have fundamental difficulty measuring such spectra in high-speed flows because their transfer functions are very complicated and difficult to estimate. The FLDI response, on the other hand, is described by three relatively-simple transfer functions for the effects of distance from the beam focus, separation distance of the twin beam foci, and photodiode response to the optical input.

Additional experiments were performed in which the FLDI instrument measured the core-flow turbulence of two high speed wind tunnel facilities: the small supersonic wind tunnel at Penn State and the very large AEDC Hypervelocity Tunnel 9. These experiments demonstrated at least the feasibility of FLDI core-flow turbulence measurements despite strong competing noise from thick turbulent sidewall boundary-layers. Unfortunately the FLDI instrument used in these experiments was limited to small beam convergence angles due to the geometry of its twin birefringent prisms. Thus there is room for considerable future work in measuring high-speed wind tunnel core flows with improved FLDI instrumentation having larger beam convergence angles and maximum beam diameters at the field lenses. In that case, much-better noise rejection away from the interferometer focal volume is expected, compared to what was obtained in the present experiments. For the PSUSWT and T9 tests, the system *f*-numbers were around *f*/9.8 and *f*/14.4, respectively. Doubling the maximum beam diameter or halving the focal lengths of the field lenses would halve these system *f*-numbers, which should be possible with careful choice of optics. Aberrations induced in the FLDI beams by poor lens design will reduce the sensitivity of the instrument and may result in worse performance than with higher *f*-numbers and cleaner beams. Doubling up the 200 mm focal length triplet field lenses used in the T9 testing presented here would give an effective focal length of 100 mm with minimal additional aberration.

Finally, a critically-important feature of the FLDI instrument, used here for the first time, is the infinitely-variable Sanderson birefringent prism in place of the traditional fixed Wollaston prism. Without the delicate adjustability of the Sanderson prism, which determines the twin laser-beam separation distance in the focal volume, the present research effort could not have been conducted.

6.2 Recommendations for Future Work

There are several directions for future research into the focusing laser differential interferometer that would improve understanding of the instrument's response to turbulent flows. The greatest difficulty in modeling of the instrument is in the transfer functions stemming from the interaction between the FLDI beams and turbulent fields. Even in a relatively simple case, such as the response of the FLDI instrument to a fully-developed Gaussian jet, there are many contributing factors to these transfer functions, all of which make verification of the models quite difficult.

A large portion of this difficulty comes from the three-dimensional nature of the turbulent flows examined in this thesis. A technique developed by Thomas[78] and extended by Rampy et al.[79,80] generates artificial two-dimensional "phase screens" that follow Kolmogorov-like spectral characteristics using hair spray applied to glass discs. If two discs are produced and rotated in opposite directions, with one motor's angular velocity being an irrational multiple of the other motor's angular velocity, effectively-infinitely-long turbulence screens are generated. This turbulence screen generation scheme could be combined with the FLDI instrument by placing this turbulence screen along the FLDI beam paths and measuring the instrument's response. This would allow validation of the beam profile transfer functions described by this thesis without the added complexity of the three-dimensionality of true turbulent flows. Additionally, while Rampy and Thomas were primarily concerned with modeling atmospheric turbulence, increasing the rate of rotation of the phase screens should effectively model higher-speed flows, as the disturbances "convect" faster past the FLDI beams.

Another useful experiment would be to measure turbulence spectra without focusing the interferometer beams. Controlling the diameter of the interferometer beams using the field lens aperture stops should give a frequency response similar to that predicted by the Gaussian beam model from above, using the constant diameter of the beam along the length of the test area. Comparison of measured spectra with and without focusing of the interferometer beams would provide insight into the degree to which the focusing of the beams is rejecting unwanted signals.

Further research must be performed to validate (or invalidate) the use of the strong Reynolds analogy to directly compare density and velocity turbulence intensities. The measured turbulence intensities in the jet testing from section 5.3.7 generally agree with one another at an x/D distance greater than about 30 diameters downstream. The density turbulence intensity was found to peak around $x/D = 10$, however, while the velocity turbulence intensity peaked much later, around $x/D = 20$. These findings are in line with published data in the literature, but they do not match with predictions using the strong Reynolds analogy.

The combination of the cross-correlation scheme from the crossed-beam schlieren technique and the focusing ability of the FLDI instrument is a natural extension of this research, and was used by Parziale[51]. This should not only improve rejection of undesired turbulent signal compared to either of these techniques by themselves, but also provide direct measurement of the convective velocity in surveyed flows. This would improve the accuracy of fits to measured turbulence spectra by reducing uncertainty on local flow velocity, and provide an extra useful diagnostic result over those already given by the FLDI instrument. Although the technique is not yet well established in the literature, the use of wavelet transforms and wavelet cross-correlation may further improve the usefulness of measured turbulence spectra by giving information about not only what frequency content the turbulence contains but also when that energy appears in the data.

References

1. Hunt, J. C. R., Durbin, P. A., and Wu, X. "Interactions between freestream turbulence and boundary layers." *Center for Turbulence Research*, Annual Research Briefs 1998, pp 113-124.

2. Schneider, S. P., "Effects of High-Speed Tunnel Noise on Laminar-Turbulent Transition," *J. Spacecraft and Rockets*, Vol. 38, No. 3, May-June 2001, pp 323-333.

3. Uberoi, M. S. "Effect of Wind-Tunnel Contraction on Free-Stream Turbulence." *J. Aero. Sci.*, Vol. 23, No. 8 (1956), pp. 754-764.

4. Laufer, J., "Aerodynamic Noise in Supersonic Wind Tunnels," *J. Aero. Sci.*, Vol. 28, No. 9, Sept. 1961, pp. 685-692.

5. Lighthill, M. J., "On Sound Generated Aerodynamically. I: General Theory," *Proc. Royal. Soc. Lond. A*, Vol. 211, 1952, pp. 564-587.

6. Lighthill, M. J., "On Sound Generated Aerodynamically. II: Turbulence as a Source of Sound," *Proc. R. Soc. Lond. A*, Vol. 222, 1954, pp. 1-32.

7. Ffowcs-Williams, J. E., and Maidanik, G., "The Mach Wave Field Radiated by Supersonic Turbulent Shear Flows," *J. Fluid Mechanics*, Vol. 21, No. 4, 1965, pp. 641-657.

8. Saric, W. S., "Boundary-Layer Receptivity to Freestream Disturbances", *Annu. Rev. Fluid Mech.*, Vol. 34, 2002. pp. 291-319

9. Morkovin, M. V., Reshotko, E., and Herbert, T. "Transition in open flow systems—a reassessment." *Bull. Am. Phys. Soc.* 39:1882. 1994.

10. Reed, H. L., and Saric, W. S., "Linear stability theory applied to boundary layers," *Annu. Rev. Fluid. Mech.* 1996. 28:389-428

11. Schlichting, H., "Über die Theorie der Turbulenzentstehung," *Forschung auf dem Gebiet des Ingenieurwesens A*, 1949/50, Vol. 16, Issue 3, pp 65-78

12. Kendall, J. M., "Wind Tunnel Experiments Relating to Supersonic and Hypersonic Boundary-Layer Transition," *AIAA Journal*, vol. 13, issue 3, pp. 290-299. March, 1975.

13. Kovasznay, L. S. G., "The hot-wire anemometer in supersonic flow," *J. Aero. Sci.*, vol. 17, pp 565-573. 1950.

14. Laurantzon, F., Tillmark, N., and Alfredsson, P. H., "What does the hot-wire measure?," Technical Report, KTH Mechanics, 2012.

15. Stine, H. A., and Scherrer, R. “Experimental investigation of the turbulent-boundary-layer temperature-recovery factor on bodies of revolution at Mach numbers from 2.0 to 3.8,” *NACA Technical Note 2664*. Ames Aeronautical Laboratory. March, 1952.

16. Smits, A. J., Hayakawa, K. and Muck, K. C., “Constant Temperature Hot-wire Anemometer Practice in Supersonic Flows,” *Experiments in Fluids Vol. 1*, Springer-Verlag, pp. 83-92, 1983.

17. Lomas, C. G. “Fundamentals of Hot-Wire Anemometry”

18. Smid, I., Akiba, M., Vieider, G., and Ploechel, L., “Development of tungsten armor and bonding to copper for plasma-interactive components,” *J. Nucl. Mat.*, vol. 258–263, Part 1, pp. 160–172. October, 1998.

19. PGM Database. http://www.pgmdatabase.com/jmpgm/main.jsp

20. Walker, D. A., and Ng, W. F., “Experimental comparison of two hot-wire techniques in supersonic flow,” *AIAA Journal*, Vol. 27, No. 8, pp 1074-1080, August, 1989.

21. Masutti, M., Spinosa, E., Chazot, O., and Carbonaro, M., "Disturbance level characterization of a hypersonic blowdown facility", *AIAA Journal*, Vol. 50, No. 12, pp 2720-2730, 2012.

22. Schneider, S. P., “Hypersonic and Hypervelocity Ground Test Facilities: A Brief Informal Summary,” *Purdue University*, Nov. 2007.

23. Lafferty, J. F., and Norris, J. D., “Measurements of Fluctuating Pitot Pressure, ‘Tunnel Noise’, in the AEDC Hypervelocity Wind Tunnel No. 9,” AIAA Paper 2007-1678, February 2007.

24. Bounitch, A., Lewis, D. R., and Lafferty, J. F., “Improved Measurements of ‘Tunnel Noise’ Pressure Fluctuations in the AEDC Hypervelocity Wind Tunnel No. 9,” AIAA Paper 2011-1200, January, 2011.

25. Berridge, D. C., Casper, K. M., Rufer, S. J., Alba, C. R., Lewis, D. R., Beresh, S. J., and Schneider, S. P., "Measurements and Computations of Second-Mode Instability Waves in Three Hypersonic Wind Tunnels", AIAA Paper 2010-5002, June, 2010.

26. Berridge, D. C., *Measurements of Second-Mode Waves in Hypersonic Boundary Layers with a High-Frequency Pressure Transducer*, Master's thesis, Purdue University, 2010.

27. Hornung, H. & Parziale, N. J., “Spectral characteristics of pitot noise,” Paper 301, *Proc. 29th Intl. Symp. on Shock Waves*, July 15-19, 2013, Madison, WI.

28. Spina, E. F., and McGinley, C. B., “Constant-temperature anemometry in hypersonic flow: critical issues and sample results,” *Experiments in Fluids, Vol. 17*, Springer-Verlag, pp. 365-374, 1994.

29. Weinstein, L. M., “Large-Field High-Brightness Focusing Schlieren System,” *AIAA Journal*, Vol. 31, No. 7, July 1993, pp 1250-1255.

30. Settles, G. S. *Schlieren and Shadowgraph Techniques*. Springer-Verlag, Berlin Heidelberg New York, 1st ed., 2001.

31. McIntyre, S. S., Stanewsky, E., and Settles, G. S., “An Optical Deflectometer for the Quantitative Analysis of Turbulent Structures,” Proc. 14th International Congress on Instrumentation in Aerospace Simulation Facilities, Rockville, MD, Oct. 1991. Pp. 34-42.

32. Alvi, F. S., Settles, G. S., and Weinstein, L. M., “A Sharp-Focusing Optical Deflectometer,” AIAA Paper 93-0629, Jan. 1993.

33. Garg, S. and Settles, G. S., “Measurements of a supersonic turbulent boundary layer by focusing schlieren deflectometry,” *Experiments In Fluids*, Vol. 25, No. 3, 1998, pp. 254–264.

34. VanDercreek, C. “Hypersonic Application of Focused Schlieren and Deflectometry,” M.S. Thesis, Department of Aerospace Engineering, University of Maryland, College Park, MD, 2010.

35. Lewis, D. R., and Coblish, J. C., “Expanded Measurement Capabilities at the AEDC Hypervelocity Wind Tunnel No. 9,” AIAA Paper 2010-4791, June 2010.

36. Fisher, M. J. and F. R. Krause, “The Crossed-Beam Correlation Technique,” J. Fluid Mechanics, Vol. 28, No. 4, 1967, pp. 705-717.

37. Fisher, M. J. and Johnston, K. D., “Turbulence Measurements in Supersonic, Shock-Free Jets by the Optical Crossed-Beam Method,” NASA TN D-5206, Feb. 1970.

38. Wilson, L. N., Krause, F. R., and Kadrmas, K. A., “Optical Measurements of Sound Source Intensities in Jets”, Basic Aerodynamic Noise Research, NASA SP-207, Washington D.C., 1969, pp. 147-160.

39. Funk, B. H., and Johnston, K. D., “Laser Schlieren Crossed-Beam Measurements in a Supersonic Jet Shear Layer,” *AIAA Journal*, Vol. 8, No. 11, 1970, pp. 2074-2075.

40. Wilson, L. N., and Damkevala, R. J., “Statistical Properties of Turbulent Density Fluctuations,” J. Fluid Mechanics, Vol. 43, No. 2, 1970, pp. 291-303.

41. Martin. R. A., "Studies of Scalar Turbulence in Air Downstream of a Heated Grid," Ph.D. Dissertation, Department of Aerospace Engineering, Iowa State University, Ames, IA, 1975.

42. Grandke, T., "Theory and Application of the Laser Shadow Technique," Experiments in Fluids Vol. 3, Springer-Verlag, 1985, pp. 77-86.

43. Grandke, T., "A Crossed Beam Laser Shadow Technique for Spatially Resolved Measurements in Turbulent Flow," Experiments in Fluids Vol. 4, Springer-Verlag, 1986, pp. 289-295.

44. Smeets, G., "Laser Interferometer for High Sensitivity Measurements on Transient Phase Objects," *IEEE Transactions on Aerospace and Electronic Systems*, Vol. 8, No. 2, pp 186–190, 1972.

45. Smeets, G., "Laser-Interferometer mit grossen, fokussierten Lichtbündeln für lokale Messungen," Institut Saint-Louis Report ISL - N 11/73, 1973.

46. Smeets, G., "Verwendung eines Laser-Differentialinterferometers zur Bestimmung lokaler Schwankungsgrössen sowie des mittleren Dichteprofils in einem turbulenten Freistrahl". Institut Saint-Louis Report ISL - N 20/74, 1974.

47. Smeets, G., "Flow Diagnostics by Laser Interferometry," *IEEE Transactions on Aerospace and Electronic Systems*, Vol. 13, No. 2, pp 82–90, 1977.

48. Smeets, G., and George, A., "Anwendungen des Laser-Differentialinterferometers in der Gasdynamik," Institut Saint-Louis Report ISL - N 28/73. 1973.

49. Parziale, N. J., "Slender-Body Hypersonic Boundary-Layer Instability," Ph.D. Dissertation, Department of Aerospace (GALCIT), California Institute of Technology, Pasadena, CA, May, 2013.

50. Parziale, N. J., Shepherd, J. E., and Hornung, H. G., "Reflected Shock Tunnel Noise Measurement by Focused Differential Interferometry," *Proc. of 42nd AIAA Fluid Dynamics Conference and Exhibit*, New Orleans, Louisiana, 2012b. AIAA-2012-3261.

51. Parziale, N. J., Shepherd, J. E., and Hornung, H. G., "Differential Interferometric Measurement of Instability at Two Points in a Hypersonic Boundary Layer," *Proc. of 51st AIAA Aerospace Sciences Meeting Including the New Horizons Forum and Aerospace Exposition*, Grapevine, Texas, 2013a. AIAA-2013-0521.

52. Parziale, N. J., Shepherd, J. E., and Hornung, H. G., “Differential Interferometric Measurement of Instability in a Hypersonic Boundary Layer,” *AIAA Journal*, Vol. 53, No. 3, pp. 750-754, 2013.

53. Sanderson, S. R., “Simple, adjustable beam splitting element for differential interferometers based on photoelastic birefringence of a prismatic bar,” *Rev. Sci. Instrum*. 76, 113703 (2005).

54. Biss, M. M., Settles, G. S., and Sanderson, S. R., "Differential schlieren-interferometry with a simple adjustable Wollaston-like prism," *Applied Optics*, 47(3):328-335, 2008.

55. Dodge, M., “Refractive properties of magnesium fluoride,” *Appl. Opt.* 23,12 1980-85, 1984.

56. Lu, F. K., "Fin-Generated Shock-Wave Boundary-Layer Interactions," Ph.D. Thesis, Mechanical Engineering Dept., Penn State University, Feb. 1988.

57. Gladstone, J. H. and Dale, T. P. “Researches of the refraction, dispersion, and sensitiveness of liquids.” *Philos. Trans. Roy. Soc. London*. Vol. 153: pp 317-343. 1864.

58. Steel, W. H. *Interferometry*. Cambridge University Press. 2nd Edition. 1983.

59. Born, M. and Wolf, E. *Principles of Optics*. Cambridge University Press. 7th edition. 1999.

60. R. Waxler, D. Horowitz, and A. Feldman, "Optical and physical parameters of Plexiglas 55 and Lexan," Appl. Opt. 18, 101-104 (1979).

61. Bendat, J. S. and Piersol, A. G. *Random Data: Analysis and Measurement Procedures*. John Wiley & Sons. 2nd Edition, 1986.

62. George, W. K. "Lectures in Turbulence for the 21st Century." Department of Thermo and Fluid Engineering, Chalmers University of Technology, Göteborg, Sweden (2005).p 64 [online] http://www.turbulence-online.com/Publications/Lecture_Notes/Turbulence_Lille/TB_16January2013.pdf

63. Chen, C. J. *Vertical Turbulent Buoyant Jets – A Review of Experimental Data*. Pergamon Press. 1980

64. Corrsin, S. “The Decay of Isotropic Temperature Fluctuations in an Isotropic Turbulence.” *J. Aero. Sci.,* 18,6: pp. 417-23. 1951.

65. Roggemann, M. C. and Welsh, B. *Imaging Through Turbulence*. CRC Press. 1996.

66. Tennekes, H. and Lumley, J. L. *A First Course in Turbulence*. The MIT Press. 1973.

67. Klebanoff, P. S. “Characteristics of turbulence in a boundary layer with zero pressure gradient.” NACA TR 1247. 1955.

68. Wygnanski, I., and Fiedler, H. "Some measurements in the self-preserving jet," *J. of Fluid Mech.*, Vol. 38, No. 3, 1969, pp. 577-612

69. Rodi, W. "A new method of analyzing hot-wire signals in highly turbulent flow, and its evaluation in a round jet," *DISA Information*, Vol. 17, 1975, pp. 9-18

70. Hussein, J. H., Capp, S. P., and George, W. K. "Velocity measurements in a high-Reynolds-number, momentum-conserving, axisymmetric, turbulent jet," *J. of Fluid Mech.*, Vol 258, 1994, pp. 31-75

71. Witze, P. O., "Centerline Velocity Decay of Compressible Free Jets," *AIAA Journal*, Vol. 12, No. 4, Apr. 1974, pp. 417-418.

72. Kleinstein, G., "Mixing in Turbulent Axially Symmetric Free Jets," *AIAA Journal of Spacecraft & Rockets*, Vol. 1, No. 4, July-Aug. 1964, pp. 403-408

73. Anderson, J., *Modern Compressible Flow: With Historical Perspective*, McGraw-Hill, New York, NY, 3rd ed., 2002.

74. Chen, C. J., and Rodi, W. *Vertical Turbulent Buoyant Jets – A Review of Experimental Data,* Pergamon Press, New York, NY, 1980

75. Panda, J., and Seasholtz, R. G., "Density Fluctuation Measurement in Supersonic Fully Expanded Jets Using Rayleigh Scattering," AIAA Paper 99-1870. 1999.

76. Bounitch, A., Lewis, D. R., and Lafferty, J. F., "Improved Measurements of 'Tunnel Noise' Pressure Fluctuations in the AEDC Hypervelocity Wind Tunnel No. 9," AIAA Paper 2011-1200, January, 2011.

77. Lafferty, J. F., and Norris, J. D., "Measurements of Fluctuating Pitot Pressure, 'Tunnel Noise', in the AEDC Hypervelocity Wind Tunnel No. 9," AIAA Paper 2007-1678, February 2007.

78. Thomas, S. "A simple turbulence simulator for adaptive optics," *Proc. SPIE*, Vol. 5490, 2004.

79. Rampy, R. "New method of fabricating phase screens for simulated atmospheric turbulence," *Proc. SPIE*, Vol. 7736, 2010.

80. Rampy, R. "Production of Phase Screens for Simulation of Atmospheric Turbulence," *Appl. Optics*, Vol. 51, No. 36, 20 Dec. 2012.

VITA

Matthew R. Fulghum

Matthew Fulghum received his Bachelor of Science degree magna cum laude in mechanical engineering with a double major in German studies in 2010 from Union College, Schenectady, NY. He came to the Pennsylvania State University as a doctoral student in July, 2010 to study high-speed fluid dynamics under Prof. Gary Settles in the Penn State Gas Dynamics Laboratory.

- Fulghum, M.R., Hargather, M.J., and Settles, G.S., "Integrated Impactor/Detector for a High-Throughput Explosive-Trace Detection Portal," *IEEE Sensors Journal*, vol.13, no.4, pp.1252-1258, April 2013.